NUCLEAR MAGNETIC RESONANCE STUDIES OF BIOFILM – POROUS MEDIA SYSTEMS

by

Catherine Mullinnix Kirkland

A dissertation submitted in partial fulfillment
of the requirements for the degree

of

Doctor of Philosophy

in

Engineering

MONTANA STATE UNIVERSITY
Bozeman, Montana

July 2017

DEDICATION

To Tim, Fergus, and Liam

ACKNOWLEDGMENTS

This material is based upon work supported, in part by the US Department of Energy, Office of Science under Award DE-SC0006376 and DE-FE0024296. Any opinions, findings and conclusions or recommendations expressed in this material are those of the author(s) and do not necessarily reflect the views of the Department of Energy.

This work is supported by the National Science Foundation (NSF) Graduate Research Fellowship Program under Grant No. DGE-1049562. The work comprising Chapter 9 was also supported by the Netherlands Organisation for Scientific Research (NWO) in conjunction with NSF as part of the Graduate Research Opportunities Worldwide program. Experiments conducted on the 22T (950 MHz) NMR instrument were supported by uNMR-NL, an NWO-funded National Roadmap Large-Scale Facility of the Netherlands (project 184.032.207).

TABLE OF CONTENTS

TABLE OF CONTENTS – CONTINUED

TABLE OF CONTENTS – CONTINUED

TABLE OF CONTENTS – CONTINUED

TABLE OF CONTENTS – CONTINUED

LIST OF TABLES

LIST OF FIGURES

LIST OF FIGURES – CONTINUED

LIST OF FIGURES – CONTINUED

Figure Page

LIST OF FIGURES – CONTINUED

Figure Page

ABSTRACT

Nuclear magnetic resonance (NMR) allows for *in-situ* non-invasive studies of opaque systems over a wide range of length and time scales, making the method uniquely suited to studies of biofilms and porous media. The research comprising this thesis uses NMR to explore biophysical, chemical, and transport properties within heterogeneous porous media systems at both a macro- and micro-scale. The macro-scale projects validate a low-field borehole NMR instrument to monitor field-scale environmental engineering applications like subsurface biofilms and microbially-induced calcite precipitation (MICP). Subsurface biofilms are central to bioremediation of chemical contaminants in soil and groundwater whereby micro-organisms degrade or sequester environmental pollutants like nitrate, hydrocarbons, chlorinated solvents and heavy metals. When composed of ureolytic microbes, subsurface biofilms can also induce calcite precipitation. MICP has engineering applications that include soil stabilization and subsurface barriers, as well as sealing of cap rocks and well-bore regions for carbon dioxide sequestration. To meet the design goals of these beneficial applications, subsurface biofilms and MICP must be monitored over space and time – a challenging task with traditional methods. The low-field borehole NMR tool recorded changes in the T_2 relaxation distribution where enhanced relaxation indicated biofilm accumulation in a sand bioreactor and in subsurface soil. Additionally, the tool was able to detect MICP in a sand bioreactor. The changed mineral surface of the sand lead to an increase in T_2 relaxation times. The complementary high-field NMR project investigated micro-scale internal structures and mass transport within biofilm granules used for wastewater treatment. Granular sludge, composed of spherical aggregates of biofilm grown without a carrier, is an innovative biological treatment method with the potential to vastly reduce the cost of wastewater treatment without sacrificing efficiency. Large gaps remain, however, in our understanding of the fundamental formation mechanisms and the factors that control granule activity and stability. Magnetic resonance imaging (MRI) identified heterogeneous internal structures within aerobic granular sludge where relaxation rates and diffusion coefficients vary. Ultimately, these results will help improve modeling for optimization of granular sludge wastewater treatment process design.

INTRODUCTION

Nuclear Magnetic Resonance (NMR) is sensitive over varying length and time scales to the physical and chemical environments, as well as translational motion, that hydrogen-bearing species experience. NMR is non-invasive, non-destructive, and can be applied to opaque samples in diverse applications including subsurface biogeochemical investigations and high-resolution imaging of micro-scale structures within biofilms. Especially in these applications, magnetic resonance can measure physical features or characteristic behaviors that are challenging to directly observe with other methods.

The experiments described in this thesis use NMR or Magnetic Resonance Imaging (MRI) to explore biofilm – porous media systems. The experiments can be broadly classified into two categories, of which the first represents the vast majority of this thesis: 1) low-field NMR detection of macro-scale biofilm accumulation and biomineralization in porous media for in-situ bioremediation applications, and 2) high-field NMR and MRI measurements of granular biofilms used in wastewater treatment to identify micro-scale internal structural features and their influence on reactive transport within the biofilm. These two categories rely on the same method, NMR, but use different hardware configurations and field strengths. The two categories also focus on biofilm systems, though the biofilms of interest in the two cases are cultivated for different applications.

Biofilms are mixed microbial aggregates, typically adhered to a surface with a sticky hydrogel called extracellular polymeric substance, or EPS [1, 2]. EPS consists of polysaccharides, proteins, DNA, and other entangled macro-molecules [3, 4]. While

some biofilms pose significant challenges to human health [5] or infrastructure [6], beneficial biofilms can be cultivated to effect biogeochemical conversions or hydrodynamic changes in the subsurface as part of a bioremediation project [7, 8]. Biofilms can also be used to induce mineral precipitation in the subsurface with applications including well-bore leakage mitigation [9] and geotechnical engineering [10, 11]. In the granular sludge system studied in the final chapter of this thesis, the biofilm granules are microbial aggregates which self-assemble under specific conditions without a support material. In this case, the granule is both the biofilm and the porous media.

The remainder of this introduction puts the two types of NMR measurements in to historical context and outlines the organization of the thesis.

Low-field NMR

In natural materials such as soils and rock formations, the use of high-field NMR, typically defined as greater than 200 MHz, poses experimental challenges. Natural porous media, in contrast to model media like glass beads, contains minerals with a wide range of magnetic susceptibilities. When placed in a background magnetic field, these contrasts in magnetic susceptibility generate internal gradients in the local, pore-scale magnetic field that broaden the spectral peaks and cause rapid signal attenuation. Reducing the strength of the applied magnetic field reduces the influence of these local gradients, allowing signal to be captured from natural materials, though with reduced signal to noise and spectral resolution than high-field methods [12]. Low-field devices typically operate in the range between several hundred kHz to 10MHz. Low-field NMR

devices include well-logging tools used in the oil and gas industry to measure the distribution of pore sizes in the formation and quantify fuel-bearing reservoirs [13, 14], surface probes that measure soil moisture or water intrusion into concrete surfaces [15-18], and small diameter probes, like the Vista Clara Javelin, to measure aquifer characteristics in the near subsurface [19].

The advent of low-cost and portable low-field NMR instrumentation in the last decade has led to an expansion of potential applications for the technology. Thus far, low-field NMR devices have not been applied in practice to monitor in-situ permeability reduction due to biofilm accumulation and biomineralization. The research within this thesis demonstrates that the Javelin low-field NMR logging tool can provide spatio-temporally resolved data regarding changing physico-chemical conditions in the near subsurface to improve monitoring capabilities and inform critical decision-making. Specifically, the device detects changes in signal relaxation response indicative of biofilm accumulation or microbially-induced calcite precipitation (MICP). Current methods to determine the extent of these processes *in situ* are limited and indirect. Using a NMR probe as a monitoring method may improve the efficacy of subsurface engineering projects involving biofilms and or MICP by allowing for simpler and more cost-effective assessment of their integrity.

High-field NMR and MRI

High-field NMR has a rich history of use in laboratory biofilm systems. For more than two decades, high-field NMR has been used to study mass transport and hydrodynamics in a variety of model bioreactors using relaxometry and displacement measurements [20-26]. Potter et al. used diffusion-weighted NMR to detect bacterial cells and measure cell density within porous media [27]. MRI allows researchers to spatially resolve biofilm accumulation in porous media or capillaries through mapping regions with differing relaxation rates, where faster relaxation indicates the presence of biofilm [28, 29]. MRI can identify internal structural features of spherical biofilm aggregates, called granular sludge or biofilm granules [30, 31].

The high-field NMR experiments move the research from macro-scale field applications of commercially available low-field NMR technology to micro-scale exploration of fundamental processes related to formation of, and reactive mass transport within, granular sludge. By their very nature as spherical biofilm aggregates, granules are composed of a variety of microniches—aerobic, anoxic, anaerobic —where diverse bio-chemical conversions can occur simultaneously within the same granule [32, 33]. As a result, granular sludge treatment processes have the potential to vastly reduce the costs of cleaning wastewater by minimizing the capital costs associated with construction of separate process reactors and clarifiers, as well as reducing ongoing operations costs associated with aeration [34, 35]. The ultimate goal of the high-field NMR experiments on biofilm granules is to fill the gaps in our understanding of fundamental formation

mechanisms and conversion processes so that full exploitation of the technology for wastewater treatment can be realized.

The high-field NMR research explores the structure and function of aerobic biofilm granules using pulsed field gradient (PFG) NMR and MRI by measuring spatially-resolved relaxation rates and diffusion coefficients of single granules in a static test tube. Ongoing experiments with flow-through cells will explore the role of wastewater particulates and particulate substrate in the formation, stability, and activity of the granules by measuring the propagator, or probability of displacement, of tracer particles. The results of these experiments will be used to refine the models used to simulate granule formation and substrate removal. These models are instrumental in process design optimization and hydraulic modeling of full-scale granular sludge wastewater treatment plants.

Outline

First, this thesis introduces NMR theory in Chapter 2, including discussions of the quantum and classical mechanical underpinnings of the technology, as well as excitation, relaxation, signal detection, basic pulse sequences, and an introduction to imaging and measurement of motion. Chapter 3 addresses more advanced NMR concepts related to encoding for diffusive motion and coherent flow, Brownstein and Tarr's [13] characterization of signal relaxation behavior in various pore geometries and multi-dimensional methods to measure molecular motion.

Chapters 4 – 7 describe the low-field NMR experiments conducted during this thesis, beginning with a review of low-field borehole NMR applications in the near subsurface. This invited manuscript is under review for publication in the *Vadose Zone Journal*. Chapter 5 presents results of a laboratory experiment using the low-field NMR logging tool to detect biofilm accumulation in a model well-bore reactor. T_2 relaxation distributions were measured over time while biofilm was cultivated in the reactor, resulting in a shortening of the mean log T_2 relaxation time. Biofilm growth was confirmed with microscopy and microbiological methods. The manuscript was published in *Groundwater Monitoring and Remediation*. Following the successful laboratory demonstration, the biofilm detection experiments were conducted in a field study at an engineered field-testing facility in Butte, Montana. Again, the low-field NMR logging tool detected accumulation and removal of biofilm in the soil surrounding the test wells by recording changes in the measured T_2 relaxation distributions. The manuscript comprising Chapter 6 is published in *Environmental Science and Technology*. Chapter 7 describes a second laboratory experiment using the low-field NMR logging tool, this time applied to the detection of calcite precipitation in a sand-filled model well-bore reactor. T_2 relaxation distributions recorded during the biomineralization process showed an increase in the mean log T_2 time and a bifurcation of the initial single relaxation mode into a small population with very fast relaxation and a larger population with slower relaxation. This manuscript is also published in *Environmental Science and Technology*.

Chapters 8 and 9 shift the focus from low-field borehole NMR experiments in porous media to high field NMR and MRI experiments on wastewater biofilms. Chapter

8 describes research the author collaborated on with Dr. Maria Pia Herrling, a summer visitor to the Montana State University Magnetic Resonance Lab from Karlsruhe Institute of Technology in Karlsruhe, Germany. As part of her research into water diffusion in various biofilm structures, including floccular sludge, granular sludge, and biofilm grown on plastic carriers, Dr. Herrling measured diffusion-relaxation correlations at MSU with the author. The manuscript has been submitted for publication in *Biotechnology and Bioengineering*. Finally, Chapter 9 describes ongoing experimental work on the structure and diffusion properties of aerobic granular sludge biofilms sampled from full-scale wastewater treatment plants in the Netherlands. High-field MRI was used to image the complex and heterogeneous internal structure of the granules. These data were collected in the Netherlands at Wageningen University and Research and at the national NMR facility at the University of Utrecht under the supervision of Dr. Henk Van As as part of an international collaboration with Dr. Merle de Kreuk at Delft University of Technology. Additional high field PFG NMR experiments related to diffusion and transport within the granules are currently being conducted at MSU using samples from Dutch treatment plants. As this chapter includes work still in progress, the data and results presented are preliminary and require further validation prior to publication in peer reviewed journals. This research will be presented at the International Water Association's 10th International Conference on Biofilm Reactors in Dublin, Ireland, in May 2017.

References

1. Characklis, W.G. and K.C. Marshall, Eds., *Biofilms*. 1990, New York: John Wiley & Sons, Inc.

2. Stoodley, P., et al., *Biofilms as complex differentiated communities.* Annual Review of Microbiology, 2002. **56**: p. 187-209.

3. Allison, D.G., *The biofilm matrix.* Biofouling, 2003. **19**(2): p. 139-150.

4. Sutherland, I.W., *Biofilm exopolysaccharides: a strong and sticky framework.* Microbiology, 2001. **147**: p. 3-9.

5. Costerton, J.W., P.S. Stewart, and E.P. Greenberg, *Bacterial biofilms: A common cause of persistent infections.* Science, 1999. **284**(5418): p. 1318-1322.

6. Camper, A.K., *Organic matter, pipe materials, disinfectants and biofilms in distribution systems*. 2014, IWA Publishing. p. 73-94.

7. Cunningham, A.B., et al., *Subsurface biofilm barriers for the containment and remediation of contaminated groundwater.* Bioremediation Journal, 2003. **7**(3-4): p. 151-164.

8. Taylor, S.W. and P.R. Jaffe, *Enhanced in-situ biodegradation and aquifer permeability reduction.* Journal of Environmental Engineering-ASCE, 1991. **117**(1): p. 25-46.

9. Cunningham, A.B., et al., *Abandoned well CO2 leakage mitigation using biologically induced mineralization: current progress and future directions.* Greenhouse Gases-Science and Technology, 2013. **3**(1): p. 40-49.

10. Dejong, J.T., et al., *Biogeochemical processes and geotechnical applications: progress, opportunities and challenges.* Geotechnique, 2013. **63**(4): p. 287-301.

11. Phillips, A.J., et al., *Engineered applications of ureolytic biomineralization: a review.* Biofouling, 2013. **29**(6): p. 715-733.

12. Sanderlin, A.B., et al., *Biofilm detection in natural unconsolidated porous media using a low-field magnetic resonance system.* Environmental Science & Technology, 2013. **47**(2): p. 987-992.

13. Brownstein, K.R. and C.E. Tarr, *Importance of classical diffusion in NMR studies of water in biological cells.* Physical Review A, 1979. **19**(6): p. 2446-2453.

14. Timur, A., *Pulsed nuclear magnetic resonance studies of porosity, movable fluid, and permeability of sandstones.* Journal of Petroleum Technology, 1969. **21**(JUN): p. 775-&.

15. Blümich, B., F. Casanova, and S. Appelt, *NMR at low magnetic fields.* Chemical Physics Letters, 2009. **477**(4–6): p. 231-240.

16. Fukushima, E., *Nuclear magnetic resonance as a tool to study flow.* Annual Review of Fluid Mechanics, 1999. **31**(1): p. 95.

17. Marble, A.E., et al., *A constant gradient unilateral magnet for near-surface MRI profiling.* Journal of Magnetic Resonance, 2006. **183**(2): p. 228-234.

18. Sucre, O., et al., *Low-field NMR logging sensor for measuring hydraulic parameters of model soils.* Journal of Hydrology, 2011. **406**(1–2): p. 30-38.

19. Walsh, D., et al., *A small-diameter NMR logging tool for groundwater investigations.* Groundwater, 2013. **51**(6): p. 914-926.

20. Gjersing, E.L., et al., *Magnetic resonance microscopy analysis of advective transport in a biofilm reactor.* Biotechnology and Bioengineering, 2005. **89**(7): p. 822-834.

21. Hornemann, J.A., et al., *Biopolymer and water dynamics in microbial biofilm extracellular polymeric substance.* Biomacromolecules, 2008. **9**(9): p. 2322-2328.

22. Seymour, J.D., et al., *Anomalous fluid transport in porous media induced by biofilm growth.* Physical Review Letters, 2004. **93**(19).

23. Seymour, J.D., et al., *Magnetic resonance microscopy of biofouling induced scale dependent transport in porous media.* Advances in Water Resources, 2007. **30**(6-7): p. 1408-1420.

24. Wagner, M., et al., *Online assessment of biofilm development, sloughing and forced detachment in tube reactor by means of magnetic resonance microscopy.* Biotechnology and Bioengineering, 2010. **107**(1): p. 172-181.

25. Lewandowski, Z., et al., *NMR imaging of hydrodynamics near microbially colonized surfaces.* Water Science and Technology, 1992. **26**(3-4): p. 577-584.

26. Van As, H. and P. Lens, *Use of H-1 NMR to study transport processes in porous biosystems.* Journal of Industrial Microbiology & Biotechnology, 2001. **26**(1-2): p. 43-52.

27. Potter, K., et al., *Assay for bacteria in porous media by diffusion-weighted NMR.* Journal of Magnetic Resonance. Series B, 1996. **113**: p. 9-15.

28. Hoskins, B.C., et al., *Selective imaging of biofilms in porous media by NMR relaxation.* Journal of Magnetic Resonance, 1999. **139**(1): p. 67-73.

29. Seymour, J.D., et al., *Magnetic resonance microscopy of biofilm structure and impact on transport in a capillary bioreactor.* Journal of Magnetic Resonance, 2004. **167**(322-327).

30. Gonzalez-Gil, G., et al., *Cluster structure of anaerobic aggregates of an expanded granular sludge bed reactor.* Applied and Environmental Microbiology, 2001. **67**(8): p. 3683-3692.

31. Lens, P.N.L., et al., *Diffusional properties of methanogenic granular sludge: H-1 NMR characterization.* Applied and Environmental Microbiology, 2003. **69**(11): p. 6644-6649.

32. Da-Wen, G. and T. Yu, *Versatility and application of anaerobic ammonium-oxidizing bacteria.* Applied Microbiology & Biotechnology, 2011. **91**(4): p. 887-894.

33. de Kreuk, M., J.J. Heijnen, and M.C.M. van Loosdrecht, *Simultaneous COD, nitrogen, and phosphate removal by aerobic granular sludge.* Biotechnology and Bioengineering, 2005. **90**(6): p. 761-769.

34. de Kreuk, M.K., N. Kishida, and M.C.M. van Loosdrecht, *Aerobic granular sludge - state of the art.* Water Science and Technology, 2007. **55**(8-9): p. 75-81.

35. Lotti, T., et al., *Pilot-scale evaluation of anammox-based mainstream nitrogen removal from municipal wastewater.* Environmental technology, 2015. **36**(9): p. 1167-77.

INTRODUCTION TO NUCLEAR MAGNETIC RESONANCE

Nuclear magnetic resonance (NMR) relies on the quantum physical property of angular momentum intrinsic to a single nucleus and the response of that nucleus to a magnetic field to study the behavior of macroscopic systems consisting of large ensembles of nuclei over varying length and time scales. The discussion in this thesis will begin with the quantum and classical mechanical basis for NMR measurements before moving into a description of basic NMR techniques for imaging and measurement of molecular motion. This chapter relies heavily on reference works by Paul Callaghan[1, 2]. Other primary original sources are referenced in the text where applicable.

Quantum Mechanics NMR Theory

For any single nucleus, there is a discrete set of energy states defined by quantum mechanics. Since we are observing the behavior of a sample composed of nuclei on the order of Avogadro's number (10^{23}), however, the range of possibilities for the ensemble appears continuous. Because of its fundamental connection to the subject of NMR, it is necessary to first discuss the quantum mechanical basis of nuclear angular momentum, often called spin angular momentum.

Spin Angular Momentum

The spin state of a nuclear isotope is described by the angular momentum, or spin, quantum number *I*, which is a fixed integer or half-integer value and characterizes the nucleus in its stable ground state. The spin quantum number *I* exists in a basis set of discrete values of the angular momentum, *m*, measured along the z-axis, where $m = -I, (-I + 1), (I - 1), I$. For example, the ^{1}H proton and ^{13}C both have $I = ½$. This means that ^{1}H and ^{13}C have two discrete energy states possible during a measurement, $m = -½$ and $m = +½$, referred to as 'spin down' and 'spin up', respectively.

The effect of 'spin' is that each nucleus has a magnetic dipole moment, $\boldsymbol{\mu}$, where $\boldsymbol{\mu} = \gamma \mathbf{s}$. The constant of proportionality, γ, is called the gyromagnetic ratio and is defined as the ratio of the magnetic dipole moment (**μ**) to the nuclear angular momentum (**s**). The gyromagnetic ratio for ^{1}H is $\gamma = 2.675 \times 10^{8}$ rad/(T s) and is among the highest of all nuclear isotopes. This intrinsic property of the hydrogen proton, as well as its abundance in nature, explains the predominance of ^{1}H NMR within the larger field of magnetic resonance research and applications.

NMR measurements are conducted in order to explore the system energy state. In other words, we measure an observable quantity to describe the energy state of the system we are interested in and which informs us about the molecular environment. When we make a measurement, we affect the quantum state of the system. In fact, we *must* affect the quantum state of the system *in order* to make a measurement. The quantum mechanical nature of a spin system is given by the eigenvalue equation

$$A|a\rangle = a|a\rangle \quad (2.1)$$

where *A* is the observable of interest, the eigenvector $|a\rangle$ is a basis state of *A*, and the eigenvalue a is the observed value of measurement *A*. The eigenvalue is a complex number, containing both amplitude and phase information.

To interpret Equation (2.1), recall that in making quantum mechanical measurements, we are faced with the Heisenberg uncertainty principle. That is, we cannot simultaneously know both the position and momentum of an atomic nucleus; we can only know the *probability* of a nucleus having a given position and momentum. If a measurement of *A* is made while the system is in state$|a\rangle$, then the observed value, or amplitude, of the measurement must be a with certainty. If the system, however, is in a general admixed state resulting from superposition, denoted by $|\Psi\rangle$, then the eigenvalue is returned with the probability, $|a_m|^2$.

To apply these concepts to the spin quantum number, *I*, consider the case where the observable of interest is the component of angular momentum about a particular axis, $I = \overline{\langle I_x \rangle}\mathbf{i} + \overline{\langle I_y \rangle}\mathbf{j} + \overline{\langle I_z \rangle}\mathbf{k}$ where **i**, **j**, and **k** are unit vectors along the x, y, and z-axes, respectively. In the case of the operator, I_z, the equation

$$\langle \Psi | I_z | \Psi \rangle = \sum_m |a_m|^2 \, m \quad (2.2)$$

gives the probability that the measurement I_z resulted in a change of energy state from some initial basis state to a final basis state. Other important operators include the raising and lowering operators, $I_+ = I_x + iI_y$ and $I_- = I_x - iI_y$, respectively. These operators convert $|-\frac{1}{2}\rangle$ a basis state to a $|+\frac{1}{2}\rangle$ state, and vice versa.

Since position and momentum of Heisenberg's uncertainty principle are also components of energy, as potential and kinetic energy, respectively, it is constructive to express changes in the quantum energy state of a system in terms of the Hamiltonian, or total energy operator, *H*. The dynamics of the spin system are described by the Schrödinger equation

$$i\hbar\frac{\partial}{\partial t}|\Psi(t)\rangle = H|\Psi(t)\rangle \quad (2.3)$$

where $\hbar$ is Planck's constant. The Schrödinger equation shows that the change in the energy state with respect to time is related to the total energy of the system. For a Hamiltonian constant in time, the evolution of the energy state with time is

$$|\Psi(t)\rangle = exp\left(-iH\frac{t}{\hbar}\right)|\Psi(0)\rangle \quad (2.4)$$

Spin Magnetism and the Zeeman Interaction

Outside of an applied magnetic field, nuclear magnetic dipoles are randomly oriented and no net magnetization occurs. However, in the presence of a static magnetic field, $\mathbf{B_0}$, we observe the Zeeman effect where the magnetic dipole moments reside in one of two quantum energy states. The nuclear magnetic dipole moments align themselves either parallel or anti-parallel to the $\mathbf{B_0}$ field, with a slight preference for parallel alignment. The parallel 'spin up' alignment corresponds to the lower energy state$|+\frac{1}{2}\rangle$, while anti-parallel 'spin down' alignment is the higher energy state$|-\frac{1}{2}\rangle$. For a proton in a static magnetic field, $\mathbf{B}_0$, along the *z*-axis, the Zeeman Hamiltonian is

$$H_{Zeeman} = -\gamma\hbar B_0 I_z \quad (2.5)$$

This means that the difference in energy between the two possible spin states is equal to $\Delta E = \gamma\hbar B_o$ and that the spins precess about the *z*-axis (Figure 2.1).

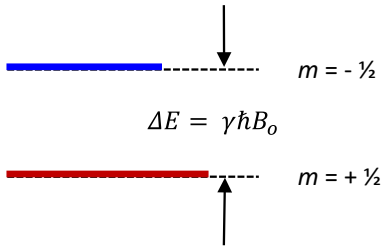

Figure 2.1. The two quantum spin states are separated by an energy difference of $\boldsymbol{\gamma\hbar B_o}$which is also the resonant frequency of spins within the system. The slight preference for the lower energy state yields a net magnetization on the order of parts per million.

Writing Equation (2.5) in terms of angular frequency and dropping Planck's constant, it is apparent that the intrinsic frequency of the system is equal to γB_0, called the Larmor frequency, ω_0. The Larmor frequency is both the precession frequency of all the spin states around the z-axis as seen in the Zeeman Hamiltonian, but also the frequency of spins 'flipping' between the two possible energy states, *m* = - ½ and *m* = + ½.

For a large number of nuclei, quantum properties can be expressed using classical statistics over the ensemble. The equation

$$\overline{\langle\Psi|I_z|\Psi\rangle} = \frac{1}{2}\left[\overline{\left|a_{\frac{1}{2}}\right|^2} - \overline{\left|a_{-\frac{1}{2}}\right|^2}\right] \quad (2.6)$$

demonstrates that the ensemble average energy state resulting from the observation I_z, $\overline{\langle\Psi|I_z|\Psi\rangle}$, is the difference between the populations in the spin up and spin down

states, expressed by $\overline{\left|a_{\frac{1}{2}}\right|^2}$ and $\overline{\left|a_{-\frac{1}{2}}\right|^2}$, respectively. The Boltzmann energy distribution is derived from statistical mechanics and governs the relative sizes of the two populations. The probability of a particular energy state, P_n, within a distribution of energy states is defined as

$$P_n = \frac{\exp\left(-\Delta E/k_B T\right)}{\sum_n \exp\left(-\Delta E/k_B T\right)} \quad (2.7)$$

where ΔE is the energy associated with each state, k_B is the Boltzmann constant, and T is the absolute temperature. Because of the slight preference of spins at thermal equilibrium for the lower energy state$|+\frac{1}{2}\rangle$, a polarization, I_z, aligned with the static magnetic field develops within a sample.

Since the energy difference between the two states, $\gamma\hbar B_o$, is orders of magnitude less than $k_B T$, the net polarization within a sample is typically in the part per million range. Moreover, there is no phase coherence between the spins, so it is not possible to directly measure I_z.

Measurement of the x-component of angular momentum, however, yields

$$\overline{\langle\Psi|I_x|\Psi\rangle} = \frac{1}{2}\left[\overline{a^*_{\frac{1}{2}} a_{-\frac{1}{2}}} + \overline{a^*_{-\frac{1}{2}} a_{\frac{1}{2}}}\right] \quad (2.8)$$

where $a^*_{\pm\frac{1}{2}}$ is the complex conjugate of a. This equation shows that the ensemble average energy state resulting from the observation I_x is the sum of the off-diagonal matrix components and reflects the phase coherence between the + ½ and – ½ spin states, where the relative phase, rather than the absolute phase, is significant.

To handle both the polarization and phase coherence, it is useful to introduce the spin density matrix ρ, a hermitian quantum mechanical operator that evolves according to the Schrödinger equation and directly provides the ensemble averaged expectation value for measurement *A*

$$\langle \Psi|A|\Psi\rangle = Tr|A\rho| = \overline{\langle A\rangle} = \sum_{\Psi} P_{\Psi}\,\langle \Psi|A|\Psi\rangle \quad (2.9)$$

where $Tr|\rho|$ is the trace of ρ—the sum of all state probabilities—and is therefore equal to 1. When *I* is the observable of interest for spin ½ nuclei, the spin density matrix is

$$\rho = \begin{bmatrix} \overline{\left|a_{\frac{1}{2}}\right|^2} & \overline{a^*_{-\frac{1}{2}} a_{\frac{1}{2}}} \\ \overline{a^*_{\frac{1}{2}} a_{-\frac{1}{2}}} & \overline{\left|a_{-\frac{1}{2}}\right|^2} \end{bmatrix} = \begin{bmatrix} \frac{1}{2} + \overline{\langle I_z\rangle} & \overline{\langle I_x - iI_y\rangle} \\ \overline{\langle I_x + iI_y\rangle} & \frac{1}{2} - \overline{\langle I_z\rangle} \end{bmatrix} \quad (2.10)$$

The major implication of the spin density matrix is that specifying the vector components of the spin quantum number $\mathbf{I} = \overline{\langle I_x\rangle}\mathbf{i} + \overline{\langle I_y\rangle}\mathbf{j} + \overline{\langle I_z\rangle}\mathbf{k}$ allows full specification of the four matrix elements and therefore defines all the energy states of an ensemble of spin ½ nuclei. Recall, these energy states are the results of a direct NMR measurement of I_x, I_y, *or* I_z. On a macroscopic level, the net magnetization of a sample in the laboratory reference frame can be defined as

$$\mathbf{M} = N\gamma\hbar\left[\overline{\langle I_x\rangle}\mathbf{i} + \overline{\langle I_y\rangle}\mathbf{j} + \overline{\langle I_z\rangle}\mathbf{k}\right] \quad (2.11)$$

where *N* is the number of spins per unit volume. Here, then, we see the connection between the macroscopic magnetization in the laboratory reference frame and the quantum energy state of a single nucleus in our sample. Since we define the direction of

the $\mathbf{B}_0$ field as the z-axis, we can directly detect the quantum states I_x and I_y via an NMR measurement, where I_x is the real component and I_y is the imaginary component.

Classical Mechanics NMR Theory

Moving from the scale of a single quantum mechanical nucleus to the macro-scale net magnetization allows use of the language of classical mechanics to describe NMR theory and practice.

Excitation

When a pulse of oscillating current in the radiofrequency (rf) range is introduced along the y-axis in the plane orthogonal to $\mathbf{B}_0$, a magnetic field $\mathbf{B}_1$ is formed along the x-axis. The $\mathbf{B}_1$ field generates a torque, tipping the net magnetization, **M**, into the transverse plane, where it precesses around the z-axis. Analogous to quantum mechanical theory where the magnetic dipole moment produces precession in a static magnetic field, on a macroscopic level the Zeeman effect also produces precession of **M** around $\mathbf{B}_0$ as the magnetic field exerts a torque on the magnetization vector according to

$$\frac{d\boldsymbol{M}}{dt} = \gamma \boldsymbol{M} \times \boldsymbol{B} \quad (2.12)$$

When the system is 'on resonance', both the oscillation of $\mathbf{B}_1$ and the precession of **M** occur at the Larmor frequency, $\omega_0 = \gamma B_0$, and the rf field is defined as

$$\boldsymbol{B}_1(t) = B_1 \cos(\omega_0 t)\,\mathbf{i} - B_1 \sin(\omega_0 t)\,\mathbf{j} \quad (2.13)$$

Performing the cross-product produces the following expressions for the time evolution of the magnetization vector in the laboratory reference frame following excitation:

$$\frac{dM_x}{dt} = \gamma\left[M_y B_0 + M_z B_1 sin\omega_0 t\right]$$

$$\frac{dM_y}{dt} = \gamma[M_z B_1 cos\omega_0 t - M_x B_0] \qquad (2.14)$$

$$\frac{dM_z}{dt} = \gamma\left[-M_x B_1 sin\omega_0 t - M_y B_1 cos\omega_0 t\right]$$

Solving Equations (2.14) for the initial condition **M**(t) = M_0**k** gives

$$M_x = M_0 sin(\omega_1 t) sin(\omega_0 t)$$

$$M_y = M_0 sin(\omega_1 t) cos(\omega_0 t) \qquad (2.15)$$

$$M_z = M_0 cos(\omega_1 t)$$

where $\omega_1 = \gamma B_1$. This solution shows that in the laboratory reference frame, the precession of **M** is a spiral, as the magnetization vector precesses around the $\mathbf{B}_0$ field at ω_0, and about the $\mathbf{B}_1$ field at ω_1 (Figure 2.2).

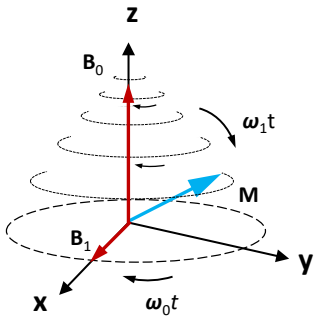

Figure 2.2 Following a 90° rf excitation pulse, the net magnetization vector, M, precesses around B_0 at ω_0 and around B_1 at ω_1 in the laboratory reference frame.

The tip angle, α, is equal to $\omega_1 t$. By controlling the duration of the rf pulse, *t*, and the amplitude of the $\mathbf{B}_1$ field, the net magnetization vector will lie in the transverse plane ($\alpha = \frac{\pi}{2}$) where the induced signal is maximized. This rf pulse is called a 90°, or $\frac{\pi}{2}$ pulse. Similarly, an rf pulse of duration 2*t* will result in **M** aligned with the –*z*-axis, called a 180°, or π pulse. The precession of **M** as it returns to equilibrium induces a current that is measured as a decaying signal by the rf coil.

Reference Frames

To simplify further descriptions of the spin dynamics that occur following excitation with a resonant rf field, it is typical to use a rotating frame of reference with angular frequency ω. Recall the Zeeman Hamiltonian for a static magnetic field, $\mathbf{B}_0$,

$$H_{Zeeman} = -\gamma B_0 I_z \quad (2.16)$$

In the rotating reference frame, an additional term is necessary to account for the frequency of the rotating frame itself, with the result

$$H_{Zeeman-rot} = -\gamma\left(B_0 - {}^{\omega}/_{\gamma}\right)I_z \quad (2.17)$$

For a reference frame rotating in the same sense as the precession (clockwise), the apparent longitudinal magnetic field will be reduced by ω. When an oscillating rf field is applied in the transverse plane to excite the spins from equilibrium, the Hamiltonian in the rotating frame becomes

$$H_{rot} = -\gamma\left(B_0 - {}^{\omega}/_{\gamma}\right)I_z - \gamma B_1 I_x \quad (2.18)$$

When the system is 'on resonance,' $\omega = \omega_0$ and the apparent longitudinal field disappears, leaving the effective magnetic field along the rotating frame x-axis with the

Hamiltonian $H_{rot} = -\gamma B_1 I_x$ (Figure 2.3). Here, the I_x operator is the linear combination of the raising and lowering operators, $\frac{1}{2}(I_+ + I_-)$, meaning that the energy change in the system with time corresponds to the flipping of spins between the 'spin up' and 'spin down' states at a rate of γB_1.

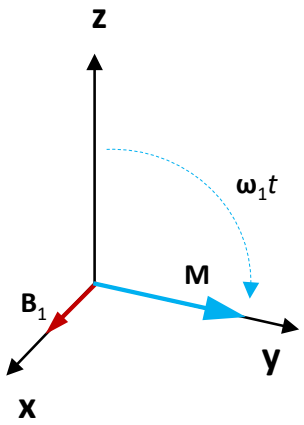

Figure 2.3. In the rotating reference frame, the static B_0 field is not apparent and M lies along the -*y*-axis following excitation with a resonant 90° rf pulse.

Relaxation

The transverse magnetization decays over time following the rf pulse as the spins return to thermal equilibrium along the *z*-axis. This process is termed relaxation. The rate at which the net magnetization decays in the transverse plane and re-forms along the *z*-axis is governed by two relaxation mechanisms, T_1 and T_2. T_1 relaxation, also called spin-lattice relaxation or longitudinal relaxation, is caused by the exchange of energy between spins and the environment, or lattice, and is related to the timescale for the net magnetization to return to thermal equilibrium along the *z*-axis. T_1 relaxation typically occurs on the order of seconds for protons at room temperature.

T_2 relaxation, also called spin-spin relaxation or transverse relaxation, is related to the timescale for the net magnetization to decay in the transverse plane due to dephasing of spin coherence caused by molecular interactions. Energy exchange between magnetic dipoles creates micro-scale magnetic fields that dephase the spins within their sphere of influence. Since some measure of phase coherence is essential for generation and measurement of the induced signal, a loss of phase coherence leads to signal attenuation with time. T_2 relaxation occurs on the order of seconds for liquids at room temperature and on the order of milliseconds for biopolymers in porous media.

Auto-correlation Functions. The time-dependence of relaxation processes is due to molecular motion. A constructive way to describe time-dependent behavior is with the use of auto-correlation functions. When stochastic variable *A* is a molecular quantity that varies as a function of time, then the auto-correlation function of *A* is

$$G(t) = \int_0^\infty A(t')A(t'+t)dt' \quad (2.19)$$

The auto-correlation function *G(t)* describes the probability that *A(t')* is correlated to *A(t' + t)* at some later time. When the system is stationary as is the case in most NMR measurements, the origin of time does not matter; only the interval of time over which measurements are collected is important. Further, in an ensemble of spins where any one spin is statistically equivalent to any other spin over an appropriate period of time, the average over time that is implied by Equation (2.19) can also be interpreted as an average over all particles. Incorporating these concepts and replacing terms into Equation (2.19) gives

$$G(t) = < A(0)A(t) > \quad (2.20)$$

where $<A(0)A(t)>$ is the well-defined ensemble average value of *A* during the interval 0 to *t*. At time zero, *G(t)* is equal to the mean squared value of *A*, $<A(0)^2>$. With increasing time, the relationship between the initial and final values of *A* decays, as the molecule 'loses memory' of its previous states. The characteristic timescale over which this process occurs is called the correlation time, τ_c. When the experimental time, *t*, is greater than the correlation time, τ_c, then there is no correlation with the initial state. The correlation time can be understood as the time for a molecule (nucleus) to rotate about its own axis and is defined by the integral

$$\tau_c = \frac{\int_0^\infty < A(0)A(t) > dt}{< A(0)^2 >} \quad (2.21)$$

Spectral Density Functions. Relaxation is caused by local spin interactions, which vary by both magnitude and the rate of fluctuation of the dipolar Hamiltonian, H_D. In a relaxation experiment where A is the fluctuation of dipolar interactions between spins resulting from molecular tumbling, spin relaxation times are sensitive to the spectrum of the auto-correlation function, its Fourier transform. This spectrum is called the spectral density function, $J(\omega)$, and describes how the magnetic field fluctuations resulting from molecular interactions depend on time and the frequency of precession, ω. For spin-½ nuclei within the Zeeman interaction created by the static magnetic field, $\mathbf{B}_0$, there are three possibilities for behavior between interacting spins. Both interacting spins may remain in their original energy states, described by $J^{(0)}(\omega)$,

$$J^{(0)}(\omega) = \frac{24}{15r_{ij}^6}\frac{\tau_c}{1+\omega^2\tau_c^2} \quad (2.22)$$

where r_{ij} is the radial distance between spin i and spin j. When one of the two spins changes its energy state, $J^{(1)}(\omega)$ results where

$$J^{(1)}(\omega) = \frac{4}{15r_{ij}^6}\frac{\tau_c}{1+\omega^2\tau_c^2} \quad (2.23)$$

Finally, if both spins flip to the other energy state, the resulting spectral density is defined as $J^{(2)}(\omega)$,

$$J^{(2)}(\omega) = \frac{16}{15r_{ij}^6}\frac{\tau_c}{1+\omega^2\tau_c^2} \quad (2.24)$$

Using these expressions for the spectral density function, the differences between the mechanisms for T_1 relaxation as opposed to T_2 relaxation is apparent. The T_1 relaxation rate at the Larmor frequency, ω_0, is given by the equation

$$\frac{1}{T_1} = (\frac{\mu_0}{4\pi})^2 \gamma^4 \hbar^2 \frac{3}{2} I(I+1)\left[J^{(1)}(\omega_0) + J^{(2)}(2\omega_0)\right] \quad (2.25)$$

Qualitatively, this equation shows that T_1 relaxation is affected by spins exchanging energy with the environment, or lattice, as they seek to return to thermal equilibrium within the Zeeman interaction. There is a contribution from spins precessing at frequency ω_0 as well as a contribution at a frequency of $2\omega_0$. There is no contribution from spins that remain in the original energy state.

Conversely, the T_2 relaxation rate at the Larmor frequency, ω_0, is given by the equation

$$\frac{1}{T_2} = (\frac{\mu_0}{4\pi})^2 \gamma^4 \hbar^2 \frac{3}{2} I(I+1)\left[\frac{1}{4}J^{(0)}(0) + \frac{5}{2}J^{(1)}(\omega_0) + \frac{1}{4}J^{(2)}(2\omega_0)\right] \quad (2.26)$$

From this expression, it is evident that T_2 relaxation also depends on the zero-frequency spectral density term, $J^{(0)}(0)$, wherein spins remain in their original energy states. This term implies that there is another energy exchange mechanism aside from the Zeeman interaction that contributes to T_2 relaxation. For this reason, T_2 relaxation will occur at the same rate or faster than T_1 relaxation, but never slower. As the precession frequency, ω_0, or the correlation time of the magnetic field fluctuations, τ_c, increases, the contribution of the zero-frequency term also increases. Faster precession frequencies and longer correlation times, therefore, cause a divergence between the T_1 and T_2 relaxation times (Figure 2.4).

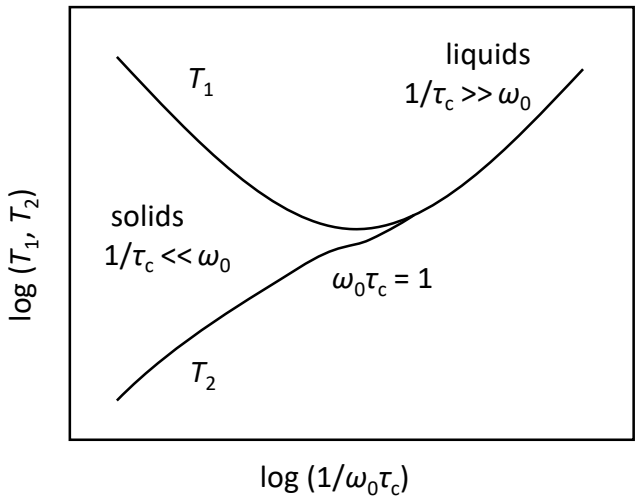

Figure 2.4. T_1 and T_2 relaxation times are nearly equal in liquids for a given Larmor frequency. In solids, T_1 and T_2 diverge with T_2 becoming much shorter than T_1 because of long correlation times, τ_c.

Moving now from quantum energy states and the scale of the molecule to the macro-scale, relaxation can be described as a process affecting the net magnetization vector of the sample evolving over time. The process of T_1 relaxation, acting only along the longitudinal axis and governed by the Zeeman interaction, can be described phenomenologically by the equation

$$\frac{dM_z}{dt} = -\frac{M_z - M_0}{T_1} \quad (2.27)$$

where M_0 is the initial equilibrium magnetization. The solution is

$$M_z(t) = M_z(0)\exp\left(-\frac{t}{T_1}\right) + M_0\left[1 - \exp\left(-\frac{t}{T_1}\right)\right] \quad (2.28)$$

The phenomenological equation describing T_2 relaxation, which occurs only in the transverse plane, is

$$\frac{dM_{x,y}}{dt} = -\frac{M_{x,y}}{T_2} \quad (2.29)$$

with the solution for a homogeneous sample

$$M_{x,y}(t) = M_{x,y}(0)\exp\left(-\frac{t}{T_2}\right) \quad (2.30)$$

These equations show that the magnetization decays with time as an exponential function and applies where the interaction terms related to transverse relaxation are weak, as in the case of liquid-state molecules. Solids and macromolecules which are rotationally constrained undergo very slow motions and rapid signal decay that is better described by more complicated equations.

Combining the expressions for the change in **M** due to both excitation and relaxation in the rotating reference frame, we obtain the Bloch equations

$$\begin{aligned}
\frac{dM_x}{dt} &= \gamma M_y\left(B_0 - {}^{\omega}/_{\gamma}\right) - \frac{M_x}{T_2} \\
\frac{dM_y}{dt} &= \gamma M_z B_1 - \gamma M_x\left(B_0 - {}^{\omega}/_{\gamma}\right) - \frac{M_y}{T_2} \qquad (2.31) \\
\frac{dM_z}{dt} &= -\gamma M_y B_1 - \frac{M_z - M_0}{T_1}
\end{aligned}$$

These equations describe the precession of the magnetization in the frequency terms, as well as the decay of the magnetization over time in the relaxation terms. Similarly, the induced signal contains complex phase and exponential decay terms.

Experimental Background

Before moving into a discussion of the practice of NMR—how to manipulate spin dynamics to extract meaningful information—it is necessary to first describe briefly the components of NMR hardware that make the measurements possible.

Experimental Equipment

A magnetic resonance system includes, on the simplest level, a magnet to create the $\mathbf{B}_0$ field, a spectrometer to deliver the pulses of current, an rf coil to transmit and receive the current to and from the sample, and a computer to control the system.

The high-field magnets in the College of Engineering Magnetic Resonance Lab at MSU (250 MHz and 300MHz) are super-conducting magnets made with a coil of copper wire several kilometers in length. The coil is maintained at a low temperature with liquid helium and nitrogen to minimize resistance within the wire, keeping the wire superconducting. The magnets have a vertical bore that holds samples ranging between approximately 5—25mm in diameter. The samples are loaded into the magnet within an rf coil. The coil is composed of a 'birdcage' of copper wire positioned so as to create an orthogonal $\mathbf{B}_1$ field and receive the induced signal. Gradient coils are often also included around the sample to spatially vary the magnitude of the applied magnetic field.

The spectrometer delivers rf pulses of current, gated to the proper pulse design according to pulse duration and frequency of current oscillation. The same coils transmit and receive the current so hardware may impose limitations on the time resolution of

some NMR measurements, especially where signal relaxation occurs on the timescale of the conversion between coil modes.

The low-field NMR magnets (245/290 kHz and 425/360 kHz) used in some of the experiments described later are down-the-borehole solid magnets measuring 4.5 feet long and 3.5 inches in diameter. These magnets are designed to be lowered into a well casing and project a vertical $\mathbf{B}_0$ field into the soil surrounding the well. The static magnetic field loses strength with radial distance from the well center, with peak sensitivity between 5—8 inches from the well center, depending on the operating frequency. The rf coil is contained within the same probe as the solid magnet. The spectrometer and computer are housed in a surface station.

Signal Detection

When the net magnetization of a sample is excited from equilibrium with an infinitesimally short resonant rf pulse, the resulting precession of **M** at the Larmor frequency in the laboratory reference frame induces a current in the rf coil according to Faraday induction. This induced current is the basis for NMR signal detection. The rf coil, a 'birdcage' (though solenoid coils are more efficient), is aligned orthogonal to the z-axis such that the coil output is an oscillating voltage, $V(t) = V_0 \cos(\omega_0 t)$. The strength of the signal is proportional to the Larmor frequency, γB_0. Higher field magnets (large $\mathbf{B}_0$) or a high gyromagnetic ratio, γ, increase the measurable signal to noise ratio and thereby improve sensitivity. Hydrogen protons have the largest gyromagnetic ratio of any stable nuclear isotope which, together with their natural abundance in materials of

interest, helps explain the prevalence of ^{1}H NMR within the larger field of magnetic resonance.

Since the initial spin density is proportional to the equilibrium polarization, $\rho(0) \sim I_z$, the resulting spin density matrix in the rotating frame following excitation has proportionality of the form

$$\rho^{rot}(t) \sim I_y \cos\big((\omega_0 - \omega)t\big) + I_x \sin\big((\omega_0 - \omega)t\big) \quad (2.32)$$

In order to separately measure the I_x and I_y components of the spin density matrix, corresponding to the real and imaginary parts of the signal, respectively, the rf coil uses the process of heterodyne detection. Heterodying with two quadrature detection channels involves mixing the induced signal voltage with the output from a reference rf oscillator orthogonal to both the z-axis and the receiving rf coil. Heterodyning is mathematically equivalent to multiplying the induced voltage by a complex signal, $\exp(i\omega t)$, and filtering out the sum frequency term, with the result that

$$V(t) = \frac{1}{2} V_0 [\cos(\omega_0 t - \omega t) - i \sin(\omega_0 t - \omega t)] \quad (2.33)$$

Thus, we directly measure $\big[I_x + iI_y\big]$ in the rotating reference frame at the heterodyne mixing frequency, ω. When $\omega = \omega_0$, the measured signal consists of two components 90° out of phase. When $\omega \neq \omega_0$, the signal will oscillate at the offset frequency, $\Delta\omega = \omega_0 - \omega$. The resulting phase factor, $\exp(i\varphi)$, can be removed during signal processing.

The complex signal $S(t)$ is well-suited to analysis with Fourier transforms between the conjugate variables, ω and t. The Fourier transform of the measured time-domain signal is expressed as

$$F\{S(t)\} = s(\omega) = \int_{-\infty}^{\infty} S(t) \exp(-i\omega t)\, dt \quad (2.34)$$

and produces a spectrum in the frequency domain, $s(\omega)$. The inverse Fourier transform of the spectrum returns the original signal by

$$F^{-1}\{s(\omega)\} = S(t) = \frac{1}{2\pi} \int_{-\infty}^{\infty} s(f) \exp(i\omega t)\, d\omega \quad (2.35)$$

where $f = {}^{\omega}/_{2\pi}$ and converts between cyclic and angular frequency.

For example, the Free Induction Decay, or FID, is the simplest NMR measurement and is the result of free precession of spins that induce an oscillating, decaying signal in the time domain. The FID consists of a single 90° rf pulse followed immediately by signal acquisition (Figure 2.5). The FID decays at a rate of ${}^{1}/_{T_2^*}$ which includes effects from an inhomogeneous magnetic field and from molecular interactions in the transverse plane.

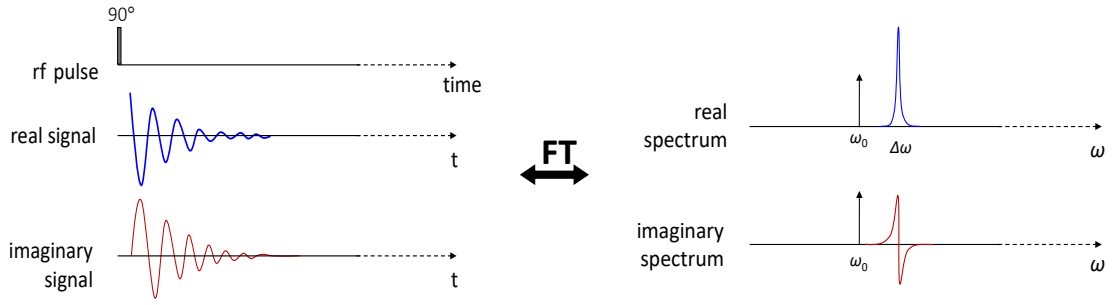

Figure 2.5. The Free Induction Decay (FID) measurement produces complex decaying signal in the time domain and a spectrum in the frequency domain.

The Fourier transform of the FID is, in the real spectrum, a Lorentzian with full-width-half-maximum (FWHM) of $1/\pi T_2{}^*$, called the absorption spectrum, and an imaginary spectrum called the dispersion spectrum. The integral of the phase-corrected absorption spectrum is equal to the amplitude of the NMR signal. The FID produces a signal

$$N\gamma Tr\left(\left[I_x + iI_y\right]\rho^{rot}(t)\right) = iM_0 \exp(-i(\omega_0 - \omega)t) \qquad (2.36)$$

which relates the observable $N\gamma\left[I_x + iI_y\right]$ operating on the spin density matrix in the rotating frame ρ^{rot} to the time and phase evolution of the magnetization.

In practice, the NMR signal is not recorded as a continuous function, but is rather sampled and digitized for later processing. A finite set of *N* points are sampled in the time domain, spaced by the dwell-time interval, *T*. When Fourier transformed, the data set in the frequency domain has a spectral width equal to the inverse of the dwell time, $1/T$, with a digital resolution of $1/NT$.

Basic Pulse Sequences

NMR measurements consist of orchestrated sequences of rf pulses and applied magnetic field gradients which manipulate spin dynamics and encode for observables of interest, as well as wait times and signal acquisition times to allow the evolution and collection of signal that illuminates some aspect of the physico-chemical system. There are several measurements fundamental to NMR which will be described here in some detail. These include inversion recovery, the Hahn spin echo, the Carr-Purcell echo train and the stimulated echo. Each of these experiments can be conceptualized on the macro-scale using the net magnetization vector, **M**, influenced by the Zeeman Hamiltonian and subject to T_1 and T_2 relaxation. More complicated measurements take elements of these basic techniques and re-combine them to provide additional information about the sample under study. Typically, the same measurement is performed N successive times and the signal is averaged across all the measurements to improve the signal-to-noise ratio. Signal adds coherently while noise adds in random phase where its average approaches zero. The time between experiment repetitions depends on the T_1 relaxation time of the sample since it is typically desirable for the net magnetization to return to its maximum along the z-axis prior to repeating the experiment.

The timing of NMR experimental elements is displayed in a pulse sequence diagram, which typically includes the rf pulse timing and sequence on the first row with time increasing to the right. Applied magnetic field gradients are included in the next rows, depending on the axis along which they are applied. Acquired signal can be shown in-line with the rf or gradient sequence or may be included separately on its own line.

Inversion Recovery. The inversion recovery experiment measures the T_1 relaxation time of a sample by first inverting **M** onto the –*z*-axis with a 180° rf pulse (Figure 2.6). **M** decays in magnitude as the spins experience spin-lattice relaxation and begin to return to thermal equilibrium. After some time τ, a 90° rf pulse tips any remaining magnetization into the transverse plane where it can be measured as it precesses at the Larmor frequency (Figure 2.7).

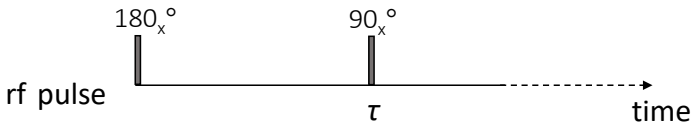

Figure 2.6. The inversion recovery pulse sequence measures T_1 relaxation by inverting the magnetization and allowing T_1 relaxation to occur before signal acquisition.

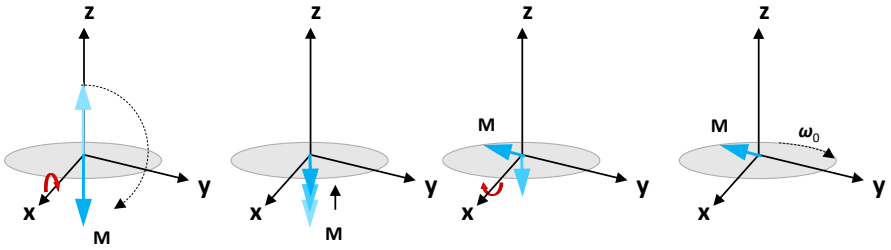

Figure 2.7. Evolution of the magnetization vector during the inversion recovery experiment.

Repeating the experiment for various τ times produces a curve of equation

$$M_y(t) = M_0(1 - 2\exp\left(-t/T_1\right) \quad (2.37)$$

As seen in Figure 2.8, at $\tau = 0.6931T_1$ the measured signal amplitude is zero as the excited net magnetization crosses the transverse plane on its return to thermal equilibrium. This result is particularly useful when only one component of a sample is of interest since it allows for suppression of signal from any spins with a T_1 time distinct from other spins. Applying an rf pulse at an interval $\tau = 0.6931T_1$ prior to the experimental pulse sequence effectively nulls the signal from spins with that particular T_1 relaxation time and allows for selective acquisition of signal from spins relaxing at a different rate. This method is particularly useful in biological tissues where the water signal can overwhelm signal from other tissue components.

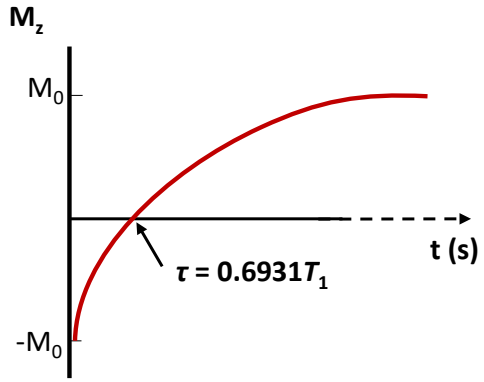

Figure 2.8. The amplitude of the net magnetization is equal to zero at $0.6931T_1$, allowing for signal from spins with a specific T_1 relaxation time to be nulled in a measurement.

Hahn Spin Echo. Despite the best efforts of hardware manufacturers to design a NMR magnet with a perfectly homogenous $\mathbf{B}_0$ field, some degree of inhomogeneity is

unavoidable. Spins that experience a slightly different magnetic field will precess at a slightly different frequency from other spins in the sample. This phenomenon leads to dephasing of spins in the transverse plane, as some move either faster or slower than the Larmor frequency. In 1950, Erwin Hahn [3] demonstrated that this component of signal attenuation is reversible through the application of a 180° rf pulse in the transverse plane at some time τ after the 90° excitation pulse (Figure 2.9).

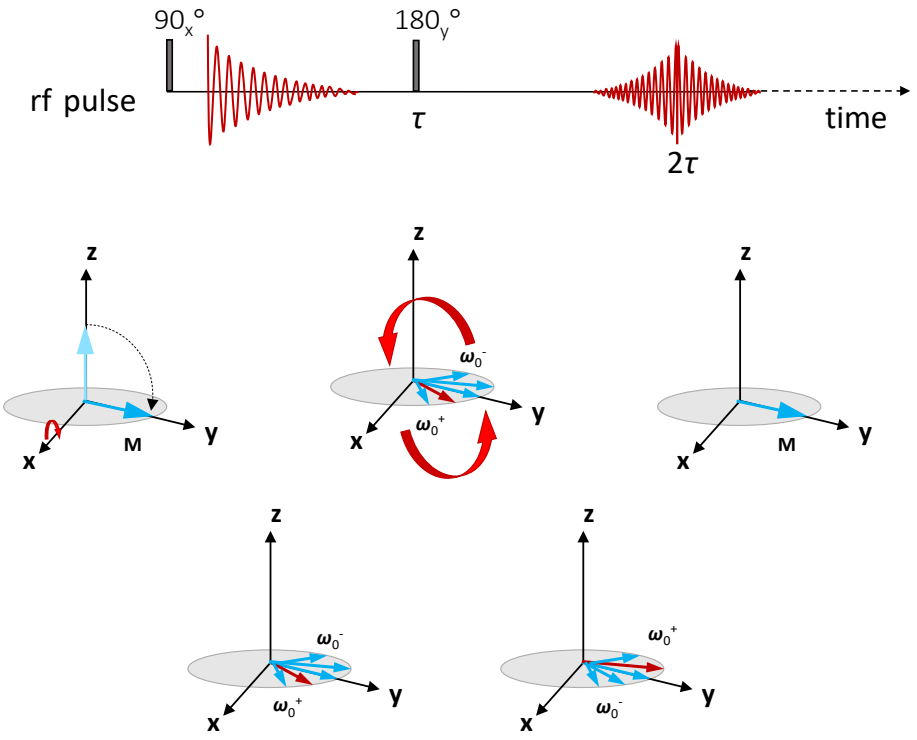

Figure 2.9. The Hahn echo pulse sequence and resulting evolution of the net magnetization. A $180°_y$ rf pulse refocuses signal to produce an echo at time 2τ following the $90°_x$ rf excitation pulse. The evolution figures are show below the position on the pulse sequence where they occur.

The 180° pulse has the effect of refocusing the signal as the faster precessing spins are placed 'behind' the slower moving spins. The spin coherence is maximized at

time 2τ, when an 'echo' in the signal forms. Since the signal is still subject to T_2 relaxation during the time 2τ, the echo amplitude is less than the initial amplitude. Only the attenuation due to magnetic field homogeneity can be re-focused. Relaxation due to homo-nuclear spin-spin interactions within the sample cannot be reversed.

CPMG Echo Train. Following Hahn's discovery of the spin echo, Carr and Purcell in 1954 [4] expanded the concept by performing successive 180° rf pulses to produce a series of echoes. Meiboom and Gill [5] modified the echo train in 1958 by use of quadrature $180_y°$ rf pulses to compensate for small turn-angle errors. The resulting experiment, the CPMG sequence, allows for the direct measurement of T_2 relaxation time in one experiment. The echo envelope decays at a rate of $1/T_2$.

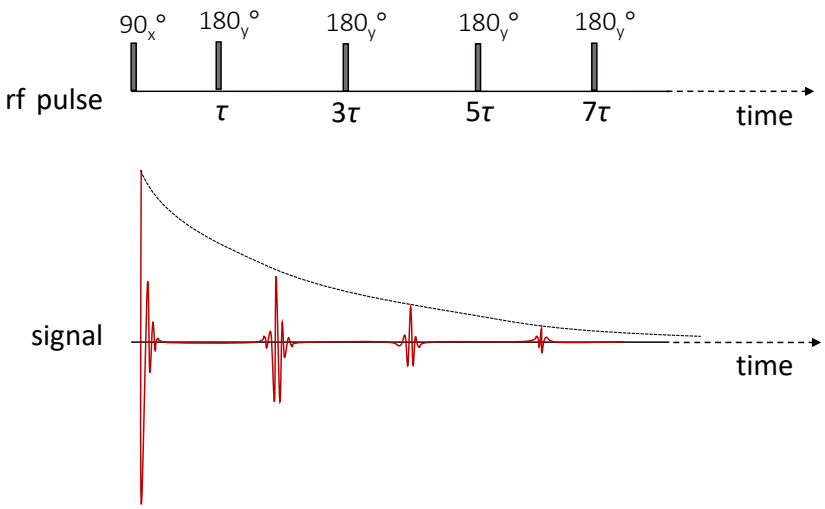

Figure 2.10. The CPMG pulse sequence, consisting of a 90° pulse followed by a series of 180° pulses, is used to measure T_2 relaxation where the echo envelope decays at a rate of $1/T_2$.

Stimulated Echo**.** For materials where the T_2 relaxation time is much shorter than the T_1 relaxation time, such as solids, phase coherence expires much faster than the sample polarization. In other words, signal is no longer measureable because of T_2 relaxation though incoherent magnetization remains in the transverse plane. The stimulated echo can be used to obtain signal from materials with short T_2 times, especially when molecular motion is the observable of interest.

The stimulated echo experiment combines elements from the previously discussed pulse sequences—inversion recovery and the spin echo. Figure 2.11 shows the pulse sequence with the induced signal on the rf pulse line. After the initial $90_x°$ excitation pulse tips **M** onto the *y*-axis, the spins relax according to both T_1 and T_2 relaxation until the time τ, when another $90_x°$ pulse is applied. The second pulse rotates the *y*-component of the magnetization into the longitudinal plane where only T_1 relaxation occurs. The

remaining polarization can be 'stored' for a time τ' ($<T_1$) while spins are free to move within the sample and interact. A third $90_x°$ pulse applied at time $\tau+\tau'$ returns the remaining magnetization to the transverse plane where it refocuses to form an echo at time $2\tau+\tau'$. Since the *x*-component of the magnetization does not respond to the second $90_x°$ pulse, a spoiler gradient is typically included in the pulse sequence between the second and third rf pulse to eliminate signal from these spins (not shown).

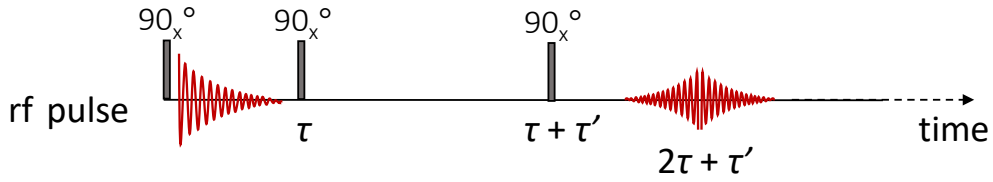

Figure 2.11. The stimulated echo experiment uses two $90°_x$ rf pulses to achieve the echo effect of a $180°_y$ rf pulse while avoiding T_2 relaxation by storing the signal in the longitudinal plane over the time, τ'.

Phase Cycling**.** Phase cycling corrects for phase and amplitude anomalies, echo artifacts, and interference from residual transverse magnetization. The quadrature channels that are used to acquire the real and imaginary components of the signal are swapped, equivalent to a 90° phase shift between the transmitter and receiver. The phase of the rf pulses in the *N* successive measurements of each experiment are also alternated by 180° to cancel coherent noise in the data. Typically, these phase cycling corrections are performed automatically in the data acquisition software.

Introduction to Magnetic Resonance Imaging

Variation or gradients in the magnetic field applied across a sample—whether due to inhomogeneities in $\mathbf{B}_0$ or by design via a $\mathbf{B}(\mathbf{r})$ field—cause broadening of the spectrum in the frequency domain. Since the ensemble of spins experiences a range of magnetic fields, the ensemble will precess at a range of frequencies. As discussed above, the spectral broadening due to inhomogeneities in the $\mathbf{B}_0$ field can be reversed with a spin echo, though translational motion by excited spins during the echo results in imperfect refocusing and attenuation of the echo amplitude. This phenomenon was initially viewed as an inconvenience, a limitation to NMR resolution. Over time, however, researchers realized that magnetic field gradients could also be useful. Since the frequency of each spin depends on the magnetic field it experiences, a known spatially-varying and time-varying magnetic field can encode for spin position at multiple times. In 1973[6], magnetic field gradients were exploited as a means of encoding for position and displacement, forming the basis of modern magnetic resonance imaging (MRI).

Gradients and **k**-space

The effect of magnetic field gradients can be described mathematically by Maxwell's equations. For samples where there is no inherent current density and the field is static or slowly varying, there is no divergence in the magnetic field, $\nabla \cdot \mathbf{B} = 0$, and no curl, $\nabla \times \mathbf{B} = 0$. These equations imply that there cannot be any gradient the *z*-direction without there also being gradients in the *x*- and *y*-directions. Furthermore,

$\partial B_x/\partial y = \partial B_y/\partial x$. As shown in Figure 2.12, if the gradient field, **B**(**r**), is added to a uniform $\mathbf{B}_0$ field, then the resulting total magnetic field, $\mathbf{B}_{tot}$ is

$$\mathbf{B}_{tot}(x, y, z) = (\mathbf{r} \cdot \nabla B_x)\mathbf{i} + \left(\mathbf{r} \cdot \nabla B_y\right)\mathbf{j} + (B_0 + \mathbf{r} \cdot \nabla B_z)\mathbf{k} \quad (2.38)$$

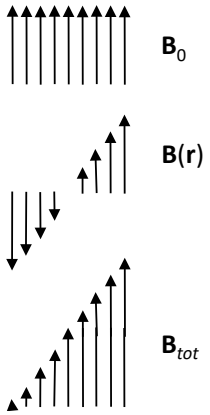

Figure 2.12. A gradient field, B(r), applied in addition to the static B_0 field produces a combined magnetic field, B_{tot}, that varies linearly with respect to position, r.

Since spins only react to the local magnetic field, rather than the total field across the sample as a whole, the actual expression for the Larmor frequency is based on the local absolute magnitude of the field and is therefore $\omega_0 = \gamma|\mathbf{B}_{tot}|$. When the magnitude B_0 is much greater than the magnitudes of the gradient fields (as is typically the case), then

$$|\mathbf{B}_{tot}| \approx B_0 + \mathbf{r} \cdot \nabla B_z \quad (2.39)$$

and the contribution of the concomitant fields may be neglected. This expression also allows us the define the gradient vector, **G** = ∇B_z. Writing Equation (2.39) in terms of frequency, we obtain

$$\omega_0(\mathbf{r}) = \gamma B_0 + \mathbf{r} \cdot \mathbf{G} \quad (2.40)$$

When the magnitude of the $B_0 \sim B(\mathbf{r})$, we must define the gradient vector in terms of the total magnetic field rather than simply the dominant component where $\mathbf{G} = \nabla|\mathbf{B}_{tot}|$ and

$$\omega_0(\mathbf{r}) = \gamma|\mathbf{B}_{tot}| + \mathbf{r} \cdot \mathbf{G} \quad (2.41)$$

For the purposes of this thesis, we will assume that B_0 is much larger than the gradient fields and Equation (2.40) will apply. It is standard that a gradient written as a capital **G** refers to a gradient applied for imaging, while the lowercase **g** is reserved for gradients used to measure motion. Both gradient vectors are functions of position. Equation (2.40) produces a complex signal equal to

$$S(t) = \iiint \rho(\mathbf{r}) \exp(-i\gamma \mathbf{r} \cdot \mathbf{G}t) d\mathbf{r} \quad (2.42)$$

which depends on the spin density matrix, $\rho(\mathbf{r})$, the gradient vector $\mathbf{G}(\mathbf{r})$, and pulse duration *t*. This expression suggests a simplification through the definition of a new variable. The vector **k**, with magnitude equal to the area under the gradient pulse, is defined as

$$\mathbf{k} = \frac{\gamma t \mathbf{G}}{2\pi} \quad (2.43)$$

Replacing terms in Equation (2.42) with the new expression for **k** yields the following Fourier relationship between the normalized signal, $S_N(\mathbf{k})$, and the spin density, $\rho(\mathbf{r})$.

$$S_N(\mathbf{k}) = \int \rho(\mathbf{r}) \exp(-i\mathbf{k} \cdot \mathbf{r})\, d\mathbf{r} \quad (2.44)$$

$$\rho(\mathbf{r}) = \frac{1}{2\pi}\int S_N(\mathbf{k})\exp(i\mathbf{k}\cdot\mathbf{r})\,d\mathbf{k} \quad (2.45)$$

The implication of Equations (2.44) and (2.45) is that the excited spin density in the sample, via a Fourier relationship, produces a complex signal—the data—which can then be Fourier transformed to produce an image of the spin density. In this manner, the NMR signal collected over time can provide a visual representation of the quantum mechanical energy dynamics occurring in the sample as a result of the observation via the spin density matrix expression in Equation (2.10).

The NMR signal can also be expressed in terms of phase, where the measured signal under the influence of the gradient, *S*, is proportional to the signal with no applied gradient, $S(0)$, by factor equal to the phase change, as given in the equation

$$S = S(0)\exp(i\varphi) \quad (2.46)$$

where the phase factor, $\exp(i\varphi)$, is a function of position and time according to $\varphi(t) = \gamma(B_0 + G_z z)t$. In the rotating frame, the first term in the expression for the phase, equal to the Larmor frequency, is eliminated, leaving only the phase shift due to the gradient, $\gamma G_z z t$. (The spatial variable is generally described by the vector, **r**, but can be simplified to the *z* coordinate when the gradient is applied in the direction of $\mathbf{B}_0\mathbf{k}$).

This Equation (2.46) shows that a gradient applied over time to a sample has the effect of 'winding up a helix of phase' through the phase shift that forms as a function of position along the applied gradient. A stronger gradient or a longer duration produces a tighter helix of phase (Figure 2.13). The inverse of *k* is the pitch of the helix, or wavelength, λ.

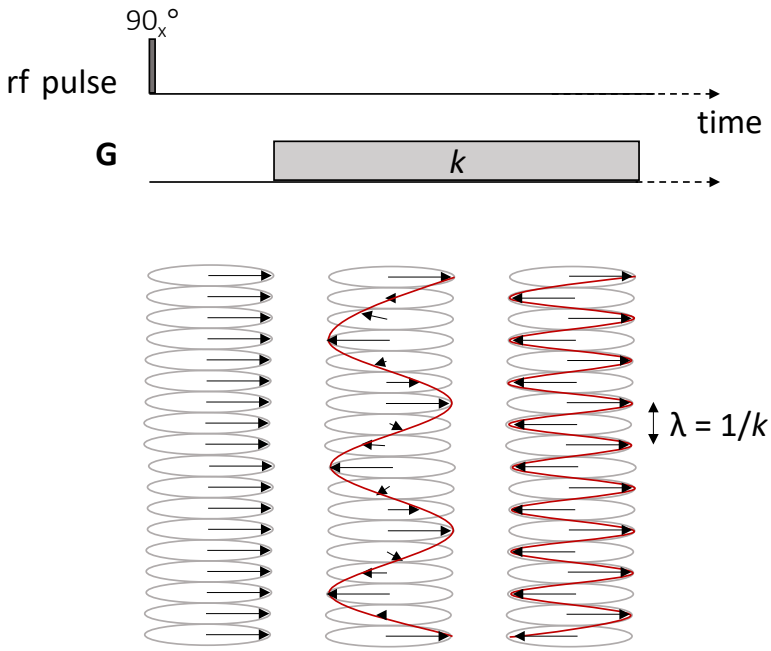

Figure 2.13. Application of a gradient produces a phase helix as spins at large *z* values experience a stronger magnetic field and precess faster than spins at smaller *z* values.

Applying a gradient pulse of opposite sign or using a 180° pulse will rephase the spins and create a signal echo (Figure 2.14), a prerequisite for data collection. A perfect echo is only possible if the excited spins remain in their initial positions, so these types of gradient sequences are used to encode for displacement.

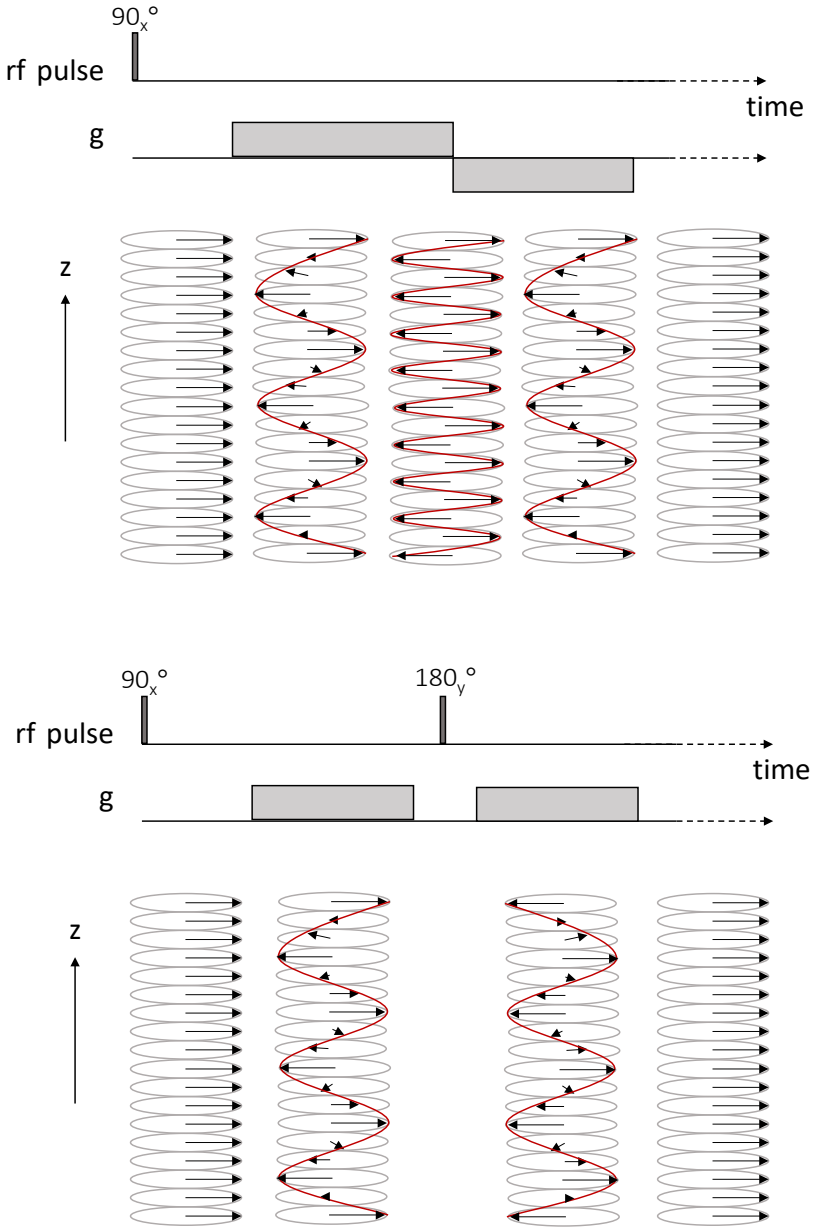

Figure 2.14. Reversing the sign of the gradient for an equal k rephases the spins to produce a signal echo (top), called a gradient echo. A 180°y pulse applied between equal gradients of the same sign (bottom) refocuses spin incoherences due to both applied gradients and background field inhomogeneities, known as a spin echo.

Signal Encoding

According to Equations (2.44) and (2.45), the measured NMR signal is a function of **k**, which is itself a function of time and the gradient with respect to position. The signal data, therefore, is collected in a 2-D domain called **k**-space by varying either the duration of the gradient pulse or the magnitude and direction of the gradient. Moving away from the **k**-space origin is equivalent to tightening the helix of phase within the sample incrementally during the measurement.

The two modes of traversing **k**-space produce very different paths through **k**-space and by extension, very different measurements. Varying the time over which the gradient pulse is applied is termed frequency encoding, or a 'read gradient,' G_{read}. Varying the gradient amplitude over a constant time interval is called phase encoding, or a 'phase gradient,' G_{phase}. A major difference between the two modes is that read gradients are applied during signal acquisition so that signal is collected during the traverse across a line of **k**-space, allowing for rapid data collection. Phase encoding, conversely, collects only one point in **k**-space at a time, making the method slower. Figures 15 and 16 show examples of hypothetical read and phase gradients applied to traverse **k**-space in an imaging sequence. Which method of signal encoding is appropriate depends on the nature of the sample and the experiment.

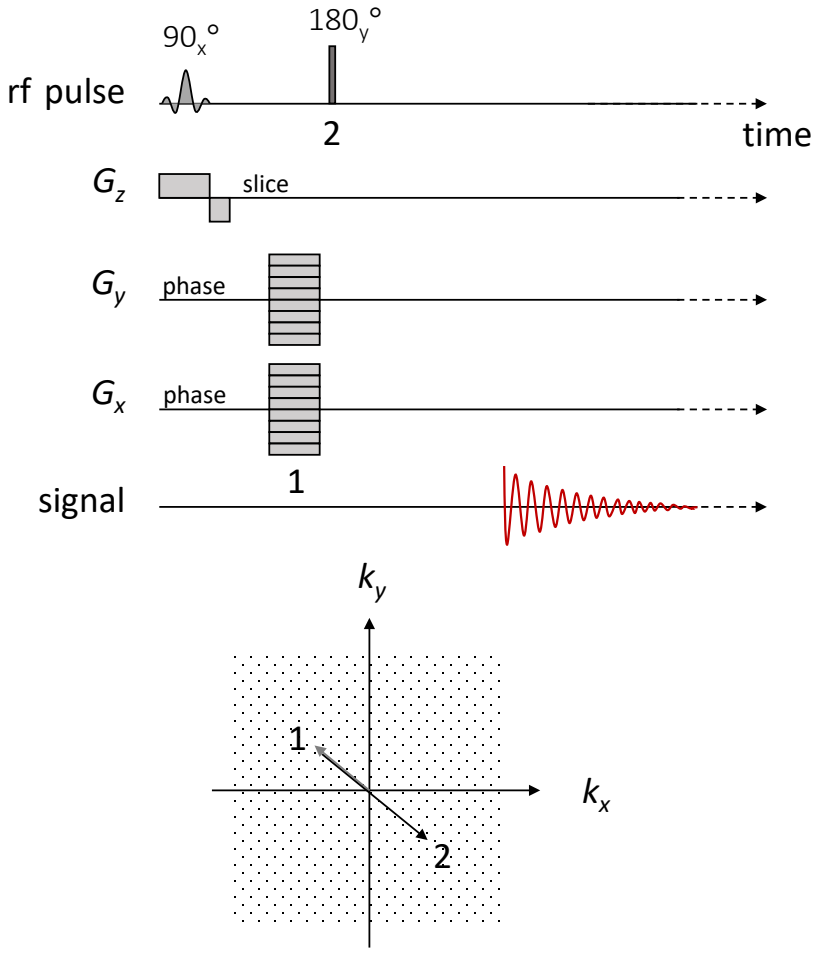

Figure 2.15. For a given slice in the sample, phase encoding collects one point in k-space for each measurement repetition. A combination of the Gx and Gy phase gradients traverses to a particular point in k-space (1). A 180° rf pulse inverts the position in k-space (2) and a data point is collected. Different combinations of Gx and Gy during measurement repetitions allow the traverse of k-space point by point.

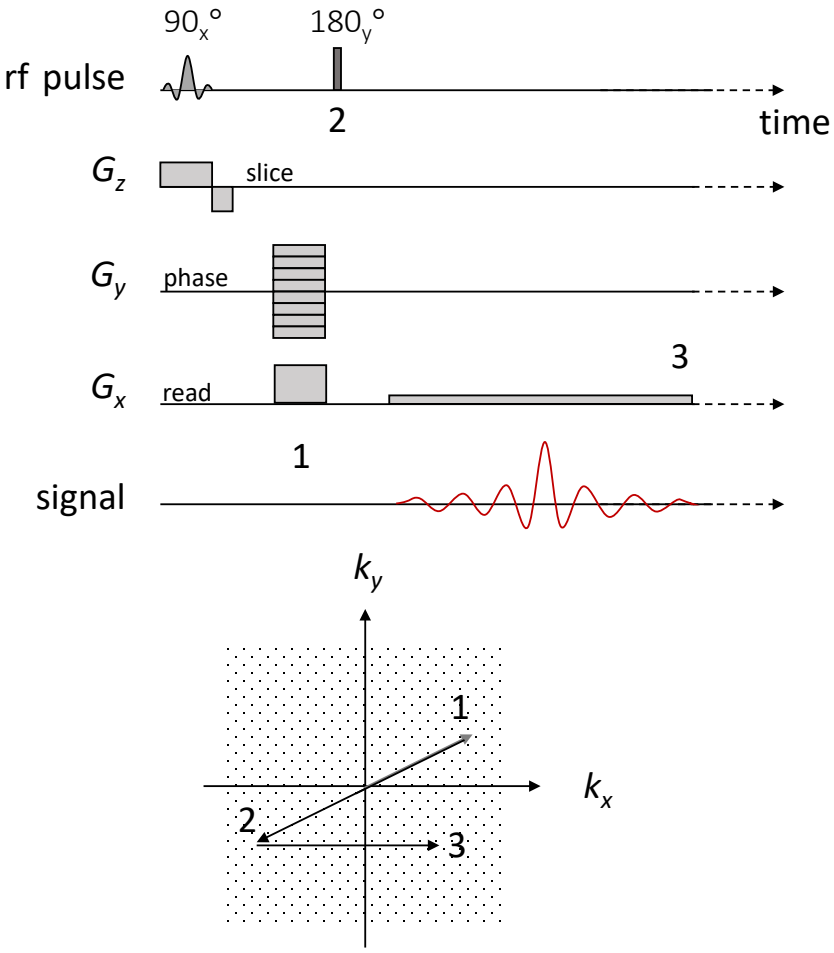

Figure 2.16. A read gradient allows for collection of multiple points in k-space during the signal acquisition window. For a given slice in k-space, a combination of phase and read gradients traverse k-space to a particular starting point (1). A 180° rf pulse inverts the k-space position to (2). A read gradient is applied during signal acquisition to collect the row of k-space data, ending at (3). The stepped phase gradient indicates that the process will be repeated from different beginning locations in k-space to acquire all the data.

The center of **k**-space contains the bulk of the information about the sample, with the outer regions of **k**-space providing the finer details and edge resolution of the image. Since **k**-space is not related to the physical space in the sample, but rather to time and

resonance frequency within the sample, skipping a single pixel of **k**-space produces artifacts in the entire image of the sample.

Selective Excitation

Pulse sequences are designed so that the combination of rf excitation pulses and applied gradients collect induced signal from specific spins of interest. Selective excitation occurs when only spins of certain frequencies are excited by an rf pulse. These spins may be selected by measuring only a limited region of the NMR spectral bandwidth, which isolates those nuclei of a certain resonant frequency, called chemical shift. Gradients and offset frequencies can also be applied to relate the measured frequency to a layer within the sample, so that the image obtained is tied to a specific location.

Central to the understanding of the concept of selective excitation is an understanding of the Fourier relationship between pulse duration and frequency bandwidth. Generally, the tip angle of spins, θ, is related to the rf field strength, B_1, and the pulse length, t according to $\theta = \gamma B_1 t$. This equation means that it is possible to control the tip angle of the spins, and thereby achieve maximum signal with a 90° rf pulse, by changing either the pulse power (B_1) or the pulse length (t). We also know that $\omega \equiv [1/t]$. By extension, a range of frequencies ($\Delta\omega$, bandwidth) is inversely proportional to a range of time (Δt, duration).

The implication of this Fourier relationship is that it is possible to select the precise bandwidth to be excited and measured by defining the appropriate pulse duration, where short pulses produce wide excitation bandwidths and long pulses produce narrow

excitation bandwidths (Figure 2.17). Selectivity can be improved by using shaped pulses that more closely resemble hat functions when Fourier transformed (Figure 2.18). For example, an rf pulse applied using a 3-lobe sinc function to control the amplitude over time produces a rectangular bandwidth in the frequency domain. Similarly, a long Gaussian rf pulse produces a narrow Gaussian bandwidth of frequencies. Spins resonating outside of the excitation bandwidth do not experience the excitation pulse and therefore do not contribute to the measured signal.

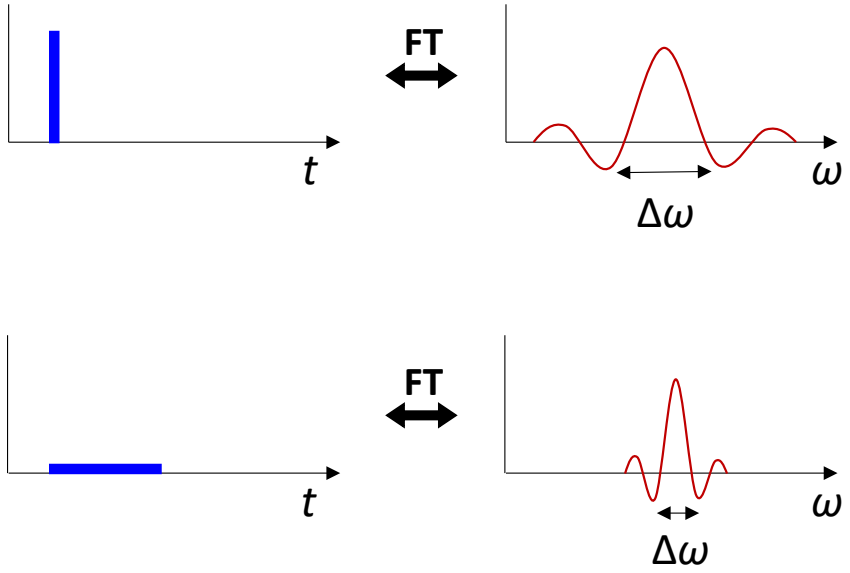

Figure 2.17. Rectangular pulses Fourier transform to spectra with a sinc function shape where a range of frequencies are excited. The pulse duration is inversely proportional to the spectral width.

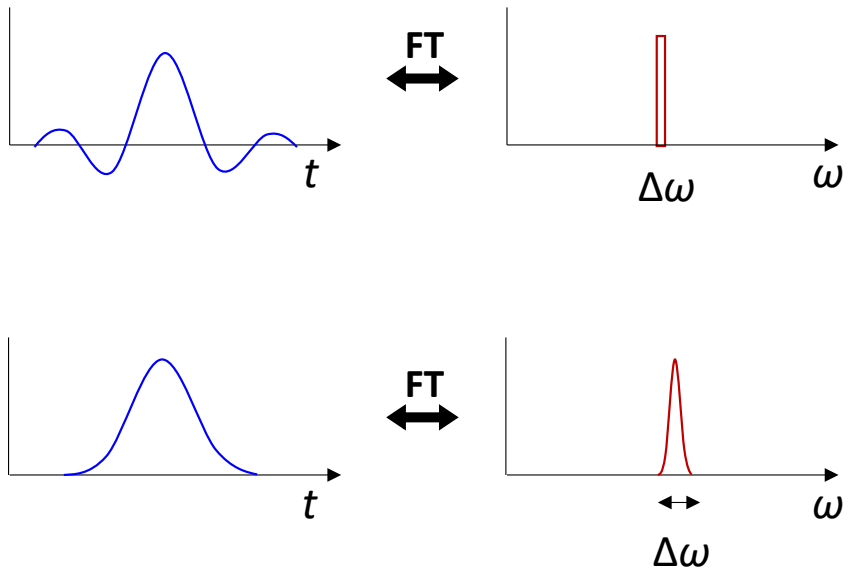

Figure 2.18. Shaped, or soft, pulses produce spectra that approximate rectangular bandwidths. Long soft pulses result in narrow bandwidths while short soft pulses excite a broad range of frequencies.

Using magnetic field gradients and setting the offset frequency appropriately relative to the Larmor frequency allows for the detection of signal from spins located in a specific layer of the sample (Figure 2.19). Under the influence of a constant gradient which produces a linearly varying magnetic field, spins located in slice 2 will precess at a higher frequency than those in slice 1.

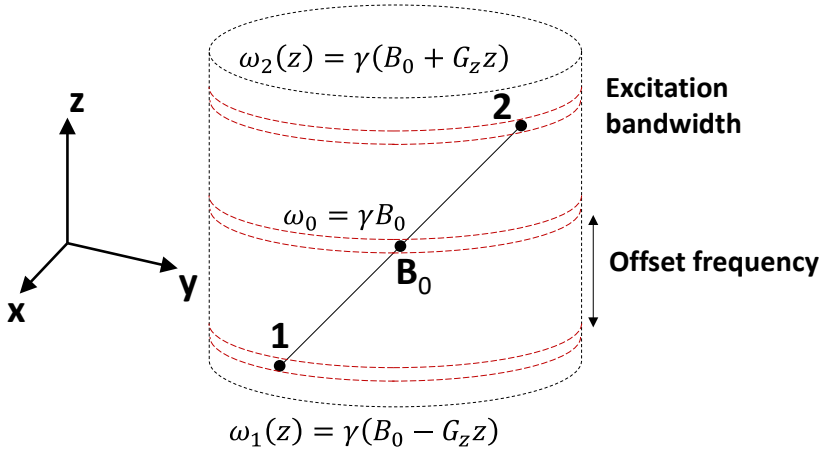

Figure 2.19. Selective excitation is achieved through a combination of magnetic field gradients and offset frequencies to collect signal from spins occupying a specific place in both the frequency spectrum and physical sample.

Image resolution depends on the spin density, $\rho(\mathbf{r})$, within a sample, as well as the T_1 and T_2 relaxation times. How much signal is generated and how long does it last? High-field magnets, like those in the MR lab, can achieve spatial resolution of approximately 10μm before diffusion effects interfere. While this is less resolution than optical methods can achieve, NMR is non-invasive and can be used to image within opaque and heterogeneous samples by exploiting the contrasts between chemical constituents with selective excitation.

Introduction to Molecular Motion Measurements

Measurements of molecular motion can be made by applying the same principles used in MRI at multiple discrete points in time to compare spins' initial position with some later position. As in MRI, using magnetic field gradients for echo formation assumes 1) that spins experience the same precession frequency during the dephasing and

rephasing gradient pulses, and 2) that the phase shift acquired during the timescale of the measurement is linearly related to the location of the spin in the sample. A spin that migrates from one point, both in the sample and on the phase helix, to another point during the measurement will carry with it the phase encoded for the initial location. Any translational motion will cause a residual phase shift that is detectable in the signal output. When the spins undergo Brownian motion, there is a distribution of phase shifts across the ensemble of spins which causes attenuation of the echo amplitude. In the case of coherent flow, the ensemble will be tagged with the same residual phase shift. The case of coherent flow will be addressed first, followed by a discussion of diffusive motion.

Normalized Echo Amplitude and **q**-space

Central to the understanding of the how the signal is affected by applied effective gradients, $\boldsymbol{g}^*(t)$, is the concept of the normalized echo amplitude, $E(t)$, where the magnetization that has been influenced by phase shifts due to translational motion at time t is compared to magnetization with no applied gradient where the starting phase for all spins is the same. Since the dephasing effect of the gradients is far greater than that due to T_2 relaxation, and since relaxation is assumed to not be correlated to position for a general case, relaxation is neglected here.

$$E(t) = \frac{M_+(z_0, t)}{M_+(z_0, 0)} = \exp(i\varphi(t)) \quad (2.47)$$

Equation (2.47) indicates that the normalized echo amplitude is equal also to the accumulated phase shift at time t. (By applying the principle of moments of the gradients

to this residual phase shift, pulse sequences can be designed to be sensitive to velocity, acceleration or higher order moments for the study of coherent flow dynamics. Further discussion of moments of the gradient will be included later in this thesis.) For spins experiencing coherent flow, the residual phase shift when the normalized echo amplitude is written in terms of signal as a function of the gradient **g** will be

$$E(\mathbf{g}) = \frac{S(\mathbf{g})}{S(0)} = \exp(i\gamma\delta\mathbf{g}\cdot\mathbf{v}\Delta) \quad (2.48)$$

where δ is the duration of the gradient pulses, Δ is the time between gradient pulses, and $\mathbf{g}\cdot\mathbf{v}\Delta$ is the displacement generally. This expression also allows the introduction of a new term, **q**, analogous to the vector **k**, and defined as

$$\mathbf{q} = \frac{\gamma\delta\mathbf{g}}{2\pi} \quad (2.49)$$

In the way that data is collected in **k**-space during image acquisition, similarly is data collected in **q**-space for measurements of molecular motion although it is the area under the pulse pair that traverses **q**-space. Each point in **q**-space contributes to the propagator, or probability of displacement, measured over the entire sample.

Propagators

To apply Equation (2.48) to an ensemble of spins, the phase term for each spin is weighted by the probability of the spin to having moved from **r** to **r'** during the time Δ. The dynamic displacement **R** is equal to **r'**- **r**. The propagator, or probability density that spins of original spin density $\rho(\mathbf{r})$ have traveled a distance **R** over all possible starting positions and paths, is defined as

$$\mathbf{P}(\mathbf{R},\Delta) = \int \rho(\mathbf{r})\, P(\mathbf{r}|\mathbf{r}+\mathbf{R},\Delta) d\mathbf{r} \quad (2.50)$$

Applying this weighting function and replacing terms defined above, the expression for the echo signal when the gradient is along the *z*-axis becomes

$$E(q,\Delta) = \int \mathrm{P}(Z,\Delta)\exp(iqZ) dZ \quad (2.51)$$

This equation expresses the Fourier relationship between the signal $E(q,\Delta)$ measured in **q**-space and the probability of dynamic displacement *Z*. The NMR signal describes the hydrodynamics of a system through measurement of the Fourier transform of the propagator, where the propagator is directly related to quantum spin states through the spin density matrix. In other cases, including unrestricted and restricted diffusion, the propagator is known and the variable of interest is directly observable in the **q**-space data.

Some translation of spins in liquid state materials is unavoidable because of random self-diffusion of molecules, even under no-flow conditions. When the translational motion of interest is this Brownian thermal motion rather than coherent flow, there is a distribution of phase shifts across the ensemble of spins, correlated to the distribution of diffusion times associated with the spins. Diffusion can be understood as a sequence of discrete, random hops. In NMR, diffusion measurements are resolved in the direction of the applied gradient, though each hop can occur in any direction.

Translational motion is measured with the pulsed gradient spin echo (PGSE) pulse sequence, shown in Figure 2.20. The phase shift for a single spin diffusing in the direction of the applied gradient, assumed to be along the *z*-axis, is $\Delta\varphi = \gamma\delta g(z_1 - z_2)$.

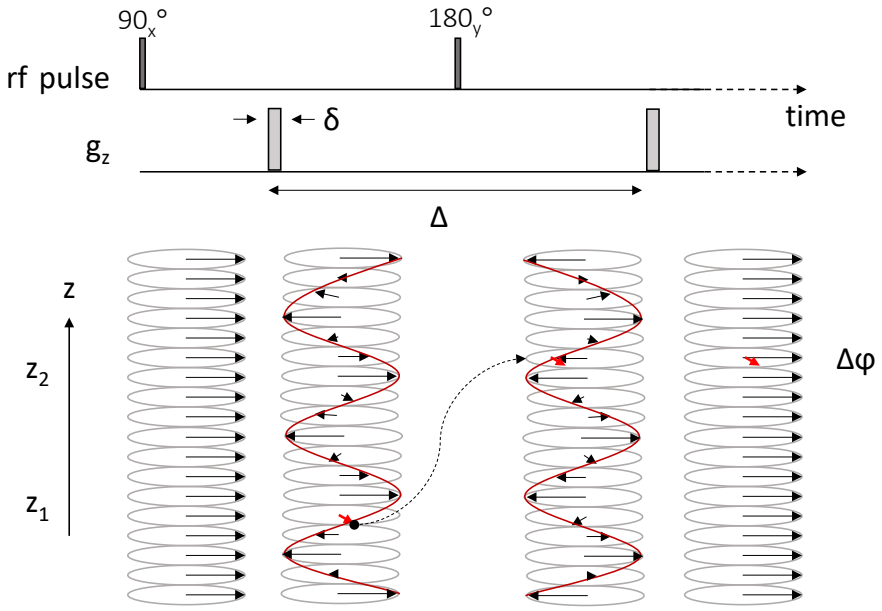

Figure 2.20. The PGSE pulse sequence measures the mean squared displacement of spins via the phase shift accumulated during the time Δ.

When measuring the propagator, the gradient pulse duration must be minimized, or 'pulsed,' so that it is possible to neglect motion of spins during the time δ. This point marks a distinction between gradients used for imaging, **G**, which are long-lasting, and those used for measurement of motion, **g**. For unrestricted diffusion, it is typically sufficient that $\delta \ll \Delta$, the time between gradient pulses when spins are free to diffuse within the sample. For spins experiencing unrestricted diffusion, the cumulative phase shift for the ensemble of spins is the Stesjkal-Tanner relationship[7]

$$\frac{S(\mathbf{g})}{S(0)} = \exp\left(-\gamma^2 g^2 \delta^2 D\left(\Delta - {}^{\delta}/_{3}\right)\right) \quad (2.52)$$

where D is the self-diffusion coefficient. Since each remaining term in Equation (2.52) is known or measureable, PGSE experiments are commonly used to measure diffusion

coefficients via measurement of the mean squared displacement $\langle Z^2(\Delta)\rangle = 2Dt$. Equation (2.52) is derived from applying a Gaussian propagator in Equation (2.51) and performing the integration, since random diffusion is described by a normal, or Gaussian, probability distribution.

For general translational motion, Equations (2.48) and (2.52) can be combined in an expression for total normalized echo amplitude

$$E(\mathbf{g}) = \exp\left(i\gamma\delta\mathbf{g}\cdot\mathbf{v}\Delta - \gamma^2 g^2\delta^2 D\left(\Delta - {}^{\delta}/_{3}\right)\right) \quad (2.53)$$

This equation shows that the measured NMR signal under the influence of applied gradients decays in time as a result of molecular diffusion and oscillates due to the phase shift caused by coherent motion. From this acquired signal, therefore, we can derive useful information about the sample's physical and chemical properties.

References

1. Callaghan, P.T., *Principles of Nuclear Magnetic Resonance Microscopy*1991, New York: Oxford University Press.

2. Callaghan, P.T., *Translational Dynamics & Magnetic Resonance: Principles of Pulsed Gradient Spin Echo NMR*2011, New York: Oxford University Press.

3. Hahn, E.L., *Spin Echoes.* Physical Review, 1950. **80**: p. 580-594.

4. Carr, H.Y. and E.M. Purcell, *Effects of diffusion on free precession in nuclear magnetic resonance experiments.* Physical Review, 1954. **94**(3): p. 630-638.

5. Meiboom, S. and D. Gill, *MODIFIED SPIN-ECHO METHOD FOR MEASURING NUCLEAR RELAXATION TIMES.* Review of Scientific Instruments, 1958. **29**(8): p. 688-691.

6. Lauterbur, P.C., *Image formation by induced local interactions: examples employing nuclear magnetic resonance.* Nature, 1973. **242**: p. 190-191.

7. Stejskal, E.O. and J.E. Tanner, *Spin diffusion measurements: Spin echoes in the presence of a time-dependent field gradient.* Journal of Chemical Physics, 1965. **42**: p. 288.

ADVANCED NMR CONCEPTS

Introduction

This chapter is a continuation of previous discussions of elementary magnetic resonance theory concepts and draws heavily from the work of Sir Paul Callaghan.[1] Here we address advanced NMR concepts related to measurement of molecular motion.

When the magnetic field across a sample is inhomogeneous, the ensemble of spins will precess over a range of frequencies, leading to line broadening in the frequency domain and reduced spectral resolution. The spin echo can correct for phase spreading due to field inhomogeneity and produces an exponential echo decay envelope where the echo attenuation results from spin-spin relaxation. While initially viewed as an inconvenience, this frequency domain line broadening due to field inhomogeneity is essential to both magnetic resonance imaging (MRI) and NMR measurements of molecular motion. When the spatial variation in the magnetic field across the sample is known, the range of frequencies produced are encoded for position. Applying the known magnetic field gradient at multiple times encodes for initial and final position and, therefore, encodes for displacement. Thus, both the time dependence of the gradients and the time dependence of molecular motion are embedded in the final phase distribution of the ensemble as recorded in the normalized echo attenuation.

There is not an exact analytical expression that describes general translational motion under any general gradient. Instead, there are analytical expressions for some forms of motion under certain gradient conditions. We can analyze the normalized echo

attenuation to provide insight into coherent, streamline flow and unrestricted self-diffusion, also called Brownian motion. This chapter will discuss NMR theory and methods to analyze coherent flow using the concept of moments of the gradient, before moving into a discussion of the Bloch-Torrey equations for diffusion and flow. The Stejskal-Tanner experiment is commonly used today to measure self-diffusion coefficients.

Next, this paper will address how the pulsed field gradient (PFG) experiment can be used to analyze general motion for which a closed form expression does not exist. The narrow pulse approximation and the low q limit allow for the propagator formalism to be applied to samples where there may be dispersion or restricted diffusion. The normalized echo attenuation obtained from PFG experiments can also provide insight into pore structures, as shown with a discussion of Brownstein-Tarr theory. This paper will also address multidimensional PFG NMR which can be used to correlate the relaxation and diffusive behavior of complex samples.

Time Varying Magnetic Fields and Phase Factors

Measurement of translational motion using NMR requires use of magnetic field gradients. The gradients are applied over as short a time interval as possible, δ, to encode for initial position and again after a mixing period, Δ, to encode for final position. When there is no translational motion, the induced signal is maximized since the phase shift created with the first gradient pulse will be fully reversed with the second inverse gradient pulse. When the effective gradients, $\mathbf{g}^*(t)$, applied to the sample are zeroed, an

echo forms in the signal which is collected by the rf coil in receive mode, expressed by the equation for the echo condition,

$$\int_0^t \mathbf{g}^*(t')dt' = 0 \qquad (3.1)$$

Coherent Flow & Moments of the Gradient

For spins experiencing coherent motion, we can analyze the residual phase shift accumulated during the measurement using the concept of moments of the gradient to design pulse sequences sensitive to velocity, acceleration, or other higher order moments. Diffusive processes like Brownian motion cause signal attenuation but do not result in a residual phase shift, so these processes are not included in the following analysis.

Using effective gradient notation, the accumulated phase, φ, for spin *j* at time *t* can be expressed as

$$\varphi_j(t) = \gamma \int_0^t \mathbf{g}^*(t') \cdot \mathbf{r}_j(t')dt' \qquad (3.2)$$

where $\mathbf{r}_j(t')$ is the spin's path. The path can be approximated using a McLaurin series expansion such that the average spin path is

$$\overline{r(t')} = \bar{r}_0 + \frac{d\,\overline{r(t')}}{dt'}\Big|_0 t' + \frac{1}{2!}\frac{d^2\overline{r(t')}}{dt'^2}\Big|_0 t'^2 + \ldots \frac{1}{n!}\frac{d^n\overline{r(t')}}{dt'^n}\Big|_0 t'^n \qquad (3.3)$$

Since the derivative of position with respect to time is simply velocity, and the second derivative is acceleration, Equation 3.3 can be re-written as

$$\overline{r(t')} = \bar{r}_0 + \bar{v}_0 t' + \frac{1}{2}\bar{a}_0 t'^2 + H.O.T. \qquad (3.4)$$

where H.O.T. refers to the higher order terms which are neglected in the simplified form. When the average spin path is expressed in this way, the very components we are

interested in—position, velocity, and acceleration—are explicit. If the expressions in Equation 3.4 and Equation 3.2 are substituted into Equation 2.48 for the normalized echo amplitude under coherent flow conditions, the resulting expression is

$$E(t) = \exp\left(i\gamma\mathbf{v}\cdot\int_0^t t'\mathbf{g}^*(t')dt' + i\gamma\boldsymbol{a}\cdot\int_0^t t'^2\mathbf{g}^*(t')dt'\right) \qquad (3.5)$$

This expression shows that the phase modulation under coherent flow conditions does not depend on position since the $\vec{r_0}$ term is multiplied by the echo condition, or zeroth moment of the gradient,

$$m_0 = \int_0^t \mathbf{g}^*(t')dt' = 0 \qquad (3.6)$$

The normalized echo amplitude is sensitive to velocity, with the first integral in Equation 3.5 equal to the first moment of the gradient, or the product of the gradient amplitude, g, the gradient pulse duration, δ, and the time between the two gradient pulses, Δ.

$$m_1 = \int_0^t \mathbf{g}^*(t')t'dt' = g\delta\Delta \qquad (3.7)$$

When the pulse sequence is designed such that the second moment of the gradient,

$$m_2 = \int_0^t \mathbf{g}(t')t'^2dt' = g\delta^2\Delta \qquad (3.8)$$

is non-zero, then the pulse sequence will be sensitive to acceleration. By employing the moment of gradient concept and solving the integrals for particular applied gradients, pulse sequences can be designed to selectively measure position, velocity, acceleration or other higher order spin dynamics. A non-zero n^{th} moment allows for measurement of the n^{th} derivative of position.

Bloch-Torrey Equations for Diffusion and Flow

Torrey[2] provides an alternative general approach to analyzing spin phase evolution in the presence of time-varying gradients by modifying the Bloch equations (Equation 2.31) with the addition of a 'transport of magnetization' term. In the Bloch-Torrey equation in Equation 3.9 or 3.10, the net magnetization vector, **M** (**r**, t) is treated as a conserved fluid in Eulerian space.

$$\frac{DM_x}{dt} = \gamma M_y\left(B_0 - {\omega}/{\gamma}\right) - \frac{M_x}{T_2} + \nabla \cdot \underline{\underline{D}} \cdot \nabla M_x \qquad (3.9)$$

$$\frac{\partial M_x}{\partial t} = \gamma M_y\left(B_0 - {\omega}/{\gamma}\right) - \frac{M_x}{T_2} + \nabla \cdot \boldsymbol{D} \cdot \nabla M_x - (\mathbf{v} \cdot \nabla) M_x \qquad (3.10)$$

If we assume that the diffusion coefficient is scalar and move to the rotating reference frame where we can neglect the static magnetic field, $\mathbf{B}_0$, we obtain

$$\frac{\partial M_+}{\partial t} = -i\gamma \mathbf{r} \cdot \mathbf{g}^*(t) M_+ - \frac{M_+}{T_2} + D\nabla^2 M_+ - (\mathbf{v} \cdot \nabla) M_+ \qquad (3.11)$$

where $M_+ = M_x + iM_y$, the transverse magnetization. The solution is

$$M_+(r,t) = A(t) \exp\left(-i\gamma \mathbf{r} \cdot \int_0^t \mathbf{g}^*(t')dt'\right) \exp({-t}/{T_2}) \qquad (3.12)$$

where A(t) is a modulation factor, the first exponential term—the phase factor—is a helical phase distribution which reduces to 1 at the echo center, and the second exponential describes transverse relaxation. Solving for A(t) yields

$$A(t) = \exp\left(-D\gamma^2 \int_0^t \left(\int_0^{t'} \mathbf{g}^*(t'')dt''\right)^2 dt'\right) \exp\left(i\gamma \mathbf{v} \cdot \int_0^t \int_0^{t'} \mathbf{g}^*(t'')dt''dt'\right) \qquad (3.13)$$

Under the echo condition $\int_0^t \mathbf{g}^*(t')dt' = 0$, A(t) is equal to the normalized echo attenuation, E(t). At any other time, there is an additional time-dependent attenuation

term arising from integrating the phase factor and averaging over all possible local position vectors, **r**, in the ensemble of spins. Since we want to be able to evaluate the attenuation due solely to diffusion, the Bloch-Torrey equations are used to evaluate signal only at the echo center.

It is also useful to note that the inner integral in both exponential terms of Equation 3.13 is zeroth moment (Equation 3.6). The double integral in second exponential results in the 1st moment, as given in Equation 3.7. The moments use the average phase evolution across the ensemble of spins and therefore only apply to advective flow. The first exponential term in the expression for A(t) is not a moment of the gradient since the inner integral is squared. Instead, the squared term yields the variance. The Stejskal-Tanner relationship results from this first exponential term, describing diffusive attenuation, when the pulsed gradient spin-echo (PGSE) pulse sequence is analyzed with the Bloch-Torrey equations.

The Stejskal – Tanner Experiment

Stejskal and Tanner first demonstrated the PGSE pulse sequence in 1965 [3]. The pulse sequence is shown in Figure 3.1, and was discussed previously in Chapter 2 (Figure 2.20). The 90° pulse excites the ensemble of spins which are then encoded for their initial position with the first gradient pulse of duration δ. The spins can move according to the hydrodynamics of the sample during the period Δ. The 180° pulse inverts any previous phase shift before the second gradient pulse encodes for final position. The echo signal occurs at time 2τ.

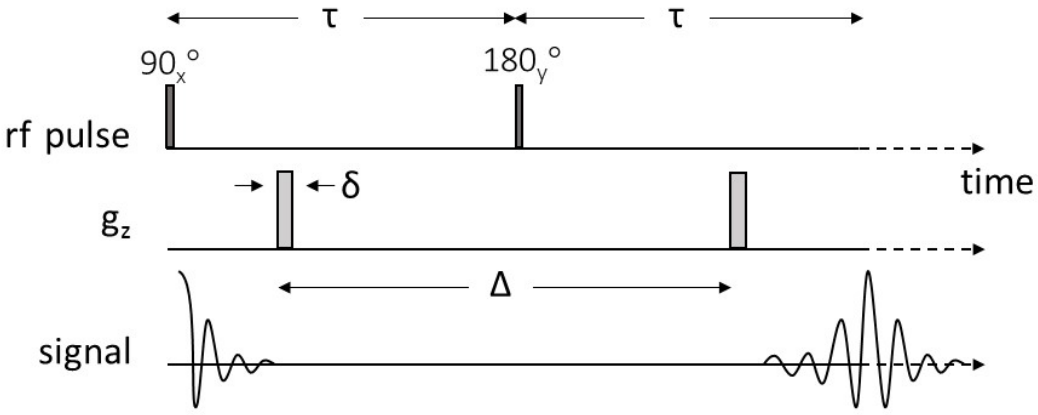

Figure 3.1. The pulsed gradient spin-echo (PGSE) sequence uses pulsed magnetic field gradients of amplitude g, duration δ, separated by a diffusion time, Δ. The echo signal occurs at time 2τ.

A variation on the PGSE experiment is the pulsed gradient stimulated echo (PGStE) experiment, shown in Figure 3.2. Rather than the single 180° used in the PGSE experiment to refocus the signal, the PGStE pulse sequence uses two 90° pulses. The first 90° pulse after the application of the encoding gradient stores the magnetization along the z-axis where it is immune to T_2 relaxation. The last 90° pulse tips the magnetization back into the transverse plane where it can be measured. The PGStE sequence is typically applied for samples where T_2 decay limits the range of Δ values that can otherwise be probed.

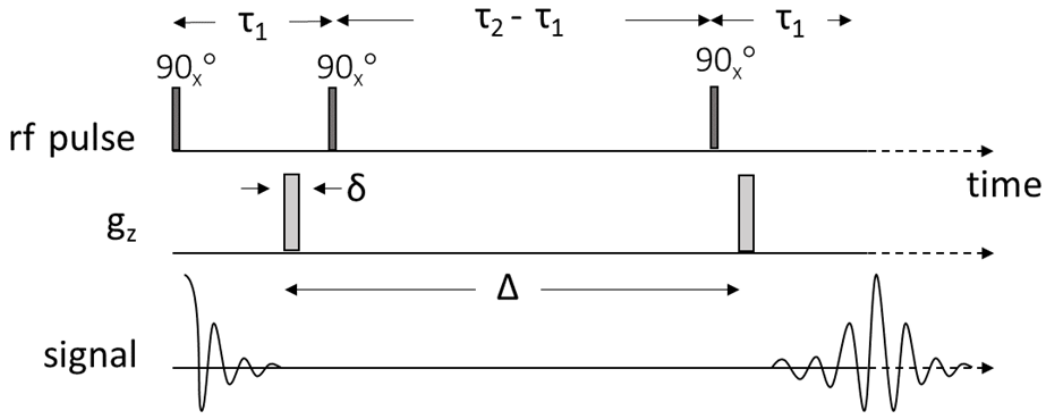

Figure 3.2. The pulsed gradient stimulated echo (PGStE) sequence uses pulsed magnetic field gradients of amplitude g, duration δ, separated by a diffusion time, Δ. Rather than creating the echo with a single 180° pulse, the PGStE sequence uses two 90° pulses to store the magnetization along the z-axis where it is not subject to T_2 relaxation.

The normalized signal in the Stejskal-Tanner experiment is given by the expression for echo amplitude attenuation,

$$E(t) = \frac{S(\mathbf{g})}{S(0)} = \exp\left(-\gamma^2 g^2 \delta^2 D\left(\Delta - {}^{\delta}/_{3}\right)\right) \qquad (3.14)$$

where *D* is the self-diffusion coefficient when the geometry and measurement timescale allows unrestricted diffusion. The echo attenuation results from incoherent phase shifts across the ensemble since the combination of rf and gradient pulses will rephase the spins. By varying the amplitude of the applied gradient, *g*, and holding experimental times constant, it is possible to remove the influence of relaxation effects. To determine the time dependence of diffusion, the diffusion time Δ can be varied between experiments.

The diffusion coefficient, *D*, can be extracted from the slope of the line that results when the natural log of the normalized signal, $ln|E(t)|$, is plotted versus $-\gamma^2 g^2 \delta^2 \left(\Delta - {}^{\delta}/_{3}\right)$. This plot is called the Stejskal-Tanner plot (Figure 3).

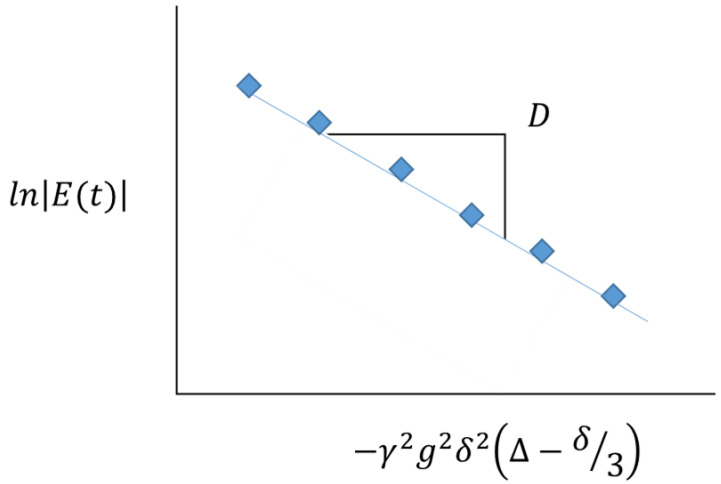

Figure 3.3. The Stejskal-Tanner plot yields the self-diffusion coefficient, *D*.

Generalized Translational Motion

Under conditions of generalized translational motion, for example where there is restricted diffusion or dispersive flow in porous media, there is not a direct analytical expression for the echo attenuation of the signal. We can, however, still use the propagator formalism to describe this type of general motion under certain circumstances. Recall that the propagator, $\overline{\mathrm{P}}(Z, \Delta)$, is the probability density function describing the likelihood that a given spin would experience a given dynamic displacement, Z, over the time period Δ (Equation 3.15). The propagator is a Fourier transform pair with the normalized echo signal, $E(q, \Delta)$.

$$E(q,\Delta) = \int \overline{\mathrm{P}}(Z,\Delta)\exp(iqZ)dZ \qquad (3.15)$$

The first condition requires that pulsed gradients used to encode for displacement be applied over a sufficiently short time period, δ, so that we can neglect the motion during that interval. Typically this translates to $\delta \ll \Delta$, but more broadly can be understood to mean that δ should be less than any characteristic timescale for motion, such as the time for a spin to diffuse across a pore.

Equation 3.15 shows that the two pulsed gradients of duration δ and separated by the time period Δ impart a phase shift to spins that have moved that is the product of two vectors: the dynamic displacement, Z = (z –z'), and the wave vector, $q = \gamma\delta\mathbf{g}$.
The expression for the normalized echo signal can be simplified when q is small, called the low-q limit. This region corresponds to very short pulses and low gradient strength. In the low-q limit, we can re-write Equation 3.15 as

$$E(\mathbf{q},\Delta) \approx 1 + iq\int \overline{P}\,(Z,\Delta)ZdZ - \frac{1}{2}q^2\int \overline{P}\,(Z,\Delta)Z^2dZ + \ldots \qquad (3.16)$$

The linear term in q describes the mean displacement due to coherent flow. When there is no flow and only Brownian motion occurs, the expression simplifies to

$$E(\mathbf{q},\Delta) \approx 1 - \frac{1}{2}q^2\langle Z^2(\Delta)\rangle \qquad (3.17)$$

Plotting the low-q data against q^2 allows for $\langle Z^2(\Delta)\rangle$, the mean squared displacement, to be directly extracted from the slope of the initial linear decay. Using Einstein's relation $\langle Z^2(\Delta)\rangle = 6Dt$ for a 3D system, or $\langle Z^2(\Delta)\rangle = 2Dt$ for a 1D system, yields the self-diffusion coefficient from the echo signal.

Brownstein-Tarr Theory

In order to correctly interpret PFG echo attenuation data in microscopically inhomogeneous porous media, it is important to examine how relaxation is affected by the sample structure and geometry. Specifically, is relaxation important over the diffusion observation time interval, Δ? Or conversely, is diffusion important over the echo time, t_E, where $t_E = 2\tau$? Several models have been developed to describe the relationship between diffusion and relaxation in porous media.

The first model holds that the relaxation rate is a function of a physical region in which the spin resides. In this case, diffusion is a migration of spins from one relaxation domain to another, termed "exchange between sites." This model provides no geometric detail but distinguishes between 'bound' water, with a correlation time, $\tau_c \approx 10^{-8}$ s, and 'free' water with $\tau_c \approx 10^{-12}$ s by assigning relative site occupancies, site residence times, and local site relaxation rates.

In the case of slow exchange, relaxation, $T^{(i)}$, occurs faster than the exchange time, τ_e, between the different relaxation domains, i, such that $T^{(i)} << \tau_e$. The exchange time can be understood as the mean timescale for a proton to sample the different relaxation domains and is related to molecular diffusion and/or chemical exchange of protons between neighboring water molecules. In the slow exchange regime, the total relaxation of the system is a multi-exponential decay since each spin will relax in a single domain and each domain will contribute proportionally to the total echo attenuation.

When relaxation proceeds more slowly than exchange ($T^{(i)} >> \tau_e$), called fast exchange, there is a single relaxation time for the system since each spin will experience

a different relaxation rate in each domain sampled during the measurement, effectively averaging the relaxation rates. Intermediate exchange results in non-exponential signal decay.

A second model relies on a geometric description to relate relaxation and diffusion in porous media. In this model, we distinguish between the relaxation of the bulk fluid in the pore space, $T_{i\mathrm{B}}$, and the relaxation of the fluid directly interacting with the pore surface, $T_{i\mathrm{S}}$. Here, the relaxation time can refer to either spin-lattice (T_1) or spin-spin relaxtion (T_2), with the general case denoted as T_i. The solid matrix introduces surface relaxation sinks that enhance relaxation of the spins nearest to the pore walls. These sinks can be paramagnetic ions within the mineral surface of the pore walls or a local hindering of rotational mobility resulting from increased dipole-dipole interactions between liquid and solid phase molecules. Clearly, the surface to volume ratio of the pore, *S/V*, is important in this model and is related to pore size and geometry. There are also differences in magnetic susceptibility between the solid matrix and the bulk liquid, resulting in internal magnetic field gradients near the pore walls. Diffusion of spins within these internal inhomogeneities in the magnetic field further enhance relaxation.

The geometric model was developed in detail by Brownstein and Tarr in 1979.[4] The authors observed fast and multi-exponential signal decay behavior in the water within biological cells. They concluded that the multi-exponential behavior was a consequence of the geometry of the cell and that it is possible to use NMR data to make inferences about the size and shape of pores (or cells). Brownstein and Tarr approached the problem by assuming diffusion of the magnetization density, M(**r**,t), according to

Fick's Laws. They integrated over the pore volume and applied the initial condition, M(**r**, 0) = M(0)/V to solve for the general normal mode solution

$$M(t) = M(0)\sum_{n=0}^{\infty} I_n \exp\left(-t/T_n\right) \qquad (3.18)$$

where $I_n = a_n \int d\mathbf{r}_V \, u_n$ and describes the relative intensity. The parameter n is the mode number, u_n is an eigenfunction, and the decay time T_n (actually T_{1n} or T_{2n}) is an eigenvalue. Equation 2.15 shows that the evolution of the net magnetization proceeds as a sum of decreasing exponential functions in time—resulting in the observed multi-exponential decay. I_n and T_n depend on *D*, the self-diffusion coefficient, *a*, the characteristic pore size, and $\bar{\rho}$, the surface relaxivity, an empirical parameter describing the average sink strength of the surface. This solution assumes that there are no relaxation sinks within the pore volume, only on the active surface of the pore.

Solving for I_n and T_n for planar, cylindrical and spherical geometries reveals the importance of the dimensionless sink strength parameter, $\bar{\rho}a/D$. For each geometry, the mode amplitude, I_n, depends on $\bar{\rho}a/D$, which can be used to assign regimes analogous to the fast and slow exchange regimes of the first model. When there is fast diffusion and $\bar{\rho}$ is weak compared to *D* such that $\bar{\rho}a/D \ll 1$ – the fast exchange regime – there is a single relaxation mode, I_0, for all geometries and the spins will experience single exponential decay with a relaxation rate, $T_0^{-1} \sim \bar{\rho}(S/V)$. In the slow exchange regime, when $\bar{\rho}$ is strong compared to D and $\bar{\rho}a/D \gg 1$, the lowest relaxation mode still dominates but there is increasing influence of the higher modes. This means that spins will exhibit multi-exponential decay during the measurement timescale. In the slow exchange regime,

therefore, relaxation time, $T_0 \sim a^2/D$, corresponds to the time to diffuse across the pore since the spin will be lost to relaxation once it interacts with the surface.

These results predict the same relationship between the decay behavior of the normalized echo amplitude and the relaxation and diffusion properties of a system as the first, non-geometric model – single exponential decay when the spins can sample the entire pore, and multi-exponential decay when they cannot. The higher mode decay rates, T_n^{-1}, are visible only in the slow exchange/slow diffusion regime, are nearly independent of $\bar{\rho}$, and are of an order $a^2/n^2\pi^2 D$. Because of this relationship, we can estimate the range of pore sizes that may exhibit multi-exponential decay when examined with PFG NMR. Assuming D = 2.5 x 10^{-5} cm^2/s and T_n is between 1 μs (due to hardware limitations) and 2 s (the relaxation of bulk water), the pore dimension, *a*, is in the range of 1 – 30 μm. This is exactly the size range of biological cells and pore sizes in natural porous media like sedimentary rock.

While it is difficult to independently and reliably estimate the average surface relaxivity, $\bar{\rho}$, the Brownstein-Tarr model is widely used to obtain pore-size distributions from multi-exponential relaxation data and complements **q**-space data as a way to characterize pore structure and geometry.

Multidimensional PFG and Relaxation NMR

Multidimensional PFG-NMR experiments encode the induced signal in multiple independent dimensions and can take the form of correlation or exchange experiments. Correlation experiments involve the measurement of two different parameters, like

diffusion (D) and T_2, at the same time to see how one parameter is related to the other. In the case of the D-T_2 experiment, for example, we are interested in how molecular translational mobility (D) is correlated with molecular rotational mobility (T_2). Exchange experiments, on the other hand, encode for one parameter at two different times to probe molecular migration between domains.

The measured signal is transformed to produce a spectrum using either the Fourier or Laplace transform. Which type of transform is appropriate for a given signal depends on the information sought from the sample. Oscillating, decaying signal collected in the time domain can be Fourier transformed to produce a spectrum of the frequencies contributing to the signal in the frequency domain. When the signal is collected under the influence of time-varying gradients and coherent flow, the Fourier transformed data will produce a spectrum of displacements, the propagator. Diffusive displacements result in a signal that decays exponentially with respect to q^2, the squared gradient pulse area. A Fourier transform of the diffusion data with respect to q produces a Gaussian displacement spectrum where the width depends on the diffusion coefficient, D.

If data is collected from a sample exhibiting multi-exponential signal decay due to a range of relaxation domains or diffusion coefficients, Fourier transformation of the signal will result in a superposition of Gaussian distributions, making it difficult to extract the relaxation rates or diffusion coefficients associated with each domain. Equation 2.19 shows the multi-exponential signal $E(q)$ collected from a sample with multiple diffusion coefficients. A Fourier transform of the signal produces a spectrum of displacements, $\bar{P}(Z)$, rather than a spectrum of diffusion coefficients, $P(D)$.

$$E(q) = \int P(D)\exp(-q^2 D\Delta)\, dD \qquad (3.19)$$

$$\bar{P}(Z) = \int P(D)(2\pi D\Delta)^{-1/2}\exp(-Z^2/2D\Delta)dD \qquad (3.20)$$

The inverse Laplace transform (ILT), $\mathcal{L}^{-1}\{E(q^2,\Delta\}$,with respect to q^2 will produce a spectrum, or distribution, of the probability of having a given diffusion coefficient, $P(D)$.

$$P(D) = \mathcal{L}^{-1}\{E(q^2,\Delta\} \qquad (3.21)$$

$$E(q^2,\Delta) = \mathcal{L}\{P(D)\} = \int_0^\infty P(D)\exp(-q^2 D\Delta)\, dD \qquad (3.22)$$

Likewise with measurements involving sub-ensembles with different relaxation rates, the ILT of relaxation data, $\mathcal{L}^{-1}\{S(t)\}$, returns a distribution of the relaxation decay rates that contribute to the multi-exponential decay, $f(R)$.

$$f(R) = \mathcal{L}^{-1}\{S(t)\} \qquad (3.23)$$

$$S(t) = \mathcal{L}\{f(R)\} = \int_0^\infty f(R)\exp(-Rt)\, dR \qquad (3.24)$$

The forward and reverse Fourier transform are well-defined, symmetric with bounds between -∞ and ∞, and easy to implement with the fast Fourier Transform (FFT) algorithm. The ILT, however, is ill-defined, asymmetric with bounds between 0 and ∞, and not easy to implement. The analytical form of the ILT, shown below for a distribution of relaxation rates,

$$f(R) = \mathcal{L}^{-1}\{S(t)\} = \frac{1}{2\pi i}\int_{\gamma-i\infty}^{\gamma+i\infty} S(t)\exp(Rt)\, dt \qquad (3.25)$$

is a contour integral in a complex plane where γ is a vertical contour positioned to the right of any singularities. This unstable expression can result in exponential divergence

when there is noise in S(t), making this analytical form not particularly useful in practice. Instead, Provencher[5] developed a regularized non-negative least squares method to perform the ILT in 1982 that uses a discrete form of the signal that allows for noise:

$$S(t_i) = \sum_{j=1}^{M} \exp(-t_i R_j)\, f(R_j) + \epsilon_i \quad (3.26)$$

where ϵ_i is the error or noise in the measurement, *i* is the discrete time interval, and *j* is the discrete relaxation rate domain. *A priori* knowledge of the system requires that $f(R_j)$>0. The optimal solution will be as simple as possible and minimize the error, ϵ_i, for a given range of R between R_{max} and R_{min}, where *R* is the relaxation rate associated with each domain.

Provencher used the Tikhonov regularization[6] to ensure parsimony (the simplest solution) where we seek a minimum value for the solution, $V(\alpha)$, where

$$V(\alpha) = \left\| \underline{\underline{K}}\underline{f} - \underline{S} \right\|^2 + \alpha^2 \left\| \underline{\underline{\Gamma}}\underline{f} \right\|^2 = minimum \quad (3.27)$$

and

$$\left\| \underline{\underline{\Gamma}}\underline{f} \right\|^2 = \int_{R_{min}}^{R_{max}} [f''(R)]^2 dR \quad (3.28)$$

In these expressions, *K(t, R)* is the kernel, α is regularization parameter, and Γ is a smoothing operator based on the curvature of *f*, the distribution, and *S* is the measured signal. The expression in Equation 2.27 is discretized such that a solution vector $\underline{f}$ has values corresponding to each element, R_j, such that

$$V(\alpha) = \sum_{i}^{N} \sum_{j}^{M} (S_i - \exp(-t_i R_j)\, f_j)^2 + \alpha^2 \sum_{j}^{M} (2f_j - f_{j+1} - f_{j-1})^2 \quad (3.29)$$

The first summation term – the residual – is called χ^2 and is minimized by selecting the value of the regularization parameter,α, that minimizes the error term in the second summation. A large value of α implies a high level of confidence in the fine details of the measurement. Too large a value of α leads to 'pearling' of the data where more detail is shown in the final distribution than exists in the original data. Hence, we seek the solution that produces the least amount of curvature in the distribution while still faithfully representing the data.

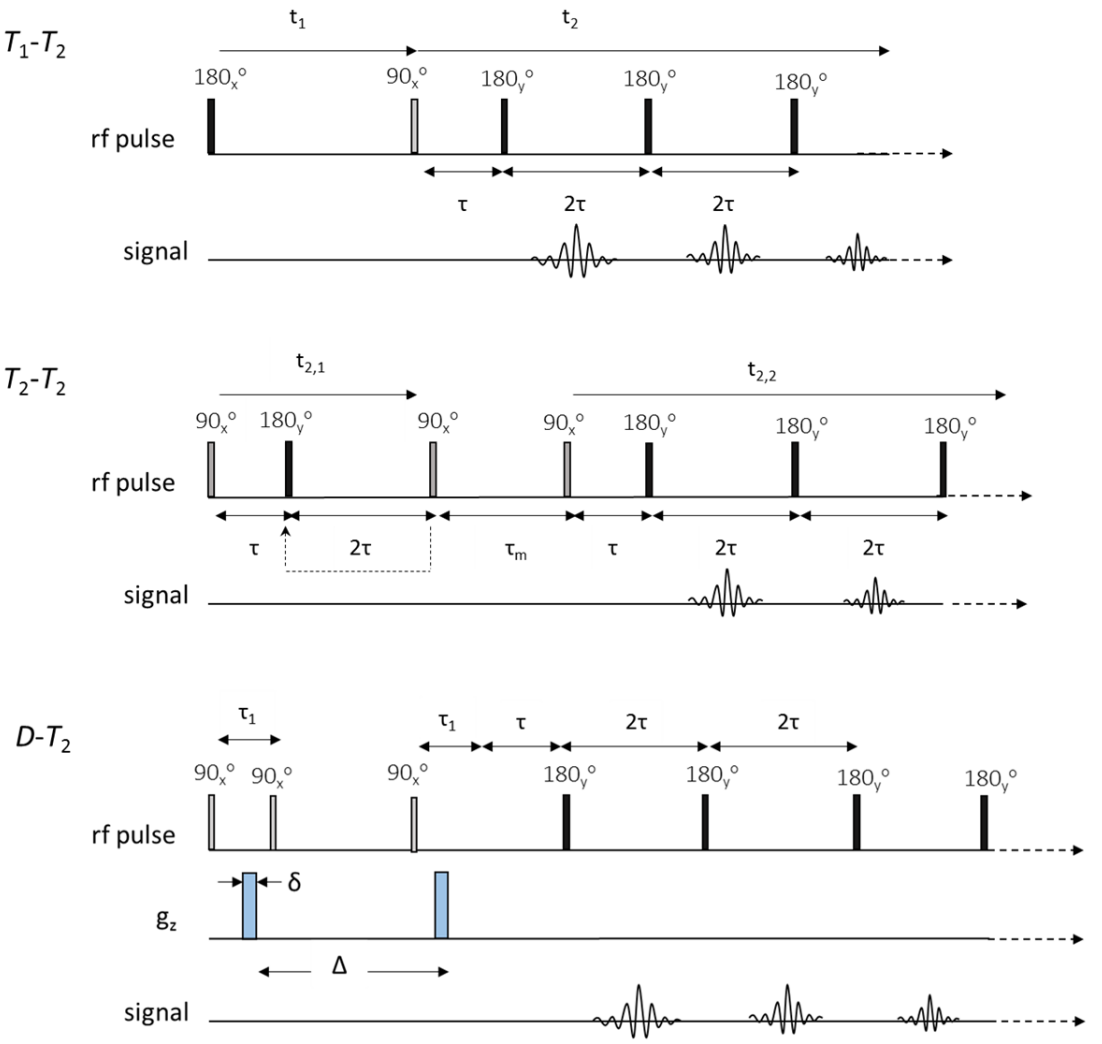

Figure 3.4. Multi-dimensional PFG-NMR correlation and exchange pulse sequences. The T_1-T_2 pulse sequence (top) and D-T_2 pulse sequence (bottom) correlate two different parameters in the same time step. The T_2-T_2 pulse sequence (middle) encodes for relaxation at two different times and gives insight to exchange between relaxation domains.

The pulse sequences used to collect multi-dimensional PFG-NMR data and correlation and exchange measurements are shown in Figure 3.4. The T_1-T_2 experiment (top) first encodes for T_1 relaxation for a given inversion time, then measures T_2 decay.

The measurement is repeated for a range of inversion times to correlate the sample's T_1 and T_2 relaxation properties.

The T_2-T_2 exchange pulse sequence (Figure 3.4, middle) encodes for T_2 relaxation at two different time periods, separated by a mixing period, τ_m, during which spins are free to migrate between relaxation domains. Magnetization is stored along the z-axis during the mixing period to preserve the relaxation encoding of the first CPMG train. The number of echoes produced during the first encoding period is varied to capture both long and short relaxation components of the first encoding period in the final recorded signal. The T_2-T_2 exchange experiment provides insight to the timescale of molecular transport between physical regions in the sample, i.e. pores, or between relaxation domains, i.e. bound vs. free water.

The pulse sequence for the diffusion – relaxation, or D-T_2, experiment is shown in Figure 4, bottom. After encoding for diffusion with the PGStE sequence, a CPMG echo train is collected to measure T_2 relaxation. The strength of the pulsed gradient, g, is varied with each repetition of the sequence to resolve the range of effective diffusion coefficients present in the sample. Data collected with the D-T_2 can be analyzed with the 2D ILT to produce distributions of both diffusion and relaxation, or the diffusion data can be analyzed with Fourier methods when sufficient positive and negative q-steps are collected. The Fourier-Laplace analysis produces a T_2-resolved propagator.

References

1. Callaghan, P.T., *Translational Dynamics & Magnetic Resonance: Principles of Pulsed Gradient Spin Echo NMR*. 2011, New York: Oxford University Press.

2. Torrey, H.C., *Bloch Equations with Diffusion Terms.* Physical Review, 1956. **104**(3): p. 563-565.

3. Stejskal, E.O. and J.E. Tanner, *Spin diffusion measurements: Spin echoes in the presence of a time-dependent field gradient.* Journal of Chemical Physics, 1965. **42**: p. 288.

4. Brownstein, K.R. and C.E. Tarr, *Importance of classical diffusion in NMR studies of water in biological cells.* Physical Review A, 1979. **19**(6): p. 2446-2453.

5. Provencher, S.W., *A constrained regularization method for inverting data represented by linear algebraic or integral equations* Computer Physics Communications, 1982. **27**(3): p. 213-227.

6. Tychonoff, A.N. and V.Y. Arsenin, *Solution of ill-posed problems*. 1977, Washington: Winston and Sons.

CHAPTER FOUR

LOW-FIELD BOREHOLE NMR APPLICATIONS IN THE NEAR SUBSURFACE ENVIRONMENT

Contribution of Authors and Co-Authors

Manuscript in Chapter 4

Author: Catherine M. Kirkland

Contributions: Researched and wrote manuscript.

Co-Author: Sarah L. Codd

Contributions: Helped write manuscript. Provided feedback and comments on the manuscript.

Manuscript Information Page

Catherine M. Kirkland, Sarah L. Codd

Vadose Zone Journal

Status of Manuscript:
____ Prepared for submission to a peer-reviewed journal
__X_ Officially submitted to a peer-review journal
____ Accepted by a peer-reviewed journal
_ ___ Published in a peer-reviewed journal

Soil Science Society of America
January, 2017

LOW-FIELD BOREHOLE NMR APPLICATIONS IN THE NEAR-SURFACE ENVIRONMENT

Abstract

The inherent heterogeneity of the near subsurface (< 200 m below the ground surface) presents challenges for agricultural water management, hydrogeologic characterization, and engineering, among other fields. Borehole nuclear magnetic resonance (NMR) has the potential not only to describe this heterogeneity in space non-destructively, but also to monitor physical and chemical changes in the subsurface over time. NMR is sensitive to parameters of interest like porosity and permeability, saturation, fluid viscosity, and formation mineralogy. Borehole NMR tools have been used to measure soil moisture in model soils and recent advances in low-field borehole NMR instrumentation allow for estimation of hydraulic properties of unconsolidated aquifers. We also present results demonstrating the potential for low-field borehole NMR tools to monitor field relevant biogeochemical processes like biofilm accumulation and microbially-induced calcite precipitation (MICP) at laboratory and field scales. Finally, this mini-review addresses some remaining challenges and areas of future research, as well as other possible applications where borehole NMR could provide valuable complementary data.

Introduction

The inherent heterogeneity of the near subsurface, defined here as< 200 m below the ground surface, presents challenges for agricultural water management, hydrogeologic characterization, and engineering, among other fields. Knowledge of the spatial heterogeneity of unconsolidated sediments is vital to accurately estimate hydraulic properties related to storage and flow and to locate confining layers. Spatially varying hydraulic properties can cause preferential flow paths and mixing of subsurface flows where conductivity and permeability are high, or alternatively, trap contaminants and impede remediation efforts where conductivity and permeability are low. For example, the increasing consumptive pressure on groundwater reserves is stimulating managed aquifer recharge (MAR) and aquifer storage and recovery (ASR) solutions which require greater sophistication in hydrogeologic investigations and modelling than conventional wellfields [1]. These methods artificially recharge aquifers with water of a sometimes differing quality than the native water, such as fresh water stored in a brackish aquifer. Extraction of the high-quality water later for re-use is maximized only when there is minimal mixing during storage as would occur in lower transmissivity zones. Furthermore, recent years have seen increased interest in harnessing the power of biogeochemical conversions to assist diverse engineering applications, including *in-situ* bioremediation of subsurface contaminants [2] and microbially-induced calcite precipitation (MICP) for fracture sealing [3] or geotechnical applications to strengthen soils [4, 5]. These methods are intended to alter the physical and chemical environment

of the pore space; proper execution of these projects requires knowledge of both temporal and spatial variations in the subsurface.

The standard reference method for obtaining the volumetric water content of porous media is gravimetric. A sample of known volume is weighed before and after oven drying to determine the water content at the time of the measurement. Gravimetric measurements are necessarily invasive, destructive, and time-consuming to perform, providing point-scale data at a single time. Neutron thermalization methods, like neutron scattering, are significantly less invasive than gravimetry and are based on a well-established, linear correlation between the sediment water content and the ratio of thermalized neutrons reaching the detector. The radioactive materials which supply the neutrons, however, impose significant regulatory barriers, making the technology less attractive as newer methods are developed [6]. Established hydrogeophysical methods for *in-situ* characterizations of soil and sediment rely on measurements of geophysical properties to infer hydrogeological properties, meaning that the methods do not provide direct measurement of water [6, 7]. For example, Electrical Resistivity Tomography (ERT), Ground Penetrating Radar (GPR), and seismic methods measure electrical conductivity or resistivity, acoustic impedance, and velocity and attenuation of seismic waves, respectively, to provide information about water content and porosity. The translation of measured geophysical data to hydrogeologic and hydraulic properties of interest requires non-trivial mathematical inversions and modelling. The many hydrogeophysical methods available have varying spatial scales and resolution; readers

should refer to several recent reviews of geophysical methods for more information [6, 7].

Nuclear magnetic resonance (NMR) methods have the potential to both characterize subsurface heterogeneity and monitor changes in the geophysical and biochemical environment over time, suggesting the importance of this technology for these fields. Low-field NMR instrumentation for field applications can take several forms – mobile single-sided instruments like the NMR MOUSE, surface NMR instruments, or borehole NMR probes. Though the focus of this mini-review is borehole NMR, single-sided NMR and surface NMR tools deserve mention. The NMR MOUSE, developed by researchers at RWTH – Aachen University in the 1990's [8], weighs approximately 1 kg and has been used in applications ranging from biomedicine, cultural heritage preservation, materials science, and measurement of moisture in soils and building materials [9, 10]. The depth of investigation for the various single-sided NMR probes is typically on the order of centimeters. The configuration of the permanent magnets and coils of wire comprising mobile, single-sided NMR tools vary according to the application and the goals of the NMR measurement. Readers may refer to the comprehensive description given by Blumich *et al*. (2008). Non-invasive explorations of near surface hydrogeologic and hydraulic properties can also be performed with surface NMR. Surface NMR uses the Earth's magnetic field and coils of wire deployed on the ground surface to collect the NMR measurement. Although surface NMR coils are easy to deploy and are entirely non-invasive, the technology faces challenges related to low signal-to-noise, a long instrument dead-time between excitation and detection which

means that water in small pores is not measured, and a relatively shallow depth of investigation (< 100 m) with vertical resolution on the order of 10 m [11]. Several reviews which provide a description of theory and recent advances in the technology have been published [11, 12].

Borehole NMR tools have been used in the oil and gas industry to identify and characterize hydrocarbon reserves since the 1960s [13] due to the sensitivity of NMR to hydraulic properties of interest, like pore size distribution, permeability and hydraulic conductivity, and fluid content and viscosity. The mathematics describing the relationship between the measured NMR signal response and these formation hydraulic properties developed alongside technical improvements to the instruments, such that now NMR tools are an indispensable part of the oil and gas industry [14, 15]. Despite the fact that the same hydraulic parameters are of interest in hydrogeology, geotechnical engineering, and soil science, the oilfield well-logging tools are too large, expensive, and impractical for most near-surface applications. As a result, the application of NMR tools to near-surface investigations in unconsolidated sediments has developed only in the last decade due to several independent and complimentary factors. Technical innovations have allowed down-sizing of the hardware, and developments in numerical methods and error estimation have improved the mathematical inversions needed for data processing [16-18]. Finally, pressures on global water supplies and the need for improved monitoring methods drive innovations in borehole NMR technology.

Recently, portable and lower-cost borehole NMR tools have been developed in both commercial [19] and non-commercial [20] forms. These tools vary significantly in

operating frequency, measurement distance from the tool, the size of the probe, vertical resolution, and the minimum echo spacing, with significant implications for the ease of use of the instrument and interpretation of the data. This paper describes recent applications of these tools related to soil water management, hydrogeology, and biogeochemical engineering in the near subsurface, as well as remaining challenges and further potential applications for the technology.

Theory

^{1}H NMR measures the response of hydrogen-bearing molecules, typically water, to perturbations in a magnetic field. As such, NMR is directly sensitive to water in soil, rock, and unconsolidated subsurface sediments. Borehole NMR tools generally consist of permanent magnets and radio-frequency (rf) induction coils. The permanent magnets create a static magnetic field, B_0, in the formation. The magnetic field strength in the formation drops off with the radial distance from the tool as does the resonant frequency at which the water will respond. The resonant frequency is called the Larmor frequency, $\omega_0 = \gamma B_0$, where γ is the gyromagnetic ratio, a constant with a value of 2.675 x 10^8 rad/(T s) for hydrogen. Pulses of current are transmitted through the rf coils, exciting hydrogen at a particular Larmor frequency. The location of the cylindrical excitation region depends on the tuning of the probe; higher Larmor, i.e. operating, frequencies produce an excitation - detection shell closer to the wellbore where the magnetic field is stronger, while lower Larmor frequencies allow measurement deeper into the undisturbed formation (Figure 4.1). The excited hydrogen protons generate a detectable signal according to Faraday induction at the Larmor frequency which is received on the rf coils.

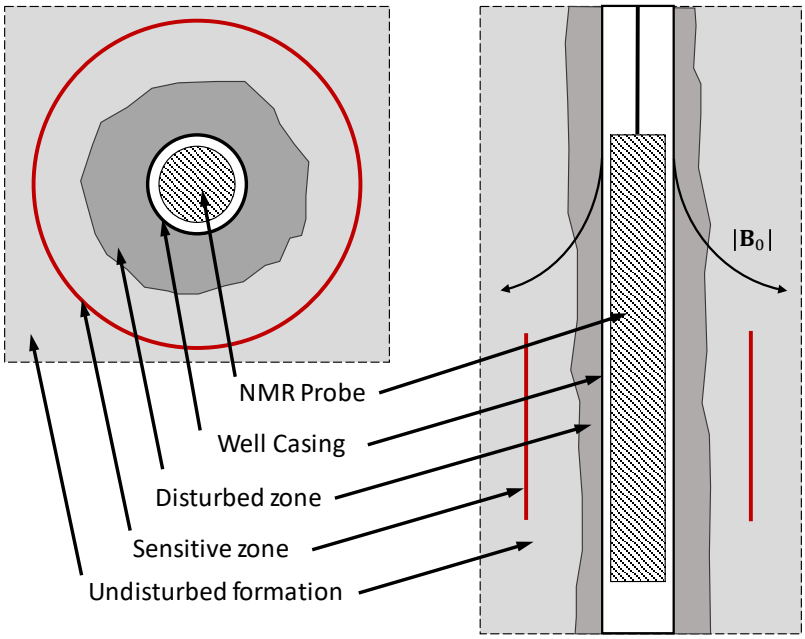

Figure 4.1. Schematic of a generalized borehole NMR wire-line logging tool with a cylindrical excitation-detection shell. The magnitude of the static magnetic field, B_0, decays with radial distance from the well. The NMR probe is tuned to excite protons (water) at a particular Larmor frequency, $\omega_0 = \gamma B_0$, which corresponds to a particular radial distance from the well. Lower frequencies produce excitation – detection shells outside the disturbed soil zone that results from traditional well-drilling methods.

The induced NMR signal amplitude decays in time as the system returns to equilibrium in a process called *relaxation* [21]. T_1 (spin-lattice) relaxation and T_2 (spin-spin) relaxation both provide information about the local physical and chemical environment. T_1 relaxation is related to the timescale for system to return to thermal equilibrium as the added energy from the excitation rf pulse dissipates into the environment, or lattice. T_2 relaxation is related to molecular interactions occurring between the excited water molecules and their interactions with the pore walls. Measurement of T_2 relaxation is robust and faster to perform, making it preferred for low-field borehole NMR [22]. T_2 relaxation is measured with the CPMG pulse sequence [23,

24] in which a series of re-focusing rf pulses, called 180° pulses, follow the 90° rf excitation pulse (Figure 4.2). The 180° pulses create a series of signal echoes where the initial signal amplitude is proportional to the volumetric water content and echo amplitudes decay at a rate of T_2^{-1}. The time between echoes is called the echo spacing, t_E.

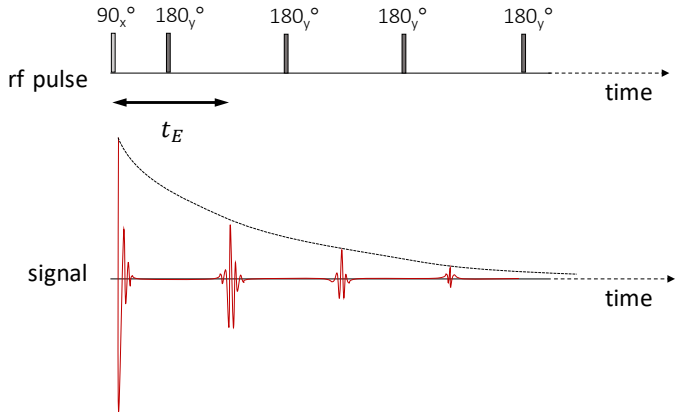

Figure 4.2. The CPMG pulse sequence consists of a 90° excitation pulse and a series of refocusing 180° pulses. The induced signal consists of a series of echoes in which the decay curve (thin dashed line) has an initial amplitude proportional to the water content and an exponential decay rate of $1/T_2$.

Data acquisition with borehole NMR tools in the field involves lowering the probe incrementally into the subsurface, either in a borehole well or in an opening made by a direct push (DP) tool. DP methods drive an instrumented steel rod into the ground using hydraulic rams and avoid the need to drill boreholes. Aside from the borehole or DP opening, NMR is non-invasive and non-destructive. An NMR measurement is collected at each depth increment to create a well log, or soil profile, describing the sediment-water relationship via T_2 relaxation. The vertical resolution of the well log depends on the

dimensions of the rf coil. The logging speed is related to the signal to noise ratio, and thus, how many measurements are collected and averaged at each depth increment.

Since natural porous media is composed of many pores of varying sizes and geometries, the signal collected during an NMR measurement is the sum of the signal from each individual pore. The resulting multi-exponential signal decay curve data is typically analysed with the inverse Laplace transform (ILT), producing a distribution of T_2 relaxation times. The integrated amplitude of the distribution provides the volume fraction of water in the measurement region—the porosity if the sediment is saturated or the water content if it is unsaturated. Such estimates can also be obtained from the initial amplitude of the signal decay curve [25].

NMR T_2 relaxation is sensitive to the physical and chemical properties of macroscopic porous media systems, including pore size, soil mineralogy, degree of water saturation, and pore fluid viscosity. The expression for the T_2 relaxation rate, typically in units of ms^{-1}, in a single pore is given by the equation

$$T_2^{-1} = T_{2B}^{-1} + T_{2S}^{-1} + T_{2D}^{-1} \quad [1]$$

where T_{2B}^{-1} is the bulk fluid relaxation rate, and T_{2S}^{-1} is the surface relaxation rate. The final relaxation term is related to diffusion in an inhomogeneous magnetic field and can influence NMR T_2 relaxation measurements where the gradient in the local magnetic field is high or when the echo spacing, t_E, of the measurement is long. Gradients, or inhomogeneities, in the static magnetic field result when the sediment is composed of materials with different magnetic susceptibilities or when the strength of the B_0 field rapidly decays in the radial direction [26]. A lower operating frequency reduces the

static field gradient. Minimizing t_E through instrument design and experimental parameter selection can reduce the impact of T_{2D} on the NMR signal response.

Many studies of porous media assume T_2 relaxation is 1) independent of the self-diffusion coefficient of water as in the 'fast diffusion' regime [27] and 2) dominated by surface relaxation [28], which can be expressed as

$$T_{2S}^{-1} = \rho\left(\frac{S}{V}\right) \quad [2]$$

where ρ is the surface relaxivity [cm/s], or the capacity of the pore wall to induce relaxation, and $\left(\frac{S}{V}\right)$ is the surface to volume ratio of the pore [cm], typically modelled as a sphere. From this expression, it follows generally that T_2 is longer in larger pores and shorter in smaller pores. Also important is the mineral surface of the solid matrix where paramagnetic species like Fe(III) and Mn lead to faster relaxation (shorter T_2) via the parameter ρ [29, 30]. In very coarse materials, the 'slow diffusion' regime [27] dominates and Eqn. [2] becomes a function of $\left(\frac{S}{V}\right)^2$ with no dependence on ρ.

The T_2 relaxation time distribution can be represented by a single parameter, the arithmetic mean of log T_2, T_{2ML}. This single parameter has been shown to estimate the mean pore size and permeability with the following equations [31],

$$T_{2ML}^{-1} = \rho\left(\frac{S}{V}\right) \quad [3]$$

$$k_{NMR} = b\varphi^m(T_{2ML})^n \quad [4]$$

where $\left(\frac{S}{V}\right)$ is the surface to volume ratio of the total pore space, ρ is the surface relaxivity, k_{NMR} is the estimated permeability from the NMR data [31] with units typically expressed in millidarcies (1 mD $\approx 10^{-11}$ cm^2), ϕ is the NMR-determined porosity, and b [mD/ms^2],

m, and *n* are empirically determined constants. Eqn. [4] is commonly known as the Schlumberger-Doll Research (SDR) equation. For consolidated sediments and when T_{2ML} is in units of milliseconds, *m* and *n* are typically 4 and 2, respectively [32, 33]. Eqn. [4] can also be written in terms of hydraulic conductivity, *K*, in units of m/s; in this case, the values and units of the empirical constants account for the inclusion of fluid density and viscosity terms. For further discussion of the empirical constants, refer to Knight *et al.* (2016). From these expressions, it is clear that accurate estimation of *k* or *K* depends on the ability of the instrument to measure T_{2S} without the influence of diffusion relaxation, T_{2D}, since the influence of T_{2B} is generally insignificant when the pore fluid is water. Alternatively, diffusion effects must be quantified and decoupled from measurement of T_2 relaxation by encoding the signal also for the effective self-diffusion of water. This is an ongoing area of research and will be further discussed in the final section of this article. The influence of the T_{2D} component is reduced by lowering the tool operating frequency, i.e. static magnetic field strength, and by minimizing t_E. Lower operating frequency also reduces the signal to noise ratio, requiring longer measurement times.

In saturated sediments, the shape of the T_2 distribution estimates the pore size distribution since T_2 relaxation depends linearly on the pore size when ρ is assumed constant; the distribution yields the relative volume of water in each size pore. Typically, water in sandstone with a T_2 relaxation time greater than 33 ms is considered ‘mobile’, while water relaxing faster than 33 ms is considered ‘bound’ in capillaries [34]. ‘Clay bound’ water is characterized by relaxation in less than 3 ms. Water signal decaying

faster than the minimum echo spacing is not detected. In the vadose zone, unlike in deeper consolidated sediments, soils have varying degrees of saturation and hydraulic conditions are dynamic on timescales ranging from hours to seasons to years. In these conditions, interpretation of the T_2 distribution as a pore size distribution is more complicated. Soil drying may concentrate dissolved species in the remaining pore water and influence bulk fluid relaxation, such that the T_{2B}^{-1} term in Eqn. [1] may become non-trivial. Additionally, large pores drain before smaller pores. Jaeger *et al.* (2009) found that the relaxation time distribution of unsaturated soil samples was strongly correlated to the soil texture, i.e. relative sand, silt, and clay content, as well as the content of soil organic matter (SOM).

To date, borehole NMR tools have been applied to the measurement of soil moisture in laboratory studies and hydrogeologic characterization of aquifers in the field. Building on those foundations, recent studies have used borehole NMR to detect and monitor biogeochemical changes in the near subsurface for applications related to bioremediation.

Measurement of Soil Moisture

Researchers at RWTH – Aachen University developed two non-commercial, small-scale, and portable borehole NMR devices for measuring soil moisture [20, 35]. Sucre *et al*. (2011) developed a single-sided borehole NMR probe, 4.8 cm in diameter, which operated at 11.8 MHz and produced a sensitive zone 4.7 mm from the exterior of the device on one side. The minimum echo spacing, which controls the fastest-decaying

signal the tool can detect, was t_E = 70 μs. Subsequently, the probe was re-designed, to increase the signal to noise ratio and increase the penetration of the sensitive zone, then again applied to measurement of soil moisture [20]. The optimized probe was 4.1 cm in diameter, 18.0 cm long, and operated at a frequency of 3.32 MHz. The sensitive zone in the soil for this instrument, unlike the previous, was a cylindrical shell 220 μm thick located 4.5 cm from the central axis, or 1.8 cm from the exterior of the casing. The minimum echo spacing was t_E = 250 μs. The optimized probe also significantly reduced the static field gradient from 24 T/m [35] to 3 T/m [20].

The two probes were tested in a similar manner to demonstrate performance [20, 35]. Each probe was placed in a tube within a larger column of model sandy soil. The model soil FH31 is a distribution of grain size classes 2% (>0.72mm), 8% (0.71-0.5mm), 30% (0.5-0.355mm), 41% (0.36-0.25mm), 16% (0.25-0.18mm), 3% (<0.18mm). In both studies, the soil moisture profile was measured first over the full depth of the column when the soil was fully saturated. Then, the water was allowed to drain from the column while the probe remained at a fixed depth, measuring the depletion of water over time from the soil pores. Next, Perlo *et al.* (2013) repeated these two steps of the experiment at different depths within the column. Figure 4.3 shows the drying of the soil column over time for 5 arbitrary and undefined vertical positions. Note that the curves have similar form and the initial water content in the saturated soil is equal within 1% for all depths measured [20]. Sucre *et al.* (2011) instead measured the soil moisture profile over the full column depth with the single-sided tool when the system reached hydraulic equilibrium after the draining described above (Figure 4.4).

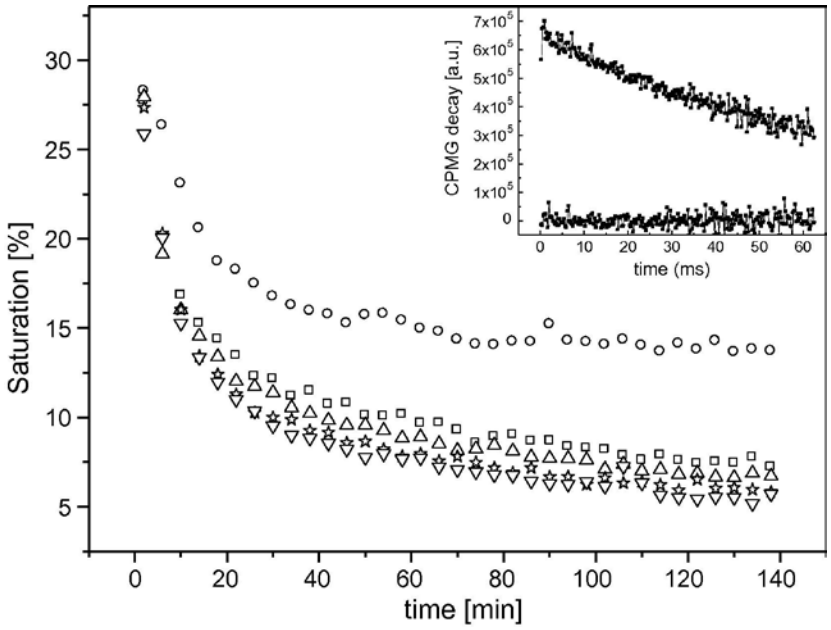

Figure 4.3. Temporal evolution during the draining process for different vertical z-positions in the column filled with a model soil FH31. The z-positions are not specified in the original article, but the asymptotic saturation value increases with depth in the column. Initial saturation for all curves was measured with a precision of 1%. In the inner box a CPMG-decay with 250 echoes recorded with 58 scans is shown. Reproduced from Perlo *et al*. (2013).

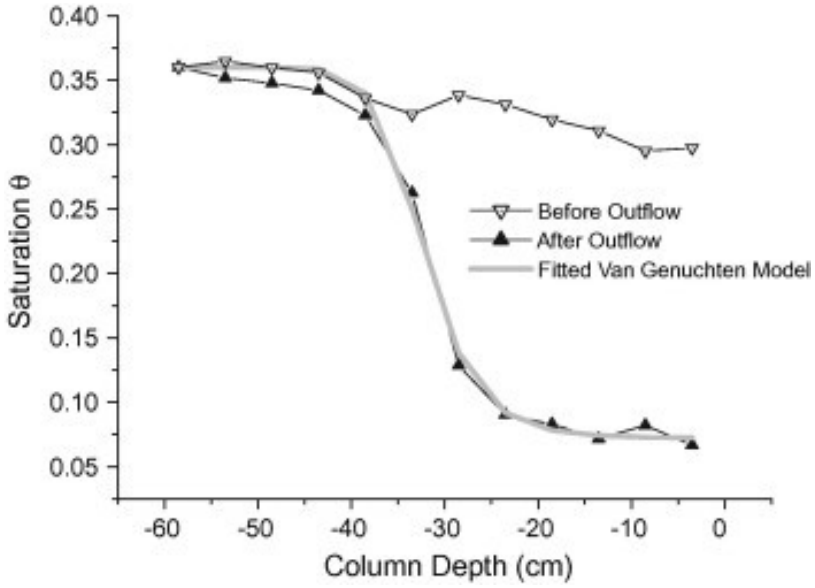

Figure 4.4. Saturation profile in a model soil FH31 under full saturation conditions (before outflow) and after the soil has been drained (after outflow). Reproduced from Sucre *et al.* (2011).

Sucre *et al.* (2011) then calculated the soil hydraulic parameters using the NMR data from the column drainage experiment. Vertical flow was simulated with the Richards Equation, using the Mualem-van Genuchten model [36, 37] for $K(\theta)$, the hydraulic conductivity, and $h(\theta)$, hydraulic head, where both depend on saturation, θ. The saturated hydraulic conductivity, K_s, and the pore connectivity parameter, τ, were obtained by an inversion analysis. The simulations generally conformed well to the experimental results (Figure 4.4), though the rapid dynamic regime of the outflow experiment produced a K_s of 9 mm/min in the highly conductive model soil FH31, compared to a literature value of 7 mm/min [35]. The probe was also used to measure soil moisture profile changes resulting from imbibition and precipitation. It should be noted here that the relatively high field strength and high static field gradient of these two

probes means that especially during soil drying, the surface relaxation component of T_2 relaxation, T_{2S}, is strongly coupled to the diffusion relaxation component, T_{2D} [35].

More recently, Vista Clara, Inc. (Mukilteo, WA) has commercialized a backpack portable system called Dart [38] which is optimized for soil and vadose zone studies shallower than 50 m. The Dart has an outer diameter of 4.5 cm and operates between 425-475 kHz, producing a sensitive zone that is at a maximum of 5 cm from the tool surface. The static field gradient is 35 G/ cm ($3.5e^{-5}$ T/m) at the sensitive zone. The system is intended to be deployed in holes made with minimal soil disturbance like DP-installed PVC or hand-augering. Recently the tool has been used to study thawing in permafrost [39]. The electronics unit running the Dart can also be used to operate a non-invasive single-sided NMR sensor called Discus, which sits on the soil surface and measures water at four levels: approximately 5, 10, 15, and 20 cm from the face of the sensor [38].

Characterization of Unconsolidated Aquifers

These next studies were conducted within the saturated, unconsolidated sediments below the vadose zone. The first portable borehole NMR device reported in literature was a commercial probe called the Javelin, by Vista-Clara, Inc. [19]. The Javelin probe is a slim, borehole logging tool originally developed for hydrogeologic analysis in open or PVC-cased boreholes as small as 5 cm in diameter [40], and can also be operated in DP mode. Several versions of the probe have been commercialized, operating in the range of 250—425 kHz, placing the sensitive region in the undisturbed formation outside

the wellbore approximately 11 – 19 cm radially from the center of the probe. The static field gradient at the sensitive region is approximately 5 G/cm (5e^{-6} T/m). What is most significant about this instrument is that the low operating frequency and static field gradient, together with the minimum t_E (on the order of 1 ms), allow a robust measurement of T_2 relaxation without the influence of diffusion relaxation, T_{2D}.

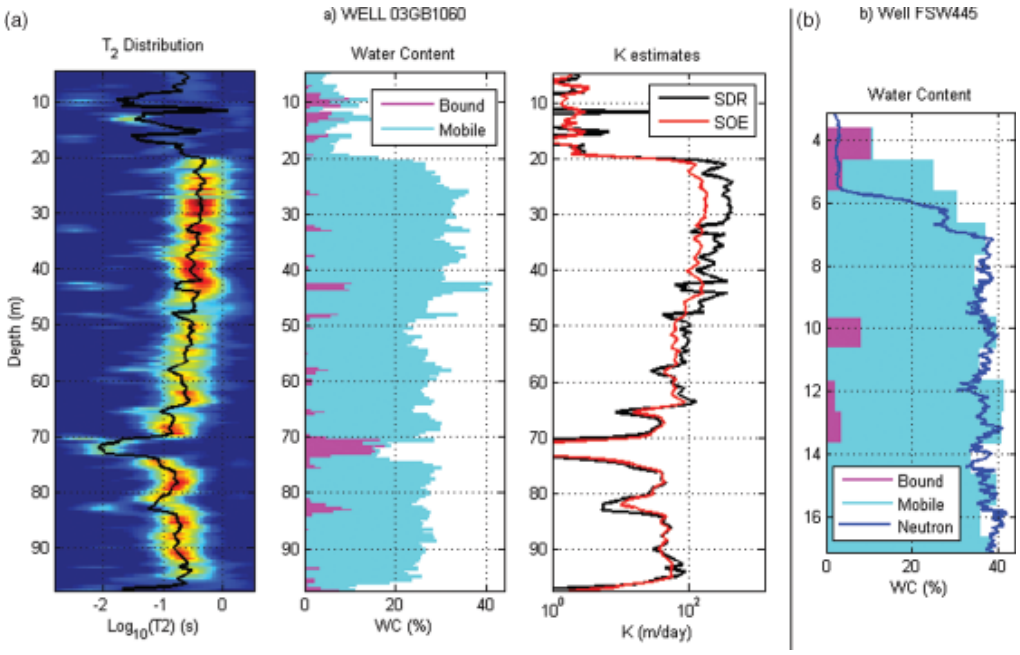

Figure 4.5. Logs from Massachussetts Military Reservation obtained May 2010 (a) NMR logs acquired in 4-inch well 03GB1060 show the T_2 distributions, the NMR measured water content, and the NMR-derived estimate of K; (b) comparison of water content measured by NMR log and neutron porosity log acquired in nearby 2-inch well FSW445. Reproduced from Walsh *et al.* (2013)

Initial field tests of the Javelin were conducted at the Massachusetts Military Reservation, near a site of known subsurface contamination from fuel spills and other activities. The 100 m NMR logging data compared well to a porosity estimation obtained by a neutron log acquired in nearby well (Figure 4.5 (b)). The T_2 distribution, NMR

estimation of water content, and NMR derived estimate of *K* – all measured as a function of depth – also allowed researchers to identify water content associated with lenses of low permeability silt which are expected to trap fluids, thereby affecting contaminant fate and transport (Figure 5 (a)).

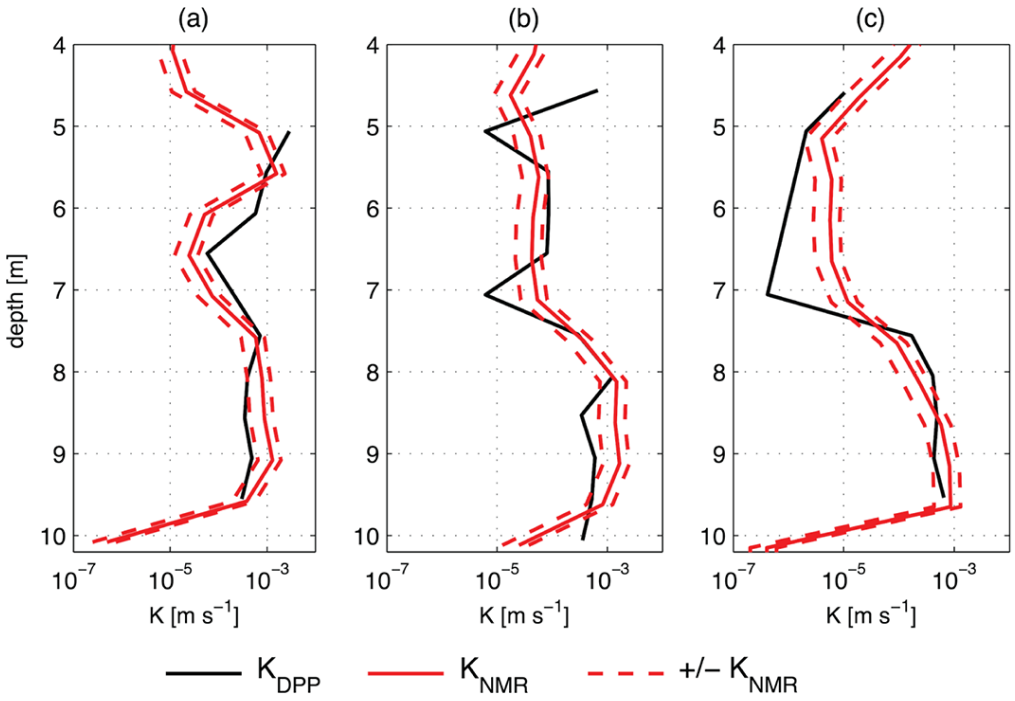

Figure 4.6. Comparison of *K* calculated from NMR logging data using the SDR equation (Eqn. [4]) and from DP permeameter (DPP) data obtained at the Larned field site. The figure shows logs from three different locations at Larned (a) Larned E, (b) Larned C, (c) Larned W. The dashed lines show the uncertainty in K_{NMR} due to the distribution in *b* values (±1σ) when fitting Eqn. 4. Reproduced from Knight *et al*. (2016).

More recently, researchers have used the Javelin tool to characterize hydraulic conductivity in unconsolidated aquifers at several field sites [41], where the goal of the research was to identify standard values for the empirical constants in Eqn. [4]. Data from 3 wells at the Larned Research Site of the Kansas Geological Survey in west-central

Kansas is shown in Figure 4.6. The NMR logging data estimation of the hydraulic conductivity, *K*, compared very well, generally within an order of magnitude, to the more established direct-push permeameter (DPP) estimates [42]. The authors found that, like in consolidated formations [32, 33], there was little variability in the constants between the different field sites. The value of the empirical constant, *b*, in Eqn. [4] when written in terms of hydraulic conductivity, varied less than 50% across 3 field sites. This result suggests that it may be possible to obtain reliable values for the empirical constants and significantly reduce the need for site specific calibration to obtain accurate estimations of *K* and *k* from NMR data [41]. Establishment of standard values for the constants will improve the cost-effectiveness and ease of use of borehole NMR technology. Previous work by the research group responsible for these measurements includes their initial demonstration in a high plains aquifer [22], groundtruthing surface NMR with the NMR logging tool [43], and determining methods to estimate uncertainties [44].

Detection of Subsurface Biogeochemical Processes

As Eqn. [1] shows, T_2 relaxation in porous media depends on the properties of the bulk fluid and the size and mineralogy of the pores. (Diffusion relaxation effects can be neglected due to the low operating frequency of the borehole tool used in the following studies.) It therefore follows that changing the properties of the pore fluid, or changing the pore geometry or mineralogy, should produce a change in the T_2 relaxation distribution from some known initial state. In application of this premise, the research group at Montana State University has been using the Javelin NMR logging tool to

monitor subsurface biogeochemical processes for bioremediation applications [45-47]. The studies included in this section were designed to assess the sensitivity of borehole NMR to 1) a change in pore fluid – from water to biofilm – both at laboratory and field scale, and 2) pore structural and mineralogical changes caused by microbially induced calcite precipitation (MICP) in a laboratory bioreactor. Both biofilm growth and MICP can be used as part of a bioremediation project.

Bioremediation can be an effective method to contain or degrade chemical contaminants in the subsurface by exploiting the fundamental biochemical processes of microbial metabolism. Once established, biofilms have been shown to degrade or contain contaminants through a variety of mechanisms: utilizing hydrocarbons and other contaminants directly as a substrate; inducing mineralization to trap contaminants; transforming heavy metals to insoluble forms; or acting as a bio-barrier to retard the migration of contamination or re-direct groundwater flow through a treatment zone. Depending on its physical properties, the biofilm extracellular polymeric substance (EPS) matrix can change soil pore connectivity, effective pore size, and hydraulic conductivity, thereby affecting the hydrodynamic properties of the porous media [48] and allowing the detection of the biofilm state with NMR [49].

Preliminary groundtruthing was demonstrated in a lab-scale bioreactor designed to model the near-wellbore environment [45]. The bioreactor was constructed with four concentric PVC pipes, each 0.76 m tall, and filled with 1 mm nominal quartz sand, creating a combined pore space and reservoir volume of approximately 40 L. Over an 8-day experimental period, biofilm was cultivated in the reactor sand-pack with a

continuously recirculating flow of substrate. Measured NMR T_{2ML} shifted from approximately 750 to 400 ms, indicating that the pore environment and bulk fluid properties were changing due to biofilm growth (Figure 4.7). Destructive sampling employing microbial population analysis and microscopy confirmed biofilm formation. This experiment demonstrated that the NMR logging tool can detect small to moderate changes in T_2 distribution associated with environmentally relevant quantities of biofilm in quartz sand.

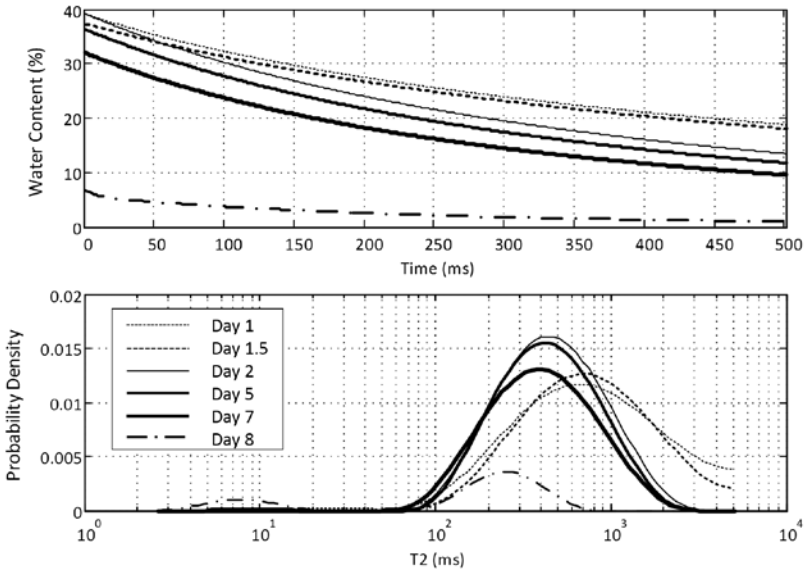

Figure 4.7. Time evolution of CPMG signal decay curves and T_2 distributions. Increased signal attenuation with biofilm formation produces steeper CPMG signal decay curves (top panel). The distribution of T_2 relaxation times (bottom panel) shifted to faster decay times as biofilm grew in the reactor. Data collected days 3 and 4 overlap the day 5 curve and are not shown. Likewise, the day 6 data is obscured by the day 7 curve and is not shown. Day 8 data was collected from the drained reactor. Reproduced from Kirkland *et al.* (2015b).

In 2014, two Javelin toosl were used to measure biofilm accumulation in an engineered test cell [46]. The test cell is 55 m by 40 m at the surface and is 6 m deep

with 2:1 side slopes (x:z). Two measurement wells were used in the study. A Javelin probe operating at approximately 400 kHz was installed in Well 1 where the soil profile was slightly more coarse grained than in Well 2. The Javelin probe in Well 2 operated at approximately 275 kHZ and was the same tool as was used in the previous laboratory study. Measured T_{2ML} relaxation times were reduced by 43% and 62%, respectively in Well 1 and Well 2, while biofilm was cultivated in the soil surrounding each well (Figure 4.8).

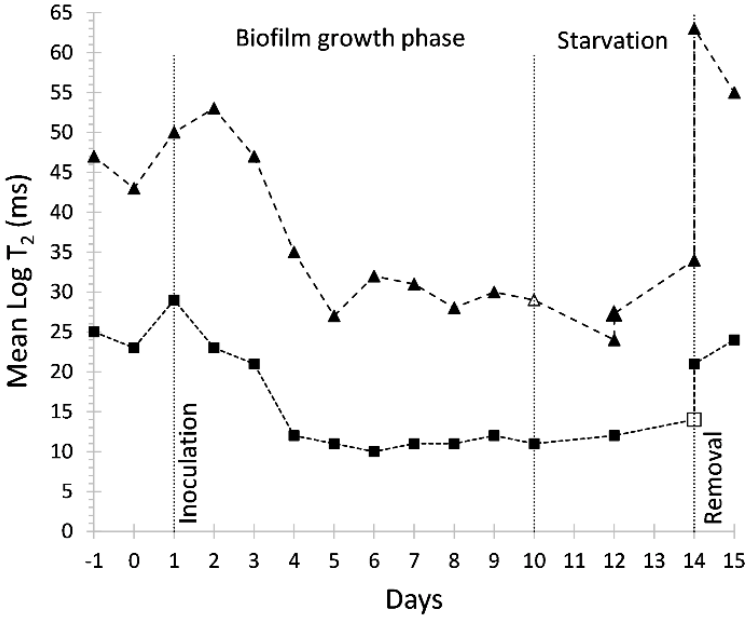

Figure 4.8. Data showing T_{2ML} measurements from two monitoring wells (triangles – Well 1 (~400 kHz), squares – Well 2 (~275 kHz)). Inoculation occurred on Day 1. Growth substrate was injected daily Days 2-10. Days 11-14, the bacteria were starved. On Day 14, the wells were flushed with high flows of groundwater from the test cell then a bleach solution was injected to oxidize remaining organics. Day 15 data was collected after flushing the bleach solution from the wells. Reproduced from Kirkland *et al.* (2015a).

Differences T_{2ML} between the wells is due to the relatively larger pores in Well 1. The reduction in T_{2ML} observed in both wells was confirmed to be a result of biofilm accumulation by bleaching and flushing the wells and observing the NMR signal's return to baseline. This result provided evidence of the NMR logging technique as a direct and non-invasive method to spatio-temporally monitor biofilm accumulation in the subsurface.

MICP has been widely researched recently due to its relevance for subsurface engineering applications including sealing leakage pathways and permeability modification [50, 51]. These applications of MICP are inherently difficult to monitor non-destructively in time and space. The Javelin probe was used to monitor MICP in the sand-filled bioreactor described previously, measuring NMR signal amplitude and T_2 relaxation over an 8-day experimental period [47]. Following inoculation with the ureolytic bacteria, *Sporosarcina pasteurii,* and pulsed injections of urea and calcium substrate, the NMR measured water content in the reactor decreased to 76% of its initial value as calcite precipitation displaced pore water. Destructive sampling confirmed final porosity was approximately 88% of the original value. The overestimation of porosity reduction by NMR can be attributed primarily to the accumulation of excess CO_2 gas in the reactor as a result of microbial metabolism. Signal decaying faster than the minimum echo spacing (1.3 ms) may also have reduced the measured NMR water content. T_2 relaxation distributions bifurcated from a single mode centered about approximately 650 ms on Day 2 into a fast decaying population (T_2 less than 10 ms) and a larger population with T_2 greater than 1000 ms by Day 8 (Figure 4.9). The combination of changes in pore

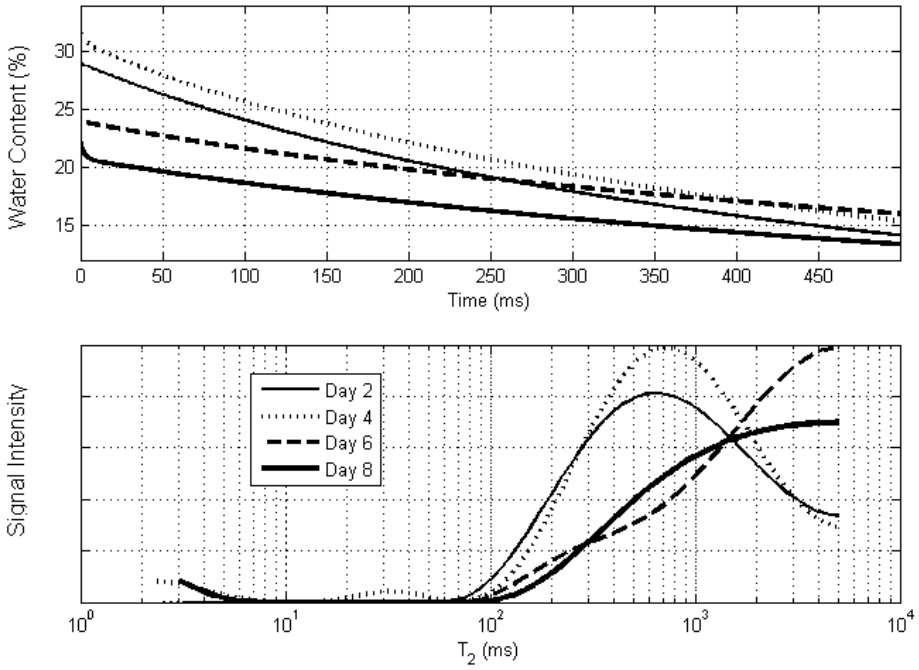

Figure 4.9. Signal decay curves (top) and the corresponding T_2 distributions (bottom) are shown with each curve representing a day. Day 2 occurred during the control period. Inoculation occurred on Day 3 (not shown). The calcium media injections occurred between Day 4 – 7. The Day 8 data was collected prior to flushing the reactor with brine and destructively sampling. Both graphs show fits to the raw data. Reproduced from Kirkland *et al.* (2016).

volume and surface mineralogy accounted for the changes in the T_2 distributions. In this system, the change in pore surface mineralogy, from quartz sand containing paramagnetic impurities to a relatively uniform calcite surface, caused a decrease in the surface relaxivity, ρ, and lead to the longer T_2 relaxation times observed. The authors attribute the very fast decaying signal to water trapped within the pores of the calcite itself, where the influence of the surface to volume ratio dominated. These results indicate the low-field NMR well-logging probe is sensitive to the physical and chemical changes caused by MICP in a laboratory bioreactor.

Outlook and Conclusions

Several technological challenges remain in the further development of low-field borehole NMR tools. As discussed above, minimizing the echo spacing, t_E, is critical for obtaining an accurate estimation of k and K from NMR data by reducing the influence of relaxation due to diffusion. Reducing the minimum t_E also expands the range of fast-decaying signals that can be measured by the instrument, a feature which may be particularly relevant where biogeochemical conversions are concerned.

Pulsed NMR tools have been used in the oil and gas industry since the early 1990's, allowing for measurements that simultaneously encode the signal for the effective diffusion coefficient of the pore fluid, D, and T_2 relaxation. The correlation of relaxation behaviour with diffusion properties allows the separation of some of the effects which combine to influence T_2 relaxation [52]. The ability to collect D-T_2 correlations improves the feasibility of using borehole NMR tools to detect degradation of organic contaminants by allowing the separation of the water and hydrocarbon signal, for example, since water and hydrocarbons have different self-diffusion coefficients [53]. The latest versions of the Javelin and Dart borehole NMR probes can now encode for effective self-diffusion and record D-T_2 correlations though the corroborating research is not yet published. While it is often possible to neglect the influence of T_{2D} for simple relaxation measurements, the addition of diffusion measurements, however, would make accurate estimation of the internal field gradient strength critical. Measuring the effective diffusion coefficient requires a long echo spacing to encode for motion. The influence of

T_{2D} over this interval must be known. Accurate estimation of these internal field gradients under field conditions remains a challenge [26].

In addition to the research discussed above, which used borehole NMR probes, several studies have been completed using traditional benchtop NMR instruments in the laboratory where the logical future application is in the unconsolidated sediments in the near surface. One such example is using borehole NMR as a probe of the redox condition of the aquifer. Injecting oxygen-rich water into a reduced aquifer can cause leaching of metals into the water, significantly degrading the water quality. Furthermore, iron (hydr)oxides are highly reactive geochemically and, as such, can be used to sequester or transform organic or inorganic contaminants. Both of these examples involve a change in local redox conditions that changes the mineralogical form of iron compounds [54], or other metals. NMR is sensitive not only to the quantity of iron present in the measurement region [55], but also to the form of the iron with Fe (III) producing faster relaxation rates than Fe(II) compounds [30, 56, 57]. Confirmation of these laboratory results in a complex field environment would broaden the range of potential applications of borehole NMR technology and vastly improve existing methods for monitoring changing redox conditions and iron mineralization in the subsurface.

As the diverse studies described here show, low field borehole NMR is a remarkably versatile technology with great potential not only to describe heterogeneity in the near subsurface non-destructively, but also to monitor physical and chemical changes in the pore scale environment over time, of importance in a range of yet unexplored applications.

References

1. Maliva, R.G., E.A. Clayton, and T.M. Missimer, *Application of advanced borehole geophysical logging to managed aquifer recharge investigations.* Hydrogeology Journal, 2009. **17**(6): p. 1547-1556.

2. Careghini, A., S. Saponaro, and E. Sezenna, *Biobarriers for groundwater treatment: a review.* Water Science and Technology, 2013. **67**(3): p. 453-468.

3. Phillips, A.J., et al., *Fracture Sealing with Microbially-Induced Calcium Carbonate Precipitation: A Field Study.* Environmental Science & Technology, 2016. **50**(7): p. 4111-4117.

4. DeJong, J.T., et al., *Bio-mediated soil improvement.* Ecological Engineering, 2010. **36**(2): p. 197-210.

5. Dejong, J.T., et al., *Biogeochemical processes and geotechnical applications: progress, opportunities and challenges.* Geotechnique, 2013. **63**(4): p. 287-301.

6. Robinson, D.A., et al., *Soil moisture measurement for ecological and hydrological watershed-scale observatories: A review.* Vadose Zone Journal, 2008. **7**(1): p. 358-389.

7. Binley, A., et al., *The emergence of hydrogeophysics for improved understanding of subsurface processes over multiple scales.* Water Resources Research, 2015. **51**(6): p. 3837-3866.

8. Blumich, B., et al., *The NMR-mouse: Construction, excitation, and applications.* Magnetic Resonance Imaging, 1998. **16**(5-6): p. 479-484.

9. Goga, N.O., et al., *Mobile NMR: applications to materials and biomedicine.* Journal of Optoelectronics and Advanced Materials, 2006. **8**(4): p. 1430-1434.

10. Blumich, B., J. Perlo, and F. Casanova, *Mobile single-sided NMR.* Progress in Nuclear Magnetic Resonance Spectroscopy, 2008. **52**(4): p. 197-269.

11. Behroozmand, A.A., K. Keating, and E. Auken, *A Review of the Principles and Applications of the NMR Technique for Near-Surface Characterization.* Surveys in Geophysics, 2015. **36**(1): p. 27-85.

12. Hertrich, M., *Imaging of groundwater with nuclear magnetic resonance.* Progress in Nuclear Magnetic Resonance Spectroscopy, 2008. **53**(4): p. 227-248.13.

Coates, G.R., L. Xiao, and M.G. Prammer, *NMR Logging: Principles and Applications*. 1999, Halliburton Energy Services: Houston.

14. Kleinberg, R.L., Kenyon, W.E., Mitra, P.P., *Mechanism of NMR relaxation of fluids in rock.* Journal of Magnetic Resonance Series A, 1994. **108**: p. 206-214.

15. Freedman, R., *Advances in NMR Logging.* Journal of Petroleum Technology, 2006. **58**(1): p. 60-66.

16. Song, Y.Q., et al., *T-1-T-2 correlation spectra obtained using a fast two-dimensional Laplace inversion.* Journal of Magnetic Resonance, 2002. **154**(2): p. 261-268.

17. Venkataramanan, L., Y.Q. Song, and M.D. Hurlimann, *Solving Fredholm integrals of the first kind with tensor product structure in 2 and 2.5 dimensions.* Ieee Transactions on Signal Processing, 2002. **50**(5): p. 1017-1026.

18. Prange, M. and Y.-Q. Song, *Quantifying uncertainty in NMR T-2 spectra using Monte Carlo inversion.* Journal of Magnetic Resonance, 2009. **196**(1): p. 54-60.

19. Walsh, D.O., et al., *Javelin: A slim-hole and microhole NMR logging tool.* Fast Times, 2010. **15**(3): p. 67-72.

20. Perlo, J., et al., *Optimized slim-line logging NMR tool to measure soil moisture in situ.* Journal of Magnetic Resonance, 2013. **233**: p. 74-79.

21. Callaghan, P.T., *Translational Dynamics & Magnetic Resonance: Principles of Pulsed Gradient Spin Echo NMR.* 2011, New York: Oxford University Press.

22. Dlubac, K., et al., *Use of NMR logging to obtain estimates of hydraulic conductivity in the High Plains aquifer, Nebraska, USA.* Water Resources Research, 2013. **49**(4): p. 1871-1886.

23. Carr, H.Y. and E.M. Purcell, *Effects of diffusion on free precession in nuclear magnetic resonance experiments.* Physical Review, 1954. **94**(3): p. 630-638.

24. Meiboom, S. and D. Gill, *Modified spin-echo method for measuring nuclear relaxation times.* Review of Scientific Instruments, 1958. **29**(8): p. 688-691.

25. Jaeger, F., et al., *Evaluation of 1H NMR relaxometry for the assessment of pore-size distribution in soil samples.* European Journal of Soil Science, 2009. **60**(6): p. 1052-1064.

26. Fay, E.L., R.J. Knight, and Y.Q. Song, *Investigating internal magnetic field gradients in aquifer sediments.* Geophysics, 2015. **80**(3): p. D281-D294.

27. Brownstein, K.R. and C.E. Tarr, *Importance of classical diffusion in NMR studies of water in biological cells.* Physical Review A, 1979. **19**(6): p. 2446-2453.

28. Kleinberg, R.L. and M.A. Horsfield, *Transverse relaxation processes in porous sedimentary rock.* Journal of Magnetic Resonance, 1990. **88**(1): p. 9-19.

29. Kenyon, W.E. and J.A. Kolleeny, *NMR surface relaxivity of calcite with adsorbed Mn2+*. Journal of Colloid and Interface Science, 1995. **170**(2): p. 502-514.

30. Keating, K. and R. Knight, *A laboratory study of the effect of Fe(II)-bearing minerals on nuclear magnetic resonance (NMR) relaxation measurements.* Geophysics, 2010. **75**(3): p. F71-F82.

31. Kenyon, W.E., et al., *A three-part study of NMR longitudinal relaxation properties of water-saturated sandstones.* SPE Formation Evaluation, 1988. **3**(3): p. 622-636.

32. Straley, C., et al., *Core analysis by low-field NMR.* The Log Analyst, 1997. **38**(2): p. 84-94.

33. Kenyon, W.E., *Petrophysical principles of applications of NMR logging.* The Log Analyst, 1997. **38**(2): p. 21-43.

34. Timur, A., *Pulsed nuclear magnetic resonance studies of porosity, movable fluid, and permeability of sandstones.* Journal of Petroleum Technology, 1969. **21**(JUN): p. 775-&.

35. Sucre, O., et al., *Low-field NMR logging sensor for measuring hydraulic parameters of model soils.* Journal of Hydrology, 2011. **406**(1–2): p. 30-38.

36. Mualem, Y., *Hysteretical models for prediction of hydraulic conductivity of unsaturated porous-media.* Transactions-American Geophysical Union, 1976. **57**(8): p. 602-603.

37. Van Genuchten, M.T., *A closed form equation for predicting the hydraulic conductivity of unsaturated soils.* Soil Science Society of America Journal, 1980. **44**(5): p. 892-898.

38. Walsh, D., *Environmental Geophysics: Portable NMR tools for measuring and monitoring soil moisture*, in *Preview*. 2015, CSIRO Publishing. p. 41-42.

39. Minsley, B.J., et al., *Evidence for nonuniform permafrost degradation after fire in boreal landscapes.* Journal of Geophysical Research: Earth Surface, 2016. **121**(2): p. 320-335.

40. Walsh, D., et al., *A small-diameter NMR logging tool for groundwater investigations.* Groundwater, 2013. **51**(6): p. 914-926.

41. Knight, R., et al., *NMR Logging to Estimate Hydraulic Conductivity in Unconsolidated Aquifers.* Groundwater, 2016. **54**(1): p. 104-114.

42. Butler, J.J., Jr., et al., *Characterizing hydraulic conductivity with the direct-push permeameter.* Ground Water, 2007. **45**(4): p. 409-419.

43. Knight, R., et al., *Field experiment provides ground truth for surface nuclear magnetic resonance measurement.* Geophysical Research Letters, 2012. **39**.

44. Parsekian, A.D., et al., *Bootstrap Calibration and Uncertainty Estimation of Downhole NMR Hydraulic Conductivity Estimates in an Unconsolidated Aquifer.* Groundwater, 2015. **53**(1): p. 111-121.

45. Kirkland, C.M., et al., *Biofilm Detection in a Model Well-Bore Environment Using Low-Field NMR.* Ground Water Monitoring and Remediation, 2015. **35**(4): p. 36-44.

46. Kirkland, C.M., et al., *In Situ Detection of Subsurface Biofilm Using Low-Field NMR: A Field Study.* Environmental Science & Technology, 2015. **49**(18): p. 11045-11052.

47. Kirkland, C.M., et al., *Detecting microbially-induced calcite precipitation (MICP) in a model well-bore using downhole low-field NMR.* Environmental Science & Technology, 2016. **10.1021/acs.est.6b04833**.

48. Cunningham, A.B., et al., *Influence of biofilm accumulation on porous-media hydrodynamics.* Environmental Science & Technology, 1991. **25**(7): p. 1305-1311.

49. Sanderlin, A.B., et al., *Biofilm detection in natural unconsolidated porous media using a low-field magnetic resonance system.* Environmental Science & Technology, 2013. **47**(2): p. 987-992.

50. De Muynck, W., N. De Belie, and W. Verstraete, *Microbial carbonate precipitation in construction materials: A review.* Ecological Engineering, 2010. **36**(2): p. 118-136.

51. Phillips, A.J., et al., *Engineered applications of ureolytic biomineralization: a review.* Biofouling, 2013. **29**(6): p. 715-733.

52. Song, Y.Q., *Recent Progress of Nuclear Magnetic Resonance Applications in Sandstones and Carbonate Rocks.* Vadose Zone Journal, 2010. **9**(4): p. 828-834.

53. Fay, E.L. and R.J. Knight, *Detecting and quantifying organic contaminants in sediments with nuclear magnetic resonance.* Geophysics, 2016. **81**(6): p. EN87.

54. Bryar, T.R. and R.J. Knight, *Sensitivity of nuclear magnetic resonance relaxation measurements to changing soil redox conditions.* Geophysical Research Letters, 2002. **29**(24).

55. Bryar, T.R., C.J. Daughney, and R.J. Knight, *Paramagnetic effects of iron(III) species on nuclear magnetic relaxation of fluid protons in porous media.* Journal of Magnetic Resonance, 2000. **142**(1): p. 74-85.

56. Keating, K. and R. Knight, *A laboratory study to determine the effect of iron oxides on proton NMR measurements.* Geophysics, 2007. **72**(1): p. E27-E32.

57. Keating, K. and R. Knight, *A laboratory study of the effect of magnetite on NMR relaxation rates.* Journal of Applied Geophysics, 2008. **66**(3-4): p. 188-196.

CHAPTER FIVE

BIOFILM DETECTION IN A MODEL WELL-BORE ENVIRONMENT USING LOW-FIELD NMR

Contribution of Authors and Co-Authors

Manuscript in Chapter 5

Author: Catherine M. Kirkland

Contributions: Helped conceive and implement study design. Collected and analyzed data. Wrote manuscript. Provided feedback and comments on the manuscript.

Co-Author: Randy Hiebert

Contributions: Helped conceive and implement study design. Provided feedback and comments on the manuscript.

Co-Author: Adrienne J. Phillips

Contributions: Helped conceive and implement study design. Provided feedback and comments on the manuscript.

Co-Author: Elliot Grunewald

Contributions: Helped conceive and implement study design. Provided supervision and oversight on data collection and analysis. Provided feedback and comments on the manuscript.

Co-Author: David O. Walsh

Contributions: Helped conceive and implement study design. Provided feedback and comments on the manuscript.

Co-Author: Joseph D. Seymour

Contributions: Provided feedback and comments on the manuscript.

Co-Author: Sarah L. Codd

Contributions: Helped conceive and implement study design. Provided feedback and comments on the manuscript.

Manuscript Information Page

Catherine M. Kirkland, Randy Hiebert, Adrienne Phillips, Elliot Grunewald, David O. Walsh, Joseph D. Seymour, Sarah L. Codd

Groundwater Monitoring and Remediation

Status of Manuscript:
____ Prepared for submission to a peer-reviewed journal
____ Officially submitted to a peer-review journal
____ Accepted by a peer-reviewed journal
_X___ Published in a peer-reviewed journal

Wiley-Blackwell
Vol. 35, No. 4, Pages 36-44, Fall 2015

BIOFILM DETECTION IN A MODEL WELL-BORE ENVIRONMENT USING LOW-FIELD NMR

Abstract

This research addresses the challenges of the lack of non-invasive methods and poor spatio-temporal resolution associated with monitoring biogeochemical activity central to bioremediation of subsurface contaminants. Remediation efforts often include growth of biofilm to contain or degrade chemical contaminants, such as nitrates, hydrocarbons, heavy metals, and some chlorinated solvents. Previous research indicates that nuclear magnetic resonance (NMR) is sensitive to the biogeochemical processes of biofilm accumulation. The current research focuses on developing methods to use low-cost NMR technology to support *in-situ* monitoring of biofilm growth and geochemical remediation processes in the subsurface. Biofilm was grown in a lab-scale radial flow bioreactor designed to model the near wellbore subsurface environment. The Vista Clara Javelin NMR logging device, a slim down-the-borehole probe, collected NMR measurements over the course of eight days while biofilm was cultivated in the sand-packed reactor. Measured NMR mean log T_2 relaxation times decreased from approximately 710 to 389ms, indicating that the pore environment and bulk fluid properties were changing due to biofilm growth. Destructive sampling employing drop plate microbial population analysis and scanning electron and stereoscopic microscopy confirmed biofilm formation. Our findings demonstrate that the NMR logging tool can

detect small to moderate changes in T_2 distribution associated with environmentally relevant quantities of biofilm in quartz sand.

Introduction

In most environments, the majority of microbial cells exist in complex communities called biofilms [1]. Bacteria preferentially attach to surfaces, anchoring themselves with a sticky gel called extracellular polymeric substance (EPS). The EPS, which consists of proteins, polysaccharides, and DNA, forms a heterogeneous matrix surrounding the bacterial cells and entrapped organic and inorganic molecules [2]. The EPS matrix has a complex structure, consisting of hydrated gel-like fibers and interconnected channels [3]. Depending on its physical properties, the EPS matrix can change soil pore connectivity, effective pore size, and hydraulic conductivity, thereby affecting the hydrodynamic properties of the porous media [4-6].

Bioremediation methods exploit these biofilm-induced changes in the soil and can be effective to contain or degrade chemical contaminants in the subsurface [7]. Once established, biofilm can consume hydrocarbons and other contaminants directly as a substrate [8-11], induce mineralization to trap contaminants [12], mediate ion exchange to remove heavy metals from aqueous solution [13] or transform heavy metals to insoluble forms [14]. *In-situ* bioremediation applications often require injection of appropriate nutrients into the subsurface in order to create redox conditions suitable for biofilm growth and contaminant transformation. In addition to being an integral part of the removal of toxins, biofilm can act as a bio-barrier to slow the migration of the

contamination or re-direct groundwater flow through a treatment zone [15] by reducing hydraulic conductivity and restricting advective flow. Furthermore, biofilms better withstand environmental stresses such as nutrient deprivation, changing pH conditions, and exposure to biocides or antimicrobial substances compared to suspended cells [16, 17], improving their effectiveness and longevity as bio-barriers.

Numerous computer models have been developed in the last several decades in an effort to better understand the physical and biochemical processes of biofilm development. In general, the recent models iteratively solve partially decoupled differential equations governing conservation of momentum, mass transport, substrate utilization, and biofilm growth [18-21]. The models help describe the changing hydrodynamics and biofilm morphology, as well as confirm the overall reduced hydraulic conductivity of the porous media resulting from biofilm accumulation that is observed experimentally.

This observed reduction in hydraulic conductivity is the typical method for determining whether biofilm is present in bioremediation applications [5, 22, 23]. Darcy's Law, $\nu = -K \frac{dh}{dl}$ describes the relationship between the specific discharge, v [L/t], and the pressure gradient along a length of porous media, dh/dl [dimensionless], where the constant of proportionality is the saturated hydraulic conductivity, K [L/t]. Biofilm accumulation in pore spaces has been shown to reduce hydraulic conductivity by approximately 99% in a field setting and up to 99.99% in laboratory experiments [15, 23].

In conjunction with hydraulic conductivity measurements, determination of biofilm presence is often assessed with heterotrophic plate counts (HPC) to quantify the number of viable cells in the bulk fluid [24]. Interpretation of this type of population data is not trivial since the cell count data pertains to suspended bacteria rather than those attached to surfaces as biofilm. Furthermore, how the number of suspended cells correlates to the number of cells existing within biofilm colonies is not well understood. To determine cell populations within the biofilm, samples of the porous media must be collected and analyzed. Direct destructive sampling of contaminated soils during remediation can be both costly and potentially hazardous. Moreover, cell count information in general provides no information regarding the in-situ physical characteristics of the biofilm, such as the thickness, structure, and density of the EPS component as this information is destroyed during sampling and plating. While these methods are useful to describe the hydraulic conductivity or biological community at a particular place and time, they are less useful for informing us about the spatial and temporal growth, maturation, and decay of the biofilm [25].

NMR provides an alternative method to monitor *in-situ* biofilm development, overcoming several of the limitations described above. The measured signal in ^{1}H NMR comes from coherently precessing hydrogen protons, or 'spins,' making NMR applicable for the study of materials containing water or organic matter, including biofilm [26, 27]. Previous research indicates that NMR is sensitive to the biogeochemical processes of biofilm growth [28] and, unlike other methods of study, allows for non-invasive and non-destructive examination of the relationship between biofilm development and porous

media hydrodynamics and mass transport over various time and length scales [29-32]. A fundamental understanding of these related processes is critical to optimize the effectiveness of bioremediation applications, making NMR methods a useful addition to the bioremediation monitoring toolkit.

The Vista Clara Javelin device is a slim, down-the-borehole NMR logging tool (4.5ft (1.37m) long, 3.5in (8.9cm) diameter) originally developed for hydrogeologic analysis in open or PVC-cased boreholes between 2 and 8in (5-20cm) in diameter [33]. Expanding from this conventional application, the research reported here uses the Javelin probe to detect changes in the signal relaxation response over time as a measurement of biofilm growth in a model sand bioreactor since biofilm accumulation enhances signal relaxation [28]. The method using a NMR logging tool as described in this article may provide an improved and non-destructive way to assess the subsurface presence of biofilm.

Theory

T_2 relaxation

Following excitation with a radio-frequency (rf) pulse, the induced NMR signal decays at a rate governed by two relaxation mechanisms—spin-lattice T_1 and spin-spin T_2 [34]. T_1 relaxation is related to the rate at which the net magnetization grows in the longitudinal direction and returns to thermal equilibrium. T_2 relaxation is related to dipolar interactions in the transverse plane and loss of phase coherence, resulting in magnetization decay and signal attenuation.

The statistical distribution of T_2 relaxation times provides information regarding the physico-chemical environments the protons experience, since environmental factors like pore fluid type and pore size control how likely protons are to experience dipolar interactions. Typically, the signal decays more rapidly in solid-like materials due to T_2 relaxation—that is, solids and gels have shorter T_2 relaxation times than liquids due to low rotational mobility enhancing dipolar coupling [34]. The T_2 relaxation time for pure water is on the order of 2-3 seconds in unrestricted environments, whereas it is on the order of milliseconds in porous materials due to restricted motion and surface interactions.

While both T_1 and T_2 relaxation times can provide information about the molecular and pore-scale environment, T_2 measurements require less time to conduct and are preferred. This experimental study uses measured changes in the T_2 distribution to infer changes in the pore scale environment due to biofilm growth within the bioreactor. Biofilm formation in porous media leads to shorter T_2 relaxation times [25, 27].

Porous media influences the NMR relaxation process in several ways. The presence of solid surfaces creates relaxation sinks and may introduce paramagnetic impurities, as well as generating susceptibility-induced magnetic field inhomogeneities. T_2 in a pore is also influenced by the viscosity and chemical properties of the bulk fluid. Furthermore, diffusion of the liquid molecules between pores, and diffusion within the pore due to local magnetic field gradients also affect the T_2 relaxation behavior of a porous media system. The expression for the rate of T_2 relaxation in porous media

includes the relaxation time of the bulk media, T_{2B}, the surface relaxation time, T_{2S}, and relaxation time due to diffusion, T_{2D} [35].

$$\frac{1}{T_2} = \frac{1}{T_{2,B}} + \frac{1}{T_{2,S}} + \frac{1}{T_{2,D}} \qquad (5.1)$$

When the bulk fluid is water, $1/T_{2B}$ is typically very small and is often neglected in literature on relaxometry in porous materials. However, as the rotational mobility of the bulk fluid decreases due to biofilm growth in the pore space, $1/T_{2B}$ increases in importance to the overall T_2 relaxation rate [36]. Surface relaxation, T_{2S}, depends on the surface relaxivity, ρ, which describes the efficiency of the mineral surface to enhance relaxation, and the surface to volume ratio, S/V [37].

$$\frac{1}{T_{2,S}} = \rho \frac{S}{V} \qquad (5.2)$$

Since biofilm is composed of bacterial cells in a hydrated gel matrix, the T_2 relaxation time of fluid contained in the biofilm is shorter than for the bulk fluid alone. As the biofilm grows into the pore spaces, proportionally more protons will be bound in, or interact with, the EPS matrix, thereby shifting the T_2 distribution toward shorter relaxation times. Enhanced T_2 relaxation due to biofilm formation is expected to be caused by reduced rotational mobility in the pore fluid as the EPS matrix contributes a gel phase and the cells produce biomacromolecules with shorter relaxation than bulk water (T_{2B}). Additional relaxation effects may be due to changes in the pore structure and surface due to the biofilm growth on the grain surfaces (T_{2S}) [38].

T_{2D} is directly related to the echo spacing, t_E, according to

$$\frac{1}{T_{2,D}} = D\frac{(\gamma G t_E)^2}{12} \qquad (5.3)$$

where D is the diffusion coefficient [$L^2\ t^{-1}$], γ is the gyromagnetic ratio of hydrogen, 2.675 x 10^8 rad/(T s), and G is the local effective magnetic field gradient [Gauss L^{-1}]. By selecting a short t_E, this term can be made sufficiently small as to be neglected. Repeating the experiment with a longer t_E indicates whether there are indeed enhanced relaxation effects due to diffusion to consider.

Materials and Methods

Bioreactor Design and Construction

The lab-scale bioreactor was designed to model the near-wellbore environment and was constructed inside an aluminum Faraday cage using four concentric PVC pipe sections (Titan Industries, Paxton, NE), ranging from the inner 8in (20cm) diameter solid pipe to the outer 20in (51cm) solid pipe (Figure 1). The two middle pipe sections, 10in (25cm) and 18in (46cm) diameter respectively, were screened over the entire length with 8 rows of 0.020in (0.051cm) wide slots spaced at 0.5in (1.3cm) intervals. All of the pipes were 2.5ft (76cm) tall. Top and bottom plates were constructed from 0.5in (1.3cm) high density rigid expanded PVC sheeting with machined 0.125in (0.32cm) concentric grooves to allow nesting and sealing of the vertical pipe sections.

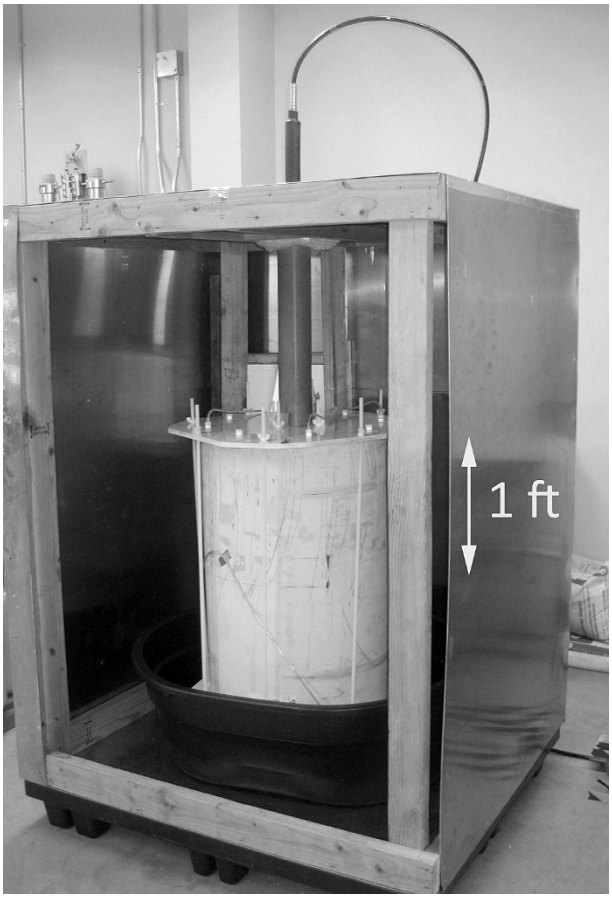

Figure 5.1. Model well-bore bioreactor. The 3.5in (8.9cm) diameter NMR logging probe was installed in the lab-scale radial flow bioreactor and Faraday cage. The purpose of the Faraday cage was to reduce external radio frequency noise caused by various electromagnetic sources in the laboratory.

The 3in (7.6cm) annulus between the slotted pipes was wet-filled with approximately 2.3ft^3 (0.065m^3.) of No. 2095 Granusil® silica (quartz) sand (Unimin Corp., Ottowa, MN) having a nominal diameter of 1 mm and a porosity of approximately 0.37. The combined volume of the pore space and annular reservoirs was approximately 40L.

The reactor was disinfected with two pore volumes (80L) of 10% bleach solution with 7g/L Tween80 (Fisher BioReagents, Waltham, MA) followed by a flush with 80L

sterile de-ionized (DI) water. Two pore volumes (80L) of sterile 2.52g/L sodium thiosulfate solution was pumped into the reactor to neutralize any remaining bleach. The sodium thiosulfate solution was flushed from the reactor with 80L of sterile buffer solution consisting of 3g/L $NaNO_3$, 0.12g/L K_2HPO_4, and 0.04g/L KH_2PO_4.

NMR measurements were made in the buffer-filled reactor with the NMR logging tool to establish a baseline T_2 distribution for the reactor prior to any biofilm growth. Later measurements were compared to this initial condition to identify changes in T_2 relaxation time distributions. Experimental constraints prevented the testing of an un-inoculated control in parallel with measurements of the biofilm reactor. These constraints are primarily associated with the uncertainties that would have been introduced by moving the NMR probe between the reactors to conduct measurements. Moving the probe during the experiment could influence the results since a slightly different shell within the reactor would be excited and measured for each placement of the probe. For these reasons, a longitudinal study of a single reactor was the preferred method for this initial experiment.

Bacterial Culture

One mL frozen stock of *Bacillus mojavensis* was cultured in 100mL of modified Brain-Heart Infusion (BHI) broth (36g/L Brain Heart Infusion (BHI) (Becton, Dickinson and Co., Sparks, MD), 3g/L $NaNO_3$, 0.75g/L NH_4Cl, 40g/L NaCl) on a shaker table at 150rpm for 48 hours. Then the 100mL inoculum was added to 10L of the modified BHI broth and mixed on a stir plate at 1150rpm for 60 hours to a concentration of

approximately $7\log_{10}$ colony-forming units (cfu)/mL. *B. mojavensis* was selected because of the abundant mucoid biofilm it produces [16, 28].

The 10L inoculum was pumped into the reactor with two peristaltic pumps (Cole-Parmer Model 7553-80 with Masterflex Easy-Load 7515-00 heads) at 650-700 mL/min through eight lines of No. 16 vinyl tubing. The pumps were turned off for approximately 11 hours to allow the bacteria to attach to the sand. Following the attachment period, radial flow of substrate through the sand promoted bacterial growth and biofilm accumulation which was monitored by the NMR probe.

No attempt was made to maintain a *B. mojavensis* monoculture within the reactor for the duration of the experiment. Following inoculation, subsequent batches of substrate were mixed and pumped into the reactor in a non-sterile manner. Sterile conditions could not be maintained due to experimental constraints imposed by the large volumes of substrate used and waste produced daily.

Following inoculation, 40L of re-circulating substrate was removed daily from the system and replaced with 40L of fresh substrate. Except during no-flow NMR measurements, the substrate was re-circulated continuously at a rate of 650-700mL/min which translates to a specific discharge of approximately 0.04cm/min and a pore velocity of approximately 0.02mm/s at the radial center of the sand annulus. This flowrate corresponds to the pore volume of the reactor being replaced every 50-60 minutes.

NMR Data Acquisition

T_2 relaxation measurements used a CPMG pulse sequence [39, 40] with excitation pulses of either 245 kHz or 290 kHz corresponding to excitation regions at 19cm and 17cm (7.5in and 7in) from the center of the probe respectively. Each excitation shell is 0.5m high and several millimeters thick. Eight experiments were repeated at the same time daily (Table 5.1). Each experiment used a repetition time, T_r, of 5s to allow for T_1 relaxation.

Observing changes in the T_2 measurement as a function of the echo spacing t_E can provide an indication of the significance of NMR diffusion relaxation effects. Measurements were made under flow and no flow conditions to determine if the fluid flow affected the T_2 measurement. Data was also collected under two probe tuning protocols. The first held the NMR excitation frequency constant for each experiment; the second allowed the NMR instrument to auto-tune with an adjustable excitation frequency periodically within each experiment. This allowed a determination of whether changes in probe tuning affected the T_2 measurement.

Exp. No.	Averages	t_E (ms)	Flow	Excitation Frequency	Duration
1	360	6.0	No	Auto-tuned	30 min
2	360	6.0	Yes	Auto-tuned	30 min
3	360	1.5	No	Constant	30 min
4	360	1.5	Yes	Constant	30 min
5	360	6.0	No	Constant	30 min
6	360	6.0	Yes	Constant	30 min
7	360	1.5	No	Auto-tuned	30 min
8	2880	1.5	Yes	Auto-tuned	4 hours

Table 5.1. NMR experiments with well-logging probe.

The data processing software uses the inverse Laplace transform to generate a T_2 distribution for the reactor excitation shell. Because of the generally low signal to noise ratio that is typical for a low-field NMR device in natural geologic material, the Javelin data interpretation software also calculates a noise-robust parameter based on the mean amplitude of the echoes in the record CPMG. The Square of Echoes (SOE) is calculated as the squared value of the mean of echoes. A reduction in the calculated SOE over the course of the experimental period indicates that the mean value of the T_2 relaxation time is decreasing as the conductivity of the porous media in the reactor decreases.

Sampling and Imaging

A sample of re-circulating substrate was collected daily during Experiment 6 (Table 5.1) and immediately serially diluted and plated [41] to estimate the quantity of viable cells in the reactor bulk fluid. While the suspended cell counts are not directly indicative of biofilm formation, or more specifically of EPS production, they provide a general measure of growth conditions and cell population within the reactor.

On day 8, the reactor was drained and NMR measurements were acquired using Experiment 7 parameters (Table 5.1). Following the measurements, the bioreactor was destructively sampled to confirm biofilm accumulation in field-relevant quantities. The sand was removed from the reactor in layers, with samples collected in sterile, pre-weighed 15mL Falcon tubes for imaging and cell population analysis. The samples were collected from the NMR probe's sensitive region in the annulus center at three depths—top (6in (15cm) deep from the top of pipe), middle (12-15in (30 – 38 cm) deep) and bottom (28in (71cm) deep). Six samples were collected for both population analysis with the drop plate method and imaging with stereoscopic and scanning electron microscopy.

Ten mL of sterile phosphate buffered saline (PBS) solution was added to each sample of sand collected for population analysis. The samples were vortexed with a Thermolyne MaxiMix II Type 37600 mixer for 30 seconds each, then sonicated for 2 minutes (Tutthauer CSU-3). Prior to serial dilution and plating, each sample was again vortexed for 30 seconds to remove attached bacteria from the sand particles and break up clumps of cells. Following plating, the buffer solution was poured off and the sand

samples were dried at 65°C for until their masses stabilized. The mass of dry sand and the plate count from each sample indicate cfu/g sand in the reactor.

For stereoscope microscopy analysis, biofouled sand samples from the radial flow reactor and clean control sand were stained with 300µL of 40µM Syto 9 (Molecular Probes, NY USA) for 30 minutes. The samples were rinsed with 0.2µm filtered (VWR, NJ, USA) distilled water and immediately imaged at 470nm excitation with a Niko SMZ 1500 (Nikon, NY, USA) stereoscope equipped with an EXFO Xcite 120 fluorescence illumination system.

Additionally, images were acquired using a Zeiss Supra 55VP scanning electron microscope (Zeiss, USA). Sand and biofilm from the radial flow reactor and control sand samples were sputter coated with iridium and high-resolution images were taken at 1.0kV at a working distance of 3-4mm.

Results and Discussion

The experimental NMR data shows a shift in the T_2 distribution to faster decay times, indicating that the fluid properties and pore environment changed due to biofilm growth (Figure 2). No significant relaxation enhancement due to diffusion, flow, or changes in probe tuning was observed. Therefore, unless otherwise noted, the data presented was collected during Experiment 8 where the level of background noise was lowest due to the high number of averages. The mean log T_2 relaxation time decreased from approximately 710ms following the buffer pulse to approximately 390ms on day 7.

Figure 2 shows the signal attenuation (top) and T_2 distributions (bottom) measured during the course of testing.

Day 1 measurements were conducted in the disinfected sand pack saturated with a phosphate buffer solution using Experiment 7 parameters and 4560 averages. Measurements taken during the inoculation of the reactor with *B. mojavensis* occurred at day 1.5. Experiments conducted on day 2 represent the first potential measurement of attached biofilm within the reactor. The signal decay curves and T_2 distributions collected days 3-5 show significant overlap.The data collected on days 6 and 7 likewise overlap and are shown in Figure 2 as a thick solid line. The dash-dot curve in both panels shows the data obtained on day 8 from the drained reactor (Experiment 7).

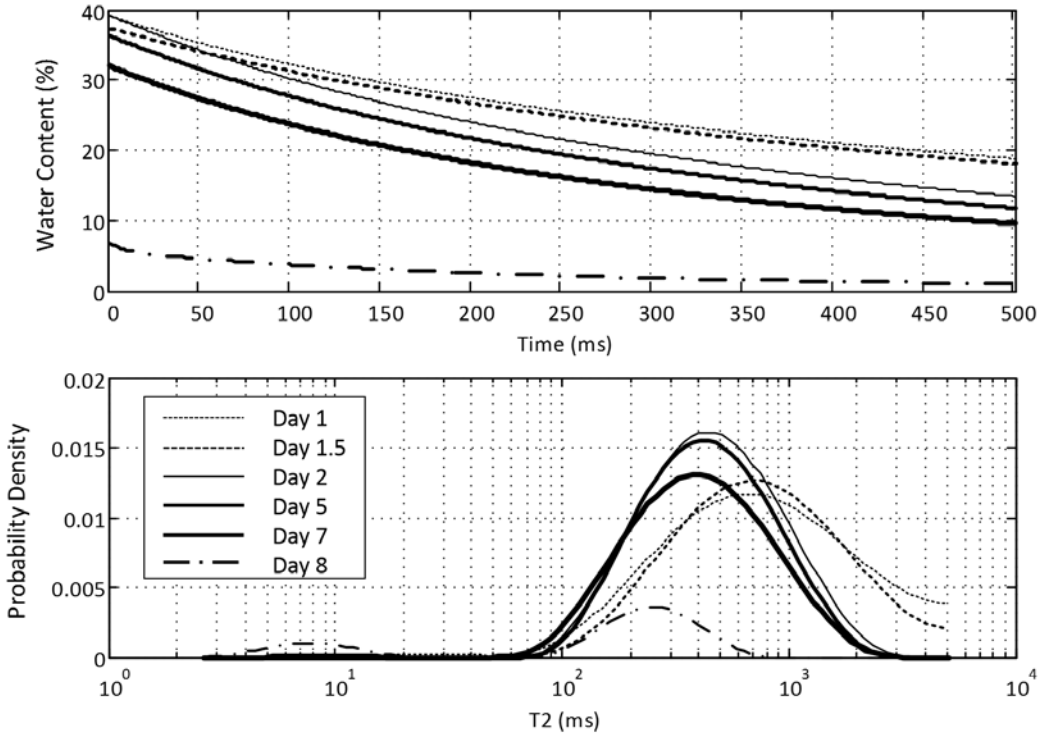

Figure 5.2. Time evolution of CPMG signal decay curves and T_2 distributions. Increased signal attenuation with biofilm formation produces steeper CPMG signal decay curves (top panel). The distribution of T_2 relaxation times (bottom panel) shifted to faster decay times as biofilm grew in the reactor. Data collected days 3 and 4 overlap the day 5 curve and are not shown. Likewise, the day 6 data is obscured by the day 7 curve and is not shown. Day 8 data was collected from the drained reactor.

By day 2, the CPMG signal decay curve is notably steeper and the T_2 distribution shows a narrower peak, centered at approximately 450ms (Figure 2). These data indicate an increase in the proportion of protons experiencing faster relaxation as would be expected in the event of biofilm formation. The rate of change of the signal response decreased after day 2, with little change recorded in the signal days 3-5. The day 6 and 7 data show a decreased signal amplitude in the top panel relative to day 5, indicating a decrease in the measured reactor water content. The NMR measurement from the drained reactor on day 8 reflects the presence of biofilm, as seen in the residual peak between

200—300ms. The smaller peak at approximately 7ms most likely originates from water or biofilm that is directly bound on and interacting with the sand surface. The lower amplitude of the signal from the drained reactor reflects the desaturation of the sandpack.

The measured reactor water content decreased from 37.3% at inoculation to 32.2% on day 7. After draining the reactor on day 8, the measured water content was 7.0% and the mean log T_2 relaxation time was 121ms. The decrease in measured water content during the growth phase is best explained by microbial gas production within the pores as a metabolic by-product. This biologically-driven reduction in water content of the reactor sandpack may have contributed to shorter T_2 relaxation times by increasing the effective saturated surface area to fluid volume ratio (S/V) in Eqn. 2. However, the magnitude of the T_2 shift between inoculation and day 7 significantly exceeds that from between day 7 and day 8 after the reactor was drained (Figure 2). The reduction in mean log T_2 relaxation time by day 7 was approximately 320ms corresponding to a water content decrease of 5.1 percentage points. The 25 percentage point reduction in water content after draining the reactor produced only a further 270ms reduction in the mean log T_2 relaxation time. T_2 relaxation times decreased nearly six times more on a water content basis [ms/% water] during the growth phase as compared to when the reactor was drained. This suggests that decrease in water content in the reactor during the experiment was likely *not* the primary mechanism causing the observed shift in the T_2 relaxation distribution. The best explanation for the observed decrease in T_2 relaxation times is biofilm accumulation in the reactor sandpack.

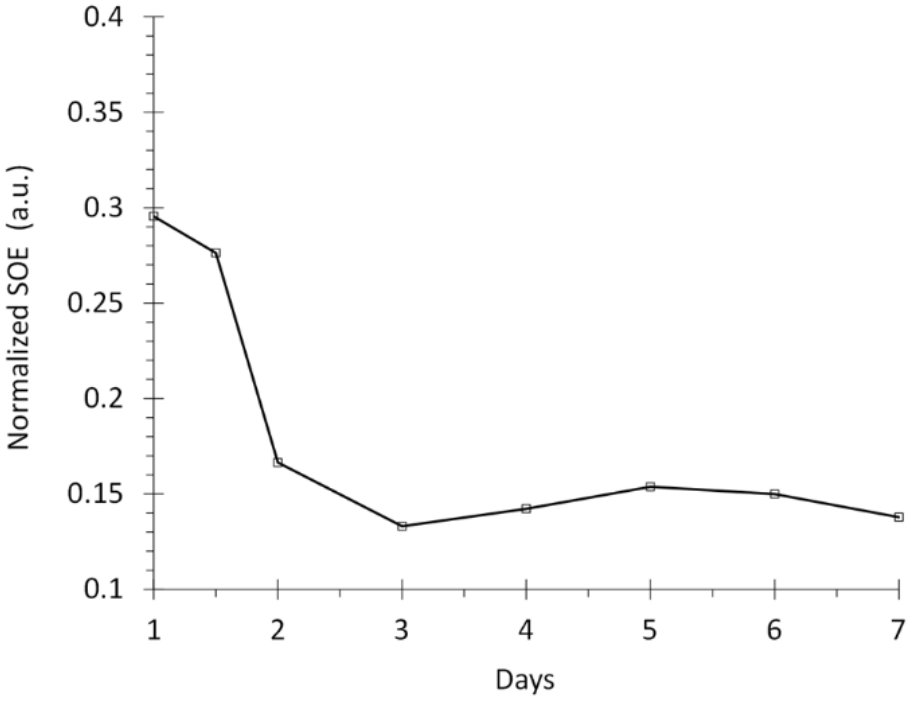

Figure 5.3. SOE Reduction. Data for the set of long-average experiments shows a decrease of approximately 53% in the squared value of the mean of echoes over the duration of the experiment.

The measured SOE, normalized with respect to water content squared, decreased 53% between day 1 and day 7 (Figure 3). The normalized SOE value shows the same trends as observed in the signal attenuation and T_2 distribution data in Figure 2, where the initial change is most significant followed by stabilization in the signal response.

HPC of the daily samples show an initial drop in cfu numbers after inoculation, followed by a steady increase over the duration of the experiment (Figure 4). From an inoculum concentration on the order of $7\log_{10}$cfu/mL injected into the reactor on day 1.5, the day 2 HPC yielded colony counts of approximately $5.5\log_{10}$cfu/mL. Combined with the NMR results showing a decrease in T_2 relaxation times over the same period, this

decline in HPC can be attributed to bacterial attachment and initial biofilm formation on the sand particles. Planktonic cells increased in number to approximately 6.5$\log_{10}$cfu/mL on days 3 and 4. These higher colony counts correspond to enhanced signal attenuation and decreases in the mean log T_2 relaxation time, though they are necessarily *not* a measurement of the cell numbers in the biofilm. The increase in SOE observed around day 5 may correspond to a biofilm sloughing event since heterotrophic plate counts from day 5 were nearly an order of magnitude higher than those from day 4, 7.4$\log_{10}$ versus 6.5$\log_{10}$ cfu/mL, respectively. After day 5, a slower rate of increase in colony numbers was observed than between days 4 and 5, suggesting a secondary attachment period may have occurred. This interpretation is supported by the NMR data which shows a decrease in the normalized SOE over the same period. In general, the HPC data and the diverse colony morphologies indicate that conditions in the bioreactor were favorable for mixed population bacterial growth.

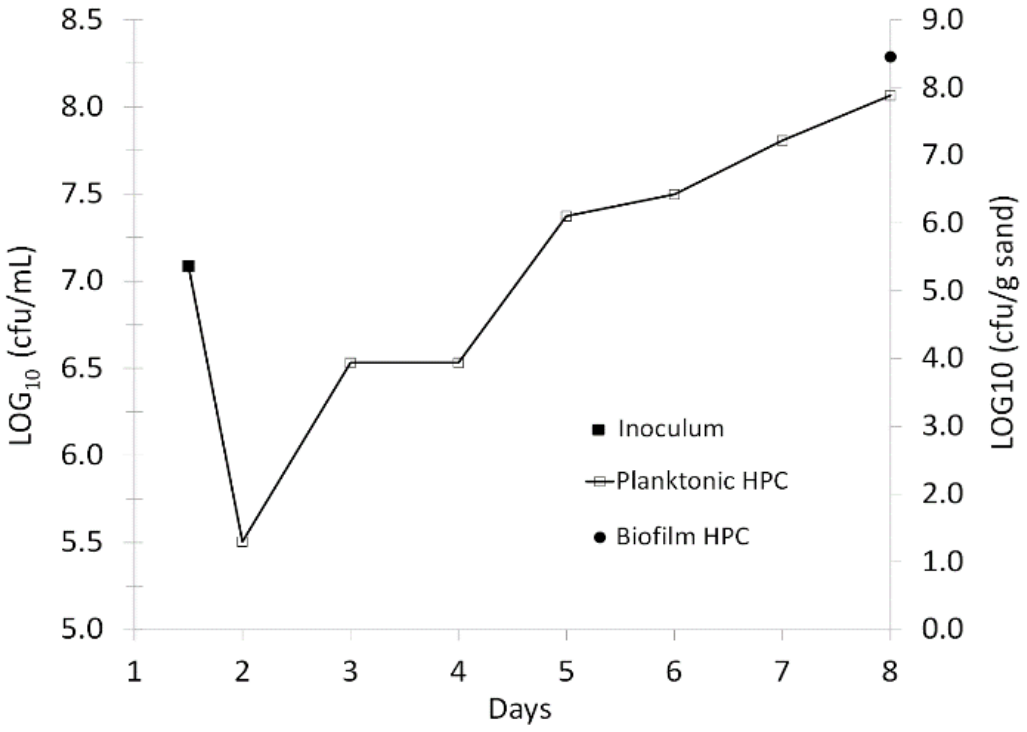

Figure 5.4. Heterotrophic Plate Counts (HPC). Daily HPC data shows a strong initial attachment of cells from approximately 7$\log_{10}$cfu/mL in the 10L inoculum to 5.5$\log_{10}$cfu/mL on day 2. Increasing colony numbers resulted in a final population of approximately 8$\log_{10}$cfu/mL by day 8. The average biofilm HPC from the sand samples was approximately 8.5$\log_{10}$ cfu/g sand, shown on the secondary axis.

When the bioreactor was drained and destructively sampled, the sand was sticky, consistent with presence of a biofilm bridging the pore spaces of the sand. Cell population analysis of sand samples indicates that attached bacterial concentrations in the bioreactor were approximately 7$\log_{10}$ to 9$\log_{10}$cfu/g dry sand, with an average in the reactor of 8.5$\log_{10}$cfu/g sand. This concentration is similar to cell counts noted in the literature for subsurface biofilms used to degrade trace organics, where populations are typically in the range of 6$\log_{10}$ to 9$\log_{10}$ cfu/g soil [15, 26].

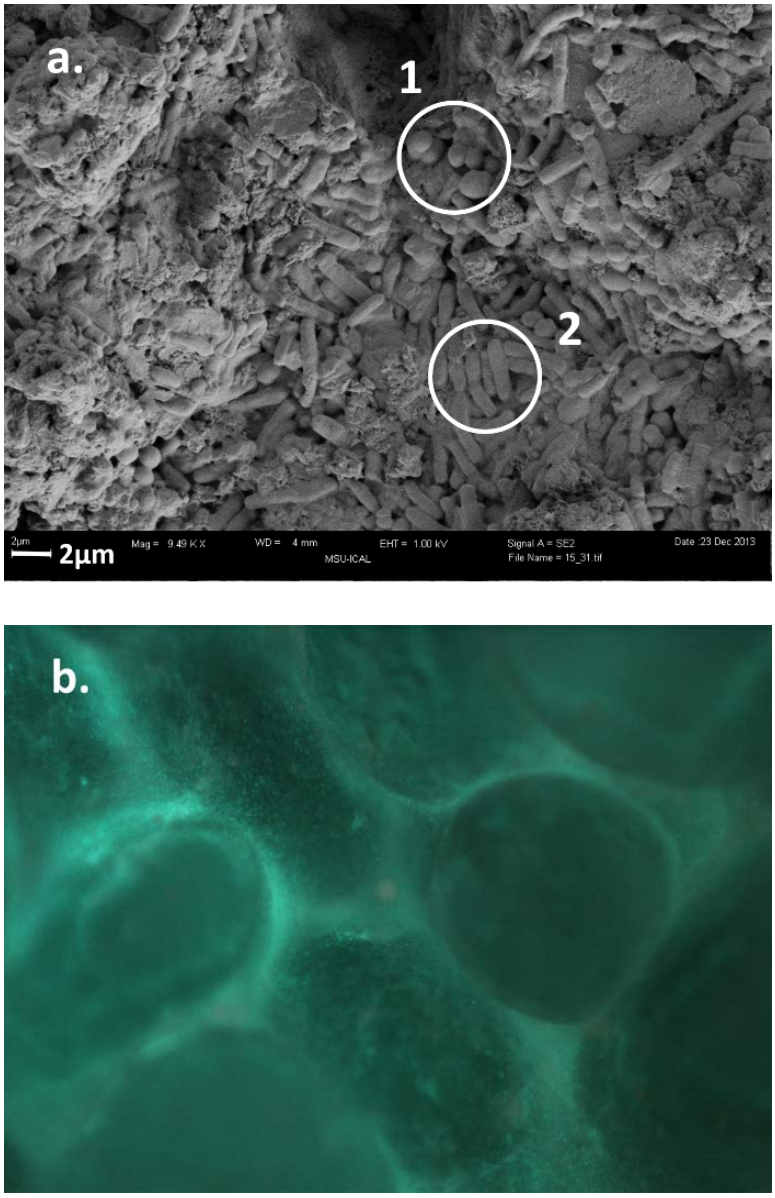

Figure 5.5. Porous media microscopy confirmed biofilm accumulation in the region of the reactor where NMR data was collected. a) Scanning electron microscope (SEM) image of mixed population bacterial cells and extracellular polymeric substance (EPS) on a sand particle collected from the middle depth of the reactor. Region 1 shows cocci bacteria while Region 2 shows rod-like cells. *Bacillus mojavensis* is a rod-shaped bacteria. Depth 15 in. Scale bar is 2 µm. b) Stereoscope image of EPS encasing the bacterial cells and binding grains of 1mm sand, Depth 15 in. 40X magnification.

SEM images (Figure 5.5) showed a mixed bacterial population of rod and cocci cells, with thicker EPS at the bottom of the reactor where the fresh nutrient supply entered the reactor. Compared to samples collected in the middle and upper regions of the reactor (Figure 5a), individual cells were less distinguishable on samples collected from the bottom due to the thicker EPS matrix (not shown). Stereoscopic microscopy qualitatively confirmed the presence of biofilm on and between sand particles (Figure 5b), where the matrix fluoresces in green and the cells are visible as bright flecks. Microscopy confirms bacterial growth and EPS production within the reactor.

Population analysis indicates both quantity and diversity of heterotrophic bacteria present without directly accounting for the presence of EPS. Microscopy of the sand can confirm the presence of the EPS matrix, but does little to elucidate the *in-situ* characteristics and hydrodynamics of the biofouled pore space. For these reasons, characterizations of observed biofilm accumulation are qualitative and indicative of EPS formation within the NMR logging tool's sensitive region but are not intended to quantify the total amount of EPS formed in the reactor.

Several studies have demonstrated that biofilm growth in soils and rock reduces the hydraulic conductivity and permeability of the media, often by several orders of magnitude [5, 15, 42, 43]. Furthermore, biofilm itself is a porous media with an internal architecture that includes voids and channels [44-46]. The enhanced NMR relaxation observed in this study could be due to the changing surface properties if the biofilm coats the porous media, represented as an increase in $1/T_{2S}$. However, if the biopolymers are distributed throughout the pore volume then the faster relaxation could be dominated by

exchange of protons between the water and the biopolymers, which would be represented as an increase in $1/T_{2B}$.

NMR studies on T_2 decay in porous media typically focus on the influence of T_{2S} and T_{2D} on the overall relaxation behavior of the medium [47-50]. When the bulk fluid in the pore space changes, however, as it does during biofilm formation, the influence of T_{2B} can no longer be neglected. In the bulk phase, the production of polymer-like EPS and biomacromolecules will enhance spin relaxation as protons bound to the polymers and dissolved organics rapidly exchange with free protons on the liquid molecules [51]. This relaxation mechanism produces shorter relaxation times than would be expected in bulk water. As the content of EPS and biomacromolecules increases within the pore space relative to the initial condition, the weighted average of 'bound' and 'free' proton T_2 times will shift in the direction of the polymer relaxation time to shorter T_2 decay times [3, 38].

From a macroscopic perspective, biofilm may act as a relatively impermeable surface, insofar as it is restrictive to convective flow within pores. At the molecular level, however, biofilm is composed of approximately 97% water [52]. For these reasons, we attribute the change in relaxation behavior observed in this experiment primarily to changes in the bulk relaxation of the pore fluid, which includes both a liquid and polymer-gel phase. In these experiments it is proposed that an increase in $1/T_{2B}$ is the best way to conceptualize the observed enhancement in the NMR T_2 relaxation.

These experiments demonstrate that a commercially available low-cost NMR logging tool can detect small to moderate changes in T_2 distribution due to biofilm

accumulation in quartz sand under laboratory conditions. Mean log T_2 relaxation times decreased from 710ms when the reactor contained a sterile buffer solution to 389ms following 7 days of biofilm cultivation. Over the same period, the noise-robust SOE parameter decreased by 53%, indicating an increase in signal attenuation and shorter T_2 relaxation times. Normalizing the data with respect to water content squared in the reactor indicates that the change in T_2 is not primarily driven by the saturation state of the porous media in the reactor, but rather by biofilm accumulation. Heterotrophic plate counts suggest that planktonic cells in the reactor increased in abundance from approximately 5.5$\log_{10}$cfu/mL on day 2 to 8$\log_{10}$cfu/mL on day 8. Population data from destructive sampling confirmed colony counts of attached cells on the order of 8$\log_{10}$cfu/g dry sand. Scanning electron and stereoscope microscopy confirmed the presence of the biofilm matrix attached to the sand particles compared to control sand. Our results, therefore, show that the measured shift in the reactor T_2 relaxation distribution toward faster signal decay times is best explained by biofilm accumulation in the reactor pore spaces.

Our findings have the potential to improve monitoring methods for bioremediation applications involving the use of bio-barriers to slow the flow of groundwater or consume chemical contaminants. Deploying an array of the NMR probes in wells in the bio-barrier zone and recording signal changes over time could provide another measure of the robustness of the bio-barrier with respect to depth. Preparations are underway to use the NMR logging tool *in situ* to detect biofilm formation at an engineered field site in Butte, Montana. Considerations for this future work include the

effects of moving the probe between measurements and potential influences of soil mineralogy and water chemical parameters that would likely be encountered in a natural setting.

References

1. Sutherland, I.W., *Biofilm exopolysaccharides: a strong and sticky framework.* Microbiology, 2001. **147**: p. 3-9.

2. Characklis, W.G. and K.C. Marshall, Eds., *Biofilms*. 1990, New York: John Wiley & Sons, Inc.

3. Vogt, S.J., et al., *Permeability of a growing biofilm in a porous media fluid flow analyzed by magnetic resonance displacement-relaxation correlations.* Biotechnology and Bioengineering, 2013. **110**(5): p. 1366-1375.

4. Seymour, J.D., et al., *Anomalous fluid transport in porous media induced by biofilm growth.* Physical Review Letters, 2004. **93**(19).

5. Cunningham, A.B., et al., *Influence of biofilm accumulation on porous-media hydrodynamics.* Environmental Science & Technology, 1991. **25**(7): p. 1305-1311.

6. Drescher, K., et al., *Biofilm streamers cause catastrophic disruption of flow with consequences for environmental and medical systems.* Proceedings of the National Academy of Sciences of the United States of America, 2013. **110**(11): p. 4345-4350.

7. LaGrega, M.D., P.L. Buckingham, and J.C. Evans, *Hazardous Waste Management*. 2nd ed. 2001, New York: McGraw-Hill.

8. Kao, C.M., et al., *Biobarrier system for remediation of TCE-contaminated aquifers.* Bulletin of Environmental Contamination and Toxicology, 2004. **72**(1): p. 87-93.

9. Kao, C.M., et al., *Enhanced PCE dechlorination by biobarrier systems under different redox conditions.* Water Research, 2003. **37**(20): p. 4885-4894.

10. Kim, G., S. Lee, and Y. Kim, *Subsurface biobarrier formation by microorganism injection for contaminant plume control.* Journal of Bioscience and Bioengineering, 2006. **101**(2): p. 142-148.

11. Komlos, J., et al., *Biofilm barriers to contain and degrade dissolved trichloroethylene.* Environmental Progress, 2004. **23**(1): p. 69-77.

12. Phillips, A.J., et al., *Engineered applications of ureolytic biomineralization: a review.* Biofouling, 2013. **29**(6): p. 715-733.

13. von der Schulenburg, D.A.G., et al., *Spatially resolved quantification of metal ion concentration in a biofilm-mediated ion exchanger.* Biotechnology and Bioengineering, 2008. **99**(4): p. 821-829.

14. Pal, A. and A.K. Paul, *Microbial extracellular polymeric substances: central elements in heavy metal bioremediation.* Indian Journal of Microbiology, 2008. **48**(1): p. 49-64.

15. Cunningham, A.B., et al., *Subsurface biofilm barriers for the containment and remediation of contaminated groundwater.* Bioremediation Journal, 2003. **7**(3-4): p. 151-164.

16. Mitchell, A.C., et al., *Resilience of planktonic and biofilm cultures to supercritical CO2.* Journal of Supercritical Fluids, 2008. **47**(2): p. 318-325.

17. Petrova, O.E. and K. Sauer, *Sticky Situations: Key Components That Control Bacterial Surface Attachment.* Journal of Bacteriology, 2012. **194**(10): p. 2413-2425.

18. Kapellos, G.E., T.S. Alexiou, and A.C. Payatakes, *Hierarchical simulator of biofilm growth and dynamics in granular porous materials.* Advances in Water Resources, 2007. **30**(6–7): p. 1648-1667.

19. Pintelon, T.R.R., et al., *The effect of biofilm permeability on bio-clogging of porous media.* Biotechnology and Bioengineering, 2012. **109**(4): p. 1031-1042.

20. von der Schulenburg, D.A.G., et al., *Three-Dimensional Simulations of Biofilm Growth in Porous Media.* AIChE Journal, 2009. **55**(2): p. 494-504.

21. Thullner, M. and P. Baveye, *Computational pore network modeling of the influence of biofilm permeability on bioclogging in porous media.* Biotechnology and Bioengineering, 2008. **99**(6): p. 1337-1351.

22. Cunningham, A.B., E.J. Bouwer, and W.G. Characklis, *Biofilms in porous media,* in *Biofilms*, W.G. Characklis and K.C. Marshall, Editors. 1990, John Wiley & Sons, Inc.: New York. p. 697-732.

23. Stewart, T.L. and H.S. Fogler, *Biomass plug development and propagation in porous media.* Biotechnology and Bioengineering, 2001. **72**(3): p. 353-363.

24. Lazarova, V. and J. Manem, *Biofilm characterization and activity analysis in water and waste-water treatment.* Water Research, 1995. **29**(10): p. 2227-2245.

25. Bayer, J.V., F. Jaeger, and G.E. Schaumann, *Proton Nuclear Magnetic Resonance (NMR) Relaxometry in Soil Science Applications.* Open Magnetic Resonance Journal, 2010. **3**: p. 15-26.

26. Potter, K., et al., *Assay for bacteria in porous media by diffusion-weighted NMR.* Journal of Magnetic Resonance. Series B, 1996. **113**: p. 9-15.

27. Hoskins, B.C., et al., *Selective imaging of biofilms in porous media by NMR relaxation.* Journal of Magnetic Resonance, 1999. **139**(1): p. 67-73.

28. Sanderlin, A.B., et al., *Biofilm detection in natural unconsolidated porous media using a low-field magnetic resonance system.* Environmental Science & Technology, 2013. **47**(2): p. 987-992.

29. Seymour, J.D., et al., *Magnetic resonance microscopy of biofouling induced scale dependent transport in porous media.* Advances in Water Resources, 2007. **30**(6-7): p. 1408-1420.

30. Seymour, J.D., et al., *Magnetic resonance microscopy of biofilm structure and impact on transport in a capillary bioreactor.* Journal of Magnetic Resonance, 2004. **167**(322-327).

31. Van As, H. and P. Lens, *Use of H-1 NMR to study transport processes in porous biosystems.* Journal of Industrial Microbiology & Biotechnology, 2001. **26**(1-2): p. 43-52.

32. Gjersing, E.L., et al., *Magnetic resonance microscopy analysis of advective transport in a biofilm reactor.* Biotechnology and Bioengineering, 2005. **89**(7): p. 822-834.

33. Walsh, D., et al., *A small-diameter NMR logging tool for groundwater investigations.* Groundwater, 2013. **51**(6): p. 914-926.

34. Callaghan, P.T., *Principles of Nuclear Magnetic Resonance Microscopy*. 1991, New York: Oxford University Press.

35. Grunewald, E. and R. Knight, *A laboratory study of NMR relaxation times in unconsolidated heterogeneous sediments.* Geophysics, 2011. **76**(4): p. G73-G83.

36. Kleinberg, R.L. and M.A. Horsfield, *Transverse relaxation processes in porous sedimentary rock.* Journal of Magnetic Resonance, 1990. **88**(1): p. 9-19.

37. Brownstein, K.R. and C.E. Tarr, *Importance of classical diffusion in NMR studies of water in biological cells.* Physical Review A, 1979. **19**(6): p. 2446-2453.

38. Codd, S.L., et al., *NMR relaxation measurements of biofouling in model and geological porous media.* Organic Geochemistry, 2011. **42**(8): p. 965-971.

39. Carr, H.Y. and E.M. Purcell, *Effects of diffusion on free precession in nuclear magnetic resonance experiments.* Physical Review, 1954. **94**(3): p. 630-638.

40. Meiboom, S. and D. Gill, *Modified spin-echo method for measuring nuclear relaxation times* Review of Scientific Instruments, 1958. **29**(8): p. 688-691.

41. Herigstad, B., M. Hamilton, and J. Heersink, *How to optimize the drop plate method for enumerating bacteria.* Journal of Microbiological Methods, 2001. **44**(2): p. 121-129.

42. Taylor, S.W. and P.R. Jaffe, *Biofilm growth and the related changes in the physical properties of a porous medium. 1. Experimental investigation.* Water Resources Research, 1990. **26**(9): p. 2153-2159.

43. Taylor, S.W. and P.R. Jaffe, *Enhanced in-situ biodegradation and aquifer permeability reduction.* Journal of Environmental Engineering-ASCE, 1991. **117**(1): p. 25-46.

44. Allison, D.G., *The biofilm matrix.* Biofouling, 2003. **19**(2): p. 139-150.

45. Stoodley, P., D. Debeer, and Z. Lewandowski, *Liquid flow in biofilm systems.* Applied and Environmental Microbiology, 1994. **60**(8): p. 2711-2716.

46. Stoodley, P., et al., *Biofilms as complex differentiated communities.* Annual Review of Microbiology, 2002. **56**: p. 187-209.

47. Anand, V., Hirasaki, George J., *Paramagnetic relaxation in sandstones: Distinguishing T1 and T2 dependence on surface relaxation, internal gradients and dependence on echo spacing.* Journal of Magnetic Resonance, 2008. **190**: p. 68-85.

48. Godefroy, S., Korb, J.-P., Fleury, M., Bryant, R.G., *Surface nuclear magnetic relaxation and dynamics of water and oil in macroporous media.* Physical Review E, 2001. **64**: p. 021605-1-13.

49. Kleinberg, R.L., Kenyon, W.E., Mitra, P.P., *Mechanism of NMR relaxation of fluids in rock.* Journal of Magnetic Resonance Series A, 1994. **108**: p. 206-214.

50. Kleinberg, R.L., S.A. Farooqui, and M.A. Horsfield, *T(1)/T(2) ratio and frequency-dependence of NMR relaxation in porous sedimentary rocks.* Journal of Colloid and Interface Science, 1993. **158**(1): p. 195-198.

51. Hills, B.P., C. Cano, and P.S. Belton, *Proton NMR relaxation studies of aqueous polysaccharide systems.* Macromolecules, 1991. **24**(10): p. 2944-2950.

52. Hornemann, J.A., et al., *Biopolymer and water dynamics in microbial biofilm extracellular polymeric substance.* Biomacromolecules, 2008. **9**(9): p. 2322-2328.

CHAPTER SIX

IN-SITU DETECTION OF SUBSURFACE BIOFILM USING LOW-FIELD NMR – A FIELD STUDY

Contribution of Authors and Co-Authors

Manuscript in Chapter 6

Author: Catherine M. Kirkland

Contributions: Helped conceive and implement study design. Collected and analyzed data. Wrote manuscript.

Co-Author: Maria P. Herrling

Contributions: Helped conceive and implement study design. Collected and analyzed data. Provided feedback and comments on the manuscript.

Co-Author: Randy Hiebert

Contributions: Helped conceive and implement study design. Provided feedback and comments on the manuscript.

Co-Author: Andrew T. Bender

Contributions: Collected and analyzed data.

Co-Author: Elliot Grunewald

Contributions: Helped conceive and implement study design. Provided supervision and oversight on data collection and analysis. Provided feedback and comments on the manuscript.

Co-Author: David O. Walsh

Contributions: Helped conceive and implement study design. Provided feedback and comments on the manuscript.

Co-Author: Sarah L. Codd

Contributions: Helped conceive and implement study design. Provided feedback and comments on the manuscript.

Manuscript Information Page

Catherine M. Kirkland, Maria P. Herrling, Randy Hiebert, Andrew T. Bender, Elliot Grunewald, David O. Walsh, Sarah L. Codd

Environmental Science and Technology

Status of Manuscript:
____ Prepared for submission to a peer-reviewed journal
____ Officially submitted to a peer-review journal
____ Accepted by a peer-reviewed journal
_X___ Published in a peer-reviewed journal

American Chemical Society
Vol. 49, No. 18, Pages 11045 - 11052, September 2015

IN-SITU DETECTION OF SUBSURFACE BIOFILM USING LOW-FIELD NMR – A FIELD STUDY

Abstract

Subsurface biofilms are central to bioremediation of chemical contaminants in soil and groundwater whereby micro-organisms degrade or sequester environmental pollutants like nitrate, hydrocarbons, chlorinated solvents and heavy metals. Current methods to monitor subsurface biofilm growth in-situ are indirect. Previous laboratory research conducted at MSU has indicated that low-field nuclear magnetic resonance (NMR) is sensitive to biofilm growth in porous media, where biofilm contributes a polymer gel-like phase and enhances T_2 relaxation. Here we show that a small diameter NMR well logging tool can detect biofilm accumulation in the subsurface using the change in T_2 relaxation behavior over time. T_2 relaxation distributions were measured over an 18 day experimental period by two NMR probes, operating at approximately 275 kHz and 400 kHz, installed in 10.2 cm wells in an engineered field testing site. The mean log T_2 relaxation times were reduced by 62% and 43%, respectively, while biofilm was cultivated in the soil surrounding each well. Biofilm growth was confirmed by bleaching and flushing the wells and observing the NMR signal's return to baseline. This result provides a direct and non-invasive method to spatio-temporally monitor biofilm accumulation in the subsurface.

Introduction

Reactive biofilm barriers, composed of attached microbial cells, extracellular polymeric substances (EPS), and entangled organic and inorganic molecules, can be cultivated in the subsurface to degrade and immobilize chemical contaminants as part of a bioremediation project [1]. Contaminants in the groundwater, including nitrates, heavy metals, hydrocarbons, and some chlorinated solvents, are consumed or transformed by bacteria attached to soil surfaces while the EPS matrix slows the groundwater flow by reducing the soil's hydraulic conductivity [2-7]. While biobarrier technology is well-established to clean contaminated groundwater [8, 9], it is challenging with current technology to monitor the in-situ accumulation and maturation of the biofilm nondestructively. Conventional methods to infer biofilm growth in the subsurface include reduced saturated hydraulic conductivity [10-12]. While hydraulic conductivity measurements can be useful for describing how easily the soil conveys water, they are less useful for monitoring the growth, maturation and decay of the biobarrier with spatial and temporal resolution.

We present results indicating a small diameter nuclear magnetic resonance (NMR) well-logging tool provides additional means of monitoring biofilm accumulation and condition over time in the subsurface by detecting changes in the NMR signal response. Chemical and physical changes in a sample can impact a wide range of NMR parameters, including NMR frequency shifts, NMR relaxation times T_1 and T_2, and diffusion coefficients [13]. NMR frequency shifts are typically caused by chemical changes in the fluid sample. However at very low magnetic fields (<1 MHz) even large

proton chemical shifts such as those between oil and water are not detectable. Diffusion coefficients require additional magnetic field gradient hardware for detection, but can be used to distinguish different viscosity fluids in a sample or determine the average pore size of a material by measuring the timescale of the restricted diffusion [9]. NMR relaxation, T_1 and T_2, is caused by the correlation time of the diffusing fluid with respect to the resonant frequency of the NMR signal, as well as paramagnetic molecules the fluid comes into contact with. For these reasons, NMR relaxation times are affected by pore size distributions, fluid viscosity, and chemical changes in the mineralogy of any solid matrix or dissolved ions. Measuring T_2 is significantly faster than measuring T_1. T_2 measurements are generally considered the most robust low field measurement considering acquisition times and signal-to-noise.

In a T_2 measurement, the induced NMR signal echoes decay at a rate of $1/T_2$, where T_2 is the spin-spin relaxation time associated with interactions in the fluid-pore environment. Analyzing the signal decay curve with the inverse Laplace transform produces a statistical distribution of T_2 relaxation times that reflect the variety of pore-scale environments occupied by hydrogen protons in the excitation shell. The T_2 relaxation time distribution in heterogeneous porous media is used, both in hydrogeologic analysis [14] and in oil and gas exploration [15-18], to estimate the pore size distribution in the formation and for fluid typing [9]. Biofilm accumulation in pores causes T_2 relaxation times to decrease compared to unclogged pores as the biofilm EPS contributes a biopolymer gel-like phase [19, 20]. Water in the EPS matrix contributes a reduced NMR relaxation signal [21] and demonstrates restricted diffusion [22].

The NMR well-logging tool used in this study measures T_2 relaxation and was designed for use in small diameter 'slim-line' boreholes for groundwater exploration and aquifer characterization [14]. In preliminary work, it was shown that this NMR logging tool can detect biofilm growth [20]. The tool was tested in a laboratory-scale model well-bore bioreactor filled with silica sand and inoculated with *Bacillus mojavensis*. Biofilm was cultivated in the reactor over 8 days, during which the measured mean log T_2 relaxation time decreased by 45%, from 710 ms to 389 ms [20]. Biofilm accumulation was confirmed with destructive sampling and subsequent heterotrophic plate counts and microscopy. The current research significantly advances previous work by showing that the same logging tool can monitor biofilm growth at field scale, 6 m underground where complex water chemical interactions exist. The NMR tool could be deployed to bioremediation sites in parallel with currently used methods to enhance the understanding of biofilm growth in-situ.

Methods

This study used two 8.9 cm diameter, 1.37 m long NMR well-logging probes (JP350 Javelin by Vista Clara, Inc., Mukilteo, WA) to monitor T_2 relaxation distributions over time as an indication of biofilm accumulation in the soil in an engineered test cell. The test cell is 55 m by 40 m at the surface and is 6m deep with 2:1 side slopes (x:z). The cell is lined with a 30 mm polyvinylchloride (PVC) liner and contains water up to 1 - 1.2 m beneath the ground surface. The test cell contains a number of boreholes of varying dimensions that were prepared for a previous experiment [7]. Two of the 10.2 cm

boreholes were used for measurements of T_2 relaxation over an 18-day experimental period.

A bleach solution consisting of 2 lb (907 g) sodium dichloro-s-triazinetrione dihydrate ($C_3H_4Cl_2N_3NaO_5$) (Spa Guard Chlorinating Concentrate, Bio-Lab Inc., Lawrenceville, GA) was pumped into the soil around the two wells at the beginning and end of the experiment. A 30 L inoculum of *Pseudomonas fluorescens* strain CPC211a was injected into each well's measurement zone and was cultivated with a pulsed flow of molasses-based substrate (10 g/L molasses (Aunt Patty's Blackstrap Molasses, Eugene, OR), 3 g/L sodium nitrate (SQM industrial grade prills, 98%, SQM North America, Atlanta, GA), 1 g/L yeast extract (Acros Organics, Geel, Belgium), 0.12 g/L potassium phosphate dibasic, and 0.04 g/L potassium phosphate monobasic (Thermo-Fisher Scientific, Waltham, MA)) for 10 days. A 4-day starvation period followed the growth phase. T_2 measurements were conducted at the well bottom daily during the growth phase, Days 1-10, and twice during the starvation phase, Days 12 and 14. Water samples were collected prior to T_2 experiments for subsequent pH measurement and microbial analysis using the drop plate method [23]. T_2 relaxation measurements were also recorded over the bottom 3-3.5 m of well depth twice during the experiment; wells were logged before inoculation and during the starvation period. At the end of the experiment, the sodium dichlor bleach solution and high groundwater flows were applied to the experimental region as a validation of biofilm growth, since these stress tests would be expected to remove EPS formed during the growth phase. The experiment was designed to distinguish normal variation in signal response due to environmental noise and probe

placement from those changes resulting from biological activity and biofilm growth. The experimental sequence of events for a single well is shown in Table 6.1; both wells received identical treatment. Additional details regarding experimental methods are provided in Supporting Information.

The two NMR probes were tuned to different frequencies, corresponding to excitation shells at different radii from the well centers. The lower frequency probe (LF) was placed in one well, called the LF well, and was tuned to 245 and 290 kHz. Two excitation shells 0.5 m in height and a few mm thick were located 17-19 cm from the LF well center. The higher frequency probe (HF), installed in the HF well, was tuned to 360 and 425 kHz, producing two excitation shells located 11-13 cm from the HF well center. The probes are identical low-field NMR tools other than the tuning frequency.

Day	Experimental Task	Purpose
(-2)-(-1)	Site Preparation	Create a 'biofilm-free' initial condition
	Injection of 75 – 115 L sodium dichlor concentrate solution	
	Flush with test cell groundwater at 45.5 L/min	
0	Well logs	Measure baseline T_2 distribution as a function of depth
	T_2 distributions measured in 0.5 m increments over the bottom 3-3.5 m saturated well depth	
1	Inoculation	Promote attachment and biofilm formation by target organism
	Injection of 30 L inoculum culture of *Pseudomonas fluorescens* CPC211a into measurement zone surrounding the NMR probe at well bottom	Measure baseline T_2 distribution at the well bottom
	T_2 measurement in fixed location at well bottom	
2-10	Biofilm Growth Phase	Promote and measure biofilm accumulation
	Injection of 380-415 L molasses-based substrate daily at 1.2 L/min	
	Measurements of T_2 relaxation distributions daily in fixed location at well bottom	

Day	Experimental Task	Purpose
11-14	Starvation Phase	Monitor biofilm resilience Establish 'initial condition' to assess signal variation due to probe re-location
	Measurements of T_2 relaxation distributions Day 12 and 14 at the well bottom	
12	Well logs	Measure T_2 distribution as a function of depth after biofilm growth Evaluate signal variation due to probe re-location
	T_2 distributions measured in 0.5 m increments over the bottom 3-3.5 m saturated well depth	
14	Biofilm Stress Tests	Monitor signal response to stresses intended to destroy biofilm
	Flush with test cell groundwater at 45.5 L/min	
	Injection of 75-115 L sodium dichlor concentrate solution	
	Measurements of T_2 relaxation distributions in fixed location at well bottom	
15	Measurement of final conditions	Verify biofilm accumulation by signal restoration after detachment and removal of biofilm
	Flush with test cell groundwater at 45.5 L/min	

Measurements of T_2
relaxation distributions in
fixed location at well bottom

Table 6.1. Experiment Overview

A diverter disk attachment was connected to the top of each probe to direct the substrate and high flows of water into the soil around the well-bore, rather than into the water column above the probe. A millimeter-scale gap was left between the disk and the well casing to ensure that the probe could be removed from the well. The disk was machined with an attachment for a standard garden hose to accommodate high volume flushing and four 0.1 cm holes for low-flow nutrient tubing (Figure 6.1). Pore velocity during the substrate injection was approximately 0.2 cm/min in the LF well and 0.4 cm/min in the HF well each probe's sensitive zone. The high volume flush created a pore velocity of approximately 9.2 cm/min in the LF well and 14.8 cm/min in the HF well.

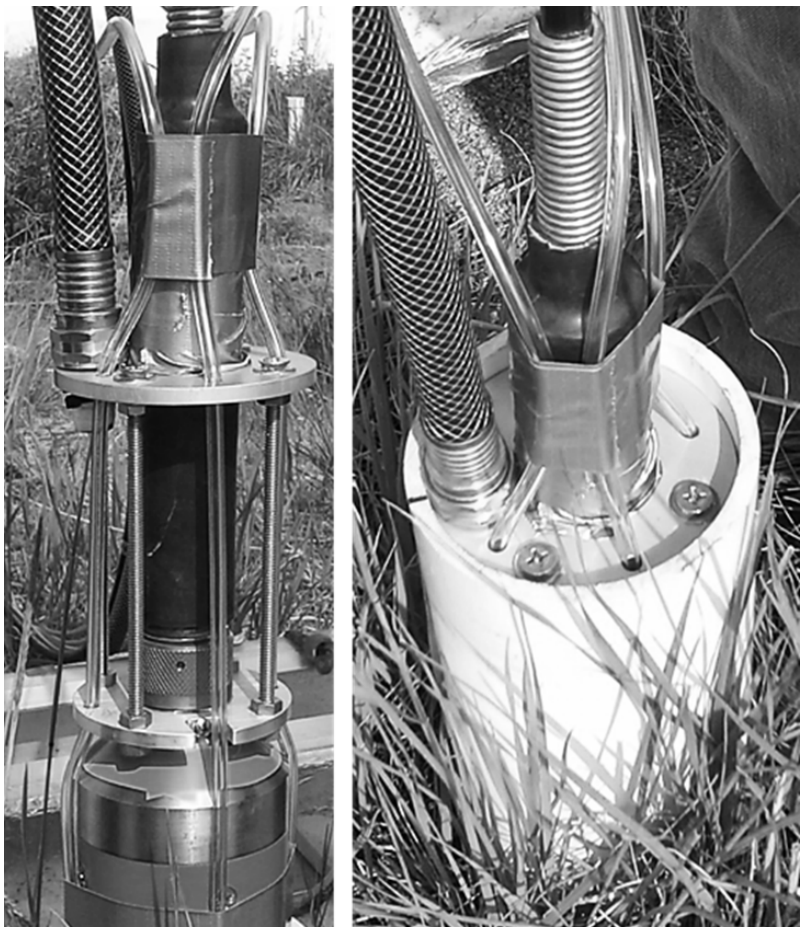

Figure 6.1. A diverter disk attachment on the top of each NMR logging tool directed substrate and high flow groundwater flushes into the biofilm growth region in the tool's sensitive zone in the soil and reduced backflow up the well casing.

For each probe, Experiment 1 and 2 (Table 6.2) constitute one standard Carr-Purcell-Meiboom-Gill (CPMG)[24, 25] measurement of approximately 27 minutes. This standard measurement was conducted 4 times in each well for a typical well-bottom measurement of approximately 2 hours Days 0-15, excluding Days 11 and 13. The data was averaged to obtain a single measurement for each day for each well. This standard measurement was also used at each 0.5 m depth increment when vertically logging the wells before and after biofilm growth on Day -1 and Day 12. An additional 12 standard

measurements were made in one or the other well on alternating days to improve the signal to noise ratio in the data collected and to confirm that 4 measurements was adequate to describe the system.

	LF Probe		HF Probe	
	Expt 1	Expt 2	Expt 1	Expt 2
Echo time, t_E (ms)	1.5	1.5	1.3	1.3
Repetition time, T_r (ms)	1500	5000	1500	5000
Acquisition time (ms)	50	500	50	500
No. of echoes	34	334	39	385
No. of averages	600	150	600	150

Table 6.2. NMR Experimental Parameters

Results and Discussion

Both the LF and HF NMR logging probes recorded changing distributions of T_2 relaxation times during the experiment with reductions of 62% and 43%, respectively, in the mean log T_2 during the biofilm growth phase (Figure 6.2). In the LF well, the T_2 relaxation time was 29 ms on Day 1 and fell to an average of 11 ms between Days 5-12. Over the same period, the HF well T_2 relaxation time fell from 50 ms to an average of 28 ms. Data from both wells initially showed a T_2 distribution with two peaks that transitioned to a single peak distribution by Day 6 (Figure 6.3 (a) and (b)).

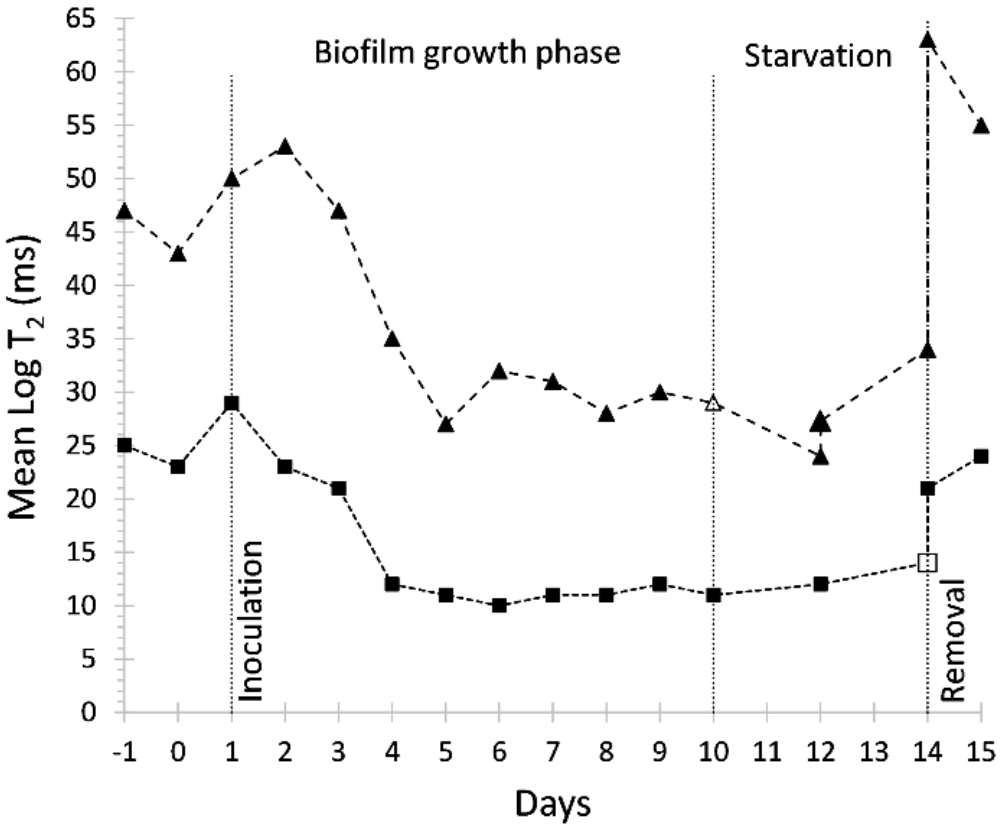

Figure 6.2. Mean log T_2. Mean log T_2 relaxation times decreased 62% (LF) and 43% (HF) indicating that protons became more rotationally constrained as biofilm was cultivated in the soil. (LF well data is shown with square markers, HF well data with triangle markers). The first measurements were performed on Day -1 after bleaching and flushing both wells. Inoculation occurred on Day 1. Substrate was injected daily Days 2-10. Days 11-14, the bacteria were starved. On Day 14, T_2 relaxation was measured, then the wells were flushed with high flows of groundwater from the test cell and T_2 was measured again. Then a bleach solution was injected to oxidize remaining organics. Day 15 data was collected after flushing the bleach solution from the wells.

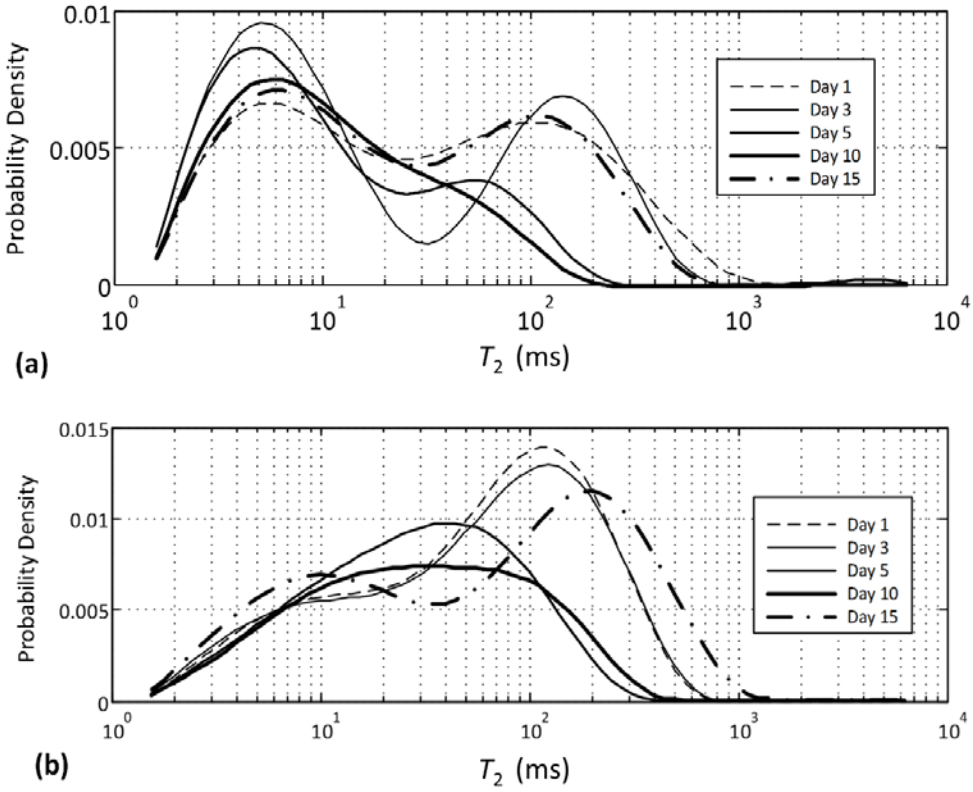

Figure 6.3. T_2 distribution for LF well (a) and HF well (b). The curves show the transition over time of the distribution of T_2 relaxation times in each well, beginning at inoculation (short dash line). As biofilm grew in the NMR probe's sensitive region, the T_2 relaxation times shifted to a single peak distribution centered about a shorter mean log T_2 time (solid lines). After flushing and bleaching each well, the T_2 relaxation distributions closely resembled the initial distributions (dash-dot lines).

In the Day 1 data, the relaxation time distribution is bimodal. Given that there was only one fluid type at this time, the relaxation distribution peaks represent the relative pore size distribution. Water in the smaller pores relaxes more quickly due to the higher S/V ratio and the more frequent interactions of the diffusing fluid molecules with the grain surfaces [26]. Water in the larger pores experiences fewer interactions on the measurement timescale and yields slower signal decay.

As bacteria grow in the soil pores, the creation of gel phase EPS and the resulting exchange of hydrogen in the polymerized structure produces a secondary relaxation mechanism [21]. We attribute the collapsing the bimodal distribution to this mechanism, where the otherwise long relaxation time components shift to shorter relaxation times. In both wells, T_2 distributions measured Day 6-12 show a single peak, on the order of 10^1 ms. The transition to shorter relaxation times is an indication of biofilm accumulation [19, 27, 28]. Data collected on Day 15 after flushing and bleaching each well shows a return to the bimodal T_2 distribution that typified the system prior to biofilm growth.

On Day 12, following two days of biofilm starvation, the two probes were raised from the well bottom to record T_2 relaxation over 3.0-3.5 m of saturated well depth in 0.5 m increments. In the HF well data set (Figure 6.2, triangles), the two data points collected on Day 12 show the difference in the measurements due to raising and replacing the probe in its original position. In the LF well dataset, the Day 12 data point (Figure 6.2, squares) was measured prior to raising the probe. The measurement made after re-positioning the probe at the bottom of the LF well was made on Day 14. For both data sets, the open marker represents the data collected after the probe was repositioned at the bottom of the well. The variance exists both because of inherent noise in the data and because the probe was likely exciting a slightly different shell within the soil where heterogeneities exist in both the soil and biofilm. The difference is 17% and 14%, respectively, in the LF and HF wells and is significantly less than the change in signal response measured during the biofilm growth phase. The lower-value data points collected on Day 14 show that the biofilm surrounding both wells remained intact and

relatively robust despite four days of starvation, compared to earlier measurements during the biofilm growth phase. This is consistent with the durability of the biobarrier originally constructed in the test cell where measured conductivity remained 2 orders of magnitude lower than the initial conductivity after approximately 6 months of starvation[7].

The higher-value data points from each well on Day 14 were measured after a high-flow flush with groundwater from the test cell. The final data point, on Day 15, was collected after the wells were each treated with the same sodium dichlor solution used in the site preparation step to oxidize organics (Supporting Information). It was expected that the high shear stress and bleach solution in the soil pores would detach and remove most of the biofilm previously formed, causing the T_2 distribution to return to longer relaxation times.

When the test cell was constructed, coarser soil from an off-site location was used in the region where the HF well was located. The finer textured soil surrounding LF well was excavated on-site, sieved, and replaced. This variation in the soil texture between the two wells explains the differing magnitudes of the two relaxation peaks seen in the Day 1 and 15 data (Figure 6.3 (a) and (b)), with relatively more of the pore space around the HF well composed of larger pores and a more even distribution of pores sizes near the LF well. It is likely that the soil mineralogy also differs between the two wells, though examination of such parameters was beyond the scope of this experiment.

More signal was recovered following removal in the HF well than in the LF well, likely due to the coarser soil and larger pores in the vicinity of the HF well. These larger

pores would allow for bleach solution and detached EPS to be transported more easily through the excitation shell. In the soil around the LF well, bleach solution penetration may have occurred along preferential flow paths and biofilm sloughed from one pore may have been trapped in another smaller pore where it may have still contributed to the measured signal. Furthermore, the initial bleach injection was performed prior to installing the NMR probes, so the bleach was free to migrate up the casing and may not have penetrated the target area at design strength. The final bleach injection, which occurred with the probes in place and below the diversion disks, would have more effectively isolated the biofilm growth area. Some soil pores may have experienced the second bleach pulse but not the first. The measurements collected Days 14 and 15 confirm that the mechanism responsible for the change in T_2 relaxation could be reversed with flushing and bleaching the wells and is consistent with biofilm growth.

T_2 measurements were recorded with respect to depth in each well prior to inoculation and again on Day 12 (Figure 6.4). These well logs show notable differences. In both well logs, there was a change in T_2 distribution over the entire measured depth after 10 days of substrate injection at the bottom of the well where the NMR logging tool was deployed. On Day -1, the two well logs show broad T_2 distributions marked by two peaks at most depth levels. After the biofilm growth phase, the Day 12 data show a single peak distribution of T_2 relaxation times centered about a shorter mean relaxation time.

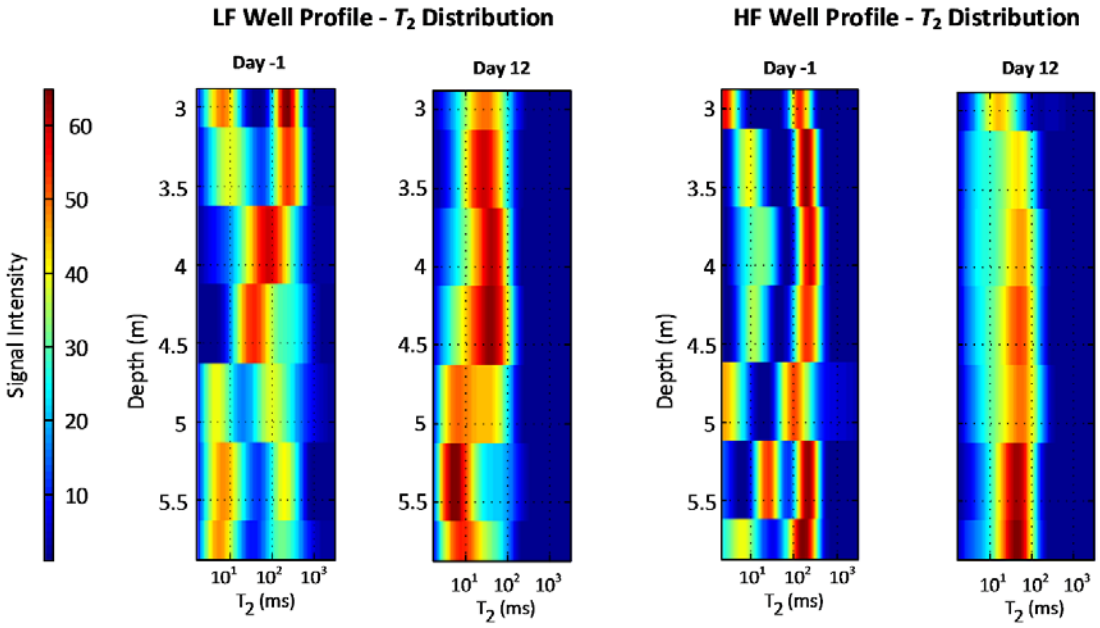

Figure 6.4. LF and HF well profiles measured Day -1 (pre-inoculation) and Day 12 of the biofilm growth phase. T_2 distribution as a function of depth shifted to faster decay times over the entire measured depth of each well when biofilm was cultivated at the well bottom.

The observed changes in the well log are consistent with biofilm cultivation at the well bottom. The changes in the distributions are most pronounced at the bottom of the well, where the substrate was injected. The diversion disk attached to the top of each probe was located approximately in the middle of the distributions shown, meaning that substrate was directly accessible to the bottom half of each well log. As biofilm accumulated in the soil pores, the substrate would have encountered increased resistance to flow through the soil [10] and the gap between the casing and the diversion disk (~1mm) would have become a preferential flow pathway. Substrate would diffuse into the soil above the probe, in addition to the substrate diffusing through the soil itself. Again the difference between the LF and HF well is instructive, as the upper levels of the

HF well show less intensity of effect than the upper levels of the LF well. The HF well is surrounded by coarser soil, making it more difficult for the biofilm to clog the soil pores. Conversely, the LF well region had smaller soil pores initially and experienced more abundant biofilm accumulation as shown by the larger reduction in mean log T_2 relaxation times.

Microbiological Data and Water Chemical Analysis

Heterotrophic plate counts (HPC) in both wells were approximately $1x10^3$ colony-forming units (cfu)/mL after bleaching and prior to inoculation, representing the culturable 'native' heterotrophic population of the test cell (Figure 5(a)). After inoculation and substrate injection, the HPC increased in both wells to approximately $1x10^5$ cfu/mL by Day 4. Prior to inoculation and following the injection of the sodium dichlor solution 2-3 days previously, pH measurements were approximately pH 8 (Figure 6.5 (b)). The pH in both wells was stable through Day 3 following inoculation. On Day 4, the pH measurements diverged with the HF well pH increasing to pH 9, while the LF well pH decreased to approximately pH 7. Also on Day 4, the NMR signal in both wells changed significantly, dropping to near the minimum for mean log T_2 relaxation time in the LF well where the effect was more pronounced (Figure 6.3). Taken together, the higher HPC values, optimum pH conditions, and faster NMR signal decay indicate that a measureable accumulation of biofilm had grown within the pore spaces of the logging tool's sensitive zone by Day 4 of the experiment. Since the HPC reflect bacterial cells which are necessarily *not* attached in biofilms, the NMR logging tool indicates itself as a

valuable addition to the bioremediation toolbox through its sensitivity to the biofilm EPS, which is not measurable with plate counts.

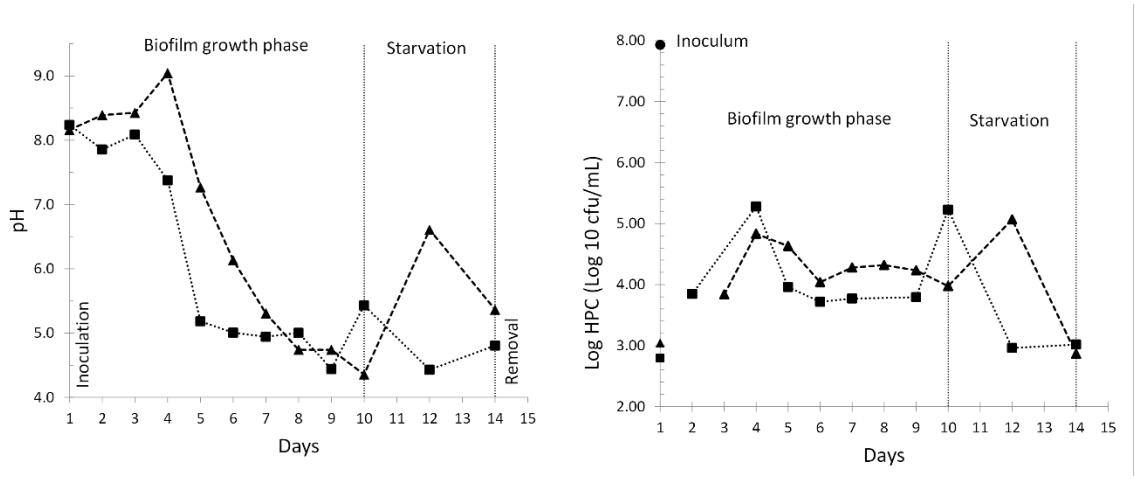

Figure 6.5. Heterotrophic Plate Counts (HPC) (a) and pH data (b). Both HPC and pH measurements decreased on Day 5 in the two wells compared to earlier values, with increased variability in the measurements noted during the starvation phase when no substrate was injected (LF well data is shown with square markers, HF well data with triangle markers). This water chemical variability was not reflected in the NMR signal response which remained consistent over the same period.

Water samples from days 5-10 of the experiment show a decrease in HPC to approximately $1x10^4$ cfu/mL and a decrease in pH to approximately 4.5-5 in both wells. Lower pH promotes bacterial attachment to surfaces [29], while not significantly adversely affecting the biofilm matrix over the relatively short time frame measured [30]. This increased adhesion of bacteria may have reduced the number of suspended cells within the bulk fluid for capture during sampling or caused preferential sampling of the well casing fluid, rather than pore water, due to biofilm clogging the soil pores. It is also possible that the acidic conditions selected for other native bacterial strains that are not

culturable on agar plates, like autolithotrophs participating in oxidation and reduction of chemical species in the soil and water.

To explore potential causes for the observed drop in pH during testing, benchtop tests were performed using isolates of the two most populous cell morphologies from the agar plates for Days 5-10. These bacteria were cultivated in 100 mL of molasses substrate in Erlenmeyer flasks. The pH of the broth decreased by more than an order of magnitude, from pH 6.2 on average to pH 5.0 on average by Day 4 of the 8-day benchtop experiment. These results are consistent with results from the field study and indicate that metabolic processes, including production of nucleic acids and CO_2, contributed to the observed decrease in pH observed in the field study.

Another possible explanation of the observed pH change is related to the redox chemistry of sulfur and iron cycling [31, 32]. The groundwater in the lined test cell was static for more than 10 years before the current field study was initiated, creating reducing conditions at the bottom of the test cell. The distinctive odor of hydrogen sulfide (H_2S) was readily perceptible in the water pumped from the cell. When exposed to the atmosphere, the reduced Fe(II) in the groundwater oxidized to form a rust-like layer of Fe(III) compounds, likely ferrihydrite, in the large-capacity water storage tanks. The injection of the sodium dichlor solution followed by substrate containing organic carbon, nitrate, and dissolved oxygen would have promoted the oxidation of reduced species in the subsurface. Heterotrophic bacteria, like *Pseudomonas fluorescens*, use the electron acceptors oxygen and nitrate to oxidize the organic carbon in the media, producing new cells, EPS, and waste products. Oxidation of sulfide leads to

acidification, as in the case of acid mine drainage [33], and may account for some of the observed decrease in pH after the initial biofilm growth between Days 1-4.

Laboratory studies have shown that NMR relaxation measurements are sensitive to changing soil redox conditions [34] as well as the mineralogic form of iron species [35, 36]. To conclude that the observed changes in relaxation response are due to biofilm growth, it is important, therefore, to consider the possible impact of geochemical changes. First, the timing of the changes is indicative of biofilm growth. Were oxidation-driven geochemical changes strongly influencing T_2 during the approximately two days between the initial bleach and inoculation, we would expect to see significant changes in the T_2 relaxation behavior of the two well systems Days -1 and 0. Instead we see relatively small changes—first a slight decrease in T_2 which may, in fact, be due to abiotic Fe(III) precipitation, then an increase during inoculum injection (Figure 6.2). The increase is most likely due to the make-up of the inoculum broth which was made with DI water rather than water from the test cell. The tight temporal relationship at the end of the experiment between the final flush and bleach and the observed recovery of long T_2 times provides further strong evidence that the oxidizing conditions themselves do not drive the shortening of the T_2 response.

A second reason we expect limited influence from mineralogical transformations pertains to competition for the electron acceptors in the subsurface. The 4 log reduction between the inoculum colony count and the Day 2 HPC (Figure 6.5a) indicates approximately 10^4 colony forming units (cfu)/mL attached to soil surfaces in the well-bore, creating strong competition for oxygen and nitrate. Oxidation of the H_2S would

have been more thermodynamically favorable compared to oxidation of iron compounds and would have occurred preferentially [37] where the electron acceptors available exceeded bacterial demand. We therefore expect the contribution of iron precipitation to be moderated and would not expect the iron-driven T_2 changes to be any larger than was observed in the small decrease between Days -1 and 0 before competing heterotrophic bacteria were present in the system.

Finally, we have also considered the magnitude of the observed T_2 shortening to assess whether biofilm growth or moderate changes in iron geochemistry are more likely mechanisms. The T_2 shortening observed during the experiment generally shows long components, $T_2 > >100$ms, transitioning to shorter relaxation time components, $T_2 << 100$ms. Thus, the dominant relaxation mechanism(s) must be ones that can result in T_2 relaxation times much shorter than 100ms.

With the exception of magnetite and hematite, the literature reports elevated, but moderate surface relaxivity for most Fe(III) minerals at a measurement frequency of 2 MHz [35]. Large reductions in relaxation times resulting from the change of Fe(II) to Fe(III) have been shown at 90 MHz [34], but this measurement frequency is more than 100 times higher than the current downhole measurements. Relaxation times exhibit significant and complex frequency dependence over this wide range. Generally, the geochemical changes are expected to show a reduced influence on T_2 at lower field strengths [38] since the amplitude of internal gradients associated with diffusion relaxation are reduced at lower field.

With evidence suggesting moderate ferrihydrite formation is unlikely to cause the absolute T_2 shortening we observe, we consider evidence of T_2 shortening due to the mechanism of biofilm polymerization. Laboratory measurements at 275 kHz by Sanderlin et al. (2012) showed growth of biofilm and polymer gels resulted in T_2 values as short as 50ms [21]. Furthermore, in previous laboratory work using the same LF probe [20], moderate biofilm growth in 1mm quartz sand resulted in a decrease in the mean log T_2 of 45% which is similar in magnitude to the changes observed in this study.

Geochemical changes in the pore fluid would have occurred slowly over the two week period, and the drop in T_2 would be expected to be considerably less than was observed. Given the timing and magnitude of the T_2 changes, and the evidence from previous lab work that biofilm has a large influence on NMR relaxation measurements, the experimental results provide compelling evidence that the low field NMR logging tools can detect and monitor biofilm growth in the subsurface. How biofilms interact with the geochemical environment will vary from field site to field site, as well as over space and time. Future experiments and implementation of these methods, therefore, should include an informed monitoring of the chemistry of extracted pore fluid and the changing NMR relaxation.

We have shown the NMR logging tools detected significant and sustained change in signal response during the biofilm growth phase, measured by changing T_2 relaxation distributions. Both the HF and LF probes were sensitive to the changes, and the differences in soil geology between the probe locations likely resulted in larger differences in the signal response than the variation between the two probes. Mean log T_2

relaxation times decreased from 29 ms to an average of 11 ms in the LF well, and from 50 ms to an average of 28 ms in the HF well while biofilm was cultivated in the surrounding soil. We have further shown that high shear flow and oxidative stress resulting from the bleach solution, applied with the intent to denature and remove biofilm from the tool's sensitive zone, produced a return of signal response similar to initial conditions. The timescale of these changes is consistent with biofilm formation and subsequent removal. These results provide an important demonstration of the advantages of incorporating an NMR measurement into future bioremediation toolkits. NMR T_2 relaxation measurements provide unique complementary data that, together with other monitoring techniques such as hydrological conductivity measurements, can improve our ability to draw the correct conclusion about the subsurface environment with regard to biofilm growth.

Supporting Information

Site Preparation

A bleach solution consisting of 2 lb (907 g) sodium dichloro-s-triazinetrione dihydrate (C3H4Cl2N3NaO5) (Spa Guard Chlorinating Concentrate, Bio-Lab Inc., Lawrenceville, GA) was pumped into each well to oxidize any pre-existing biofilm. The solution was mixed in a 55 gal (208 L) drum using enough water to dissolve the granules, approximately 20-30 gallons (75-115 L). The solution was pumped to the target region through a standard garden hose using a 1/3 hp centrifugal pump (AMT Pump Model 3680-975-97 by Gorman Rupp, Royersford, PA) operating at approximately 12 gpm

(45.5 L/min). The bleach solution was allowed to react in the wells overnight, and was followed by a 30 min high-flow (12 gpm (45.5 L/min)) flush of groundwater from the test cell to detach EPS and dead cells and purge any remaining bleach solution. Then, the probes were lowered to the bottom of the wells, approximately 18 ft (5.5 m) deep and 15 ft (4.5 m) below the water table in the test cell.

Bacterial Culture

The target organism, *Pseudomonas fluorescens* CPC211A, is the environmental isolate used in the original experiments in the test cell and, therefore, was known to grow successfully in that environment.[7] The bacteria was cultured from cryo-stock using a nutrient broth consisting of 10 g/L molasses (Aunt Patty's Blackstrap Molasses, Eugene, OR), 3 g/L sodium nitrate (SQM industrial grade prills, 98%, SQM North America, Atlanta, GA), 1 g/L yeast extract (Acros Organics, Geel, Belgium), 0.12 g/L potassium phosphate dibasic, and 0.04 g/L potassium phosphate monobasic (Thermo-Fisher Scientific, Waltham, MA). The inoculum was cultured in successively larger volumes at ambient temperature without mixing over seven days to produce a final inoculum volume of 60 L with a viable cell count of 8.5×10^7 colony forming units (cfu)/mL.

The active biofilm growth region of the well-bore environment was designed to be approximately 18 gal (67 L) of pore space, corresponding to the height of the NMR logging device (4.5 ft), a 9 in (22.9 cm) radius and an estimated porosity of 0.3 [7]. This active region of soil in each well was conditioned with 15 gal (56.7 L) of substrate prior to injection of the inoculum broth. The substrate was pumped at a rate of 1.2 L/min with a peristaltic pump (Masterflex L/S Model 900-1255, Cole-Parmer, Vernon Hills, IL)

down each well casing to the sensitive zone of the NMR probe using four lines of 1/8-inch (3.2mm) ID vinyl tubing (Clearflex, McMaster-Carr, Santa Fe Springs, CA). Then 30 L (7.9 gal) of inoculum was injected into each well, followed by 5 gal (18.9L) of fresh substrate to push the bacteria into the soil from the well casing. Finally, water from the test cell was injected for approximately 1-2 minutes to rinse the injection tubing. No attempt was made to maintain a monoculture.

During the biofilm growth phase of the experiment, Days 1-10, the molasses substrate was prepared just prior to use in 50-55 gal plastic drums using groundwater from the lined test cell. Groundwater was pumped from another of the test cell's eleven 4 inch (10.2 cm) wells located 36 ft (11 m) from the nearest experimental well and stored prior to use in a large capacity water storage tank (Ace Roto-Mold, Den Hartog Industries, Hospers, IA). Each well received approximately 100-110 gal (379-416 L) per day of substrate over a 5-6 hour period. This translates to a Darcy velocity at the logging tool's excitation shell of approximately 4.2 cm/hr and an interstitial velocity of 14.4 cm/hr in the LF well during substrate injection, and 7.2 cm/hr and 23.4 cm/hr, respectively, in the HF well. NMR measurements were collected during the pumping of substrate. There was no pumping or flow in the wells for the remainder of each day following substrate injection. Continuous flow of substrate was not feasible given experimental constraints.

NMR Measurements

T_2 relaxation measurements were conducted using a Carr-Purcell-Meiboom-Gill (CPMG) pulse sequence [24, 25], consisting of a 90° excitation pulse followed by a series of 180° refocusing pulses separated by the echo spacing, t_E. Frequencies and echo spacings for each probe were fixed. The repetition time, T_r, which is the time between 90° rf excitation pulses, was either 1500 ms or 5000 ms for each measurement (Table 6.2). Faster repetition of the excitation pulse, with a T_r of 1500 ms, allowed for the rapid collection of data from the fastest decaying components of the NMR signal; recording 600 averages improved resolution of the early part of the decay curve [14]. A longer repetition time of 5000 ms, recorded with 150 averages, allowed signal to be collected from the slower decaying components, such as water in larger pores.

Microbiological and Water Chemical Analysis

Two 10-15 mL samples of water were collected daily in sterile 15 mL Falcon tubes (Becton, Dickinson and Co., Sparks, MD) from each well prior to injection of fresh substrate. Flow on the substrate injection pumps was reversed and allowed to flow for 2-3 minutes in order to collect a water sample from each well's biofilm growth region. The samples were placed on ice in the field and then frozen for later analysis at the conclusion of the field test. The samples were analyzed for pH (VWR sympHony benchtop SB70P pH meter) and by drop plate for heterotrophic plate count (HPC) [23].

Samples were drop plated on Difco tryptic soy agar (Becton, Dickinson and Co., Sparks, MD) plates in duplicate and cultured at room temperature on the benchtop and in anaerobic pouches (BD GasPak EZPouch, Becton, Dickinson and Co., Sparks, MD). The

aerobically grown plates produced higher and more consistent numbers of culturable heterotrophic cells.

Results and Discussion

Another measure of signal attenuation is given by the Square of Echoes (SOE) method which is used to improve the low signal to noise ratio that is typical for a low-field NMR device in natural geologic material. The SOE is the squared value of the mean echo in the signal decay curve. A reduction in the SOE value over the course of the experiment qualitatively indicates that the log mean value of T2 relaxation is also decreasing. When normalized with respect to water content squared, data from the field test shows an SOE decrease of 91% in the LF well and 70% in the HF well during the biofilm growth phase of the experiment. The percent reduction is calculated using the SOE at inoculation (Day 1) and the average of SOE values Day 5-12 when the values were stable (Figure 6.6).

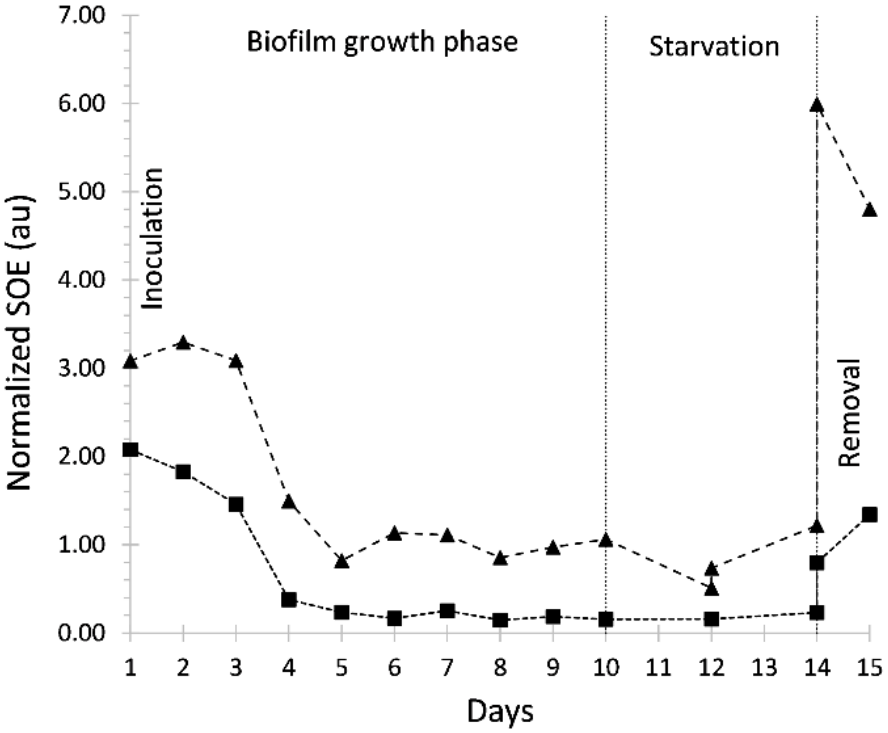

Figure 6.6. Square of Echoes (SOE) data from the HF (triangles) and LF (squares) wells shows a decrease of 70% and 90% respectively.

References

1. LaGrega, M.D., P.L. Buckingham, and J.C. Evans, *Hazardous Waste Management*. 2nd ed. 2001, New York: McGraw-Hill.

2. Kao, C.M., et al., *Biobarrier system for remediation of TCE-contaminated aquifers.* Bulletin of Environmental Contamination and Toxicology, 2004. **72**(1): p. 87-93.

3. Kao, C.M., et al., *Enhanced PCE dechlorination by biobarrier systems under different redox conditions.* Water Research, 2003. **37**(20): p. 4885-4894.

4. Kim, G., S. Lee, and Y. Kim, *Subsurface biobarrier formation by microorganism injection for contaminant plume control.* Journal of Bioscience and Bioengineering, 2006. **101**(2): p. 142-148.

5. Pal, A. and A.K. Paul, *Microbial extracellular polymeric substances: central elements in heavy metal bioremediation.* Indian Journal of Microbiology, 2008. **48**(1): p. 49-64.

6. Taylor, S.W. and P.R. Jaffe, *Enhanced in-situ biodegradation and aquifer permeability reduction.* Journal of Environmental Engineering-ASCE, 1991. **117**(1): p. 25-46.

7. Cunningham, A.B., et al., *Subsurface biofilm barriers for the containment and remediation of contaminated groundwater.* Bioremediation Journal, 2003. **7**(3-4): p. 151-164.

8. Careghini, A., S. Saponaro, and E. Sezenna, *Biobarriers for groundwater treatment: a review.* Water Science and Technology, 2013. **67**(3): p. 453-468.

9. Callaghan, P.T., *Translational Dynamics & Magnetic Resonance: Principles of Pulsed Gradient Spin Echo NMR.* 2011, New York: Oxford University Press.

10. Cunningham, A.B., et al., *Influence of biofilm accumulation on porous-media hydrodynamics.* Environmental Science & Technology, 1991. **25**(7): p. 1305-1311.

11. Taylor, S.W. and P.R. Jaffe, *Biofilm growth and the related changes in the physical properties of a porous medium. 1. Experimental investigation.* Water Resources Research, 1990. **26**(9): p. 2153-2159.

12. Vandevivere, P. and P. Baveye, *Effect of bacterial extracellular polymers on the saturated hydraulic conductivity of sand columns.* Applied and Environmental Microbiology, 1992. **58**(5): p. 1690-1698.

13. Johns, M., et al., *Mobile NMR and MRI: Developments and Applications*. New Developments in NMR. 2015: Royal Society of Chemistry.

14. Walsh, D., et al., *A small-diameter NMR logging tool for groundwater investigations.* Groundwater, 2013. **51**(6): p. 914-926.

15. Kleinberg, R.L., Kenyon, W.E., Mitra, P.P., *Mechanism of NMR relaxation of fluids in rock.* Journal of Magnetic Resonance Series A, 1994. **108**: p. 206-214.

16. Kleinberg, R.L. and M.A. Horsfield, *Transverse relaxation processes in porous sedimentary rock.* Journal of Magnetic Resonance, 1990. **88**(1): p. 9-19.

17. Timur, A., *Pulsed nuclear magnetic resonance studies of porosity, movable fluid, and permeability of sandstones.* Journal of Petroleum Technology, 1969. **21**(JUN): p. 775-&.

18. Godefroy, S., et al., *Surface nuclear magnetic relaxation and dynamics of water and oil in macroporous media.* Physical Review E, 2001. **64**(2): p. 021605-1 - 021605-13.

19. Codd, S.L., et al., *NMR relaxation measurements of biofouling in model and geological porous media.* Organic Geochemistry, 2011. **42**(8): p. 965-971.

20. Kirkland, C.M., et al., *Biofilm Detection in a Model Well-Bore Environment Using Low-Field NMR.* Groundwater Monitoring and Remediation, 2015: p. DOI:10.1111/gwmr.12117.

21. Sanderlin, A.B., et al., *Biofilm detection in natural unconsolidated porous media using a low-field magnetic resonance system.* Environmental Science & Technology, 2013. **47**(2): p. 987-992.

22. Vogt, S.J., et al., *Permeability of a growing biofilm in a porous media fluid flow analyzed by magnetic resonance displacement-relaxation correlations.* Biotechnology and Bioengineering, 2013. **110**(5): p. 1366-1375.

23. Herigstad, B., M. Hamilton, and J. Heersink, *How to optimize the drop plate method for enumerating bacteria.* Journal of Microbiological Methods, 2001. **44**(2): p. 121-129.

24. Carr, H.Y. and E.M. Purcell, *Effects of diffusion on free precession in nuclear magnetic resonance experiments.* Physical Review, 1954. **94**(3): p. 630-638.

25. Meiboom, S. and D. Gill, *Modified spin-echo method for measuring nuclear relaxation times* Review of Scientific Instruments, 1958. **29**(8): p. 688-691.

26. Korb, J.P., S. Godefroy, and M. Fleury, *Surface nuclear magnetic relaxation and dynamics of water and oil in granular packings and rocks.* Magnetic Resonance Imaging, 2003. **21**(3-4): p. 193-199.

27. Bayer, J.V., F. Jaeger, and G.E. Schaumann, *Proton Nuclear Magnetic Resonance (NMR) Relaxometry in Soil Science Applications.* Open Magnetic Resonance Journal, 2010. **3**: p. 15-26.

28. Jaeger, F., E. Grohmann, and G.E. Schaumann, *1H NMR relaxometry in natural humous soil samples: insights in microbial effects on relaxation time distributions.* Plant and Soil, 2006. **280**(1-2): p. 209-222.

29. Kristian Stevik, T., et al., *Retention and removal of pathogenic bacteria in wastewater percolating through porous media: a review.* Water Research, 2004. **38**(6): p. 1355-1367.

30. Chen, M.J., Z. Zhang, and T.R. Bott, *Effects of operating conditions on the adhesive strength of Pseudomonas fluorescens biofilms in tubes.* Colloids and Surfaces B: Biointerfaces, 2005. **43**(2): p. 61-71.

31. Juncher Jørgensen, C., et al., *Microbial Oxidation of Pyrite Coupled to Nitrate Reduction in Anoxic Groundwater Sediment.* Environmental Science & Technology, 2009. **43**(13): p. 4851-4857.

32. Melton, E.D., et al., *The interplay of microbially mediated and abiotic reactions in the biogeochemical Fe cycle.* Nat Rev Micro, 2014. **12**(12): p. 797-808.

33. Evangelou, V.P. and Y.L. Zhang, *A review: Pyrite oxidation mechanisms and acid mine drainage prevention.* Critical Reviews in Environmental Science and Technology, 1995. **25**(2): p. 141-199.

34. Bryar, T.R. and R.J. Knight, *Sensitivity of nuclear magnetic resonance relaxation measurements to changing soil redox conditions.* Geophysical Research Letters, 2002. **29**(24).

35. Keating, K. and R. Knight, *A laboratory study to determine the effect of iron oxides on proton NMR measurements.* Geophysics, 2007. **72**(1): p. E27-E32.

36. Keating, K. and R. Knight, *A laboratory study of the effect of Fe(II)-bearing minerals on nuclear magnetic resonance (NMR) relaxation measurements.* Geophysics, 2010. **75**(3): p. F71-F82.

37. Benjamin, M.M., *Water Chemistry*. Series in Water Resources and Environmental Engineering. 2002, New York, NY: McGraw-Hill.

38. Koenig, S.H. and K.E. Kellar, *Theory of 1/T-1 and 1/T-2 NMRD profiles of solutions of magnetic nanoparticles* Magnetic Resonance in Medicine, 1995. **34**(2): p. 227-233.

CHAPTER SEVEN

DETECTING MICROBIALLY-INDUCED CALCITE PRECIPITATION (MICP) IN A MODEL WELL-BORE USING DOWNHOLE LOW-FIELD NMR

Contribution of Authors and Co-Authors

Manuscript in Chapter 7

Author: Catherine M. Kirkland

Contributions: Helped conceive and implement study design. Collected and analyzed data. Wrote manuscript.

Co-Author: Sam Zanetti

Contributions: Helped implement study design. Collected and analyzed data.

Co-Author: Elliot Grunewald

Contributions: Helped conceive and implement study design. Provided supervision and oversight on data collection and analysis. Provided feedback and comments on the manuscript.

Co-Author: David O. Walsh

Contributions: Provided feedback and comments on the manuscript.

Co-Author: Sarah L. Codd

Contributions: Helped conceive and implement study design. Provided feedback and comments on the manuscript.

Co-Author: Adrienne J. Phillips

Contributions: Helped conceive and implement study design. Provided feedback and comments on the manuscript.

Manuscript Information Page

Catherine M. Kirkland, Sam Zanetti, Elliot Grunewald, David O. Walsh, Sarah L. Codd, Adrienne J. Phillips

Environmental Science and Technology

Status of Manuscript:
____ Prepared for submission to a peer-reviewed journal
____ Officially submitted to a peer-review journal
____ Accepted by a peer-reviewed journal
_X___ Published in a peer-reviewed journal

American Chemical Society
Vol. 51, No. 3, Pages 1537-1543, February 2017

DETECTING MICROBIALLY-INDUCED CALCITE PRECIPITATION (MICP) IN A MODEL WELL-BORE USING DOWNHOLE LOW-FIELD NMR

Abstract

Microbially-induced calcite precipitation (MICP) has been widely researched recently due to its relevance for subsurface engineering applications including sealing leakage pathways and permeability modification. These applications of MICP are inherently difficult to monitor non-destructively in time and space. Nuclear magnetic resonance (NMR) can characterize the pore size distributions, porosity, and permeability of subsurface formations. This investigation used a low-field NMR well-logging probe to monitor MICP in a sand-filled bioreactor, measuring NMR signal amplitude and T_2 relaxation over an 8-day experimental period. Following inoculation with the ureolytic bacteria, *Sporosarcina pasteurii*, and pulsed injections of urea and calcium substrate, the NMR measured water content in the reactor decreased to 76% of its initial value. T_2 relaxation distributions bifurcated from a single mode centered about approximately 650 ms into a fast decaying population (T_2 less than 10 ms) and a larger population with T_2 greater than 1000 ms. The combination of changes in pore volume and surface minerology accounts for the changes in the T_2 distributions. Destructive sampling confirmed final porosity was approximately 88% of the original value. These results indicate the low-field NMR well-logging probe is sensitive to the physical and chemical changes caused by MICP in a laboratory bioreactor.

Introduction

Biofilms form when bacteria secrete a matrix of extracellular polymeric substance (EPS), attaching themselves to solid surfaces in colonies akin to multicellular organisms and buffering their micro-scale environment[1]. Bacterial biofilms are known to induce metal corrosion [2], cause persistent infections [3], treat wastewater [4], or remediate contaminated groundwater [5]. When composed of ureolytic microbes, biofilms can also induce calcite precipitation [6], a process referred to as biomineralization or microbially-induced calcite precipitation (MICP). Many strains of bacteria found naturally in soil and groundwater are ureolytic, meaning they can hydrolyze urea for energy and a source of nitrogen [7]. Catalyzed by the microbially produced urease enzyme, water cleaves urea to form ammonia and carbon dioxide which, due to a pH increase, shifts the carbonate equilibrium toward bicarbonate and carbonate. Then, with sufficient calcium and carbonate activity, calcium carbonate ($CaCO_3$ or calcite) precipitates (Eqn. 7.1).

$$(NH_2)_2CO + 2H_2O + Ca^{2+} \Rightarrow 2NH_4^+ + CaCO_3(s) \qquad (7.1)$$

Sporosarcina pasteurii, the ureolytic bacteria used in this experiment, forms a thin biofilm in porous media [8] where the EPS matrix, a 3-dimensional diffusion-limited hydrogel, can either facilitate or inhibit MICP over microscales. The organic molecules comprising the EPS matrix restrict mass transfer, creating localized chemical gradients within the hydrogel structure [6]. Ca^{2+} ions are not used in metabolic processes and accumulate near cell surfaces where ureolysis produces an alkaline environment. Thus, the microbial biofilm matrix provides nucleation sites for calcite precipitation [9]. In

porous media, the precipitated calcite binds together media grains and fills pore spaces [10].

MICP has engineering applications [11] that include soil stabilization [10, 12] and subsurface barriers [13], sealing of cap rocks and well-bore regions for carbon dioxide sequestration [14-16], and limestone and concrete remediation [9]. Many of these beneficial applications of MICP occur in the subsurface, raising the question of how the process can best be monitored spatio-temporally. Nuclear magnetic resonance (NMR) is commonly used non-destructively and non-invasively to characterize the pore size distributions, porosity, and permeability of subsurface geologic formations [17]. These are the same physical properties affected by MICP, indicating that NMR well-logging tools may have potential for monitoring subsurface engineering applications of MICP. This study used a low-field NMR well-logging tool designed for subsurface hydrogeologic investigations [18] to detect changes in NMR signal response indicative of MICP in the pore spaces of sand-filled radial-flow bioreactor.

Background

There are limited examples in the scientific literature where NMR methods have been applied to the study of biomineralization in porous media relevant for engineering applications [8, 19]. These previous studies have used high field strength magnetic resonance imaging (MRI) along with other NMR methods to probe hydrodynamic properties of biomineralization in model porous media systems.

Fridjonsson *et al*. [8] used high-field NMR to measure changes in hydrodynamic dispersion resulting from MICP in model porous media to compare flow dynamics

between systems influenced by either solid precipitates or a biofilm matrix. The authors used a combination of NMR displacement measurements, relaxation mapping, MRI, and microscopy methods.

Sham *et al.* [19] used MRI and NMR flow measurements on both a model bead pack and a Bentheimer sandstone rock core to examine structure and transport properties of each system following MICP. The authors report a reduction of 3.7% in absolute porosity in the bead pack, which correlated to a 98% reduction in permeability. In the sandstone, a 7.2% reduction in absolute porosity yielded a 96.5% reduction in permeability. In both systems, preferential fouling of the inlet region of the column was observed.

The low-field NMR well-logging tool used in this study (Javelin JP350, Vista Clara, Inc., Mukilteo, WA) is sensitive to biofilm growth in the pore spaces of a sand-filled bioreactor [20] and in the subsurface soil of an engineered field testing site [21]. In both of these studies, biofilm growth caused enhanced relaxation with T_2 relaxation times decreasing by approximately 40 – 60%.

These previous studies show 1) NMR methods are useful for analyzing changes resulting from MICP in porous media and 2) the well-logging tool is sensitive to small changes over time in the micro-scale pore environment. To our knowledge, field scale low-field NMR instruments have not been applied to the measurement or monitoring of MICP. In the current study, $CaCO_3$ precipitation was expected to change the NMR signal response by reducing the liquid fraction from which the signal is obtained, causing a decrease in signal amplitude over time as the pores accumulate calcite. MICP will also

change the pore sizes and mineral surface of the porous media, thereby influencing the signal relaxation response. A correlation between the signal response and reduction of porosity due to MICP may indicate the use of a NMR well-logging tool as a sensor for biomineralization in field applications where optical or destructive monitoring methods are not possible. This study represents a first step toward that end by demonstrating that a NMR well-logging tool is sensitive to MICP.

NMR Theory

The NMR well-logging tool is sensitive to the hydrogen protons in water, called 'spins,' such that the behavior of the NMR signal over time is related to the various micro-scale water environments in the surrounding formation. The tool measures 1.37 m long and 8.9 cm in diameter and is designed to be lowered into small-diameter cased or uncased borehole wells (Figure 7.1) [18]. The dual frequency probe used in this experiment operates at approximately 250 and 300 kHz, and is composed of an array of permanent magnets and radio-frequency (RF) induction coils [18]. The permanent magnets establish a static magnetic field, B_0, along the direction of the borehole, where the field strength depends on the radial distance from the tool. The RF pulses produce two mm-scale cylindrical excitation shells at radial distances of 17-19 cm from the probe center and in the middle of the reactor's sand annulus. The excited shells are 50 cm in height. Only spins in these two excitation shells contribute to the measured NMR signal response, which is averaged over all the spins in each shell.

The initial amplitude of the NMR signal is proportional to the amount of water in the excitation shell and reflects the volumetric water content, or porosity, of the porous

media. The NMR signal amplitude decreases when water is displaced by mineral formation in the pores.

The observed decay rate reflects spin-spin, or T_2, relaxation, which occurs as protons interact with each other in the transverse plane. These interactions cause a dephasing of spin coherence and signal attenuation. In geologic materials, the observed T_2 relaxation rate comprises the bulk relaxation rate of the pore fluid, $\frac{1}{T_{2B}}$, the surface relaxation rate, $\frac{1}{T_{2S}}$, related to interactions between the fluid and the pore walls, and the diffusion relaxation rate, $\frac{1}{T_{2D}}$, related to diffusion of fluids within pores due to inhomogeneities in the local magnetic field (Equation 7.2) [22, 23].

$$\frac{1}{T_2} = \frac{1}{T_{2B}} + \frac{1}{T_{2S}} + \frac{1}{T_{2D}} \qquad (7.2)$$

At the low magnetic field strength used in this study, the experimental parameter of the echo spacing, t_E, can be selected to make the influence of diffusion relaxation, T_{2D}, sufficiently small to be neglected [20, 23]. For the current study, changes in the fluid properties of the pore liquid, such as viscosity, are not expected be a significant factor in the overall change of the system T_2 relaxation time [8]. The influence of changes in T_{2B} can therefore also be neglected. Changes in surface relaxation, T_{2S}, are expected to dominate changes in the observed T_2 of this experimental system.

The low-field NMR signal response in most saturated natural geologic media is dominated by surface relaxation [22, 24]. Surface relaxation occurs as excited spins approach and interact with the pore walls. Thus, the rate of surface relaxation is most

strongly related to pore size and the mineral surface of the solid matrix. Surface relaxation occurs faster in small pores with a high surface-area-to-volume-ratio because the diffusing water molecules are more likely to interact with the grain surface. The surface relaxation rate also depends on the propensity of the surface for inducing relaxation, a characteristic referred to as surface relaxivity, ρ. Greater concentrations of paramagnetic ions like Fe^{3+} and Mn^{2+} produce higher magnitudes of ρ and faster relaxation rates [25, 26]. In heterogeneous materials with a range of pore sizes or variable ρ, there may be a distribution of relaxation rates making up the bulk response. Thus, an Inverse Laplace Transform yields a decay-time distribution that can be interpreted as a distribution of pore environments.

In our experiments, we expect MICP to have several combined influences on the NMR response. First, we expect that growth of calcite within the pore space will reduce the total porosity and water content. We also expect the growth of $CaCO_3$ to influence the observed relaxation rate due to changes in mineralogy and pore size [27-29]. The quartz sand used in this study is coarse-grained and contains small percentages of paramagnetic species including iron oxide (Fe_2O_3) at a mean weight percent of 0.04 (2095 Granusil® silica sand, Unimin Corp., Ottawa, MN). We expect that $CaCO_3$ forming on the quartz grain surfaces will decrease the total macro-pore dimension which could drive faster relaxation rates. On the other hand, $CaCO_3$ precipitating on the grain surface may shield water from the paramagnetic ions on the sand, thus decreasing the average ρ of the grain surface. A lower average ρ would tend to decrease the surface relaxation rate in the macro-pores, resulting in longer overall T_2. Further, the $CaCO_3$ may form

microcrystalline structures that incorporate significant micro-porosity of nanometer scale. We expect water in the very small geometry of these micro-pores to exhibit very short relaxation times. Thus, we anticipate these changes in the pore structure concurrent with MICP will manifest themselves as multiple changes to the NMR T_2 relaxation time distribution. These observed changes are expected to indicate which mechanism dominates in the bioreactor where there exists a particular initial pore size distribution and surface minerology.

Materials and Methods

Bioreactor

The radial flow bioreactor is designed to model the near well-bore environment and consists of four concentric polyvinyl chloride (PVC) pipe sections sealed with grooved top and bottom plates (Figure 7.1). The reactor is the same as was used in a previous study to detect biofilm growth in sand using the same NMR logging tool [20]. In the current experiment, the height of the reactor was 50 cm. The inner and outer pipes are solid while the two inner pipes are slotted to allow radial flow through the sand annulus between them. The inner and outer annuli are the influent and effluent reservoirs, respectively. The sand annulus measures 7.6 cm wide and was filled with 1 mm nominal quartz sand (2095 Granusil® silica sand, Unimin Corp., Ottawa, MN). The liquid volume of the reactor is approximately 30 L, including the sand pore volume and influent and effluent reservoirs.

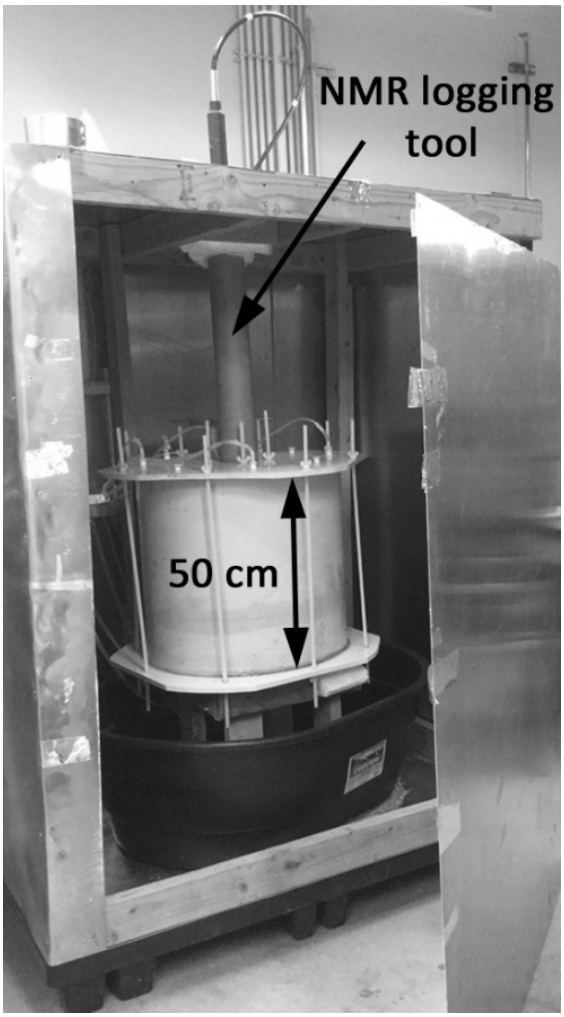

Figure 7.1. The radial flow bioreactor and NMR logging tool were housed in a Faraday cage to reduce detection of electromagnetic noise from the laboratory.

Media and Injection Strategy

Two kinds of substrate media were used in this study, a bacterial growth medium (growth medium) and a calcite mineralization-promoting medium (calcium medium). Both were urea- and yeast extract-based (1 g/L yeast extract (Arcos Organics, Gheel, Belgium), 20 g/L urea, 1 g/L NH_4Cl, and 24 g/L NaCl). The calcium medium contained an added 49 g/L $CaCl_2 \cdot 2H_2O$. Commercial-grade chemicals were used for urea (Urea

Fertilizer, Espoma, Millville, NJ), calcium chloride (various brands of commercial ice melt), and sodium chloride (Morton Table Salt, Chicago, IL). Media were mixed just prior to use in a non-sterile manner using tap water.

A pulsed-flow injection strategy promoted an even distribution of $CaCO_3$ precipitation by balancing reaction and transport rates [30]. Each 30 L pulse of substrate was pumped at a flow rate of 1 L/min, producing a pore velocity of approximately 0.4 cm/min and ensuring that the fresh substrate would penetrate the full width of the sandpack. Calcium medium was injected four times per day during the biomineralization phase Days 4 – 7. A 2-hour batch reaction period (no flow) followed each injection of calcium medium. One pulse of growth medium was injected each evening to stimulate the bacteria for the following day's calcium medium injections. A 10 L brine rinse (24 g/L NaCl) was injected into the reactor first each morning to reduce mixing of the two substrate media in the influent reservoir and minimize clogging of the slotted pipe.

Bacterial Culture

The bacteria used in this experiment, *Sporosarcina pasteurii* (ATCC 11859), formerly known as *Bacillus pasteurii*, is widely used in laboratory experiments related to urea hydrolysis and biomineralization [11]. *S. pasteurii* is a non-pathenogenic natural soil organism capable of producing relatively large amounts of the urease enzyme needed to catalyze urea hydrolysis [11]. For the inoculum, one mL of frozen stock of *S. pasteurii* was cultured in 100 mL of growth medium on a shaker table at 150 rpm for 24 hours. The 100 mL culture was then added to 10 L fresh growth medium and mixed on a stir plate at 1150 rpm for 24 hours. Finally, the 10 L culture was added to 20 L of fresh

growth medium and mixed as before to produce a final inoculum volume of 30 L. No attempt was made to maintain a monoculture in the inoculum or in the reactor.

The reactor was inoculated by first injecting 5 L of fresh growth medium to condition the reactor at a flowrate of 1 L/min, followed by the 30L inoculum. An additional 5 L of fresh growth medium was injected last. Bacteria were allowed to attach to the sand for approximately 15 hours with no flow before the first injection of calcium medium. There was no calcium present in the reactor during the 3-day control period or during inoculation. The initial period was used as the control. Note that previous experiments have shown no permeability reduction was achieved when urea and calcium containing solutions were injected into glass bead filled columns that were not inoculated with ureolytic microbes [31].

NMR Measurements

Low-field NMR measurements typically consist of repeated scans which are stacked and averaged to reduce noise in the data. In this study, two experiments were conducted sequentially and together constitute one CPMG scan for measurement of T_2 relaxation. Experiment 1 collects T_1-weighted fast-decaying signal (t_E=1.3ms, T_r=800ms, 54 echoes, 360 averages). Experiment 2, on the other hand, collects the signal from spins with longer relaxation times (t_E=1.3ms, T_r=5000ms, 334 echoes, 60 averages). All NMR measurements were collected under no flow conditions. Measurements during the control period, Days 1 – 3, consisted of 24 CPMG scans. Three (3) CPMG scans were stacked and averaged for each daily measurement during the biomineralization phase,

Days 4 – 8, because of the timing of repeated substrate injections on a 2-hour cycle. Data presented here was collected with a noise level of approximately 1.4%.

As only one tool was available on loan for a limited period, it was not possible to run replicate experiments. However, previous work with this tool [20, 21] has allowed multiple experimental runs whilst monitoring biofouling in both a sand pack and in the subsurface. The tool's performance has been consistent and repeatable.

Sampling

Influent and effluent samples were collected for each injection of brine, calcium medium, and growth medium. The sample pH was measured shortly after collection, then the sample was filtered (0.2 µm membrane, VWR International, Radnor, PA) and refrigerated for later analysis with the Jung Assay [32] to evaluate the sample urea concentration. After the final measurement on Day 8, the reactor was drained and destructively sampled. The outer pipe was cut away in sections, leaving the biomineralized sand annulus exposed for sampling (Figure 7.2). Twenty-four (24) cores were collected: 2 radial cores of approximately 1 inch diameter (2.5 cm) and 3 inch length (7.5 cm) at each of 3 depths were sampled in 4 orthogonal directions. Each core sample was divided into 3 subsamples which were then weighed and subjected to nitric acid digestion to remove the solid precipitates. The liquid was extracted for calcium content analysis by ICP-MS using an Agilent 7500ce (Santa Clara, CA) with a collision cell (helium mode) and a certified environmental calibration standard from CPI International (product number 4400-12 1116NCO2). Additionally, micrograph images were acquired using a Zeiss Supra 55VP scanning electron microscope (Zeiss, USA).

Biomineralized sand samples from the reactor and control sand samples were sputter coated with iridium and high-resolution images were taken at 1.0 kV at a working distance of 3—4 mm.

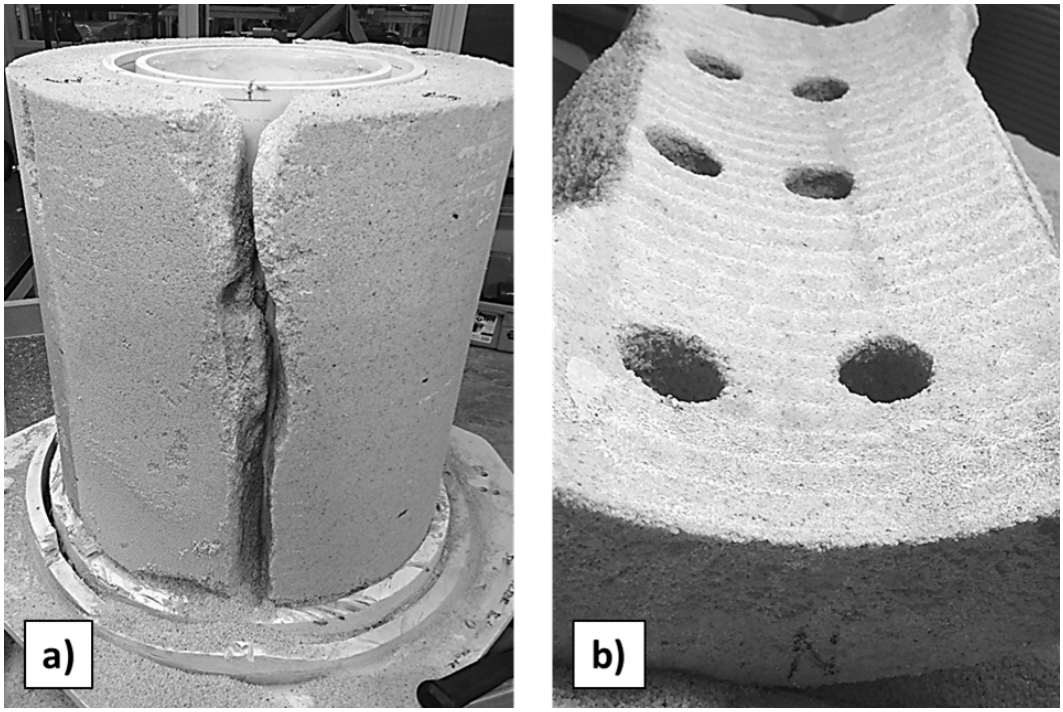

Figure 7.2. The biomineralized sand annulus was destructively sampled to quantify $CaCO_3$ precipitation. a) The outer pipes of the bioreactor were cut away to expose the biomineralized sand annulus. A saw was used to cut the annulus into quarters, producing the large crack shown here. b) Six radial core samples were collected from each quarter.

Results and Discussion

The influence of $CaCO_3$ precipitation on the NMR signal response is reflected in the daily signal decay curves and resulting T_2 distributions where significant changes were observed over time. Representative data, collected on Days 2, 4, 6, and 8, are presented in Figure 7.3; the top panel shows fits to recorded signal decay curves, and the

bottom panel presents the T_2 distributions for those decay curves. First, we will address the change in water content which corresponds to a drop in the porosity of the sandpack. Then we will discuss the relaxation distributions, which give insight to changes in the relaxation mechanism.

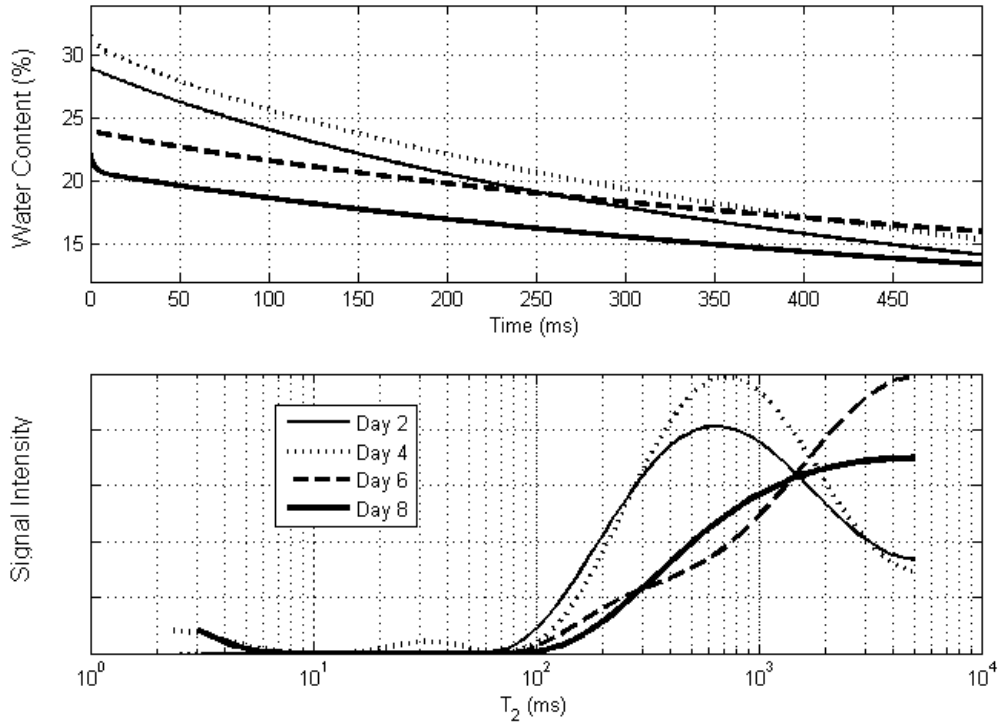

Figure 7.3. Signal decay curves (top) and the corresponding T_2 distributions (bottom) are shown with each curve representing a day. Day 2 occurred during the control period. Inoculation occurred on Day 3 (not shown). The calcium media injections occurred between Day 4 – 7. The Day 8 data was collected prior to flushing the reactor with brine and destructively sampling. Both graphs show fits to the raw data.

Water Content and Porosity

Decreasing signal amplitude over time is an indication of $CaCO_3$ precipitation, since $CaCO_3$ will displace water in the pore volume. During the control period the initial porosity indicated by the NMR-measured total water content was approximately 30% which is slightly less than the 35-39% expected from a sand pack with relatively uniform grains. The observation of entrained air leaving the system after the first flow pulse following inoculation, and the subsequent increase in the water content signal on Day 4, leads us to conclude that the sand pack was not fully saturated during the control period. This also explains why the measured water content value of ~30% is less than the expected value of 35-39%. The NMR-measured total water content in the reactor decreased to approximately 76% of its original value between the control period (Day 2 data) and the end of the biomineralization phase on Day 8 (Figure 7.3, top panel, and Figure 7.4). This reduction in total water content indicates that the pore volume within the reactor decreased significantly during the biomineralization phase. If we consider Day 4 to represent full saturation, then the NMR-estimated porosity reduction is 70% of the initial value, indicating the sensitivity of the NMR measurement to partial saturation.

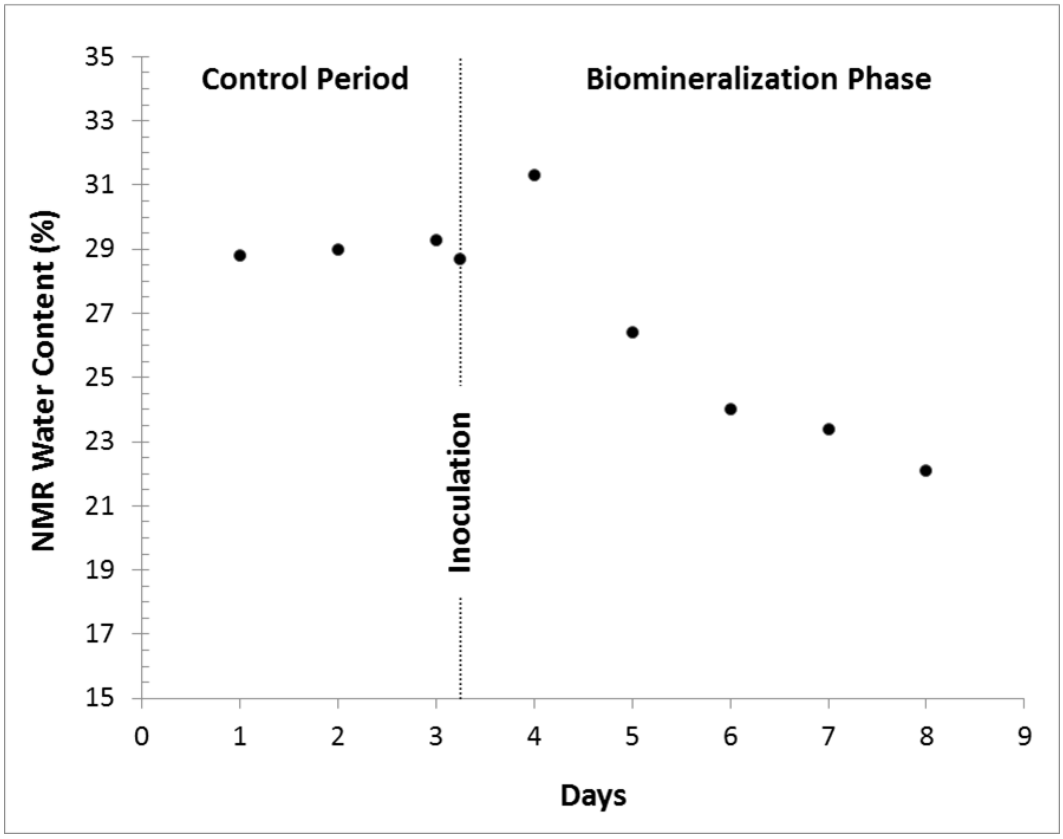

Figure 7.4. The measured total water content in the radial flow reactor decreased from approximately 29% during the control period Days 1-3 to approximately 22% by Day 8. Note that the increase on Day 4 is real and well outside expected error bounds. The increase follows the observation of entrained air leaving the bioreactor, indicating the desired fully saturated state may not have been obtained until after the control period.

$CaCO_3$ formation was confirmed by scanning electron microscopy (SEM). There appeared to be a relatively uniform $CaCO_3$ coating on the sand samples viewed with SEM. Figure 7.5 shows an SEM micrograph showing the crystals formed on a grain of sand from the reactor (a) and the surface of a control sand grain (b). The surface of the $CaCO_3$ -encrusted sand reveals micro-scale cavities and pores between crystals. No bacteria were visible in the sand samples viewed with SEM; it is most likely that the cells are entombed within the crystals.

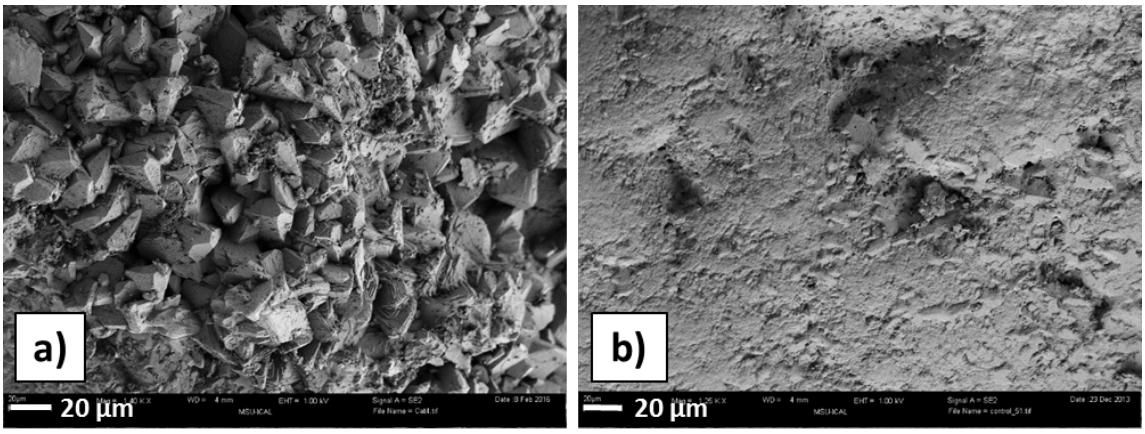

Figure 7.5. SEM image of a) $CaCO_3$ crystals attached to a grain of sand from the reactor following 4 days of MICP and b) control sand without $CaCO_3$. Scale bar is 20 µm. Note that the $CaCO_3$ crystals completely cover the sand surface and the sand is not visible in (a), whereas in (b) the smooth sand surface is observed.

Several methods were applied to estimate the volume of $CaCO_3$ formed in the reactor in order to independently determine the reduction in pore volume achieved. These methods include a mass balance on urea, ICP-MS detection of Ca^{2+}, and gravimetric methods. An initial porosity estimate of 37%, typical for the sand in the reactor, was used in these calculations. Because the reactor was not fully saturated during the control period, the total porosity is greater than the NMR water content. The results of these three methods are in good agreement with each other and support the NMR data showing a significant pore volume reduction due to calcite precipitation. Mass balance on urea: Influent and effluent samples of each pulse of media were analyzed using the Jung Assay [32] to quantify the urea content. A mass balance on urea showed that approximately 4.2 kg of urea was consumed within the reactor, stoichiometrically producing approximately 6.9 kg of calcite. This mass of calcite would occupy at maximum approximately 15% of the pore space in the sand annulus. Since $CaCO_3$ also

formed in the tubing and on the reactor walls, we consider the urea mass balance method to provide an approximation of the upper bound of $CaCO_3$volume. ICP-MS: ICP-MS was used to measure the concentration of Ca^{2+} in the acid extraction liquid from 24 samples of biomineralized sand from the reactor. A mean value of 9.36 g/L Ca^{2+} was obtained with a sample standard deviation of 1.89 g/L, which equates to an average total mass of 6.3 kg $CaCO_3$ within the sand. The ICP-MS data translates to an average pore volume reduction of approximately 12% (+/- 2.4%). Gravimetric method: The 24 sand samples were also weighed before and after the acid digestion removed the precipitate, resulting in an average mass of calcite of 63.6 mg $CaCO_3$/g sand with a sample standard deviation of 13 mg/g. By this method, the average total mass within the sandpack was 5.5 kg calcite. The gravimetric method indicates that approximately 11% (+/- 2.2%) of the pore space in the sand annulus was occupied by $CaCO_3$at the end of the experiment. Unlike the mass balance method, ICP-MS and gravimetry account only for $CaCO_3$ attached to the sand. On the basis of these complementary and independent methods, we estimate that $CaCO_3$ occupied approximately 11 – 12% of the pore space in the sandpack by Day 8 of the experiment.

This estimated porosity reduction is significantly higher than those previously reported in other NMR/MICP studies [8, 19]. The pulsed flow injection strategy used here promotes relatively uniform $CaCO_3$ precipitation, as evidenced by the small standard deviation of the samples collected from the reactor. The uniform calcite precipitation implies spatially uniform porosity reduction. Consequently, only an insignificant reduction in permeability was observed in this study.

Compared to the methods described above which found final porosity to be approximately 88% of the original value, NMR measurements of water content overestimate the porosity reduction achieved. Final NMR water content was 76% of the initial value, or 70% of the Day 4 value. The overestimation can be attributed to carbon dioxide (CO_2) gas production inside the reactor. The excess CO_2 produced by microbial oxidation of the yeast extract in the substrate can be trapped in the reactor pore spaces, displacing water and reducing signal amplitude without changing the pore geometry. Gas formation was also observed in previous NMR studies of MICP [8, 19]. Furthermore, signal decaying in the interval before the first echo acquisition will underestimate the water content and may explain in part the NMR overestimation of porosity reduction.

Relaxation

The tall initial peak (Day 2 data) in the bottom panel of Figure 7.3, centered about approximately 600-700 ms and associated with water in large pores, first increases then decreases in amplitude over time as the biomineralization phase proceeds. At the same time, there is an increase in both the occurrence of very fast T_2 relaxation times less than 10 ms, and an increase in the proportion of spins experiencing very long relaxation times, greater than 1000 ms. At the left-hand limit of the T_2 distribution (Figure 7.3, bottom), the NMR logging tool cannot capture NMR signal that decays faster than the measurement echo time (t_E=1.3ms). We note that since the time of this study, the echo time of the Javelin tool has been reduced to 0.7 ms. At the right of the distribution, signals with T_2 between 1-5 s are not tightly resolved on the T_2-axis because the signal is sampled only to 500 ms. However, the amplitude of these long signals is accurately

measured (Figure 7.3, top). By Day 8 of the experiment, the mean log T_2 time of the distribution had increased to greater than 1000 ms from approximately 650 ms during the control period.

The data shows that T_2 relaxation in the macro-pores of the sandpack is more significantly affected by the reduction in ρ than by the decrease in the macro-pore dimension. As seen in the SEM images (Figure 7.5a), the $CaCO_3$ crystals are on the order of 10^1 μm thick. In a large pore on the order of 10^2 μm in diameter, there is a relatively minor change in pore dimension due to calcite precipitation. On the other hand, the relatively thin and uniform coating of $CaCO_3$ crystals is sufficient to minimize molecular interactions between the pore fluid and paramagnetic species on the sand, making the surface much less likely to induce relaxation. The combination of a large change to ρ and a small change to the pore size explains the lengthening of the overall mean log T_2 relaxation time. At the same time, $CaCO_3$ precipitation also creates micro-pores between and within the crystals. In these pores, the pore size effect dominates and T_2 relaxation occurs rapidly for the small population of spins within the crystals.

Previous NMR/MICP studies reporting the opposite [19] or no relaxation effect [8] are not at odds with this interpretation of the data. Both previous studies used smaller diameter (~100 – 250 μm) model porous media (borosilicate or polystyrene beads, respectively) with a low initial ρ and small initial pore size, where we would expect more potential influence from a change in the pore geometry than from a reduction in ρ. We expect if $CaCO_3$ precipitation had continued to progress in the current experimental system, the reduction in the macro-pore dimension would eventually become the

dominate influence, driving relaxation times to decrease. Thus, the potential complexity of the relaxation response leaves open the possibility of different relaxation signatures in other porous materials where pore sizes or surface properties are more heterogeneous.

Our results show that changes in NMR signal response due to MICP include 1) a decrease in signal amplitude over time, indicating a reduction in porosity, and 2) a lengthening of the overall T_2 relaxation time in the quartz sand of the bioreactor. NMR measured water content in the reactor decreased to approximately 76% of the initial value, which corresponds well to the measured reduction in porosity to approximately 88% of the typical initial value. The extent of the decrease in porosity, and the corresponding minimal change in permeability, is related to the pulsed-flow injection strategy employed to achieve the MICP. T_2 relaxation distributions bifurcated from a single mode centered about approximately 650 ms during the control period into a very fast decaying population (T_2 less than 10 ms), associated with water in the porous $CaCO_3$, and a larger population with relaxation times greater than 1000 ms, corresponding to the bulk water in the large crystal-coated pores. Slower relaxation is caused by $CaCO_3$ crystals on the mineral surface of the macro-pores shielding paramagnetic species from the pore fluid, reducing ρ of the pore. In the $CaCO_3$ micro-pores, the pore size effect dominated and enhanced relaxation. Future work will evaluate the NMR signal response to MICP in natural soils and porous rock where surface relaxivity and pore sizes are more heterogeneous. This study demonstrates that a NMR well-logging tool is sensitive to MICP and has potential as a sensor for biomineralization in field applications where optical or destructive monitoring methods are not possible.

References

1. Stoodley, P., et al., *Biofilms as complex differentiated communities.* Annual Review of Microbiology, 2002. **56**: p. 187-209.

2. Beech, I.B. and J. Sunner, *Biocorrosion: towards understanding interactions between biofilms and metals.* Current opinion in biotechnology, 2004. **15**(3): p. 181-6.

3. Costerton, J.W., P.S. Stewart, and E.P. Greenberg, *Bacterial biofilms: A common cause of persistent infections.* Science, 1999. **284**(5418): p. 1318-1322.

4. de Kreuk, M., J.J. Heijnen, and M.C.M. van Loosdrecht, *Simultaneous COD, nitrogen, and phosphate removal by aerobic granular sludge.* Biotechnology and Bioengineering, 2005. **90**(6): p. 761-769.

5. Cunningham, A.B., et al., *Subsurface biofilm barriers for the containment and remediation of contaminated groundwater.* Bioremediation Journal, 2003. **7**(3-4): p. 151-164.

6. Decho, A.W., *Overview of biopolymer-induced mineralization: What goes on in biofilms?* Ecological Engineering, 2010. **36**(2): p. 137-144.

7. Ferris, F.G., et al., *Kinetics of calcite precipitation induced by ureolytic bacteria at 10 to 20 degrees C in artificial groundwater.* Geochimica Et Cosmochimica Acta, 2003. **67**(8): p. 1701-1722.

8. Fridjonsson, E.O., et al., *NMR measurement of hydrodynamic dispersion in porous media subject to biofilm mediated precipitation reactions.* Journal of Contaminant Hydrology, 2011. **120-21**: p. 79-88.

9. De Muynck, W., N. De Belie, and W. Verstraete, *Microbial carbonate precipitation in construction materials: A review.* Ecological Engineering, 2010. **36**(2): p. 118-136.

10. DeJong, J.T., et al., *Bio-mediated soil improvement.* Ecological Engineering, 2010. **36**(2): p. 197-210.

11. Phillips, A.J., et al., *Engineered applications of ureolytic biomineralization: a review.* Biofouling, 2013. **29**(6): p. 715-733.

12. van Paassen, L.A., et al., *Quantifying Biomediated Ground Improvement by Ureolysis: Large-Scale Biogrout Experiment.* Journal of Geotechnical and Geoenvironmental Engineering, 2010. **136**(12): p. 1721-1728.

13. Mortensen, B.M., et al., *Effects of environmental factors on microbial induced calcium carbonate precipitation.* Journal of Applied Microbiology, 2011. **111**(2): p. 338-349.

14. Mitchell, A.C., et al., *Microbially Enhanced Carbon Capture and Storage by Mineral-Trapping and Solubility-Trapping.* Environmental Science and Technology, 2010. **44**(13): p. 5270-5276.

15. Phillips, A.J., et al., *Fracture Sealing with Microbially-Induced Calcium Carbonate Precipitation: A Field Study.* Environmental Science & Technology, 2016. **50**(7): p. 4111-4117.

16. Phillips, A.J., et al., *Potential CO2 Leakage Reduction through Biofilm-Induced Calcium Carbonate Precipitation.* Environmental Science & Technology, 2013. **47**(1): p. 142-149.

17. Behroozmand, A.A., K. Keating, and E. Auken, *A Review of the Principles and Applications of the NMR Technique for Near-Surface Characterization.* Surveys in Geophysics, 2015. **36**(1): p. 27-85.

18. Walsh, D., et al., *A small-diameter NMR logging tool for groundwater investigations.* Groundwater, 2013. **51**(6): p. 914-926.

19. Sham, E., et al., *Monitoring bacterially induced calcite precipitation in porous media using magnetic resonance imaging and flow measurements.* Journal of Contaminant Hydrology, 2013. **152**: p. 35-43.

20. Kirkland, C.M., et al., *Biofilm Detection in a Model Well-Bore Environment Using Low-Field NMR.* Groundwater Monitoring and Remediation, 2015: p. DOI:10.1111/gwmr.12117.

21. Kirkland, C.M., et al., *In Situ Detection of Subsurface Biofilm Using Low-Field NMR: A Field Study.* Environmental Science & Technology, 2015. **49**(18): p. 11045-11052.

22. Grunewald, E. and R. Knight, *A laboratory study of NMR relaxation times in unconsolidated heterogeneous sediments.* Geophysics, 2011. **76**(4): p. G73-G83.

23. Kleinberg, R.L. and M.A. Horsfield, *Transverse relaxation processes in porous sedimentary rock.* Journal of Magnetic Resonance, 1990. **88**(1): p. 9-19.

24. Kleinberg, R.L., Kenyon, W.E., Mitra, P.P., *Mechanism of NMR relaxation of fluids in rock.* Journal of Magnetic Resonance Series A, 1994. **108**: p. 206-214.

25. Bryar, T.R., C.J. Daughney, and R.J. Knight, *Paramagnetic effects of iron(III) species on nuclear magnetic relaxation of fluid protons in porous media.* Journal of Magnetic Resonance, 2000. **142**(1): p. 74-85.

26. Foley, I., S.A. Farooqui, and R.L. Kleinberg, *Effect of paramagnetic ions on NMR relaxation of fluids at solid surfaces.* Journal of Magnetic Resonance Series A, 1996. **123**(1): p. 95-104.

27. Kenyon, W.E. and J.A. Kolleeny, *NMR surface relaxivity of calcite with adsorbed Mn2+*. Journal of Colloid and Interface Science, 1995. **170**(2): p. 502-514.

28. Coates, G.R., et al., *A new characterization of bulk-volume irreducible using magnetic resonance.* Log Analyst, 1998. **39**(1): p. 51-63.

29. Zhang, Q., et al. *Some exceptions to default NMR rock and fluid properties*. in *Transactions of the SPWLA Annual Logging Symposium (Society of Professional Well Log Analysts)*. 1998.

30. Ebigbo, A., et al., *Darcy-scale modeling of microbially induced carbonate mineral precipitation in sand columns.* Water Resources Research, 2012. **48**.

31. Wheeler, L.A., *Establishment of ureolytic biofilms and their influence on the permeability of pulse-flow porous media column systems.* 2009, Montana State University, Bozeman, MT.

32. Jung, D., et al., *New colorimetric reaction for endpoint, continuous-flow and kinetic measurement of urea* Clinical Chemistry, 1975. **21**(8): p. 1136-1140.

CHAPTER EIGHT

NMR INVESTIGATION OF WATER DIFFUSION IN DIFFERENT BIOFILM STRUCTURES

Contribution of Authors and Co-Authors

Manuscript in Chapter 8

Author: Maria P. Herrling

Contributions: Conceived the concept and designed the experiment. Conducted diffusion measurements, characterized the biomass. Analyzed the data and wrote the manuscript.

Co-Author: Jessica Weisbrodt

Contributions: Conducted diffusion experiments. Collected and characterized the biomass. Analyzed data.

Co-Author: Catherine M. Kirkland

Contributions: Assisted with data collection for D-T_2 measurements. Assisted with data analysis for D-T_2 measurements. Provided feedback and comments on manuscript.

Co-Author: Nathan H. Williamson

Contributions: Assisted with data analysis using the Gamma distribution. Provided feedback and comments on manuscript.

Co-Author: Susanne Lackner

Contributions: Discussed the data and Provided feedback and comments on manuscript.

Co-Author: Sarah L. Codd

Contributions: Provided feedback and comments on the manuscript.

Co-Author: Joseph D. Seymour

Contributions: Provided supervision and oversight on D-T_2 data collection and analysis. Provided feedback and comments on the manuscript.

Co-Author: Gisela Guthausen

Contributions: Conceived the concept and designed the experiment. Developed data analysis tools, analyzed the data, and discussed the data. Provided feedback and comments on the manuscript.

Co-Author: Harald Horn

Contributions: Designed the experiment and discussed the data. Provided feedback and comments on the manuscript.

Manuscript Information Page

Maria P. Herrling, Jessica Weisbrodt, Catherine M. Kirkland, Nathan H. Williamson, Susanne Lackner, Sarah L. Codd, Joseph D. Seymour, Gisela Guthausen, Harald Horn.

Biotechnology and Bioengineering

Status of Manuscript:
____ Prepared for submission to a peer-reviewed journal
__X_ Officially submitted to a peer-review journal
____ Accepted by a peer-reviewed journal
____ Published in a peer-reviewed journal

Wiley-Blackwell
Submitted February 10, 2017

NMR INVESTIGATION OF WATER DIFFUSION IN DIFFERENT BIOFILM STRUCTURES

Abstract

Mass transfer in biofilms is determined by diffusion. Different mostly *invasive* approaches have been used to measure diffusion coefficients in biofilms, however data on heterogeneous biomass under realistic conditions is still missing. To *non-invasively* elucidate fluid-structure-interactions in complex multispecies biofilms pulsed field gradient-nuclear magnetic resonance (PFG-NMR) was applied to measure the water diffusion in five different types of biomass aggregates: one type of sludge flocs, two types of biofilm, and two types of granules. Data analysis is an important issue when measuring heterogeneous systems and is shown to significantly influence the interpretation and understanding of water diffusion. With respect to numerical reproducibility and physico-chemical interpretation, different data processing methods were explored: (bi)-exponential data analysis and the Γ distribution model. Furthermore, the diffusion coefficient distribution in relation to relaxation was studied by D-T_2 maps obtained by 2D inverse Laplace transform (2D ILT). The results show that the effective diffusion coefficients for all biofilm samples ranged from 0.36 to 0.96 relative to that of water. NMR diffusion was linked to biofilm structure (e.g. biomass density, organic and inorganic matter) as observed by magnetic resonance imaging and to traditional biofilm parameters: Diffusion was most restricted in granules with compact structures, and fast diffusion was found in heterotrophic biofilms with fluffy structures. The effective

diffusion coefficients in the biomass were found to be broadly distributed because of internal biomass heterogeneities, such as gas bubbles, precipitates, and locally changing biofilm densities. Thus, estimations based on biofilm bulk properties in multispecies systems can be overestimated and mean diffusion coefficients might not be sufficiently informative to describe mass transport in biofilms and the near bulk.

Introduction

Biofilms or more generally biomass aggregates are pervasive in natural aquatic systems [1, 2] as well as in technical systems [3]. Their substrate conversion depends on bulk and internal structures influencing the mass transfer into the matrix. Generally, this mass transfer in biomass aggregates is driven by diffusion and plays a key role for metabolic activity [4-6]. The investigation and understanding of mass transfer and substrate consumption is essential for the development of strategies to improve design and operation of biofilm-based technical applications as well as for modeling. In-depth knowledge is required - especially for multispecies biofilms under technical and realistic conditions.

To experimentally explore fluid-structure-interactions, several analytical methods have been applied. Imaging techniques [7] and micro sensors [8, 9] have been used the most. Furthermore, mathematical modeling leads to mechanistic understanding of mass transfer phenomena in complex biofilm systems [10]. Biofilm modeling in combination with imaging indicates that rough biofilms show higher mass transfer of substrates compared to smooth biofilms under stagnation conditions. The larger interfacial surface

of a rough biofilm provides better contact to substrates [11]. The diffusion coefficient *D* of substrates into the biofilm is assumed constant over the biofilm depth [12]. In transport models, *D* is usually set to 20-30 % less than D_{water} [12]. Diffusion of water and nutrients strongly varies between different biofilm systems, geometries, and growth conditions. Actual mass fluxes inside biofilms are unknown, and a generalization of mass transport is not possible. Therefore, data on heterogeneous systems is needed to address measures for mass transport in real systems. Pulsed-field gradient nuclear magnetic resonance (PFG-NMR) allows the measurement of translational diffusion completely *non-invasively* and *non-destructively* [13, 14], also in micro-porous systems and in restricted geometry.

In biofilm research, alginate is often used as model system due to the chemical composition which is comparable to the biofilms' extracellular polymeric substances (EPS). Gel heterogeneities were detected in transverse relaxation T_2 maps [15]. Filtration processes have been imaged in hollow fiber membranes using alginate as model system [16]. Basic knowledge gained from investigations of artificial biofilms can be transferred to real biofilm systems. Monoculture and multispecies biofilms were investigated by NMR flow and diffusion in porous media and flow cells to study water dynamics and biofilm growth at different time and length scales [17-21]. Furthermore, combined diffusion and Magnetic Resonance Imaging (MRI) linked mass transfer to biofilm structure [7, 20]. Diffusion strongly depends on biofilm systems, growth conditions and biofilm geometries. For example, in methanogenic granular sludge internal heterogeneities significantly influenced the mass transfer [22]. Strong correlations between the diffusion of substrates and biofilm parameters have been reported [4, 23, 24].

For example, Renslow et al. (2010) correlated the effective diffusion coefficient with biofilm depth by means of PFG-NMR and imaging in *Shewanella oneidensis* biofilms. The same was found for phototrophic *Phormidium* biofilms [25]. Other studies also confirm that *D* is biofilm-specific and depth-dependent with a linear decrease of *D* with biofilm depth [26, 27].

Mass transport and diffusion in biofilms are difficult to analyze and to model because of the high complexity of these biomass aggregates. Apart from the influence of specific compounds, PFG-NMR measurements and data interpretation deserve scrutiny. Different data processing approaches are summarized in Röding, Bernin [28], [29]. The most commonly used data processing approach for PFG-NMR data is the (bi)-exponential fit. Diffusion coefficients are obtained by fitting a single exponential function to the measured signal attenuation, leading to effective or apparent diffusion coefficients. An alternative and recently introduced approach is the Γ distribution model which offers mean diffusion coefficients and their distribution width. Different data processing schemes are compared for biomass aggregates in this study to show their limitations and relevance. For mathematical description we refer to [28], Röding, Williamson [29]. Water diffusion coefficients in multispecies biofilms with diverse geometries and data processing schemes are compared in this paper. To identify fluid-structure interactions, five different types of biofilms or biomass aggregates were investigated: sludge flocs, fluffy and compact biofilms grown on carriers, and aerobic and (an)aerobic granules. The goals of the study were to i) characterize the biomass by means of physico-chemical parameters and imaging, ii) compare D_{water} in different structures to identify correlations

between biomass properties and water diffusion, iii) compare PFG-NMR data processing schemes, including (bi)-exponential fit, Γ distribution and 2D inverse Laplace transform.

Materials and Methods

Biofilm Sample Preparation

Activated sludge flocs, carrier based biofilms, and granules were chosen to cover a broad range of physical morphologies which are technically relevant, e.g. for wastewater treatment. The properties and functionalities are summarized in Table 8.1. Sludge flocs (sludge) were collected from a full-scale wastewater treatment plant in Weinheim (Germany). The sludge is a mixed culture of auto- and heterotrophic biomass used for carbon (C), nitrogen (N) and phosphorus (P) removal from wastewater. The sludge was rinsed and sieved to a size fraction < 200 µm prior to characterization. Two different carrier based biofilms were investigated. Fluffy biofilms (biofilm_1) grown on K1 carrier materials (plastic carrier, diameter: 10 mm, AnoxKaldnes, Sweden) were cultivated in a laboratory-scale moving bed biofilm reactor fed with acetate [30]. Biofilm_1 comprised heterotrophic biomass and was mainly used for removal of easily degradable carbon compounds. Compact biofilms (biofilm_2) on K3 (plastic carrier, diameter: 25 mm, AnoxKaldnes, Sweden) were obtained from a full-scale wastewater treatment plant (AnoxKaldnes' Biofarm) in Malmö, Sweden. Biofilm_2 comprised multiple species, i.e. heterotrophs, nitrifiers, denitrifiers and anammox bacteria [31] and was mainly used for N removal. Two different types of granules, i.e. granulated biofilms, were also selected for the investigation. Aerobic granules (granules_1) were cultivated in

a laboratory-scale sequencing batch reactor (SBR) with acetate as the main substrate. Granules_1 were used for N, P and easily degradable C removal. Large sized granules with an approximate diameter of 10 mm were manually selected. Additionally, (an)aerobic granules (granule_2) were collected from a side-stream SBR of a full-scale wastewater treatment plant in Heidelberg (Germany). Granules_2 mainly contributed to the removal of N and some slowly degradable C compounds. Granules_2 were rinsed and sieved to a size fraction of 700-900 µm.

Parameter	Sludge	Biofilm_1	Biofilm_2	Granules_1	Granules_2
microbes	autotrophic	heterotrophic	autotrophic	autotrophic	autotrophic
removal	C/N/P	C	N	C/N/P	N/C
TSS	6 g/L TSS	86 mg TSS/carrier	270 mg TSS/carrier	40 mg TSS/granule	3 g/L TSS
VSS [%]	80	90	69	78	80
biofilm thickness [µm]	< 200*	< 200	< 1000	10 000*	400-700*
biofilm density [g/L]	1033 ±15	<1010	1047 ±4	1029 ±2	1046 ±14
Ca [g/kg TSS]	37	n.m.	490	97	286
P [g/kg TSS]	53	n.m.	132	49	72
Fe [g/kg TSS]	37	n.m.	590	0.6	327
S [g/kg TSS]	10	n.m.	6	6.8	84
Si [g/kg TSS]	2	n.m.	65	0.2	37

Table 8.1: Characterization of the biofilms. The abbreviation n.m. means not measured. Data marked with asterisk (*) refer to diameter of the granules. “C” refers to carbon removal, “N” to nitrogen removal and “P” to phosphorous removal. The density of water at 20°C is 998 g/L.

All biofilms were rinsed prior to the experiment to remove particulate matter and stored in tap water at 4°C. Biofilms were imaged by light microscope SMT4 (Mikroskop Technik Rathenow) in combination with a DSLR camera (Canon EOS 600D) and characterized by their total suspended solid concentration (TSS) and volatile suspended solid concentration (VSS) according to DIN-EN-12880 (2001). The biomass density was determined by pycnometer measurement (n=4, 10 ml, Blaubrand) according to DIN ISO 35079 and the solids density was calculated according to Loosdrecht, Nielsen [32]. Element analysis was conducted by atomic emission spectroscopy (ICP-OES, Varian VistaPro, Agilent Technologies, l detection limit: 10 µg/L) after acid digestion. ICP-OES data for biofilm_1 is not available due to low biofilm mass.

MRI and PFG-NMR

MRI. MRI experiments were performed on a 200 MHz MRI instrument (Bruker Avance 200 SWB, Bruker BioSpin GmbH, Rheinstetten, Germany) with a magnetic flux B_0 of 4.7 T, 150 mm vertical bore and equipped with a Bruker gradient system micro2.5 and a ^{1}H-NMR bird-cage (25 mm inner diameter). All measurements were performed temperature controlled at 25°C using the Bruker software ParaVision. The often used multi-slice multi-echo imaging sequence (MSME) [14, 33] was applied to acquire predominantly proton density-weighted images due to the minimum echo time used in the experiments. The biofilms were imaged using the same acquisition parameters as in a previous study [34] with T_R = 10 s, τ_E = 50 ms, number of averages = 4, pixel matrix 128x128, slice thickness 0.8 mm. To maintain the original structure, sludge and granules_2 were filled into glass vials with 1 mL of tap water from Karlsruhe to avoid

osmotic stress. The Karlsruhe tap water (average values of 2015, Stadtwerke Karlsruhe) had a pH of 7.2, total organic carbon concentration of 0.84 mg/L and an electrical conductivity of 653 µS/cm ($c(Ca^{2+})$ = 110 mg/L, $c(Na^{+})$ = 11.1 mg/L, $c(K^{+})$ = 1.7 mg/L, $c(Cl^{-})$ = 22.8 mg/L, $c(HCO^{-})$ = 232 mg/L).

Wet biofilm_1, biofilm_2 and granules_1 were placed into plastic wrap (without bulk water) and directly inserted into the bird-cage. The measured signal intensity is encoded on a gray-scale and physically corresponds to the proton density, slightly weighted by the transverse relaxation T_2. The slightly T_2-weighted proton density images allow the discrimination of the main components within the biofilm system, being either ^1H containing liquid (signal) or solid or gas (no signal intensity in MSME images). Additionally, materials without ^1H, i.e. minerals, do not show up in the ^1H images.

Diffusion Measurements. Translational motion was measured by PFG-NMR, i.e. the pulsed application of magnetic field gradients which encode and decode the position across an ensemble of molecules at different times. The time between the encoding and decoding pulses is the diffusion time Δ. The PFG-NMR acquisition parameters are summarized in Table 8.2. Biomass samples were measured using the PFG stimulated echo (PFG-STE) [13] on the above described NMR spectrometer equipped with the Bruker software Topspin and a Diff30 probe, which allowed *z*-gradients g of up to 12 T/m. Acquisition parameters were chosen according to Table 8.2, measurement I. The logarithmic, normalized signal attenuation $\ln(S/S_0)$ was measured as a function of q, where $q = \gamma\delta g$, γ being the gyromagnetic ratio, δ the gradient pulse duration, and g the gradient amplitude. Complementary measurements were performed on a 250 MHz MRI

tomograph (Bruker Avance 250 SWB, Bruker BioSpin GmbH, Rheinstetten, Germany) also equipped with a Diff30 Probe (maximum gradient 17 T/m) employing acquisition parameters of measurement II and III, (Table 8.2). Images taken at the beginning and end of the experiments showed stable biofilm structure. All diffusion measurements were performed as single measurements at 25°C.

Acquisition Parameter	Measurement I	Measurement II	Measurement III
	PFG-STE	PFG-STE	D_T_2_STE
gradient pulse duration	3 ms	1 ms	1.136 ms
diffusion time	40, 100, 200, 400, 500, 800 ms	50, 100, 200 ms	100 ms
first rf pulse delay	4.26 ms	21.21 ms	21.21 ms
recycle delay	8 s	900 ms	12 s
diffusion gradient amplitude	0.016 T/m to 0.5 T/m linear in 32 steps	-0.32 T/m to +0.32 T/m linear in 64 steps	0.015 T/m to 0.2 T/m linear in 64 steps
number of scans	4	16	32
number of dummy scans	1	0	4
gradient direction	*z*	*z*	*z*

Table 8.2: Acquisition parameters for PFG-NMR diffusion measurements. Measurement II and III were used to characterize biofilm_1.

Data Processing

(Bi)-exponential Model. D_{water} was obtained by fitting a single exponential function to the measured signal attenuation as it is expected for a homogeneous liquid of small molecules [35]. In the biofilm matrix, the motion of water is partially restricted. The samples are highly heterogeneous; therefore, a *D*-distribution is expected. However, as little is known about the details and mechanisms, the question about an appropriate model is essential for a confident data interpretation. As a first approach, the commonly used (bi)-exponential function $\frac{S}{S_0} = A_1 \exp\left(-D_1 q^2 \left(\Delta - \frac{\delta}{3}\right)\right) + A_2 \exp\left(-D_2 q^2 \left(\Delta - \frac{\delta}{3}\right)\right)$ (eq. 1) with the gradient duration δ. D_1 and D_2 in biofilms were obtained, meaning that there is a fast (D_1) and a slow (D_2) diffusion fraction described by the relative amplitudes A_i. D_1 makes up more than 80 % of the signal amplitude and is the dominant part. A small portion with signal amplitudes of 4-20% can be associated with D_2 (in the range of 10^{-10} to 10^{-11} m^2/s), which is significantly lower than D_1. Due to the dominant relative signal amplitude, the discussion focuses on D_1 in the following. The relative effective diffusion coefficient is defined by $f_{D\_exp} = D_1 / D_{water}$ (eq. 2), which is used to compare the diffusion properties of the samples.

Data was processed using self-written scripts in Matlab® (version R2012a, Matlab Works Inc.; Natick, Massachusetts, USA) which take special care of the small amplitude of the second diffusion contribution. This (bi)-exponential rather than a mono-exponential approach is essential for accurately describing the majority of the data to avoid miss- or over interpretation due to numerical errors during data processing. Only data points with signal above the noise level were used in the fits.

Gamma Distribution Model. For heterogeneous systems, the Stejskal-Tanner approach for self-diffusion of homogeneous liquids composed of small molecules does not apply necessarily. *D*-distributions are physically more meaningful than a discrete number of *D* in these highly complex and heterogeneous systems. Apart from the conventionally used (bi)-exponential function for modelling the signal attenuation, a recently developed approach by Röding *et al*. was used to reveal the distribution of diffusion coefficients [28, 29]. The Γ distribution function is a generalization of distribution functions known in mathematical statistics. One of the advantages is that the equation for the experimentally observed magnetization as a function of q^2 becomes rather simple and accurate, for details we refer to Röding *et al.* (2012). Data was processed using self-written scripts (Matlab®) to obtain D_{mean} and the distribution width σ. The relative effective diffusion coefficient within the Γ distribution is defined by $f_{D\_g} = D_{mean}/D_{mean,\ water}$ (eq. 3). The ratio between D_{mean}/D_1 listed in Table 8.4 indicates the difference between the data analysis approaches and underlines the importance of using a physical and numerically appropriate model.

2D Inverse Laplace Transform. Another approach to model data deviating from a strictly mono-exponential behavior is a purely numerical approach, the inverse Laplace transform (ILT). Diffusion measurements can additionally be combined with relaxation measurements, and the data can be Laplace transformed in two dimensions. In the present case, D-T_2 maps were obtained by performing a 2D inverse Laplace transform (2D ILT) [19, 36, 37] to correlate diffusion and relaxation measurements for biofilm_1.

Results and Discussion

Biofilm and Biomass Characterization: Comparison of Common Quantities and Images

Biomass is commonly characterized by i.e. thickness, density, elemental composition, TSS, and VSS, which do not consider spatial and structural inhomogeneities. On the other hand, mass transport and diffusion properties strongly depend on these spatial inhomogeneities but are not unique in the sense of a one-to-one correspondence of structure and diffusion coefficient. In a first approach, the microscopic findings and the macroscopic chemical parameters were collected and compared to link these physical parameters to water diffusion.

As evident in stereomicroscopic and MRI images (Table 8.3), sludge consisted of a complex, but loose network of flocs with a small-scale heterogeneity. The measured biomass density of 1033 g/L is within the expected biomass densities for active sludge flocs with 1020-1060 g/L [38] and is higher than pure water density (998 g/L at 20°C). The mineral content was relatively low with 37 g Ca per kg TSS. It is expected that the water diffusion is hindered in the sludge flocs, and is therefore, slower than free water.

Compared to the heterogeneous structure of the sludge flocs, biofilm_1 comprised a fluffy and homogenous structure (Table 8.3). The fluffiness of the biofilm is indicative for the low biofilm density (not distinguishable from free water) and high VSS of 90%. The pycnometer measurements for biofilm_1 were not reproducible due to low density and low biomass concentration. Furthermore, spatial variation in biomass density, which influences water dynamics in the biomass, cannot be captured by a simple pycnometer

measurement. Another approach is to get insight into the biomass structure and density by MRI. MRI image contrast delivers qualitative information: biofilm_1 was visible in the slightly T_2-weighted images due to the reduced T_2 in the biofilm compared to bulk water. This effect is based mainly on the exchange of protons between EPS biopolymers (mainly OH-groups) and water molecules [39] as well as by the different molecular mobility of molecules in biofilm matrix and water. In proton-density weighted images, biofilm_1 was hardly distinguishable from bulk water because of similar proton concentration [34]. Based on this knowledge, the density was estimated to be ~1010 g/L.

Biofilm_2 was cultivated for ~12 months in a WWTP, TSS and mineral accumulation were significantly higher than in all other biofilms, therefore, diffusion is expected to be highly restricted. The iron content was especially high due to iron-accumulating bacteria (anammox) [31]. The internal structure was heterogeneous: outer biofilm layers were less dense than layers close to the carrier material reflected in the gray values of corresponding MRI voxels. Solids (precipitates, possibly $CaCO_3$) and gas bubbles (air, CO_2, N_2 gas due to microbial activity) appear black with the usual phase susceptibility artifacts. The local heterogeneities in biofilm structure can be related to advanced biofilm age, density and growth conditions. Those heterogeneities suggest that there are regions in the biofilm which for which water diffusion is restricted to a larger extent than in other regions.

Biomass	Stereomicroscopic Image	MRI
Sludge	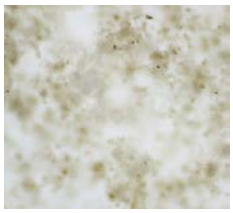	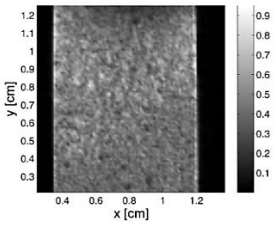
Biofilm_1		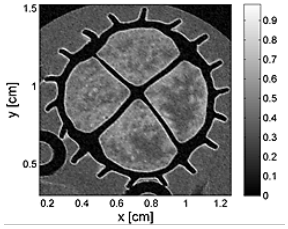
Biofilm_2		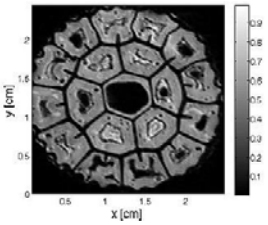
Granules_1		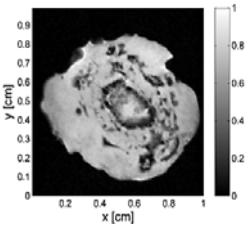
Granules_2	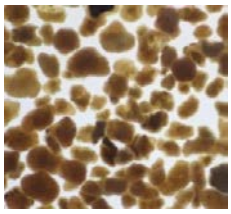	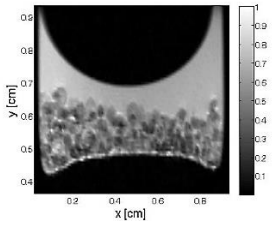

Table 8.3: Summary of stereomicroscopic images and MRI (slightly T_2-weighted image) of the investigated biofilms. The resolution for MRI images was approximately 100 µm x 100 µm.

Under certain cultivation conditions, biofilm formation is also possible without carrier material, commonly known as granules. Due to high shear stress applied during cultivation, the surface of granules_1 and granules_2 were compact and smooth. However, in the large granules_1 strong internal heterogeneities became apparent in the MRI images, such as structural layers of microorganisms and precipitates which might lower diffusion in the biomass. The biomass density was within the conventional range for aerobic granules (1005 g/L-1070 g/L), which depends among others on the cultivation conditions and volume fraction of solid [40-42]. Granules with a high solids content of precipitates can have biomass densities up to 1200 g/L [43]. Granules_2 originated from a WWTP accumulated significantly more minerals (e.g. Ca, P, Fe, P) than granules_1, which were cultivated in a lab scale reactor. Furthermore, biomass density of granules_2 was in the same range as biofilm_2. As density is known to be one of the most important parameters for diffusion in biomass (Renslow et al. 2010) the correlation between usually measured parameters and diffusion coefficients were explored.

Diffusion of Water in the Presence of Biomass

To relate biofilm geometry and composition to water diffusion, PFG-NMR diffusion experiments were carried out on different biomasses. As mentioned, the biofilm's heterogeneity poses some challenges for modelling diffusion in these systems. The logarithmic signal attenuation was measured as a function of q^2, results of biofilm_2 and granules_2 are shown in Figure 8.1 together to provide examples of the data and the numerical fits. Diffusion data from the biofilms were interpreted with both the (bi)-exponential fit (indicated as (bi.)-exp.-func.) and the gamma distribution model

(indicated by Γ distr.). The levels for good description of the data are depicted in form of 2 % and 4 % of the maximum amplitude, respectively, corresponding to the goodness of Γ distr. fit to the data. A significant difference in the signal attenuation between the samples is evident (inset in Figure 8.1), which can be explained by the different biomass properties (see Table 8.1) influencing the water dynamics significantly. The compact morphology and low VSS lead to a reduced water diffusion in granules_2 compared to biofilm_2. The (bi.)-exp.-func. leading to D_1 and D_2 does not describe the measured data sufficiently well, especially the first data points (inset in Figure 8.1). The reason is found in the discrete approach which is physically not really appropriate for a multicomponent system. A discrepancy results between D_1 (from the (bi.)-exp fit) compared to D_{mean} (from the Γ distr. fit). The Γ distr. represents the measured data above the noise level significantly better than the (bi.)-exp.-func., resulting in lower residuals leading to a better data quality and higher accuracy. The results for D_1 and D_{mean} differ by 15 % (biofilm_2) and 5 % (granules_2) which supports the above argument. The findings are in agreement with previously published results for other heterogeneous samples such as motor oils, where a better description of measured diffusion data was achieved by Γ distr. [44]. The importance of an appropriate data analysis is obvious as the diffusion coefficients influence simulation for substrate conversion in biological systems.

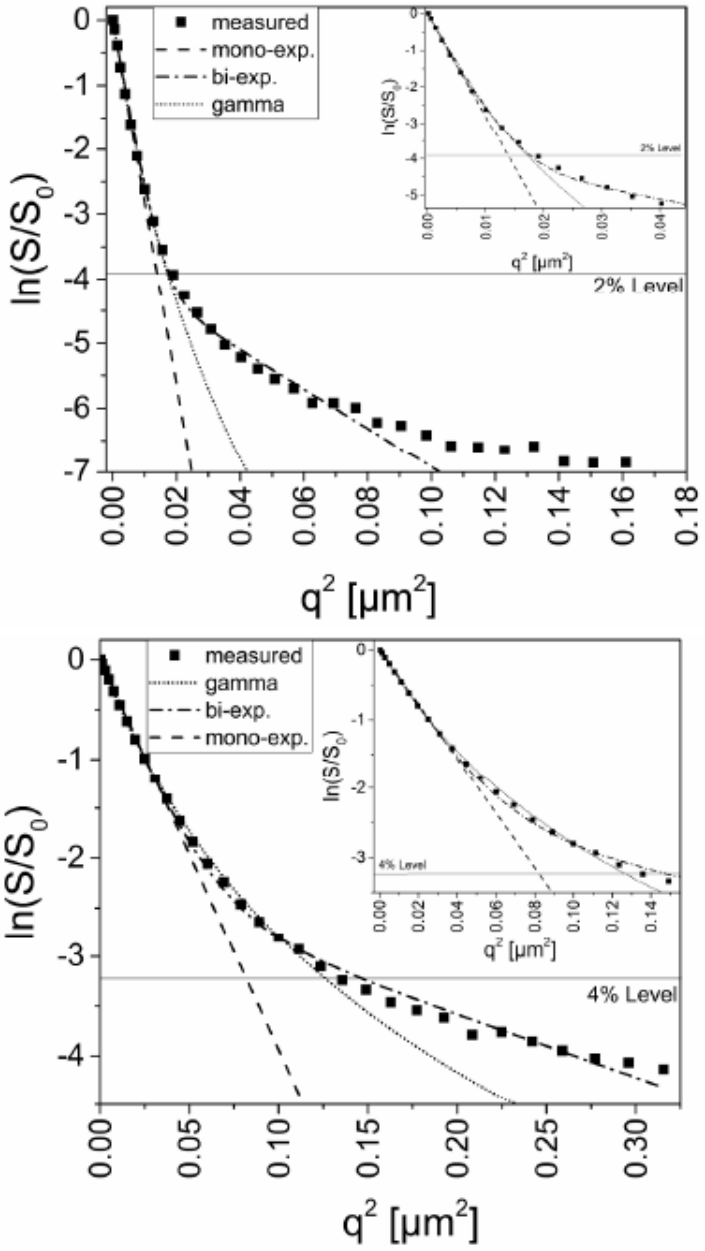

Figure 8.1: The logarithmic signal attenuation of biofilm_2 (top) and granules_2 (bottom) are depicted exemplarily for all biofilm samples as a function of q^2. The mono- and bi-exponential decay functions and the gamma distribution model were fitted to the data. The levels for good description of the data are depicted in form of 2% and 4% of the maximum amplitude, respectively, corresponding to the goodness of fit of the gamma model to the data. Deviations of the mono-exponential model are evident.

Influence of Biomass Structure on Water Dynamics

D_1 and D_{mean} were obtained by (bi.)-exp.-func. and Γ distr., respectively (Table 8.4). D_{water} = 2.09 $m^2/s \cdot 10^{-9}$ was slightly lower than the reported values [19, 45] due to different water purity and temperature. When comparing the two data processing approaches, D_{mean} and D_1 for water were similar within approximately 2%. D_{mean}/D_1 is close to 1 for free water as expected.

Sample	(bi).-exp.-func. D_1 [m^2/s] $\cdot 10^{-9}$	(bi).-exp.-func. D_{r_exp} [-]	Relative Amplitude of D_1 Contribution A_{rel} [-]	Γdistr. D_{mean} [m^2/s] $\cdot 10^{-9}$	Γdistr. D_{r_g} [-]	Γ distr. width σ [m^2/s] $\cdot 10^{-10}$	Ratio D_{mean}/D_1 [-]
Water	2.09*	1	-	2.04	1	$3.19 \cdot 10^{-3}$	0.98
Sludge	1.45	0.69	0.93	1.62	0.79	8.55	1.11
Biofilm_1	1.76	0.84	0.97	1.96	0.96	5.17	1.12
Biofilm_2	1.47	0.70	0.95	1.69	0.83	7.18	1.15
Granules_1	1.27	0.61	0.94	1.60	0.78	4.96	1.26
Granules_2	0.76	0.36	0.84	0.73	0.36	4.71	0.95

Table 8.4: Summary of diffusion coefficients (at Δ 200 ms) of the used biofilms gained by two different data analysis approaches. Diffusion coefficients D_1 and D_{mean} obtained by (bi)-exponential fit (indicated by (bi.)-exp.-func.) and gamma distribution (indicated by Γ distr.), respectively. Data indicated by asterisk (*) were fitted using mono-exponential function. D_r is the relative effective diffusion coefficient for both data processing approaches, see Eq. 2 and 3.

D_1 and D_{mean} measured in the presence of biofilms deviated by 20-30 % (D_1/D_{mean} between 0.95-1.26). This indicates a good overall agreement for both data processing approaches despite the better fitting of the measured data by Γ distribution. D_{mean} is typically slightly larger than D_1 (Table 8.4) as in the (bi)-exponential fit only D_1 with A_{rel} > 84% was considered. The minor part of the signal is associated with D_2, which is in the range of 10^{-10} to 10^{-11} m^2/s. D_2 might be assigned to intracellular water [46]. Previous studies have also demonstrated that water diffusion coefficients in biofilms are lower than in pure water due to restricted diffusion in the biomass matrix, cells, and EPS, resulting in a wide range of diffusion coefficients between 10^{-9} and 10^{-13} m^2/s [46]. f_{D_exp} and f_{D_g} vary strongly with the type of biofilm. The lowest f_{D_g} was found for granules_2 (0.36) and highest f_{D_g} for the biofilm_1 (0.96). Diffusion was most restricted in granules_2 likely due to the compact structure and high content of inorganic matter (Table 8.1). In comparison, the diffusion coefficients in heterotrophic biofilm_1 were closest to D_{water} because of the fluffy structure and high VSS of 90%. Results are within the typical range of reported relative diffusion coefficients for biofilm from 0.2 to 0.8 [47-49] except biofilm_1.

In Figure 8.2, D_1 and D_{mean} are directly compared for the different biofilm samples. The "error" bars for D_{mean} represent the width of the Γ distr. σ, listed in Table 8.4: σ for pure water was very small and not visible, whereas σ for all biofilms was large. Sludge and biofilm_2 show the highest σ possibly due to their highly heterogeneous internal structure (Table 8.4). The diffusion coefficients D_1 and D_{mean} vary for all biomass, with biofilm_1 showing fastest and granules_2 showing lowest diffusion

coefficients. The water diffusion in sludge and biofilm_2 are similar, although the biomass structure parameters differ significantly. As visible in Table 8.3, these biomasses comprise completely different morphologies being either an open network or a compact biofilm. Furthermore, biomass structural parameters (e.g. VSS, biofilm thickness and density) differ strongly and suggest that the diffusion in biofim_2 is more hindered than in the sludge. However, this is not the case. This leads to the conclusion that the assumptions regarding mass transfer in biofilms based on bulk physical properties are not directly related to the classical parameters or optical appearance.

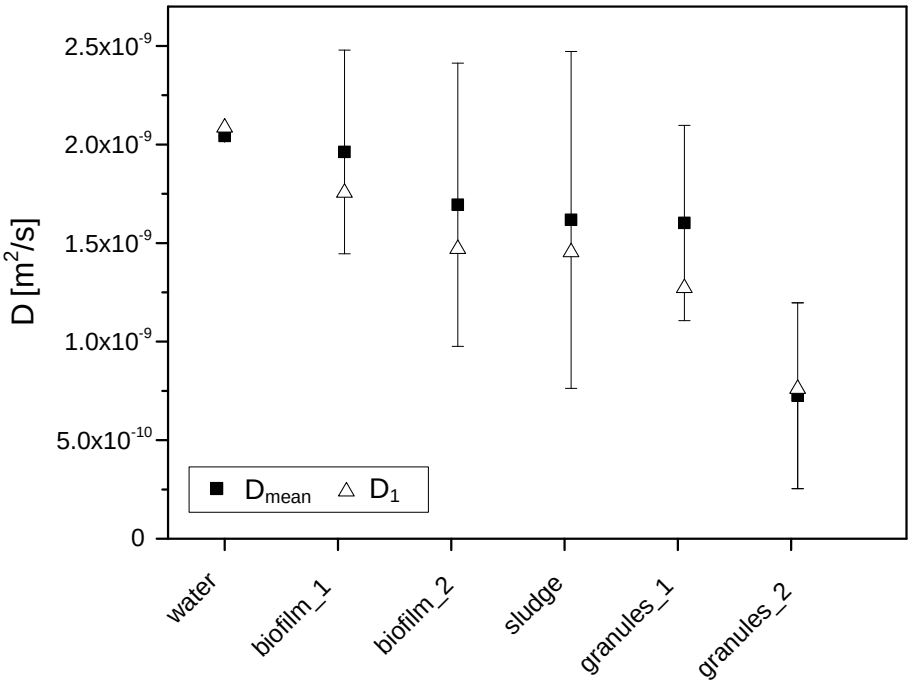

Figure 8.2: Diffusion coefficients D_1 and D_{mean} obtained by (bi)-exponential fit and Γ distribution for water and different biomasses measured with a diffusion time Δ= 200 ms. "Error" bars around D_{mean} represent not statistical errors but the width of the Γ distribution σ (Table 8.2).

No clear correlations are found between certain integral biofilm properties and diffusion coefficients: the biofilm thickness and geometry seemed to have a minor influence on *D* in the present case. For example, biofilm_2 and granules_2 had similar densities, but *D* differed by approximately 50% when using both data processing methods. Liquid channels in biofilm_2 correspond to an enhanced water diffusion within the biomass resulting in similar apparent diffusion values as highly porous sludge.

The broad range of relative diffusion coefficients highlights the fact that biofilm structure determines the mass transfer and ultimately the performance of productive biofilms, such as the mentioned wastewater biofilms or fungal bio pellets [50]. Whether the measured water diffusion can be transferred to relevant substrates for biofilms remains unclear. The substrates' molecular weight, interaction with the surroundings as well as diffusivity and penetration into the biofilm differ from water molecules and could be explored by heteronuclear NMR diffusion measurements and theoretical models can help to answer this question. Using a simple calculation, we estimated the difference between COD (chemical oxygen demand) turnover for the highest (biofilm_1) and lowest (granule_2) diffusion coefficient. The oxygen flux can roughly be estimated by: $D/\Delta z$ * (concentration DO at biofilm surface – concentration DO at z) (eq. 4), where z is the biofilm depth and DO the dissolved oxygen concentration. D_{mean} was used a diffusion coefficient due to the best fit of the data. Keeping all biofilm related parameters constant (only changing *D*) the lower diffusion results in 20 % less turnover based on flux estimates, thus knowing the diffusion coefficient is highly relevant for biofilm modelling. Further infestations are planned in the future.

Besides that, the results contribute to link transport processes to biofilm structure which was shown for nanoparticle and metal transport in biofilms [27, 51]. The comparison of classical integral quantities with optical and MRI images shows that the approach of just using one measure for biofilm characterization is insufficient. A comprehensive characterization on different time and length scales is needed when aiming for an understanding of biofilms and the processes of mass transport and especially diffusion. The link between structure, diffusion and biological activity deserves further research.

Influence of Diffusion Time on Water Dynamics

In homogeneous liquids of small molecules, D is independent of diffusion time Δ. In porous media, D decreases with increasing Δ due to barriers like physical restriction and adhesion of water molecules [14]. Biofilms can also be regarded as porous media consisting of biofilm matrix and bulk water. Our results show, that D_1 decreased with Δ for all biofilms (Figure 8.3). D_1 was selected as the trends were most pronounced. D_{mean} showed a similar but less marked effect. Water diffusion was most restricted in granules_2, indicated by the strong decline of D_1 and low diffusion coefficient asymptote of 6.5 $m^2/s \cdot 10^{-10}$ at 400 ms, followed by granules_1. A different composition of EPS and microbial communities as well as the length scales of the heterogeneous internal structures are already visible in MRI images (Table 3) and are possible explanations for our observations. The mobility of water molecules may also be decreased due to entrapment in EPS molecules [46, 52]. As already mentioned, sludge and biofilm_2 both displayed fast diffusion, similar distribution width, and a small dependence on Δ.

Biofilm_1 did not show a strong diffusion barrier; only a slight decline of D_1 relative to D_{water} was found which leads to the conclusion that mainly unrestricted bulk water is observed. The calculated D also include the diffusion in the near bulk water which may be influenced by the presence of the biofilm, as has been shown for emulsions [53].

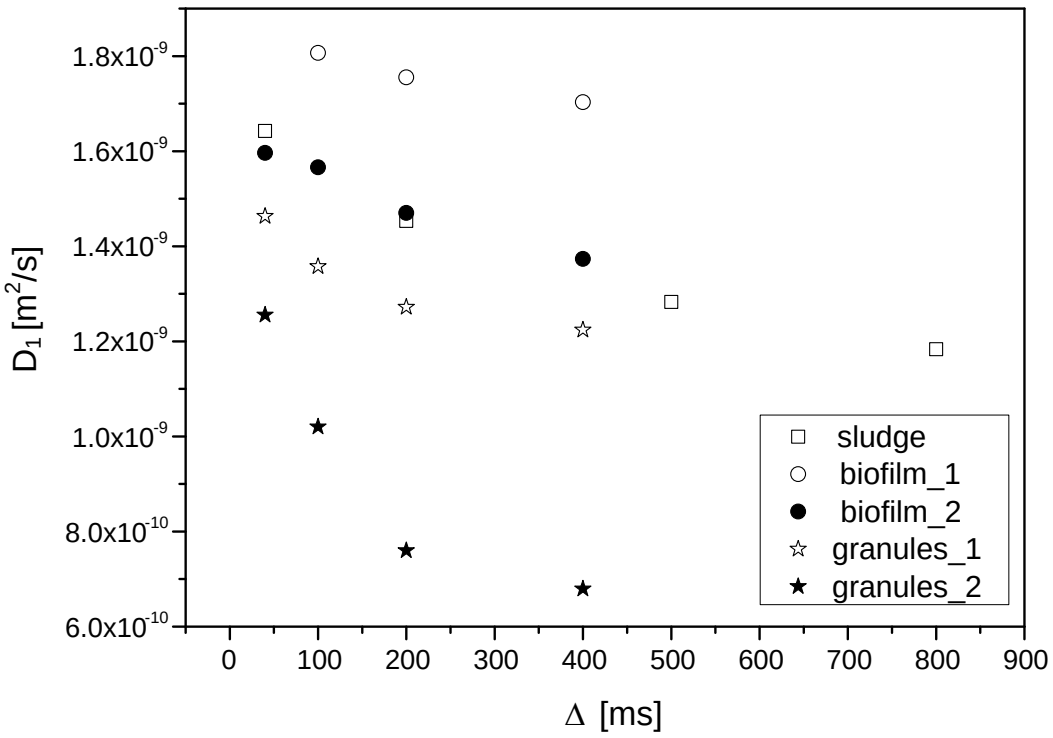

Figure 8.3: Diffusion coefficients D_1 of biofilms at different diffusion times Δ. Classically, the dependence of the diffusion coefficients on diffusion time is a hint on hindered or restricted diffusion and is most pronounced in the granules. Data points for 500 ms and 800 ms are only given for sludge.

The distributions of the effective diffusion coefficients obtained within Γ distr. are shown in Figure 8.4. Granule_2 exhibits the narrowest distribution (σ of 4.71 $m^2/s \cdot 10^{-10}$) together with the slowest D_{mean}. Faster diffusion was found for sludge and biofilm_2 with a broader distribution (σ of 8.55 and 7.18 $m^2/s \cdot 10^{-10}$). Narrow distributions, but with

faster D_{mean} were found for biofilm_1 and granules_1. The sludge and biofilm_2 results demonstrate that increased internal heterogeneity over small length scales in the biomass tends to broader distributions. The distributions give unique indications for the estimation of the overall diffusion properties of diverse biofilm systems that single parameters determined by (bi.)-exp.-func. cannot express. However, the Γ distr. model also depicts portions of ^{1}H-NMR signals which are diffusing significantly faster than free water ($D_{water} = 2.04 \cdot 10^{-09}$ m^2/s) highlighted in gray. This portion differed for all biofilms and was especially pronounced for biofilm_1. Possible explanations for this phenomenon are convection due to temperature or enhanced diffusion by concentration gradients. Larger bulk water compartments, which were evident for biofilm_1 (Table 8.3), are more prone to convective transport, resulting in larger influence on *D*. Additionally, it is known that diffusion can increase in the presence of small concentrations of nonpolar compounds, such as methanol or acetonitrile in water mixtures [54]. The convection could also be a result of vibrations induced by the large field gradients as it is difficult to immobilize the granules and biofilm carriers.

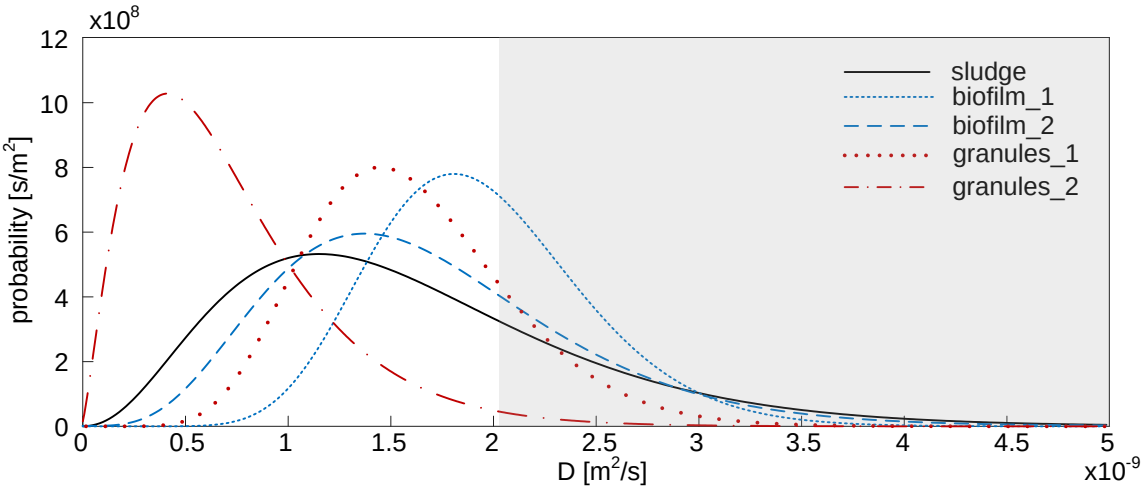

Figure 8.4: Distribution of the diffusion coefficients according to Γ distribution. $D = D_{mean}$ for free water is $2.04 \cdot 10^{-9}$ m^2/s. Gray region indicates diffusion values, which are larger than free water.

Correlation of Diffusion and Transverse Relaxation

The effective D-T_2 relaxation correlation was measured for biofilm_1 and compared to free water (Figure 8.5) using a regularization parameter $\alpha = 1*10^8$ and 64 steps during 2D-ILT. The peak in the upper edge of the maps is an artifact of 2D-ILT due to insufficient sampling of higher gradients. To confirm the location of the main peak in the 2D distribution, a single line of data was extracted in each dimension to produce a 1D spectrum of diffusion and relaxation as the 1D ILT is numerically more stable than the 2D [55]. As expected, bulk water is characterized by $D_{water} = 2.4 \times 10^{-9}$ m^2/s with a reasonably narrow distribution width and by an average T_2 of 2.6 s.

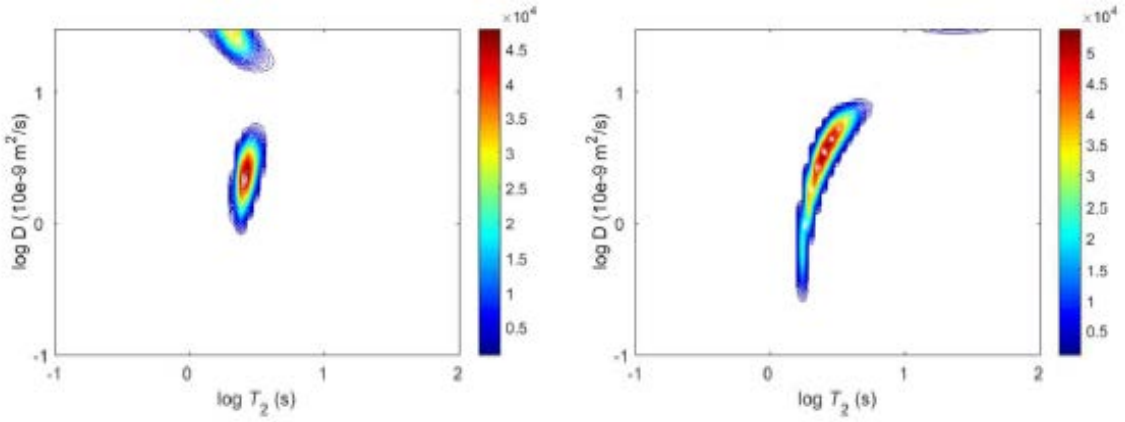

Figure 8.5: Effective diffusion spin-spin relaxation correlation maps for free water (left) and biofilm_1 (right) at a diffusion time of 100 ms. Data was processed using 2D-ILT and reveals the correlation between diffusion and transverse relaxation both being influenced by the structural properties of the biomass.

Compared to free water, the presence of biofilm_1 produces a significant shift of a portion of the signal to smaller D and lower T_2. Typically, T_2 and D in biofilms are less than that of bulk water [19, 34]. These results are consistent with previous observations. Another portion of signal attributed to the bulk water, about T_2 of 3 s, shifts towards larger D. This strongly points to convection as a possible explanation for the observation of larger diffusion coefficients in 1D diffusion experiments as well as in the correlation experiment. As mentioned earlier this could well be due to vibrations induced by the gradients and enhanced by the biofilm as it is hard to immobilize the plastic carriers in the test tubes. It should be noted that the effect is well known and occurs in low viscosity liquids even at almost no temperature gradient if the solid structures in the sample cannot be completely immobilized.

Conclusions

In this study, the water diffusion coefficients and their distributions were determined using PFG-NMR for five different biomass samples. Diffusion data was processed using conventional (bi)-exponential data analysis, the Γ distribution model and 2D ILT for data interpretation. Stereomicroscopic images are compared to MRI images and insights of D-T_2 correlation maps are introduced. The experimental results lead to the following conclusions: Similar diffusion coefficients for both data processing approaches, (bi)-exponential data analysis and Γ distribution model, were obtained with 5-26% difference between D_{mean} and D_1. A better representation of the data was achieved by the Γ distribution function with respect to numerical reproducibility and physico-chemical interpretation. No direct correlation between D_{water} and typical biofilm properties (e.g. compactness, mineral content, VSS) was observed. D_{mean} is not sufficient to describe the mass transport in multispecies biomass. Additional information is provided by MRI images and distributions of D_{water} in the biomass obtained by Γ distribution model: some areas in the biofilm seem to have exhibited more restricted transport than others, associated to gas bubbles, precipitates, and changing biofilm densities. D-T_2 correlation maps confirmed these findings and proved a shift in T_2. More research in this field is needed, especially regarding the spatial distribution of diffusion coefficients in multispecies biomass where NMR methods are a promising approach (e.g. diffusion-weighted imaging).

References

1. Costerton, J.W., et al., *Microbial Biofilms.* Annual Review of Microbiology, 1995. **49**: p. 711-745.

2. Sutherland, I.W., *The biofilm matrix - an immobilized but dynamic microbial environment.* Trends in Microbiology, 2001. **9**(5): p. 222-227.

3. Metcalf & Eddy, I., *Wastewater engineering : treatment and reuse*. Fourth edition ed. 2003, Boston: McGraw-Hill, 2003.

4. Stewart, P.S., *Diffusion in biofilms.* Journal of Bacteriology, 2003. **185**(5): p. 1485-1491.

5. Flemming, H.-C. and J. Wingender, *The biofilm matrix.* Nature Reviews Microbiology, 2010. **8**(9): p. 623-633.

6. Wäsche, S., H. Horn, and D.C. Hempel, *Influence of growth conditions on biofilm development and mass transfer at the bulk/biofilm interface.* Water Research, 2002. **36**: p. 4775-4784.

7. Neu, T.R., et al., *Advanced imaging techniques for assessment of structure, composition and function in biofilm systems.* FEMS Microbiology Ecology, 2010. **72**(1): p. 1-21.

8. Guimera, X., et al., *Dynamic characterization of external and internal mass transport in heterotrophic biofilms from microsensors measurements.* Water Research, 2016. **102**: p. 551-560.

9. Billings, N., et al., *Material properties of biofilms-a review of methods for understanding permeability and mechanics.* Reports on Progress in Physics, 2015. **78**(3).

10. Horn, H. and S. Lackner, *Modeling of Biofilm Systems: A Review*, in *Productive Biofilms*, K. Muffler and R. Ulber, Editors. 2014, Springer-Verlag Berlin: Berlin. p. 53-76.

11. Li, C.Y., et al., *Assessing the influence of biofilm surface roughness on mass transfer by combining optical coherence tomography and two-dimensional modeling.* Biotechnology and Bioengineering, 2016. **113**(5): p. 989-1000.

12. IWA, *IWA Task Group on Biofilm Modeling: Mathematical Modeling of Biofilms*. 2006: IWA Publishing.

13. Callaghan, P.T., *Translational Dynamics and Magnetic Resonance: Principles of Pulsed Gradient Spin Echo NMR*. 2011, Oxford: Oxford Press.

14. Callaghan, P., *Principles of Nuclear Magnetic Resonance Microscopy*. 1991: Oxford University Press. 516.

15. Fabich, H., et al., *Microbial and algal alginate gelation characterized by magnetic resonance.* Journal of Biotechnology, 2012. **61**(3): p. 320– 327.

16. Arndt, F., et al., *New Insights into Sodium Alginate Fouling of Ceramic Hollow Fiber Membranes by NMR Imaging.* AIChE Journal, 2016. **62**(7): p. 2459-2467.

17. Seymour, J.D., et al., *Magnetic resonance microscopy of biofouling induced scale dependent transport in porous media.* Advances in Water Resources, 2007. **30**(6-7): p. 1408-1420.

18. Seymour, J.D., et al., *Anomalous fluid transport in porous media induced by biofilm growth.* Physical Review Letters, 2004. **93**(19).

19. Vogt, S.J., et al., *Permeability of a growing biofilm in a porous media fluid flow analyzed by magnetic resonance displacement-relaxation correlations.* Biotechnology and Bioengineering, 2013. **110**(5): p. 1366-1375.

20. Manz, B., et al., *Investigation of Biofilm Structure, Flow Patterns and Detachment with Magnetic Resonance Imaging.* Water Science and Technology, 2005. **52**(7): p. 1-6.

21. Herrling, M.P., et al., *Determining the Flow Regime in a Biofilm Carrier by Means of Magnetic Resonance Imaging.* Biotechnology and Bioengineering, 2015. **112**(5): p. 1023-1032.

22. Lens, P.N.L., et al., *Diffusional properties of methanogenic granular sludge: H-1 NMR characterization.* Applied and Environmental Microbiology, 2003. **69**(11): p. 6644-6649.

23. Bishop, P.L., T.C. Zhang, and Y.C. Fu, *Effects of biofilm structure, microbial distributions and mass transport on biodegradation processes.* Water Science and Technology, 1995. **31**(1): p. 143-152.

24. Debeer, D., et al., *Effects of biofilm structures on oxygen distribution and mass transport.* Biotechnology and Bioengineering, 1994. **43**(11): p. 1131-1138.

25. Ramanan, B., et al., *Magnetic Resonance Imaging of Mass Transport and Structure Inside a Phototrophic Biofilm.* Current Microbiology, 2013. **66**(5): p. 456-461.

26. McLean, J.S., O.N. Ona, and P.D. Majors, *Correlated biofilm imaging, transport and metabolism measurements via combined nuclear magnetic resonance and confocal microscopy.* Isme Journal, 2008. **2**(2): p. 121-131.

27. Phoenix, V.R. and W.M. Holmes, *Magnetic resonance imaging of structure, diffusivity, and copper immobilization in a phototrophic biofilm.* Applied and Environmental Microbiology, 2008. **74**(15): p. 4934-4943.

28. Röding, M., et al., *The gamma distribution model for pulsed-field gradient NMR studies of molecular-weight distributions of polymers.* Journal of Magnetic Resonance, 2012. **222**: p. 105-111.

29. Röding, M., N. Williamson, and M. Nydén, *Gamma convolution models for self-diffusion coefficient distributions in PGSE NMR.* Journal of Magnetic Resonance, 2015. **261**: p. 6-10.

30. Herrling, M.P., et al., *Short and long term biosorption of silica-coated iron oxide nanoparticles in heterotrophic biofilms.* Science of The Total Environment, 2016. **544**: p. 722-729.

31. Gilbert, E.M., et al., *Low Temperature Partial Nitritation/Anammox in a Moving Bed Biofilm Reactor Treating Low Strength Wastewater.* Environmental Science & Technology, 2014. **48**(15): p. 8784-8792.

32. Loosdrecht, M.C.M.v., et al., *Experimental Methods in Wastewater Treatment*. 2016: Intl Water Assn, IWA.

33. Kimmich, R., *NMR - Tomography, Diffusometry, Relaxometry.* Springer Verlag, 1997.

34. Ranzinger, F., et al., *Direct surface visualization of biofilms with high spin coordination clusters using Magnetic Resonance Imaging.* Acta Biomaterialia, 2016. **31**: p. 167-177.

35. Callaghan, P.T., *Principles of Nuclear Magnetic Resonance Microscopy*. 1991, New York: Oxford University Press.

36. Lee, J.H., et al., *2-Dimensional Inverse Laplace Transform Nmr - Altered Relaxation-Times Allow Detection of Exchange-Correlation.* Journal of the American Chemical Society, 1993. **115**(17): p. 7761-7764.

37. Callaghan, P.T., S. Godefroy, and B.N. Ryland, *Diffusion-Relaxation Correlation in Simple Pore Structures.* Journal of Magnetic Resonance, 2003. **162**(2): p. 320-327.

38. Dammel, E.E. and E.D. Schroeder, *Density of activated sludge solids.* Water Research, 1991. **25**(7): p. 841-846.

39. Sanderlin, A.B., et al., *Biofilm detection in natural unconsolidated porous media using a low-field magnetic resonance system.* Environmental Science & Technology, 2013. **47**(2): p. 987-992.

40. Winkler, M.K.H., et al., *Factors influencing the density of aerobic granular sludge.* Applied Microbiology and Biotechnology, 2013. **97**(16): p. 7459-7468.

41. de Kreuk, M.K., M. Pronk, and M.C.M. van Loosdrecht, *Formation of aerobic granules and conversion processes in an aerobic granular sludge reactor at moderate and low temperatures.* Water Research, 2005. **39**(18): p. 4476-4484.

42. Etterer, T. and P.A. Wilderer, *Generation and properties of aerobic granular sludge.* Water Science and Technology, 2001. **43**(3): p. 19-26.

43. Juang, Y.-C., et al., *Stable aerobic granules for continuous-flow reactors: Precipitating calcium and iron salts in granular interiors.* Bioresource Technology, 2010. **101**(21): p. 8051-8057.

44. Foerster, E., H. Nirschl, and G. Guthausen, *NMR Diffusion and Relaxation for Monitoring of Degradation in Motor Oils.* Applied Magnetic Resonance, 2017. **48**(1): p. 51-65.

45. Renslow, R.S., et al., *In Situ Effective Diffusion Coefficient Profiles in Live Biofilms Using Pulsed-Field Gradient Nuclear Magnetic Resonance.* Biotechnology and Bioengineering, 2010. **106**(6): p. 928-937.

46. Vogt, M., H.C. Flemming, and W.S. Veeman, *Diffusion in Pseudomonas aeruginosa biofilms: a pulsed field gradient NMR study.* Journal of Biotechnology, 2000. **77**(1): p. 137-146.

47. Stewart, P.S., *A review of experimental measurements of effective diffusive permeabilities and effective diffusion coefficients in biofilms.* Biotechnology and Bioengineering, 1998. **59**(3): p. 261-272.

48. Wood, B.D., M. Quintard, and S. Whitaker, *Calculation of effective diffusivities for biofilms and tissues.* Biotechnology and Bioengineering, 2002. **77**(5): p. 495-516.

49. Horn, H., H. Reiff, and E. Morgenroth, *Simulation of growth and detachment in biofilm systems under defined hydrodynamic conditions.* Biotechnology and Bioengineering, 2003. **81**(5): p. 607-617.

50. Hille, A., et al., *Effective Diffusivities and Mass Fluxes in Fungal Biopellets.* Biotechnology and Bioengineering, 2009. **103**(6): p. 1202-1213.

51. Peulen, T.-O. and K.J. Wilkinson, *Diffusion of Nanoparticles in a Biofilm.* Environmental Science & Technology, 2011. **45**(8): p. 3367-3373.

52. Belton, P.S., *NMR and the mobility of water in polysaccharide gels.* International Journal of Biological Macromolecules, 1997. **21**(1-2): p. 81-88.

53. Guan, X.Z., et al., *PFG-NMR on W1/O/W2-emulsions: Evidence for molecular exchange between water phases.* European Journal of Lipid Science and Technology, 2010. **112**(8): p. 828-837.

54. Derlacki, Z.J., et al., *Diffusion coefficients of methanol and water and the mutual diffusion coefficient in methanol-water solutions at 278 and 298 K.* Journal of Physical Chemistry, 1985. **89**(24): p. 5318-5322.

55. Kausik, R. and M.D. Hurlimann, *Sensitivity and resolution of two-dimensional NMR diffusion-relaxation measurements.* Journal of Magnetic Resonance, 2016. **270**: p. 12-23.

STRUCTURE AND DIFFUSION OF AEROBIC GRANULAR SLUDGE USING MAGNETIC RESONANCE

Abstract

Magnetic resonance imaging (MRI) and nuclear magnetic resonance (NMR) allow non-invasive measurements describing both internal structures and transport properties of opaque, complex materials like biofilms [1-3]. High-field MRI was used to image aerobic granules collected from full-scale wastewater treatment plants in the Netherlands. T_1 and T_2 relaxation-weighted images reveal heterogeneous internal structures that include high and low density regions and solid inclusions. Additionally, pulsed field gradient (PFG) NMR methods and multi-dimensional correlation and exchange experiments were used to measure diffusion and transport properties within undisturbed granules. Our results show differences in rates of water diffusion within the heterogeneous granule structure and suggest that models employing a single diffusion coefficient may be insufficient to capture the complexity of transport behaviour within the granules.

Introduction

Compared to conventional activated sludge systems where the biomass exists in dispersed flocs, aerobic granular sludge offers numerous benefits for wastewater treatment including compact design, lower energy costs, and excellent biomass retention [4]. By their very nature as spherical biofilm aggregates, granules are composed of a

variety of microniches—aerobic, anoxic, anaerobic —where diverse bio-chemical conversions can occur simultaneously within the same granule [5, 6] (Figure 9.1). In the last two decades, research into the formation, structure, and metabolism of granular sludge has flourished [7-12] and today full-scale reactors are in operation in several countries, including the Netherlands [13].

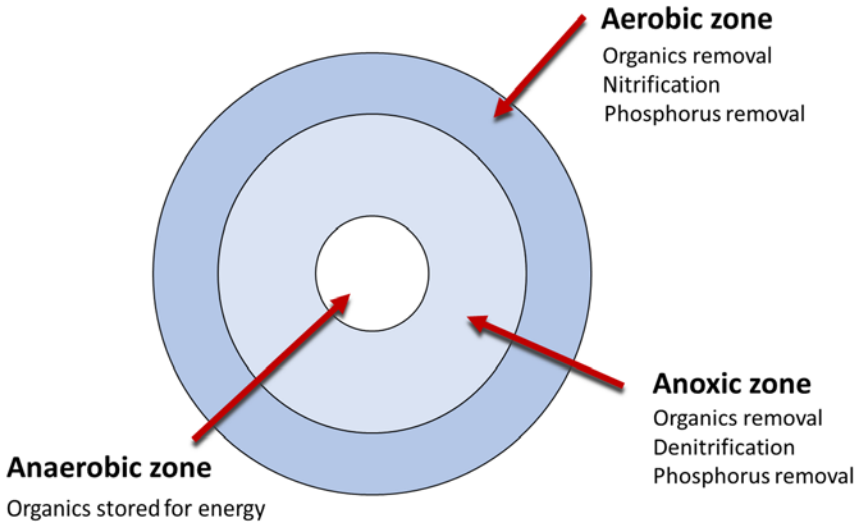

Figure 9.1. A conceptual model of aerobic granular sludge shows the different redox zones within the granule as concentric structural layers where distinct biochemical conversions occur simultaneously.

While it is known that hydrodynamic shear, substrate type and loading rate, oxygen concentration, microbial growth rate, and microbial strain are all important parameters in the formation of aerobic biofilm granules, the governing parameter has yet to be identified [14]. Under appropriate operating conditions, floccular sludge self-assembles into millimetre-scale biofilm granules in which EPS provides a robust framework. The biofilm matrix of the granule has a complex structure [15], consisting of

hydrated gel-like fibers allowing for phenotypic heterogeneity and differentiation of cells within the colony analogous to a multi-cellular organism [16-18]. Early MRI experiments on anaerobic granules provided evidence of a cluster structure [19] while imaging of methanogenic granules showed that the EPS matrix is organized in concentric layers and the granules appear to have 'hollow' centers [20].

This complex morphology influences rates of diffusion and substrate utilization in a manner that is not entirely well-defined. Moreover, granular sludge reactors may take months or even years to reach steady state conditions, making experimental studies using parametric analysis on large scale reactors infeasible. Mathematical models have been developed to simulate substrate removal and the distribution of microbial populations and processes within the biofilm granule [21-24], but their utility is limited by a lack of knowledge. Until these models are refined with robust experimental results related to the formation and activity of granular sludge, the technology will not by fully exploited for wastewater treatment.

The current research explores how the internal granular structure is related to reactive mass transport in the granule, with the goal of understanding how wastewater components move through the granule and are degraded or captured, and how granule activity is related to the structure of the aggregate. Most granules used in laboratory research have been grown on simple soluble substrates like acetate, while natural wastewaters contain complex substrates, including slowly biodegradable particulates [25-27]. These particulates must be hydrolyzed before they are available to bacteria for conversion, which influences the granulation kinetics, the resulting granule morphology,

as well as reactor performance and the required operational conditions [26]. Specifically, the research will examine in the future how particulates and complex contaminants commonly found in wastewater influence the morphology and mass transport properties of aerobic granular sludge [13, 25, 27].

NMR and MRI can provide spatially-resolved data on granule structure, composition, and reaction-diffusion properties non-invasively and non-destructively under various hydrodynamic conditions. These capabilities represent a significant advantage over conventional methods like microscopy and micro-electrode studies which are necessarily invasive and destructive. These methods also tend to be limited in terms of the range of length scales that can be probed. For example, micro-electrodes provide point or 1D data. Optical methods can achieve a high spatial resolution, but over a limited field of view. NMR and MRI can better bridge multiple length scales, such as in the case of a 5 mm sample field of view with 50 μm^2 pixel resolution. As the research described in this chapter is in the early stages of a multi-year international collaborative project, this chapter will focus on two main research questions, each explored with different NMR and MRI methods.

The first current research question is related to the internal granule structure. Does the internal structure of aerobic granules used in practice for wastewater treatment conform to the conceptual model shown in Figure 9.1? Secondary questions are related to how consistent the observed structure is between samples from the same treatment plant, from different treatment plants, over time as the granules age, and between laboratory granules and those treating real wastewater. Imaging experiments give insight

to these structural questions.

Secondly, the current research explores how diffusive transport varies within a granule by measuring the effective water diffusion coefficient using PFG-NMR methods. Specifically, how large is the range of D_{eff} within the granules? Multi-dimensional diffusion – relaxation correlation (D-T_2), relaxation – relaxation correlation (T_1-T_2), and relaxation exchange (T_2-T_2) experiments can also provide information about how the diffusive behaviour of water is related to structural regions with different relaxation rates, and the timescale of exchange of water between those different regions.

Material and Methods

Sample Collection and Preparation

Samples of aerobic granular sludge were collected during the aeration phase of the treatment cycle from sequencing batch reactors at the Utrecht and Garmerwolde wastewater treatment plants in the Netherlands (Figure 9.2). The samples, which ranged in volume from several hundred millilitres to several litres, were stored in airtight plastic containers in the refrigerator without substrate addition. Granules from other sources, including anammox granules from the B-stage of the Dokhaven treatment plant, anammox granules treating the rejection water at Sluisjesdijk treatment plant, laboratory VFA-producing granules, granules produced from extracted and re-constituted EPS, and control samples of alginate beads were also imaged using the same parameters for comparison with the aerobic granules. For the MRI experiments, a single granule was added to tap water in a 5 mm NMR sample tube. The granules were elevated within the

sample tube by either a plug of Teflon tape, a stack of alginate beads, or a 3-D printed polymer frame (Figure 9.3).

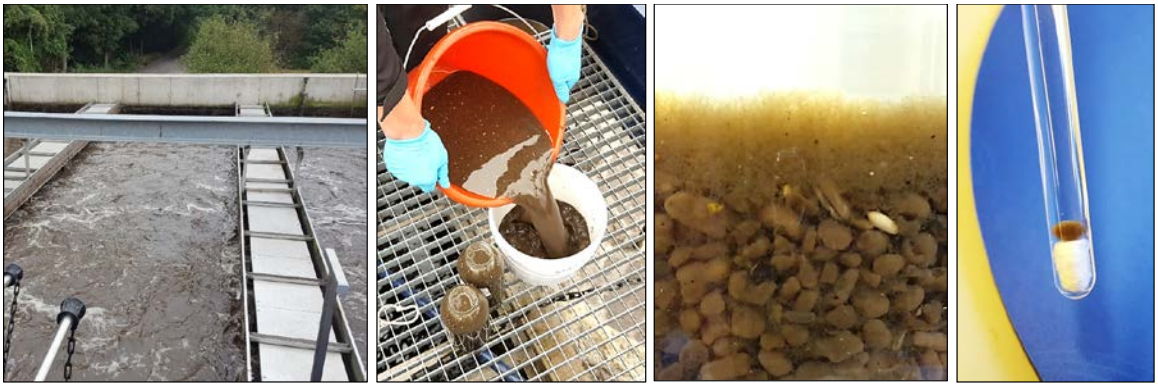

Figure 9.2. (Left to right) Samples were collected from the Utrecht wastewater treatment plant's Nereda ™ sequencing batch reactor. The granules settle first with the floccular sludge on top. A single granule was then placed in a 5 mm NMR sample tube for imaging experiments.

Samples for the PFG-NMR measurements and multi-dimensional correlation and exchange measurements were collected from Garmerwolde treatment plant as described above and stored in tap water in the refrigerator until measurements were collected, approximately 4 months after sampling. As these measurements are not spatially resolved in 2D, a stack of granules in tap water was added to the 5 mm NMR sample tube to maximize the signal obtained from the granules relative to bulk water signal.

Figure 9.3. The granule samples were placed in 5 mm NMR sample tubes, elevated with either Teflon tape (left), a stack of alginate beads (center), or a 3-D printed frame (right). The granules shown include an extracted EPS granule, a VFA-producing laboratory grown granule, and an anammox granule from the B-stage of Dokhaven treatment plant.

NMR and MRI Measurements

1H NMR and MRI are sensitive to hydrogen protons, typically water in most biological systems. NMR relaxation rates provide information on the physico-chemical environments in which different water populations exist. Timing of the pulses which make up the NMR measurement can be adjusted to accentuate contrast between these different water populations and distinguish between intercellular water, rotationally restricted water in the EPS matrix, and free water in the bulk phase. T_1 relaxation- and T_2 relaxation-weighted images provide such a contrast and were collected on MRI tomographs operating at 7 T and 22 T using parameters found in Table 9.1. The MRI images were collected on both fresh granules (several days after sampling) and on aged samples (approximately 2 months after sampling). The granules were also imaged using

traditional microscopy techniques including scanning electron microscopy (SEM) and transmission electron microscopy (TEM).

	22 T		7 T
	T_1 weighted	T_2 weighted	T_2 map
Repetition time, Tr (s)	0.550	5	6
Echo time, tE, (ms)	5.3	5.3	5.2
Number of echoes	16	16	128
Spatial resolution (μm)	47 x 47	47 x 47	47 x 47
Slice thickness (μm)	100	100	100
Measurement time	9 min 23 s	10 min 40 s	13 h 39 min

Table 9.1. MRI measurement parameters. The 22 T MRI system at uNMR-NL, an NWO-funded National Roadmap Large-Scale Facility of the Netherlands, located at Utrecht University, produced high-resolution and high-contrast images with a minimal measurement time. The 7 T MRI system at Wageningen University achieved similar resolution with longer measurement times.

Additionally, pulsed field gradient (PFG) NMR methods were used to measure diffusion coefficients in aged granules from Garmerwolde treatment plant. The samples were approximately 4 months old at the time of measurement. Experiments were performed on a 250 MHz (5T) Bruker Avance III superconducting magnet with using a high-power probe, Micro 5 gradient set (with a 2.81 T/m maximum gradient) and a 5 mm radio-frequency coil. Two-dimensional correlation and exchange experiments were also conducted to relate diffusion to T_2 relaxation and to examine exchange between different T_2 populations.

The pulsed-gradient stimulated-echo (PGStE) experiment was used to collect diffusion data for these granules given the relatively fast signal decay rates observed for

the Garmerwolde granules during imaging. During the diffusion time, Δ, the stimulated echo experiment allows for the net magnetization to be stored in the longitudinal plane where it is not subject to T_2 relaxation processes (Figure 3.2). Therefore, measurable signal remains following extended diffusion times in the range of tens to hundreds of milliseconds.

Data Analysis

T_2 Maps. Multi-slice multi-echo (MSME) images produce a stack of 2-D images showing the echo amplitude per pixel in each sample slice. An image is collected of each echo in the signal decay, such that the stack of images for each slice shows the attenuation of signal in each pixel. Fitting the echo attenuation in each pixel as an exponential decay produces the effective T_2 relaxation rate in each pixel. These rates, or the relaxation times, can be displayed in a 2D image of the sample where the pixel intensity corresponds to the effective relaxation rate, $R_{2,\text{eff}}$, or the effective relaxation time, $T_{2,\text{eff}}$. T_2 map data was analysed with both IDL software at WUR by Dr. Frank Vergeldt and also at MSU by the author using Prospa v3.13.

Diffusion Images. PGStE data for the 1D image was analysed first in Prospa by Fourier transforming the echo data in the read direction. The data was then exported to Matlab as a magnitude image where a fitting function was applied in the **q**-direction to calculate the effective diffusion coefficient at each point in the 1D image. Diffusion-weighted images collected in Paravision 5.1 were analysed in Prospa v3.13. A Prospa macro first created a matrix of **q**-space data for each image slice prior to using the

standard Prospa makeDiffMap macro to produce an image in which the pixel intensity corresponds to the apparent diffusion coefficient (ADC) in the sample.

Multidimensional Correlation and Exchange Experiments. Data collected for correlation and exchange experiments were analysed in Matlab using the 2D Inverse Laplace Transform (ILT) which uses a non-negative least squares fitting function with a regularization parameter to minimize the error in the solution.

Results and Discussion

MRI of Granule Internal Structure

The initial research goal of this project was to simply identify internal structural features within the granules and determine how consistent those features are across granule sources, types, and over time. T_1 and T_2 relaxation-weighted images of granules from wastewater treatment plants reveal heterogeneous internal structures that include high and low density regions and solid inclusions. Images of granules from both the Utrecht and Garmerwolde treatment plants reflected similar heterogeneity, though it was significantly more difficult to collect high quality images from the Garmerwolde granules because of rapid signal decay. For that reason, most of the images included here are of granules collected from the Utrecht wastewater treatment plant.

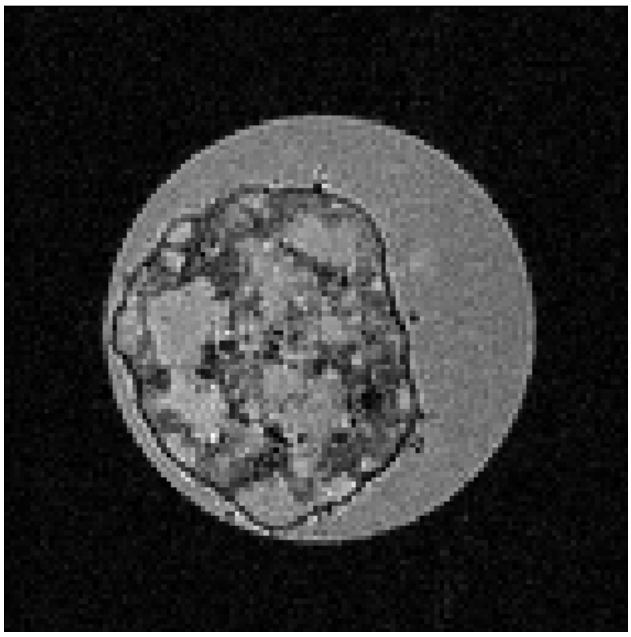

Figure 9.4. The third echo of a T_1-weighted image of a Nereda® granule (Utrecht wastewater treatment plant) obtained from the 22 T MRI shows high contrast between areas of differing density within the granule. Spatial resolution is 47 x 47 x 100 μm^3, echo time = 16 ms, repetition time = 550 ms. Because of the long echo time, brighter regions in the granule correspond to less dense regions where diffusion is less restricted. Darker areas indicate either decreased proton density, in the case of solid inclusions, or more rotationally restricted water as would be found in cell clusters. All granules were imaged in a 5mm tube of tap water, which is the relatively brighter fluid surrounding the granule.

Figure 9.4 shows a fresh granule from the Utrecht treatment plant with characteristic dark, dense regions and brighter less dense regions. Relatively bright bulk water is visible in the sample tube outside the granule. This image is T_1-weighted with a short repetition time of 550 ms to enhance signal collection from the more dense regions of the granule. It is also, however, an image of the third echo in the decay train making the image also T_2-weighted. The combination of T_1- and T_2-weighting provides excellent contrast between regions of differing density and water mobility.

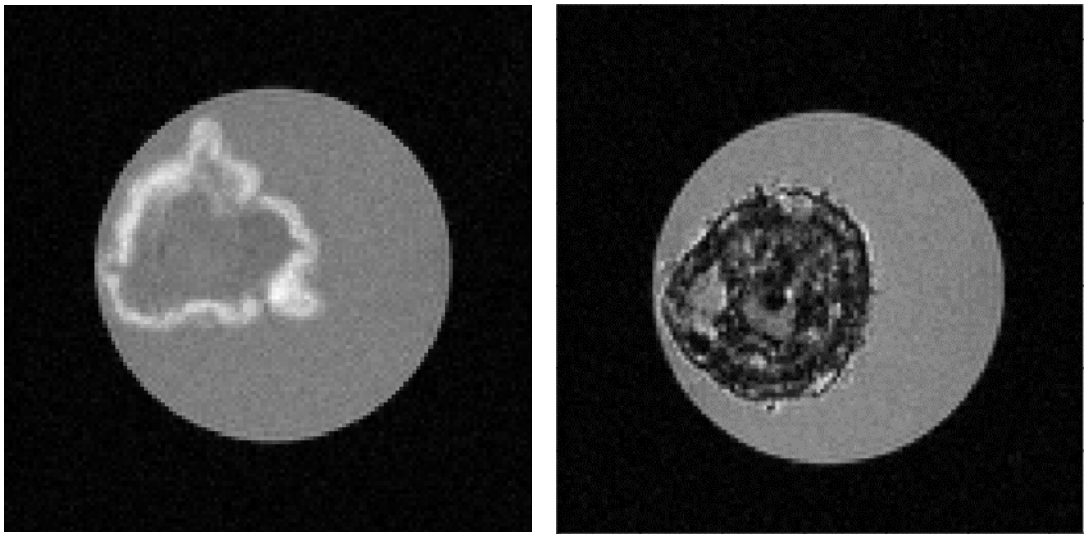

Figure 9.5. The first echoes of T_1-weighted images of a laboratory VFA-producing granule (left) and a Nereda® granule (Garmerwolde wastewater treatment plant) obtained from the 22 T MRI show the high structural variability observed between laboratory and treatment plant granules. Spatial resolution is 47 x 47 x 100 μm^3, echo time = 5.3 ms, repetition time = 550 ms. In the left image, the bright regions correspond to biomass, which is selectively highlighted with T_1-weighting relative to the bulk water outside the granule. The right image, collected under the same measurement parameters, shows dense biomass in the dark regions where the signal has already decayed due to T_2 relaxation during the 5.3 ms echo time.

Figure 9.5 compares a laboratory-grown volatile fatty acid (VFA) producing granule with a fresh granule from the Garmerwolde treatment plant. The VFA granule appears in this image to be hollow, as was later confirmed with traditional microscopy after sectioning the granule. The Garmerwolde granule, on the other hand, exhibits a similar heterogeneous structure as seen in Figure 9.4, though more dense overall. Since the VFA and Garmerwolde granules contain different bacterial populations and grow under different operating conditions – anaerobic for the VFA granules and aerobic for the Garmerwolde granules – it is not possible with these data to draw any conclusions about the internal structural differences between laboratory and treatment plant granules in

general. However, as a starting point, it shows how different the internal structure can be.

T_2 Maps. Effective T_2 maps of granules from the Utrecht treatment plant for different age granules (Figure 9.6) show the same heterogeneous internal structure observed in Figures 9.4 and 9.5. The maps were produced from MSME images (32 echoes) made on the 22 T system in the national NMR lab in Utrecht. Spatial resolution is 47 x 47 x 100 microns. The effective T_2 maps also show that neither the structure nor the T_2 relaxation behaviour changes significantly over the timescale of approximately 2 months. The image on the left in Figure 9.6 shows a fresh granule from Utrecht, while the right image shows a different granule from the same sample, imaged after 2 months of storage in the refrigerator. In both $T_{2,\,\mathrm{eff}}$ maps, the bulk water T_2 relaxation time is approximately 18 ms, which is approximately equal to the maximum internal T_2 time in the granule 'voids.' In the dense biomass regions of the granules, the minimum T_2 times are approximately 6 ms with the apparent transition between 'voids' and biomass occurring around a T_2 time of 12 ms. T_2 maps of alginate beads collected in the same system with the same measurement parameters produced the same bulk water relaxation time and a relatively uniform relaxation time within the bead of approximately 13 ms (not shown).

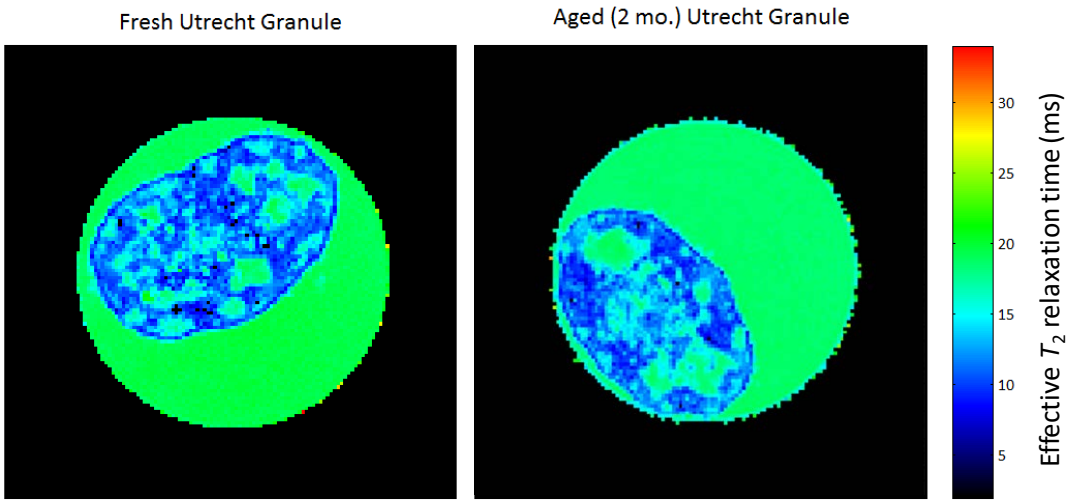

Figure 9.6. T_2 maps of granules from Utrecht wastewater treatment plant. The image on the left was taken of a fresh aerobic granule, while the image on the right was collected from the same sample of granules after aging for 2 months. The T_2 relaxation times range between approximately 18 ms in the bulk water and in the less dense regions of the granules to approximately 6 ms in the dense cell clusters of the granules. There is no discernible difference between the fresh and aged granules in terms of T_2 relaxation. The spatial resolution is 47 x 47 x 100 microns.

Boundary Layer. A dark apparent boundary layer is visible on the surface of both the Utrecht granule in Figure 9.4 and the Garmerwolde granule in Figure 9.5, but was not observed on any of the granules produced in laboratory reactors. This layer is very sharp and well-defined in the MRI images, particularly those from the 22 T system. Two recent studies have examined the surfaces of granular sludge and may provide insight into the nature of the material observed in the MRI images. Poot *et al*. recently found evidence of stratification of ammonia-oxiding bacteria (AOB) and nitritre-oxidizing bacteria (NOB) at the surface of aerobic granules grown in low-strength wastewater [28] using fluorescent in-situ hybridization (FISH). The authors suggest that the position of the AOB on the granule surface provides a competitive advantage to the AOB in terms of

oxygen competition with the NOB, and also protects the NOB colonies from detachment. In order to achieve complete nitritation for subsequent anaerobic ammonium oxidation, NOB populations must be repressed relative to AOB populations. Thus, the layer may be a dense biomass region, composed primarily of nitrifiers. Manas *et al.* reported formation of calcium and phosphorus precipitates on the surfaces of anaerobic granules, observed using SEM-EDX imaging [29]. These authors report that 'rings' of the mineral were visible in the largest granules imaged, suggesting successive periods of mineralization and overgrowth. The Garmerwolde granule shown in Figure 9.5 appears to show successive rings as described by Manas *et al*.

As part of the effort to identify the apparent boundary layer observed with MRI, SEM-EDX imaging was applied to the outer surfaces of samples of the same type of granules used in the MRI experiments. A single Garmerwolde granule was also cut with a razor blade prior to imaging with SEM-EDX to compare the internal and exterior physical properties. Results (not shown) indicate that while some mineral precipitates had formed in the granules collected from treatment plants, there was no significant precipitate layer on the surface of the granule. The sectioned granule appeared to show a more dense organic region at the surface, but the quality of the section was not high enough to make a conclusive determination.

Images were also made using transmission electron microscopy (TEM) to more directly observe the surface layer of aerobic granules from Garmerwolde treatment plant. TEM imaging involves embedding an osmium-treated sample in resin which is then

baked until solid. The samples are then sectioned with a diamond blade to thicknesses of 70-90 nm and imaged in the electron microscope.

Figure 9.7 shows dense cell clusters at the surface of a granule in the top of the image, with the embedding resin outside of the granule at the bottom. The black areas on the edges of the image are the copper frame which holds the thin sectioned sample. There is no precipitate or solid particulate debris visible on the granule surface. Figure 9.8 shows the edge of an internal cell cluster where the lower left area of the image is an internal 'void' space. No cells are visible in the void, though some EPS matrix material is visible in this and other TEM images of the less dense regions as imaged by MRI. When viewed at the same scale, the granule exterior exhibits greater cell density than the interior cluster, which may account for the dark apparent boundary layer.

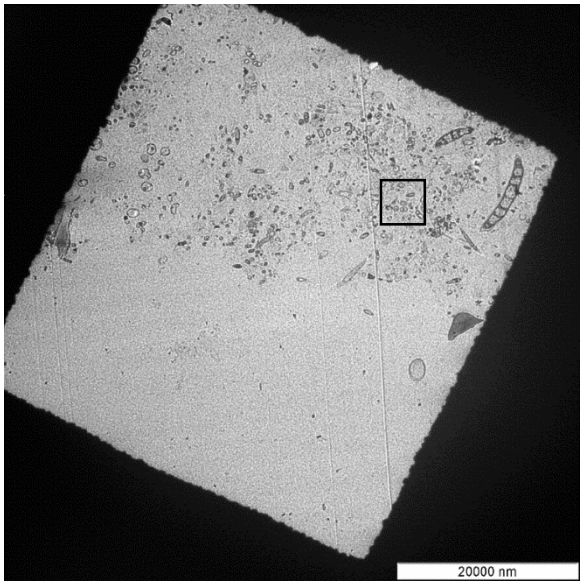

Figure 9.7. TEM image showing the outer surface of a Garmerwolde granule (top of half of image) relative to the embedding resin at the bottom. The cells shown extend approximately 20-30 microns into the granule. Scale bar is 20 µm. A (~ 5µm)^2 box is shown for reference to Figure 9.8.

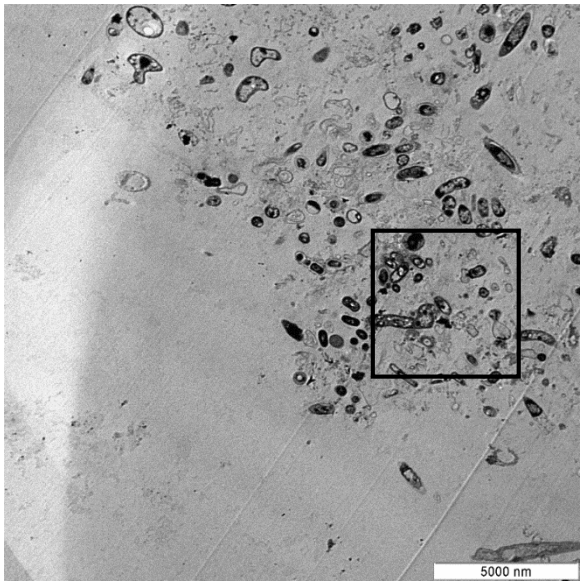

Figure 9.8. TEM image of the edge of an internal cell cluster and corresponding 'void' region. Scale bar is 5 μm. A (~ 5μm)^2 box is shown for reference to Figure 9.7.

PFG and Multidimensional NMR

In addition to imaging experiments, PFG-NMR diffusion measurements and 2D correlation and exchange measurements were recently collected at MSU at 5T field strength using a stack of 4-month-old granules collected from Garmerwolde treatment plant in a 5mm sample tube. These measurements confirm the presence of multiple T_2 populations, a distribution of T_1 populations, and variable diffusion coefficients within the granules.

The PGStE pulse sequence was used in conjunction with imaging in the read direction to produce a 1D image of the diffusion coefficients through a stack of alginate beads and one aerobic granule in tap water (Figure 9.9, top). At a diffusion time, Δ, of 100 ms, the average effective water diffusion coefficient within the granule was approximately 1 x 10^{-9} m^2/s while the measured bulk water diffusion coefficient was

approximately 1.8 x 10^{-9} m^2/s. The alginate beads exhibited slightly faster diffusion than the granule with an effective water diffusion coefficient of 1.5 x 10^{-9} m^2/s on average. All of the measured effective diffusion coefficients are lower than the typical free water diffusion coefficient of approximately 2 x 10^{-9} m^2/s.

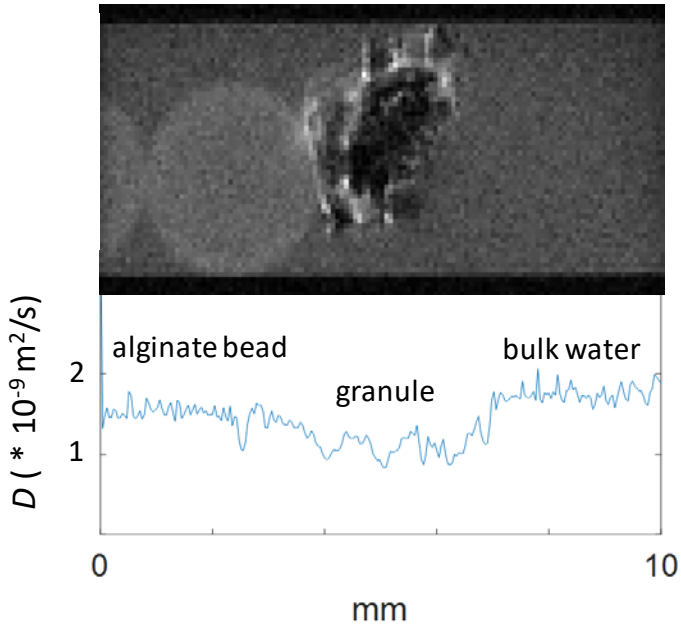

Figure 9.9. A 1D image of the diffusion coefficients was collected over a stack of alginate beads and a single aged Garmerwolde granule in DI water. The top 2D image shows the sample. The bottom image shows the calculated 1D diffusion coefficient for each point in the image.

Diffusion-weighted images were collected of aged anammox granules sampled from the B-Stage of the Dokhaven treatment plant in the Netherlands (Figure 9.10). The images were collected on the 5 T system at MSU in a 10 mm NMR sample tube with a spatial resolution of 78 µm x 78 µm x 300 µm and 16 averages. Eight gradient values were used, ranging from 0 – 1 T/m. The resulting map of apparent diffusion coefficients (ADC) shows reduced diffusion rates in the biomass within the granules and near-free-

water diffusion rates in the central ‘void’ regions. Unfortuately, the spin echo-based pulse sequence and diffusion measurement parameters used were not able capture and resolve apparent diffusion coefficients in the dense outer layer of the granules. Future work will involve optimizing the diffusion-weighted imaging measurement using a stimulated echo to overcome the rapid signal loss in the outer granule layer.

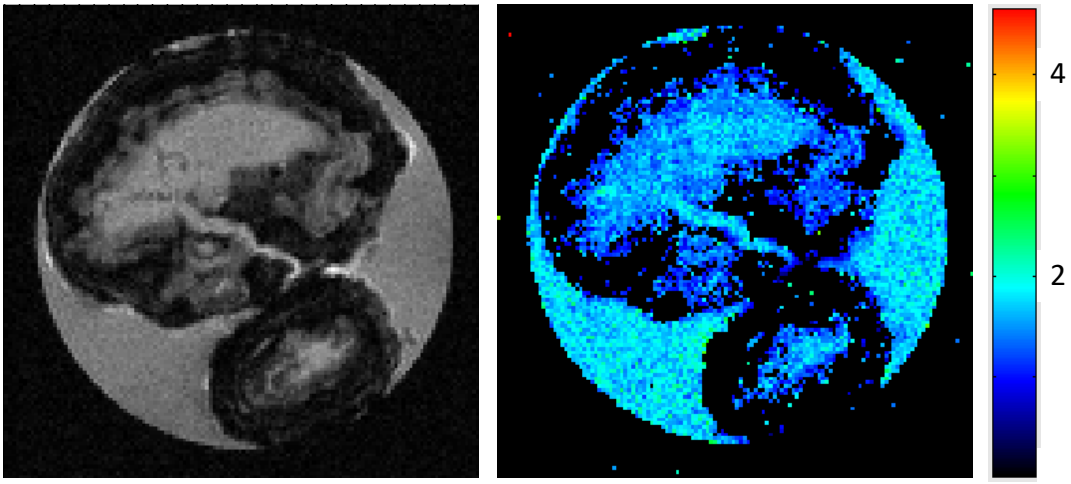

Figure 9.10. Two anammox granules from the B-stage of Dokhaven treatment plant were imaged on the 5 T system at MSU using diffusion weighting (left). The resulting ADC map (right) shows reduced apparent diffusion coefficients within the biofilm matrix, but was not able to quantify diffusion coefficients in the dense exterior regions of the granules due to rapid signal attenuation.

Diffusion – relaxation (D-T_2) correlation measurements were also collected, both on the 5 T system at MSU and on a 0.3 T system at Wageningen University (WUR) in the Netherlands (not shown). The D-T_2 correlation measured at MSU with $\Delta = 50$ ms used a stack of aged granules from Garmerwolde in DI water. The correlation (Figure 9.11) shows multiple T_2 populations with the largest peak corresponding to free water. The distribution of diffusion coefficients suggests that the biomass, with the shorter

relaxation times, has a range of water diffusion coefficients which extends to lower values.

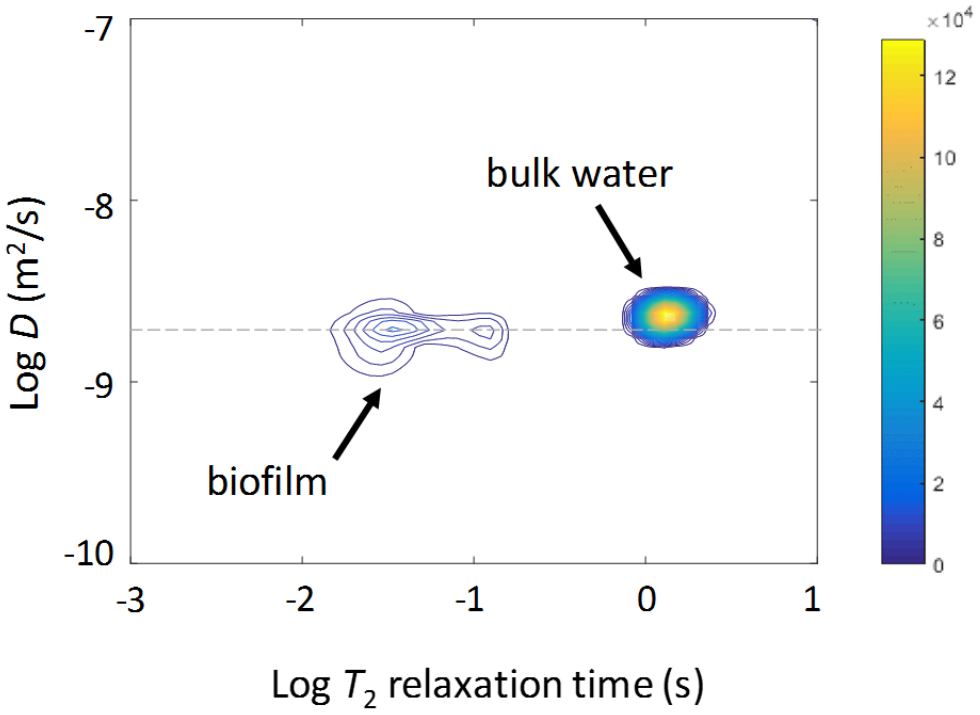

Figure 9.11. *D*-T_2 correlation was measured for a stack of aged Garmerwolde granules in tap water on a 5 T system at MSU.

The T_2 portion of the *D*-T_2 correlation is very similar to the 1D T_2 distribution measured on the stack of aged Garmerwolde granules on the 5 T system at MSU (Figure 9.12). Here, the large peak on the order of T_2 = 1-2 seconds corresponds to bulk water outside the granules. When compared to T_2 maps measured on the 7 T system at WUR (Figure 9.12, right), the small peak at approximately 100-200 ms corresponds to the water in the 'void' regions of the granules. The relatively large population with T_2 relaxation times of approximately 70 – 20 ms corresponds to the water within the dense biomass regions of the granule.

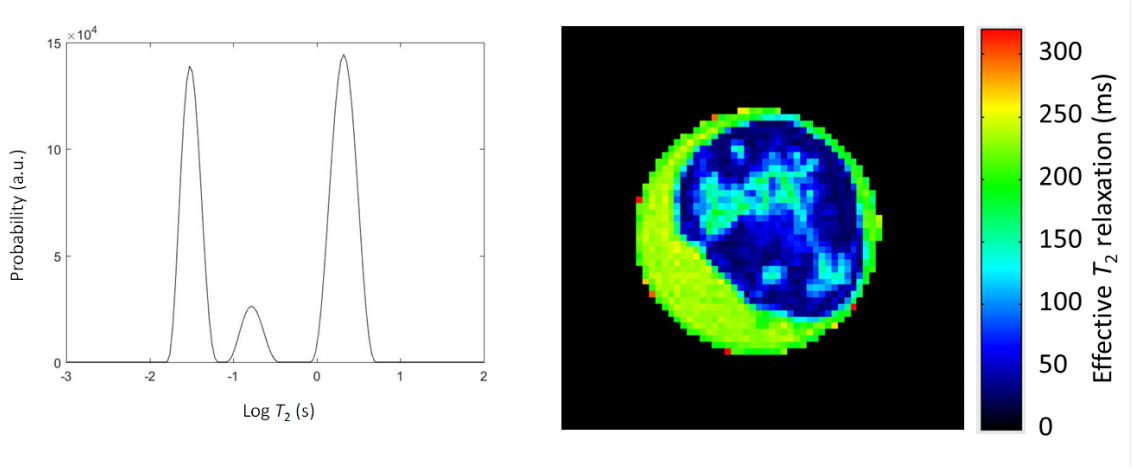

Figure 9.12. The 1D T_2 distribution measured on the 5 T system at MSU on a stack of aged (4 month old) Garmerwolde granules (left) corresponds well to the T_2 map of a fresh Utrecht granule measured on the 7 T system at WUR (right) and the T_2 distribution measured as part of the D- T_2 correlation shown in Figure 9.11. The intensity of the free water peak is diminished in the current figure due to the loading of the sample tube to maximize sample coming from the granules and minimize the volume of bulk water.

In addition to the D-T_2 correlation, $T_1 - T_2$ correlation was also measured on the 5 T system at MSU (Figure 9.13). This correlation again shows the expected T_2 distribution as well as a broadening of the T_1 distribution relative to bulk water which indicates the presence of more solid-like material in the granule.

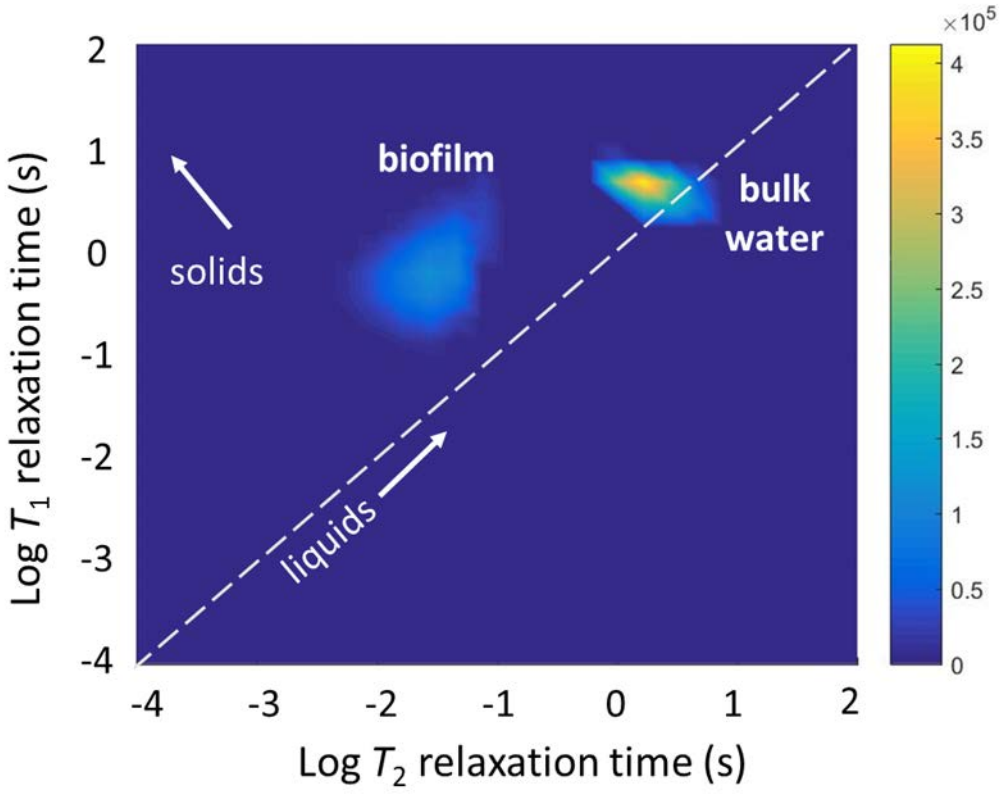

Figure 9.13. The T_1-T_2 correlation measured on the 5 T system at MSU on a stack of aged (4 month old) Garmerwolde granules.

$T_2 - T_2$ exchange was measured on the 5 T system at MSU using mixing times, τ_m, of 0 ms and 150 ms (Figure 9.14). The measurement recorded at τ_m = 150 ms does not show the classic off-diagonal peaks that would definitively show exchange between the different T_2 populations. However, since there is a distribution of T_1 relaxation populations present as well, exchange may result in averaging. Further data analysis and measurement optimization is necessary to determine the extent of exchange between T_2 populations.

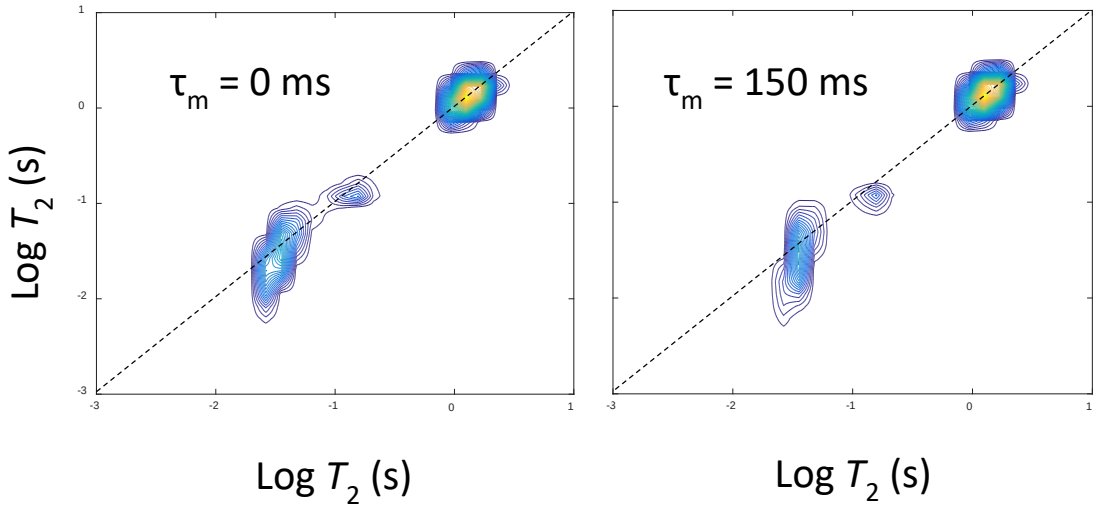

Figure 9.14. T_2-T_2 exchange measurements conducted on the 5T MSU system using a stack of aged Garmerwolde granules in DI water do not exhibit off-diagonal exchange peaks.

Measurements are ongoing at the time of thesis submission. Preliminary results indicate that aerobic granules from municipal treatment plants in the Netherlands exhibit a heterogeneous structure comprised of dense cell clusters and 'voids' containing diffuse EPS matrix. The structures observed are closer to the cluster structure observed in some anaerobic granules [19] than to the concentric ring schematic shown in Figure 9.1. The structures were stable over a storage period of several months. The apparent boundary layer visibile in the MRI images appears to be of organic origin, composed of dense cell clusters.

The preliminary findings also suggest that a distribution of diffusion coefficients exists within each individual granule in which diffusion is slower than bulk water within the dense biomass regions and on the order of free water in the 'voids.' This finding suggests that models employing a single diffusion coefficient, often based on invasive

micro-electrode measurements on laboratory granules, may be insufficient to capture the complexity of transport behaviour within granules treating wastewater. Further work is necessary to optimize measurement parameters and pulse sequences in order to measure spatially-resolved apparent diffusion coefficients in the dense biomass regions of the granules. Rapid signal decay renders spin-echo methods ineffective, but also suggests significant differences in diffusion behavior exist in these regions. Finally, this research demonstrates that NMR and MRI methods can provide novel and reliable data regarding the structure and transport properties of aerobic granular sludge.

Future Work

Future experiments are planned to repeat the PFG-NMR and 2D correlation and exchange experiments described above on fresh granule samples to produce data more relevant for inclusion in mathematical models. Furthermore, propagator measurements will be collected using a flow cell with a packed bed of granules to investigate the timescale for exchange between the bulk flowing water and the intergranular water which can shed light on not only transport properties of the system but also reaction kinetics. Tracer particles will also be added to the flow to explore the fate of particulates within the granular sludge system.

Acknowledgements

Experiments at the 22T (950 MHz) NMR instrument were supported by uNMR-NL, an NWO-funded National Roadmap Large-Scale Facility of the Netherlands (project 184.032.207)

References

1. Codd, S.L., et al., *Magnetic Resonance Microscopy of Biofilm and Bioreactor Transport*, in *NMR Imaging in Chemical Engineering*, S. Stapf and S.-I. Han, Editors. 2006, Wiley: USA.

2. Van As, H. and P. Lens, *Use of H-1 NMR to study transport processes in porous biosystems.* Journal of Industrial Microbiology & Biotechnology, 2001. **26**(1-2): p. 43-52.

3. Windt, C.W., F.J. Vergeldt, and H. Van As, *Correlated displacement-T-2 MRI by means of a Pulsed Field Gradient-Multi Spin Echo method.* Journal of Magnetic Resonance, 2007. **185**(2): p. 230-239.

4. Lin, Y., et al., *Characterization of alginate-like exopolysaccharides isolated from aerobic granular sludge in pilot-plant.* Water Research, 2010. **44**(11): p. 3355-3364.

5. Da-Wen, G. and T. Yu, *Versatility and application of anaerobic ammonium-oxidizing bacteria.* Applied Microbiology & Biotechnology, 2011. **91**(4): p. 887-894.

6. de Kreuk, M., J.J. Heijnen, and M.C.M. van Loosdrecht, *Simultaneous COD, nitrogen, and phosphate removal by aerobic granular sludge.* Biotechnology and Bioengineering, 2005. **90**(6): p. 761-769.

7. Beun, J.J., M.C.M. van Loosdrecht, and J.J. Heijnen, *Aerobic granulation in a sequencing batch airlift reactor.* Water Research, 2002. **36**(3): p. 702-712.

8. de Kreuk, M.K. and M.C.M. van Loosdrecht, *Selection of slow growing organisms as a means for improving aerobic granular sludge stability.* Water Science and Technology, 2004. **49**(11-12): p. 9-17.

9. de Kreuk, M.K. and M.C.M. van Loosdrecht, *Formation of aerobic granules with domestic sewage.* Journal of Environmental Engineering-ASCE, 2006. **132**(6): p. 694-697.

10. Liu, Y. and J.H. Tay, *The essential role of hydrodynamic shear force in the formation of biofilm and granular sludge.* Water Research, 2002. **36**(7): p. 1653-1665.

11. Nicolella, C., M.C.M. van Loosdrecht, and J.J. Heijnen, *Wastewater treatment with particulate biofilm reactors.* Journal of Biotechnology, 2000. **80**(1): p. 1-33.

12. Tay, J.H., Q.S. Liu, and Y. Liu, *The role of cellular polysaccharides in the*

formation and stability of aerobic granules. Letters in Applied Microbiology, 2001. **33**(3): p. 222-226.

13. Pronk, M., et al., *Full scale performance of the aerobic granular sludge process for sewage treatment.* Water Research, 2015. **84**: p. 207-217.

14. de Kreuk, M.K., N. Kishida, and M.C.M. van Loosdrecht, *Aerobic granular sludge - state of the art.* Water Science and Technology, 2007. **55**(8-9): p. 75-81.

15. Vogt, S.J., et al., *Permeability of a growing biofilm in a porous media fluid flow analyzed by magnetic resonance displacement-relaxation correlations.* Biotechnology and Bioengineering, 2013. **110**(5): p. 1366-1375.

16. Stoodley, P., et al., *Biofilms as complex differentiated communities.* Annual Review of Microbiology, 2002. **56**: p. 187-209.

17. Sauer, K., et al., *Pseudomonas aeruginosa displays multiple phenotypes during development as a biofilm.* Journal of Bacteriology, 2002. **184**(4): p. 1140-1154.

18. Stewart, P.S. and M.J. Franklin, *Physiological heterogeneity in biofilms.* Nature Reviews Microbiology, 2008. **6**(3): p. 199-210.

19. Gonzalez-Gil, G., et al., *Cluster structure of anaerobic aggregates of an expanded granular sludge bed reactor.* Applied and Environmental Microbiology, 2001. **67**(8): p. 3683-3692.

20. Lens, P.N.L., et al., *Diffusional properties of methanogenic granular sludge: H-1 NMR characterization.* Applied and Environmental Microbiology, 2003. **69**(11): p. 6644-6649.

21. Eberl, H.J., et al., *A three-dimensional numerical study on the correlation of spatial structure, hydrodynamic conditions, and mass transfer and conversion in biofilms.* Chemical Engineering Science, 2000. **55**(24): p. 6209-6222.

22. Kreft, J.U., et al., *Individual-based modelling of biofilms.* Microbiology-Sgm, 2001. **147**: p. 2897-2912.

23. Picioreanu, C., J.U. Kreft, and M.C.M. van Loosdrecht, *Particle-based multidimensional multispecies Biofilm model.* Applied and Environmental Microbiology, 2004. **70**(5): p. 3024-3040.

24. Picioreanu, C., M.C.M. van Loosdrecht, and J.J. Heijnen, *Effect of diffusive and convective substrate transport on biofilm structure formation: A two-dimensional modeling study.* Biotechnology and Bioengineering, 2000. **69**(5): p. 504-515.

25. de Kreuk, M.K., et al., *Behavior of polymeric substrates in an aerobic granular*

sludge system. Water Research, 2010. **44**(20): p. 5929-5938.

26. Wagner, J., et al., *Effect of particulate organic substrate on aerobic granulation and operating conditions of sequencing batch reactors.* Water Research, 2015. **85**: p. 158-166.

27. Pronk, M., et al., *Effect and behaviour of different substrates in relation to the formation of aerobic granular sludge.* Applied Microbiology and Biotechnology, 2015. **99**(12): p. 5257-5268.

28. Poot, V., et al., *Effects of the residual ammonium concentration on NOB repression during partial nitritation with granular sludge.* Water Research, 2016. **106**: p. 518-530.

29. Manas, A., et al., *Location and chemical composition of microbially induced phosphorus precipitates in anaerobic and aerobic granular sludge.* Environmental Technology, 2012. **33**(19): p. 2195-2209.

CONCLUSIONS

The work comprising this thesis demonstrates the versatility of NMR as a method to explore complex and heterogeneous biofilm – porous media systems. NMR measurements were applied at field strengths ranging from 250 kHz to 950 MHz to study opaque systems ranging from macro-scale subsurface soils to millimeter scale granular sludge biofilms. In all cases, the NMR measurements provided data non-destructively.

The low-field NMR experiments conducted during this thesis included 1) a laboratory study to detect biofilm accumulation in a laboratory model well-bore reactor, 2) a field demonstration to detect biofilm accumulation in natural subsurface soils, and 3) a laboratory study to detect microbially-induced calcite precipitation in the same model well-bore reactor. In each of these experiments, T_2 relaxation distributions were measured over time to compare the signal response at the initial, clean condition to the final, biofouled condition. Identification of the typical signal response for biofilm accumulation and calcite precipitation in porous media may lead to the application of low-field borehole NMR tools as sensors for bioremediation projects involving a biobarrier.

The laboratory and field-scale studies to detect biofilm accumulation measured a shortening of the mean log T_2 relaxation time (T_{2ML}) due to biofilm growth. In the lab study, T_{2ML} decreased by approximately 50%, while in the field study the decrease was approximately 60% in the LF well (~275 kHz) and approximately 40% in the HF well (~400 kHz). Biofilm growth was confirmed with microscopy and microbiological

methods in the lab study and by oxidizing and flushing the biofilm from the sensitive zone in the field study.

In the lab study using the low-field borehole NMR tool to detect calcite precipitation, T_2 relaxation distributions recorded during the biomineralization process showed an increase in the mean log T_2 time and a bifurcation of the initial single relaxation mode into a small population with very fast relaxation and a larger population with slower relaxation. This result indicates that, in the relatively large pores of the sandpack, the effect of changing the mineral surface of the pore space had a more significant impact on T_2 relaxation than the reduction in the pore size. The possibility remains that a shortening of T_{2ML} could be observed if the pores were initially smaller than those in the reactor sandpack. In addition to the change in the T_2 distribution, the NMR measured water content in the reactor decreased to 76% of the initial value as calcite displaced water in the pores and as excess CO_2 gas collected. Calcite precipitation was confirmed with destructive sampling followed by SEM imaging and acid digestion to quantify calcium present. These measurements indicate that approximately 12% of the pore space was occupied by calcite at the end of the experiment. The results of this experiment indicate that low-field NMR is sensitive to calcite precipitation, though further research is needed to evaluate the influence of initial pore size and mineral surface on the T_2 relaxation response.

The studies conducted at high magnetic field strength include collaborative work with Dr. Maria Pia Herrling, a summer visitor to the Montana State University Magnetic Resonance Lab from Karlsruhe Institute of Technology in Karlsruhe, Germany and

collaborative work conducted in part in the Netherlands with Dr. Merle de Kreuk and Dr. Henk Van As as part of an NSF-funded 4-month visit by the author. In both cases, the system of interest was biofilm used in wastewater treatment.

As part of her research into water diffusion in various biofilm structures, including floccular sludge, granular sludge, and biofilm grown on plastic carriers, Dr. Herrling measured diffusion-relaxation correlations at MSU with the author. In this study, we found no direct correlation between the water self-diffusion coefficient, D_{water}, and typical biofilm properties like biofilm density and concentration of volatile suspended solids. Additionally, the mean self-diffusion coefficient, D_{mean}, is not sufficient to describe diffusion behavior in multi-species biofilms. High resolution MRI found some areas in the biofilm exhibited restricted diffusion due to the presence of precipitates and differing biofilm densities. The D-T_2 correlations confirmed these findings and showed shorter T_2 relaxation in the carrier with biofilm attached.

The final experimental work included in this thesis describes ongoing experimental work on the structure and diffusion properties of aerobic granular sludge biofilms sampled from full-scale wastewater treatment plants in the Netherlands. High-field MRI was used to image the complex and heterogeneous internal structure of the granules. Additional high field PFG NMR experiments related to diffusion and transport within the granules are currently being conducted at MSU using samples from Dutch treatment plants. Preliminary findings from this work show a heterogeneous, cluster-like structure in the aerobic granules obtained from the Utrecht treatment reactor, and a more dense, heterogeneous structure in granules collected from the Garmerwolde treatment

plant, where the dense biomass regions and less dense EPS regions have differing diffusive properties. These results have implications for modeling to optimize reactor performance since the presence of multiple diffusion coefficients is not currently accounted for in the models. Furthermore, the presence of inactive EPS regions may affect granule activity and performance, or serve some other useful function not yet understood. This experimental work is ongoing.

Thus, this thesis demonstrates that low-field borehole NMR has potential for use as an *in-situ* sensor of biofilm accumulation and calcite precipitation for field applications related to bioremediation. Moreover, high field PFG NMR and MRI can provide spatially resolved data related to the structure and transport properties of aerobic granular sludge biofilms used for wastewater treatment—data that is extremely challenging, if not impossible, to obtain with other methods.

REFERENCES CITED

Allison, D.G., *The biofilm matrix.* Biofouling, 2003. **19**(2): p. 139-150.

Anand, V., Hirasaki, George J., *Paramagnetic relaxation in sandstones: Distinguishing T_1 and T_2 dependence on surface relaxation, internal gradients and dependence on echo spacing.* Journal of Magnetic Resonance, 2008. **190**: p. 68-85.

Arndt, F., et al., *New Insights into Sodium Alginate Fouling of Ceramic Hollow Fiber Membranes by NMR Imaging.* AIChE Journal, 2016. **62**(7): p. 2459-2467.

Bayer, J.V., F. Jaeger, and G.E. Schaumann, *Proton Nuclear Magnetic Resonance (NMR) Relaxometry in Soil Science Applications.* Open Magnetic Resonance Journal, 2010. **3**: p. 15-26.

Beech, I.B. and J. Sunner, *Biocorrosion: towards understanding interactions between biofilms and metals.* Current opinion in biotechnology, 2004. **15**(3): p. 181-6.

Behroozmand, A.A., K. Keating, and E. Auken, *A Review of the Principles and Applications of the NMR Technique for Near-Surface Characterization.* Surveys in Geophysics, 2015. **36**(1): p. 27-85.

Belton, P.S., *NMR and the mobility of water in polysaccharide gels.* International Journal of Biological Macromolecules, 1997. **21**(1-2): p. 81-88.

Benjamin, M.M., *Water Chemistry*. Series in Water Resources and Environmental Engineering. 2002, New York, NY: McGraw-Hill.

Beun, J.J., M.C.M. van Loosdrecht, and J.J. Heijnen, *Aerobic granulation in a sequencing batch airlift reactor.* Water Research, 2002. **36**(3): p. 702-712.

Billings, N., et al., *Material properties of biofilms-a review of methods for understanding permeability and mechanics.* Reports on Progress in Physics, 2015. **78**(3).

Binley, A., et al., *The emergence of hydrogeophysics for improved understanding of subsurface processes over multiple scales.* Water Resources Research, 2015. **51**(6): p. 3837-3866.

Bishop, P.L., T.C. Zhang, and Y.C. Fu, *Effects of biofilm structure, microbial distributions and mass transport on biodegradation processes.* Water Science and Technology, 1995. **31**(1): p. 143-152.

Blumich, B., et al., *The NMR-mouse: Construction, excitation, and applications.* Magnetic Resonance Imaging, 1998. **16**(5-6): p. 479-484.

Blümich, B., F. Casanova, and S. Appelt, *NMR at low magnetic fields.* Chemical Physics Letters, 2009. **477**(4–6): p. 231-240.

Blumich, B., J. Perlo, and F. Casanova, *Mobile single-sided NMR.* Progress in Nuclear Magnetic Resonance Spectroscopy, 2008. **52**(4): p. 197-269.

Brownstein, K.R. and C.E. Tarr, *Importance of classical diffusion in NMR studies of water in biological cells.* Physical Review A, 1979. **19**(6): p. 2446-2453.

Bryar, T.R., C.J. Daughney, and R.J. Knight, *Paramagnetic effects of iron(III) species on nuclear magnetic relaxation of fluid protons in porous media.* Journal of Magnetic Resonance, 2000. **142**(1): p. 74-85.

Bryar, T.R. and R.J. Knight, *Sensitivity of nuclear magnetic resonance relaxation measurements to changing soil redox conditions.* Geophysical Research Letters, 2002. **29**(24).

Butler, J.J., Jr., et al., *Characterizing hydraulic conductivity with the direct-push permeameter.* Ground Water, 2007. **45**(4): p. 409-419.

Callaghan, P.T., *Principles of Nuclear Magnetic Resonance Microscopy*. 1991, New York: Oxford University Press.

Callaghan, P.T., *Translational Dynamics & Magnetic Resonance: Principles of Pulsed Gradient Spin Echo NMR*. 2011, New York: Oxford University Press.

Callaghan, P.T., S. Godefroy, and B.N. Ryland, *Diffusion-Relaxation Correlation in Simple Pore Structures.* Journal of Magnetic Resonance, 2003. **162**(2): p. 320-327.

Camper, A.K., *Organic matter, pipe materials, disinfectants and biofilms in distribution systems*. 2014, IWA Publishing. p. 73-94.

Careghini, A., S. Saponaro, and E. Sezenna, *Biobarriers for groundwater treatment: a review.* Water Science and Technology, 2013. **67**(3): p. 453-468.

Carr, H.Y. and E.M. Purcell, *Effects of diffusion on free precession in nuclear magnetic resonance experiments.* Physical Review, 1954. **94**(3): p. 630-638.

Characklis, W.G. and K.C. Marshall, Eds., *Biofilms*. 1990, New York: John Wiley & Sons, Inc.

Chen, M.J., Z. Zhang, and T.R. Bott, *Effects of operating conditions on the adhesive strength of Pseudomonas fluorescens biofilms in tubes.* Colloids and Surfaces B: Biointerfaces, 2005. **43**(2): p. 61-71.

Coates, G.R., et al., *A new characterization of bulk-volume irreducible using magnetic resonance*. Log Analyst, 1998. **39**(1): p. 51-63.

Coates, G.R., L. Xiao, and M.G. Prammer, *NMR Logging: Principles and Applications*. 1999, Halliburton Energy Services: Houston.

Codd, S.L., et al., *Magnetic Resonance Microscopy of Biofilm and Bioreactor Transport*, in *NMR Imaging in Chemical Engineering*, S. Stapf and S.-I. Han, Editors. 2006, Wiley: USA.

Codd, S.L., et al., *NMR relaxation measurements of biofouling in model and geological porous media.* Organic Geochemistry, 2011. **42**(8): p. 965-971.

Costerton, J.W., *Introduction to biofilm.* International Journal of Antimicrobial Agents, 1999. **11**(3-4): p. 217-221.

Costerton, J.W., et al., *Microbial Biofilms.* Annual Review of Microbiology, 1995. **49**: p. 711-745.

Costerton, J.W., P.S. Stewart, and E.P. Greenberg, *Bacterial biofilms: A common cause of persistent infections.* Science, 1999. **284**(5418): p. 1318-1322.

Cunningham, A.B., E.J. Bouwer, and W.G. Characklis, *Biofilms in porous media*, in *Biofilms*, W.G. Characklis and K.C. Marshall, Editors. 1990, John Wiley & Sons, Inc.: New York. p. 697-732.

Cunningham, A.B., et al., *Influence of biofilm accumulation on porous-media hydrodynamics.* Environmental Science & Technology, 1991. **25**(7): p. 1305-1311.

Cunningham, A.B., et al., *Abandoned well CO_2 leakage mitigation using biologically induced mineralization: current progress and future directions.* Greenhouse Gases-Science and Technology, 2013. **3**(1): p. 40-49.

Cunningham, A.B., et al., *Subsurface biofilm barriers for the containment and remediation of contaminated groundwater.* Bioremediation Journal, 2003. **7**(3-4): p. 151-164.

Dammel, E.E. and E.D. Schroeder, *Density of activated sludge solids.* Water Research, 1991. **25**(7): p. 841-846.

Da-Wen, G. and T. Yu, *Versatility and application of anaerobic ammonium-oxidizing bacteria.* Applied Microbiology & Biotechnology, 2011. **91**(4): p. 887-894.

de Kreuk, M., J.J. Heijnen, and M.C.M. van Loosdrecht, *Simultaneous COD, nitrogen, and phosphate removal by aerobic granular sludge.* Biotechnology and Bioengineering, 2005. **90**(6): p. 761-769.

de Kreuk, M.K., et al., *Behavior of polymeric substrates in an aerobic granular sludge system.* Water Research, 2010. **44**(20): p. 5929-5938.

de Kreuk, M.K., N. Kishida, and M.C.M. van Loosdrecht, *Aerobic granular sludge - state of the art.* Water Science and Technology, 2007. **55**(8-9): p. 75-81.

de Kreuk, M.K., M. Pronk, and M.C.M. van Loosdrecht, *Formation of aerobic granules and conversion processes in an aerobic granular sludge reactor at moderate and low temperatures.* Water Research, 2005. **39**(18): p. 4476-4484.

de Kreuk, M.K. and M.C.M. van Loosdrecht, *Selection of slow growing organisms as a means for improving aerobic granular sludge stability.* Water Science and Technology, 2004. **49**(11-12): p. 9-17.

de Kreuk, M.K. and M.C.M. van Loosdrecht, *Formation of aerobic granules with domestic sewage.* Journal of Environmental Engineering-ASCE, 2006. **132**(6): p. 694-697.

De Muynck, W., N. De Belie, and W. Verstraete, *Microbial carbonate precipitation in construction materials: A review.* Ecological Engineering, 2010. **36**(2): p. 118-136.

Debeer, D., et al., *Effects of biofilm structures on oxygen distribution and mass transport.* Biotechnology and Bioengineering, 1994. **43**(11): p. 1131-1138.

Decho, A.W., *Overview of biopolymer-induced mineralization: What goes on in biofilms?* Ecological Engineering, 2010. **36**(2): p. 137-144.

DeJong, J.T., et al., *Bio-mediated soil improvement.* Ecological Engineering, 2010. **36**(2): p. 197-210.

Dejong, J.T., et al., *Biogeochemical processes and geotechnical applications: progress, opportunities and challenges.* Geotechnique, 2013. **63**(4): p. 287-301.

Derlacki, Z.J., et al., *Diffusion coefficients of methanol and water and the mutual diffusion coefficient in methanol-water solutions at 278 and 298 K.* Journal of Physical Chemistry, 1985. **89**(24): p. 5318-5322.

Dlubac, K., et al., *Use of NMR logging to obtain estimates of hydraulic conductivity in the High Plains aquifer, Nebraska, USA.* Water Resources Research, 2013. **49**(4): p. 1871-1886.

Drescher, K., et al., *Biofilm streamers cause catastrophic disruption of flow with consequences for environmental and medical systems.* Proceedings of the National Academy of Sciences of the United States of America, 2013. **110**(11): p. 4345-4350.

Eberl, H.J., et al., *A three-dimensional numerical study on the correlation of spatial structure, hydrodynamic conditions, and mass transfer and conversion in biofilms.* Chemical Engineering Science, 2000. **55**(24): p. 6209-6222.

Ebigbo, A., et al., *Darcy-scale modeling of microbially induced carbonate mineral precipitation in sand columns.* Water Resources Research, 2012. **48**.

Etterer, T. and P.A. Wilderer, *Generation and properties of aerobic granular sludge.* Water Science and Technology, 2001. **43**(3): p. 19-26.

Evangelou, V.P. and Y.L. Zhang, *A review: Pyrite oxidation mechanisms and acid mine drainage prevention.* Critical Reviews in Environmental Science and Technology, 1995. **25**(2): p. 141-199.

Fabich, H., et al., *Microbial and algal alginate gelation characterized by magnetic resonance.* Journal of Biotechnology, 2012. **61**(3): p. 320– 327.

Fay, E.L. and R.J. Knight, *Detecting and quantifying organic contaminants in sediments with nuclear magnetic resonance.* Geophysics, 2016. **81**(6): p. EN87.

Fay, E.L., R.J. Knight, and Y.Q. Song, *Investigating internal magnetic field gradients in aquifer sediments.* Geophysics, 2015. **80**(3): p. D281-D294.

Ferris, F.G., et al., *Kinetics of calcite precipitation induced by ureolytic bacteria at 10 to 20 degrees C in artificial groundwater.* Geochimica Et Cosmochimica Acta, 2003. **67**(8): p. 1701-1722.

Flemming, H.-C. and J. Wingender, *The biofilm matrix.* Nature Reviews Microbiology, 2010. **8**(9): p. 623-633.

Foerster, E., H. Nirschl, and G. Guthausen, *NMR Diffusion and Relaxation for Monitoring of Degradation in Motor Oils.* Applied Magnetic Resonance, 2017. **48**(1): p. 51-65.

Foley, I., S.A. Farooqui, and R.L. Kleinberg, *Effect of paramagnetic ions on NMR relaxation of fluids at solid surfaces.* Journal of Magnetic Resonance Series A, 1996. **123**(1): p. 95-104.

Freedman, R., *Advances in NMR Logging.* Journal of Petroleum Technology, 2006. **58**(1): p. 60-66.

Fridjonsson, E.O., et al., *NMR measurement of hydrodynamic dispersion in porous media subject to biofilm mediated precipitation reactions.* Journal of Contaminant Hydrology, 2011. **120-21**: p. 79-88.

Fukushima, E., *Nuclear magnetic resonance as a tool to study flow.* Annual Review of Fluid Mechanics, 1999. **31**(1): p. 95.

Gilbert, E.M., et al., *Low Temperature Partial Nitritation/Anammox in a Moving Bed Biofilm Reactor Treating Low Strength Wastewater.* Environmental Science & Technology, 2014. **48**(15): p. 8784-8792.

Gjersing, E.L., et al., *Magnetic resonance microscopy analysis of advective transport in a biofilm reactor.* Biotechnology and Bioengineering, 2005. **89**(7): p. 822-834.

Godefroy, S., et al., *Surface nuclear magnetic relaxation and dynamics of water and oil in macroporous media.* Physical Review E, 2001. **64**(2): p. 021605-1 - 021605-13.

Goga, N.O., et al., *Mobile NMR: applications to materials and biomedicine.* Journal of Optoelectronics and Advanced Materials, 2006. **8**(4): p. 1430-1434.

Gonzalez-Gil, G., et al., *Cluster structure of anaerobic aggregates of an expanded granular sludge bed reactor.* Applied and Environmental Microbiology, 2001. **67**(8): p. 3683-3692.

Grunewald, E. and R. Knight, *A laboratory study of NMR relaxation times in unconsolidated heterogeneous sediments.* Geophysics, 2011. **76**(4): p. G73-G83.

Guan, X.Z., et al., *PFG-NMR on W1/O/W2-emulsions: Evidence for molecular exchange between water phases.* European Journal of Lipid Science and Technology, 2010. **112**(8): p. 828-837.

Guimera, X., et al., *Dynamic characterization of external and internal mass transport in heterotrophic biofilms from microsensors measurements.* Water Research, 2016. **102**: p. 551-560.

Hahn, E.L., *Spin Echoes.* Physical Review, 1950. **80**: p. 580-594.

Herigstad, B., M. Hamilton, and J. Heersink, *How to optimize the drop plate method for enumerating bacteria.* Journal of Microbiological Methods, 2001. **44**(2): p. 121-129.

Herrling, M.P., et al., *Determining the Flow Regime in a Biofilm Carrier by Means of Magnetic Resonance Imaging.* Biotechnology and Bioengineering, 2015. **112**(5): p. 1023-1032.

Herrling, M.P., et al., *Short and long term biosorption of silica-coated iron oxide nanoparticles in heterotrophic biofilms.* Science of The Total Environment, 2016. **544**: p. 722-729.

Hertrich, M., *Imaging of groundwater with nuclear magnetic resonance.* Progress in Nuclear Magnetic Resonance Spectroscopy, 2008. **53**(4): p. 227-248.

Hille, A., et al., *Effective Diffusivities and Mass Fluxes in Fungal Biopellets.* Biotechnology and Bioengineering, 2009. **103**(6): p. 1202-1213.

Hills, B.P., C. Cano, and P.S. Belton, *Proton NMR relaxation studies of aqueous polysaccharide systems.* Macromolecules, 1991. **24**(10): p. 2944-2950.

Horn, H. and S. Lackner, *Modeling of Biofilm Systems: A Review*, in *Productive Biofilms*, K. Muffler and R. Ulber, Editors. 2014, Springer-Verlag Berlin: Berlin. p. 53-76.

Horn, H., H. Reiff, and E. Morgenroth, *Simulation of growth and detachment in biofilm systems under defined hydrodynamic conditions.* Biotechnology and Bioengineering, 2003. **81**(5): p. 607-617.

Hornemann, J.A., et al., *Biopolymer and water dynamics in microbial biofilm extracellular polymeric substance.* Biomacromolecules, 2008. **9**(9): p. 2322-2328.

Hoskins, B.C., et al., *Selective imaging of biofilms in porous media by NMR relaxation.* Journal of Magnetic Resonance, 1999. **139**(1): p. 67-73.

IWA, *IWA Task Group on Biofilm Modeling: Mathematical Modeling of Biofilms*. 2006: IWA Publishing.

Jaeger, F., et al., *Evaluation of 1H NMR relaxometry for the assessment of pore-size distribution in soil samples.* European Journal of Soil Science, 2009. **60**(6): p. 1052-1064.

Jaeger, F., E. Grohmann, and G.E. Schaumann, *1H NMR relaxometry in natural humous soil samples: insights in microbial effects on relaxation time distributions.* Plant and Soil, 2006. **280**(1-2): p. 209-222.

Johns, M., et al., *Mobile NMR and MRI: Developments and Applications*. New Developments in NMR. 2015: Royal Society of Chemistry.

Juang, Y.-C., et al., *Stable aerobic granules for continuous-flow reactors: Precipitating calcium and iron salts in granular interiors.* Bioresource Technology, 2010. **101**(21): p. 8051-8057.

Juncher Jørgensen, C., et al., *Microbial Oxidation of Pyrite Coupled to Nitrate Reduction in Anoxic Groundwater Sediment.* Environmental Science & Technology, 2009. **43**(13): p. 4851-4857.

Jung, D., et al., *New colorimetric reaction for endpoint, continuous-flow and kinetic measurement of urea* Clinical Chemistry, 1975. **21**(8): p. 1136-1140.

Kao, C.M., et al., *Biobarrier system for remediation of TCE-contaminated aquifers.* Bulletin of Environmental Contamination and Toxicology, 2004. **72**(1): p. 87-93.

Kao, C.M., et al., *Enhanced PCE dechlorination by biobarrier systems under different redox conditions.* Water Research, 2003. **37**(20): p. 4885-4894.

Kapellos, G.E., T.S. Alexiou, and A.C. Payatakes, *Hierarchical simulator of biofilm growth and dynamics in granular porous materials.* Advances in Water Resources, 2007. **30**(6–7): p. 1648-1667.

Kausik, R. and M.D. Hurlimann, *Sensitivity and resolution of two-dimensional NMR diffusion-relaxation measurements.* Journal of Magnetic Resonance, 2016. **270**: p. 12-23.

Keating, K. and R. Knight, *A laboratory study to determine the effect of iron oxides on proton NMR measurements.* Geophysics, 2007. **72**(1): p. E27-E32.

Keating, K. and R. Knight, *A laboratory study of the effect of magnetite on NMR relaxation rates.* Journal of Applied Geophysics, 2008. **66**(3-4): p. 188-196.

Keating, K. and R. Knight, *A laboratory study of the effect of Fe(II)-bearing minerals on nuclear magnetic resonance (NMR) relaxation measurements.* Geophysics, 2010. **75**(3): p. F71-F82.

Kenyon, W.E., *Petrophysical principles of applications of NMR logging.* The Log Analyst, 1997. **38**(2): p. 21-43.

Kenyon, W.E., et al., *A three-part study of NMR longitudinal relaxation properties of water-saturated sandstones.* SPE Formation Evaluation, 1988. **3**(3): p. 622-636.

Kenyon, W.E. and J.A. Kolleeny, *NMR surface relaxivity of calcite with adsorbed Mn2+.* Journal of Colloid and Interface Science, 1995. **170**(2): p. 502-514.

Kim, G., S. Lee, and Y. Kim, *Subsurface biobarrier formation by microorganism injection for contaminant plume control.* Journal of Bioscience and Bioengineering, 2006. **101**(2): p. 142-148.

Kimmich, R., *NMR - Tomography, Diffusometry, Relaxometry.* Springer Verlag, 1997.

Kirkland, C.M., et al., *In Situ Detection of Subsurface Biofilm Using Low-Field NMR: A Field Study*. Environmental Science & Technology, 2015. **49**(18): p. 11045-11052.

Kirkland, C.M., et al., *Biofilm Detection in a Model Well-Bore Environment Using Low-Field NMR.* Ground Water Monitoring and Remediation, 2015. **35**(4): p. 36-44.

Kirkland, C.M., et al., *Detecting microbially-induced calcite precipitation (MICP) in a model well-bore using downhole low-field NMR.* Environmental Science & Technology, 2016. **10.1021/acs.est.6b04833**.

Kleinberg, R.L., Kenyon, W.E., Mitra, P.P., *Mechanism of NMR relaxation of fluids in rock.* Journal of Magnetic Resonance Series A, 1994. **108**: p. 206-214.

Kleinberg, R.L., S.A. Farooqui, and M.A. Horsfield, *T(1)/T(2) ratio and frequency-dependence of NMR relaxation in porous sedimentary rocks.* Journal of Colloid and Interface Science, 1993. **158**(1): p. 195-198.

Kleinberg, R.L. and M.A. Horsfield, *Transverse relaxation processes in porous sedimentary rock.* Journal of Magnetic Resonance, 1990. **88**(1): p. 9-19.

Knight, R., et al., *Field experiment provides ground truth for surface nuclear magnetic resonance measurement.* Geophysical Research Letters, 2012. **39**.

Knight, R., et al., *NMR Logging to Estimate Hydraulic Conductivity in Unconsolidated Aquifers.* Groundwater, 2016. **54**(1): p. 104-114.

Koenig, S.H. and K.E. Kellar, *Theory of 1/T-1 and 1/T-2 NMRD profiles of solutions of magnetic nanoparticles* Magnetic Resonance in Medicine, 1995. **34**(2): p. 227-233.

Komlos, J., et al., *Biofilm barriers to contain and degrade dissolved trichloroethylene.* Environmental Progress, 2004. **23**(1): p. 69-77.

Korb, J.P., S. Godefroy, and M. Fleury, *Surface nuclear magnetic relaxation and dynamics of water and oil in granular packings and rocks.* Magnetic Resonance Imaging, 2003. **21**(3-4): p. 193-199.

Kreft, J.U., et al., *Individual-based modelling of biofilms.* Microbiology-Sgm, 2001. **147**: p. 2897-2912.

Kristian Stevik, T., et al., *Retention and removal of pathogenic bacteria in wastewater percolating through porous media: a review.* Water Research, 2004. **38**(6): p. 1355-1367.

LaGrega, M.D., P.L. Buckingham, and J.C. Evans, *Hazardous Waste Management*. 2nd ed. 2001, New York: McGraw-Hill.

Lauterbur, P.C., *Image formation by induced local interactions: examples employing nuclear magnetic resonance.* Nature, 1973. **242**: p. 190-191.

Lazarova, V. and J. Manem, *Biofilm characterization and activity analysis in water and waste-water treatment.* Water Research, 1995. **29**(10): p. 2227-2245.

Lee, J.H., et al., *2-Dimensional Inverse Laplace Transform Nmr - Altered Relaxation-Times Allow Detection of Exchange-Correlation.* Journal of the American Chemical Society, 1993. **115**(17): p. 7761-7764.

Lens, P.N.L., et al., *Diffusional properties of methanogenic granular sludge: H-1 NMR characterization.* Applied and Environmental Microbiology, 2003. **69**(11): p. 6644-6649.

Lewandowski, Z., et al., *NMR imaging of hydrodynamics near microbially colonized surfaces.* Water Science and Technology, 1992. **26**(3-4): p. 577-584.

Li, C.Y., et al., *Assessing the influence of biofilm surface roughness on mass transfer by combining optical coherence tomography and two-dimensional modeling.* Biotechnology and Bioengineering, 2016. **113**(5): p. 989-1000.

Lin, Y., et al., *Characterization of alginate-like exopolysaccharides isolated from aerobic granular sludge in pilot-plant.* Water Research, 2010. **44**(11): p. 3355-3364.

Liu, Y. and J.H. Tay, *The essential role of hydrodynamic shear force in the formation of biofilm and granular sludge.* Water Research, 2002. **36**(7): p. 1653-1665.

Loosdrecht, M.C.M.v., et al., *Experimental Methods in Wastewater Treatment*. 2016: Intl Water Assn, IWA.

Lotti, T., et al., *Pilot-scale evaluation of anammox-based mainstream nitrogen removal from municipal wastewater.* Environmental technology, 2015. **36**(9): p. 1167-77.

Maliva, R.G., E.A. Clayton, and T.M. Missimer, *Application of advanced borehole geophysical logging to managed aquifer recharge investigations.* Hydrogeology Journal, 2009. **17**(6): p. 1547-1556.

Manas, A., et al., *Location and chemical composition of microbially induced phosphorus precipitates in anaerobic and aerobic granular sludge.* Environmental Technology, 2012. **33**(19): p. 2195-2209.

Manz, B., et al., *Investigation of Biofilm Structure, Flow Patterns and Detachment with Magnetic Resonance Imaging.* Water Science and Technology, 2005. **52**(7): p. 1-6.

Marble, A.E., et al., *A constant gradient unilateral magnet for near-surface MRI profiling.* Journal of Magnetic Resonance, 2006. **183**(2): p. 228-234.

McLean, J.S., O.N. Ona, and P.D. Majors, *Correlated biofilm imaging, transport and metabolism measurements via combined nuclear magnetic resonance and confocal microscopy.* Isme Journal, 2008. **2**(2): p. 121-131.

Meiboom, S. and D. Gill, *Modified spin-echo method for measuring nuclear relaxation times.* Review of Scientific Instruments, 1958. **29**(8): p. 688-691.

Melton, E.D., et al., *The interplay of microbially mediated and abiotic reactions in the biogeochemical Fe cycle.* Nat Rev Micro, 2014. **12**(12): p. 797-808.

Metcalf & Eddy, I., *Wastewater engineering : treatment and reuse*. Fourth edition ed. 2003, Boston: McGraw-Hill, 2003.

Minsley, B.J., et al., *Evidence for nonuniform permafrost degradation after fire in boreal landscapes.* Journal of Geophysical Research: Earth Surface, 2016. **121**(2): p. 320-335.

Mitchell, A.C., et al., *Microbially Enhanced Carbon Capture and Storage by Mineral-Trapping and Solubility-Trapping.* Environmental Science and Technology, 2010. **44**(13): p. 5270-5276.

Mitchell, A.C., et al., *Resilience of planktonic and biofilm cultures to supercritical CO2.* Journal of Supercritical Fluids, 2008. **47**(2): p. 318-325.

Mortensen, B.M., et al., *Effects of environmental factors on microbial induced calcium carbonate precipitation.* Journal of Applied Microbiology, 2011. **111**(2): p. 338-349.

Mualem, Y., *Hysteretical models for prediction of hydraulic conductivity of unsaturated porous-media.* Transactions-American Geophysical Union, 1976. **57**(8): p. 602-603.

Neu, T.R., et al., *Advanced imaging techniques for assessment of structure, composition and function in biofilm systems.* FEMS Microbiology Ecology, 2010. **72**(1): p. 1-21.

Nicolella, C., M.C.M. van Loosdrecht, and J.J. Heijnen, *Wastewater treatment with particulate biofilm reactors.* Journal of Biotechnology, 2000. **80**(1): p. 1-33.

Packer, K.J. and C. Rees, *Pulsed NMR studies of restricted diffusion .1. Droplet size distributions in emulsions.* Journal of Colloid and Interface Science, 1972. **40**(2): p. 206-218.

Pal, A. and A.K. Paul, *Microbial extracellular polymeric substances: central elements in heavy metal bioremediation.* Indian Journal of Microbiology, 2008. **48**(1): p. 49-64.

Parsekian, A.D., et al., *Bootstrap Calibration and Uncertainty Estimation of Downhole NMR Hydraulic Conductivity Estimates in an Unconsolidated Aquifer.* Groundwater, 2015. **53**(1): p. 111-121.

Perlo, J., et al., *Optimized slim-line logging NMR tool to measure soil moisture in situ.* Journal of Magnetic Resonance, 2013. **233**: p. 74-79.

Petrova, O.E. and K. Sauer, *Sticky Situations: Key Components That Control Bacterial Surface Attachment.* Journal of Bacteriology, 2012. **194**(10): p. 2413-2425.

Peulen, T.-O. and K.J. Wilkinson, *Diffusion of Nanoparticles in a Biofilm.* Environmental Science & Technology, 2011. **45**(8): p. 3367-3373.

Pfeuffer, J., et al., *Restricted diffusion and exchange of intracellular water: Theoretical modelling and diffusion time dependence of 1H NMR measurements on perfused glial cells.* NMR in Biomedicine, 1998. **11**: p. 19-31.

Pfeuffer, J., U. Flögel, and D. Leibfritz, *Monitoring of cell volume and water exchange time in perfused cells by diffusion-weighted 1H NMR spectroscopy.* NMR in Biomedicine, 1998. **11**: p. 11-18.

Phillips, A.J., et al., *Fracture Sealing with Microbially-Induced Calcium Carbonate Precipitation: A Field Study.* Environmental Science & Technology, 2016. **50**(7): p. 4111-4117.

Phillips, A.J., et al., *Engineered applications of ureolytic biomineralization: a review.* Biofouling, 2013. **29**(6): p. 715-733.

Phillips, A.J., et al., *Potential CO2 Leakage Reduction through Biofilm-Induced Calcium Carbonate Precipitation.* Environmental Science & Technology, 2013. **47**(1): p. 142-149.

Phoenix, V.R. and W.M. Holmes, *Magnetic resonance imaging of structure, diffusivity, and copper immobilization in a phototrophic biofilm.* Applied and Environmental Microbiology, 2008. **74**(15): p. 4934-4943.

Picioreanu, C., J.U. Kreft, and M.C.M. van Loosdrecht, *Particle-based multidimensional multispecies Biofilm model.* Applied and Environmental Microbiology, 2004. **70**(5): p. 3024-3040.

Picioreanu, C., M.C.M. van Loosdrecht, and J.J. Heijnen, *Effect of diffusive and convective substrate transport on biofilm structure formation: A two-dimensional modeling study.* Biotechnology and Bioengineering, 2000. **69**(5): p. 504-515.

Pintelon, T.R.R., et al., *The effect of biofilm permeability on bio-clogging of porous media.* Biotechnology and Bioengineering, 2012. **109**(4): p. 1031-1042.

Poot, V., et al., *Effects of the residual ammonium concentration on NOB repression during partial nitritation with granular sludge.* Water Research, 2016. **106**: p. 518-530.

Potter, K., et al., *Assay for bacteria in porous media by diffusion-weighted NMR.* Journal of Magnetic Resonance. Series B, 1996. **113**: p. 9-15.

Prange, M. and Y.-Q. Song, *Quantifying uncertainty in NMR T-2 spectra using Monte Carlo inversion.* Journal of Magnetic Resonance, 2009. **196**(1): p. 54-60.

Pronk, M., et al., *Effect and behaviour of different substrates in relation to the formation of aerobic granular sludge.* Applied Microbiology and Biotechnology, 2015. **99**(12): p. 5257-5268.

Pronk, M., et al., *Full scale performance of the aerobic granular sludge process for sewage treatment.* Water Research, 2015. **84**: p. 207-217.

Provencher, S.W., *A constrained regularization method for inverting data represented by linear algebraic or integral equations* Computer Physics Communications, 1982. **27**(3): p. 213-227.

Ramanan, B., et al., *Magnetic Resonance Imaging of Mass Transport and Structure Inside a Phototrophic Biofilm.* Current Microbiology, 2013. **66**(5): p. 456-461.

Ranzinger, F., et al., *Direct surface visualization of biofilms with high spin coordination clusters using Magnetic Resonance Imaging.* Acta Biomaterialia, 2016. **31**: p. 167-177.

Renslow, R.S., et al., *In Situ Effective Diffusion Coefficient Profiles in Live Biofilms Using Pulsed-Field Gradient Nuclear Magnetic Resonance.* Biotechnology and Bioengineering, 2010. **106**(6): p. 928-937.

Robinson, D.A., et al., *Soil moisture measurement for ecological and hydrological watershed-scale observatories: A review.* Vadose Zone Journal, 2008. **7**(1): p. 358-389.

Röding, M., et al., *The gamma distribution model for pulsed-field gradient NMR studies of molecular-weight distributions of polymers.* Journal of Magnetic Resonance, 2012. **222**: p. 105-111.

Röding, M., N. Williamson, and M. Nydén, *Gamma convolution models for self-diffusion coefficient distributions in PGSE NMR.* Journal of Magnetic Resonance, 2015. **261**: p. 6-10.

Sanderlin, A.B., et al., *Biofilm detection in natural unconsolidated porous media using a low-field magnetic resonance system.* Environmental Science & Technology, 2013. **47**(2): p. 987-992.

Sauer, K., et al., *Pseudomonas aeruginosa displays multiple phenotypes during development as a biofilm.* Journal of Bacteriology, 2002. **184**(4): p. 1140-1154.

Seymour, J.D., et al., *Magnetic resonance microscopy of biofilm structure and impact on transport in a capillary bioreactor.* Journal of Magnetic Resonance, 2004. **167**(322-327).

Seymour, J.D., et al., *Anomalous fluid transport in porous media induced by biofilm growth.* Physical Review Letters, 2004. **93**(19).

Seymour, J.D., et al., *Magnetic resonance microscopy of biofouling induced scale dependent transport in porous media.* Advances in Water Resources, 2007. **30**(6-7): p. 1408-1420.

Sham, E., et al., *Monitoring bacterially induced calcite precipitation in porous media using magnetic resonance imaging and flow measurements.* Journal of Contaminant Hydrology, 2013. **152**: p. 35-43.

Song, Y.Q., *Recent Progress of Nuclear Magnetic Resonance Applications in Sandstones and Carbonate Rocks.* Vadose Zone Journal, 2010. **9**(4): p. 828-834.

Song, Y.Q., et al., *T-1-T-2 correlation spectra obtained using a fast two-dimensional Laplace inversion.* Journal of Magnetic Resonance, 2002. **154**(2): p. 261-268.

Staudt, C., et al., *Volumetric measurements of bacterial cells and extracellular polymeric substance glycoconjugates in biofilms.* Biotechnology and Bioengineering, 2004. **88**(5): p. 585-592.

Stejskal, E.O. and J.E. Tanner, *Spin diffusion measurements: Spin echoes in the presence of a time-dependent field gradient.* Journal of Chemical Physics, 1965. **42**: p. 288.

Stewart, P.S., *A review of experimental measurements of effective diffusive permeabilities and effective diffusion coefficients in biofilms.* Biotechnology and Bioengineering, 1998. **59**(3): p. 261-272.

Stewart, P.S., *Diffusion in biofilms.* Journal of Bacteriology, 2003. **185**(5): p. 1485-1491.

Stewart, P.S. and M.J. Franklin, *Physiological heterogeneity in biofilms.* Nature Reviews Microbiology, 2008. **6**(3): p. 199-210.

Stewart, T.L. and H.S. Fogler, *Biomass plug development and propagation in porous media.* Biotechnology and Bioengineering, 2001. **72**(3): p. 353-363.

Stoodley, P., D. Debeer, and Z. Lewandowski, *Liquid flow in biofilm systems.* Applied and Environmental Microbiology, 1994. **60**(8): p. 2711-2716.

Stoodley, P., et al., *Biofilms as complex differentiated communities.* Annual Review of Microbiology, 2002. **56**: p. 187-209.

Straley, C., et al., *Core analysis by low-field NMR.* The Log Analyst, 1997. **38**(2): p. 84-94.

Sucre, O., et al., *Low-field NMR logging sensor for measuring hydraulic parameters of model soils.* Journal of Hydrology, 2011. **406**(1–2): p. 30-38.

Sutherland, I.W., *Biofilm exopolysaccharides: a strong and sticky framework.* Microbiology, 2001. **147**: p. 3-9.

Sutherland, I.W., *The biofilm matrix - an immobilized but dynamic microbial environment.* Trends in Microbiology, 2001. **9**(5): p. 222-227.

Tay, J.H., Q.S. Liu, and Y. Liu, *The role of cellular polysaccharides in the formation and stability of aerobic granules.* Letters in Applied Microbiology, 2001. **33**(3): p. 222-226.

Taylor, S.W. and P.R. Jaffe, *Biofilm growth and the related changes in the physical properties of a porous medium. 1. Experimental investigation.* Water Resources Research, 1990. **26**(9): p. 2153-2159.

Taylor, S.W. and P.R. Jaffe, *Enhanced in-situ biodegradation and aquifer permeability reduction.* Journal of Environmental Engineering-ASCE, 1991. **117**(1): p. 25-46.

Thullner, M. and P. Baveye, *Computational pore network modeling of the influence of biofilm permeability on bioclogging in porous media.* Biotechnology and Bioengineering, 2008. **99**(6): p. 1337-1351.

Timur, A., *Pulsed nuclear magnetic resonance studies of porosity, movable fluid, and permeability of sandstones.* Journal of Petroleum Technology, 1969. **21**(JUN): p. 775-&.

Torrey, H.C., *Bloch Equations with Diffusion Terms.* Physical Review, 1956. **104**(3): p. 563-565.

Tychonoff, A.N. and V.Y. Arsenin, *Solution of ill-posed problems*. 1977, Washington: Winston and Sons.

Van As, H. and P. Lens, *Use of H-1 NMR to study transport processes in porous biosystems.* Journal of Industrial Microbiology & Biotechnology, 2001. **26**(1-2): p. 43-52.

Van Genuchten, M.T., *A closed form equation for predicting the hydraulic conductivity of unsaturated soils.* Soil Science Society of America Journal, 1980. **44**(5): p. 892-898.

van Paassen, L.A., et al., *Quantifying Biomediated Ground Improvement by Ureolysis: Large-Scale Biogrout Experiment.* Journal of Geotechnical and Geoenvironmental Engineering, 2010. **136**(12): p. 1721-1728.

Vandevivere, P. and P. Baveye, *Effect of bacterial extracellular polymers on the saturated hydraulic conductivity of sand columns.* Applied and Environmental Microbiology, 1992. **58**(5): p. 1690-1698.

Venkataramanan, L., Y.Q. Song, and M.D. Hurlimann, *Solving Fredholm integrals of the first kind with tensor product structure in 2 and 2.5 dimensions.* Ieee Transactions on Signal Processing, 2002. **50**(5): p. 1017-1026.

Vogt, M., H.C. Flemming, and W.S. Veeman, *Diffusion in Pseudomonas aeruginosa biofilms: a pulsed field gradient NMR study.* Journal of Biotechnology, 2000. **77**(1): p. 137-146.

Vogt, S.J., et al., *Permeability of a growing biofilm in a porous media fluid flow analyzed by magnetic resonance displacement-relaxation correlations.* Biotechnology and Bioengineering, 2013. **110**(5): p. 1366-1375.

von der Schulenburg, D.A.G., et al., *Spatially resolved quantification of metal ion concentration in a biofilm-mediated ion exchanger.* Biotechnology and Bioengineering, 2008. **99**(4): p. 821-829.

von der Schulenburg, D.A.G., et al., *Three-Dimensional Simulations of Biofilm Growth in Porous Media.* AIChE Journal, 2009. **55**(2): p. 494-504.

Wagner, J., et al., *Effect of particulate organic substrate on aerobic granulation and operating conditions of sequencing batch reactors.* Water Research, 2015. **85**: p. 158-166.

Wagner, M., et al., *Online assessment of biofilm development, sloughing and forced detachment in tube reactor by means of magnetic resonance microscopy.* Biotechnology and Bioengineering, 2010. **107**(1): p. 172-181.

Walsh, D., *Environmental Geophysics: Portable NMR tools for measuring and monitoring soil moisture*, in *Preview*. 2015, CSIRO Publishing. p. 41-42.

Walsh, D., et al., *A small-diameter NMR logging tool for groundwater investigations.* Groundwater, 2013. **51**(6): p. 914-926.

Walsh, D.O., et al., *Javelin: A slim-hole and microhole NMR logging tool.* Fast Times, 2010. **15**(3): p. 67-72.

Wäsche, S., H. Horn, and D.C. Hempel, *Influence of growth conditions on biofilm development and mass transfer at the bulk/biofilm interface.* Water Research, 2002. **36**: p. 4775-4784.

Wheeler, L.A., *Establishment of ureolytic biofilms and their influence on the permeability of pulse-flow porous media column systems.* 2009, Montana State University, Bozeman, MT.

Windt, C.W., F.J. Vergeldt, and H. Van As, *Correlated displacement-T-2 MRI by means of a Pulsed Field Gradient-Multi Spin Echo method.* Journal of Magnetic Resonance, 2007. **185**(2): p. 230-239.

Winkler, M.K.H., et al., *Factors influencing the density of aerobic granular sludge.* Applied Microbiology and Biotechnology, 2013. **97**(16): p. 7459-7468.

Wood, B.D., M. Quintard, and S. Whitaker, *Calculation of effective diffusivities for biofilms and tissues.* Biotechnology and Bioengineering, 2002. **77**(5): p. 495-516.

Xavier, J.B., et al., *Biofilm-control strategies based on enzymic disruption of the extracellular polymeric substance matrix - a modelling study.* Microbiology-Sgm, 2005. **151**: p. 3817-3832.

Zhang, Q., et al. *Some exceptions to default NMR rock and fluid properties*. in *Transactions of the SPWLA Annual Logging Symposium (Society of Professional Well Log Analysts)*. 1998.